REPORT DOCUMENTATION PAGE

Form Approved OMB NO. 0704-0188

The public reporting burden for this collection of information is estimated to average 1 hour per response, including the time for reviewing instructions, searching existing data sources, gathering and maintaining the data needed, and completing and reviewing the collection of information. Send comments regarding this burden estimate or any other aspect of this collection of information, including suggesstions for reducing this burden, to Washington Headquarters Services, Directorate for Information Operations and Reports, 1215 Jefferson Davis Highway, Suite 1204, Arlington VA, 22202-4302. Respondents should be aware that notwithstanding any other provision of law, no person shall be subject to any oenalty for failing to comply with a collection of information if it does not display a currently valid OMB control number.
PLEASE DO NOT RETURN YOUR FORM TO THE ABOVE ADDRESS.

1. REPORT DATE (DD-MM-YYYY)	2. REPORT TYPE	3. DATES COVERED (From - To)
14-01-2019	Final Report	25-Jun-2013 - 31-Dec-2016

4. TITLE AND SUBTITLE
Final Report: Electron-Phonon Coupling in Atomic-Scale Two-Dimensional Chalcogenide Nanosheets

5a. CONTRACT NUMBER
W911NF-13-1-0201

5b. GRANT NUMBER

5c. PROGRAM ELEMENT NUMBER
611102

6. AUTHORS

5d. PROJECT NUMBER

5e. TASK NUMBER

5f. WORK UNIT NUMBER

7. PERFORMING ORGANIZATION NAMES AND ADDRESSES
North Carolina State University
2701 Sullivan Drive
Admin Srvcs III, Box 7514
Raleigh, NC 27695 -7514

8. PERFORMING ORGANIZATION REPORT NUMBER

9. SPONSORING/MONITORING AGENCY NAME(S) AND ADDRESS (ES)
U.S. Army Research Office
P.O. Box 12211
Research Triangle Park, NC 27709-2211

10. SPONSOR/MONITOR'S ACRONYM(S)
ARO

11. SPONSOR/MONITOR'S REPORT NUMBER(S)
63599-MS-YIP.17

12. DISTRIBUTION AVAILIBILITY STATEMENT
Approved for public release; distribution is unlimited.

13. SUPPLEMENTARY NOTES
The views, opinions and/or findings contained in this report are those of the author(s) and should not contrued as an official Department of the Army position, policy or decision, unless so designated by other documentation.

14. ABSTRACT

15. SUBJECT TERMS

16. SECURITY CLASSIFICATION OF:			17. LIMITATION OF ABSTRACT	15. NUMBER OF PAGES	19a. NAME OF RESPONSIBLE PERSON
a. REPORT	b. ABSTRACT	c. THIS PAGE			Linyou Cao
UU	UU	UU	UU		19b. TELEPHONE NUMBER 919-515-5407

RPPR Final Report
as of 15-Jan-2019

Agency Code:

Proposal Number: 63599MSYIP **Agreement Number: W911NF-13-1-0201**
INVESTIGATOR(S):

Name: Linyou Cao
Email: lcao2@ncsu.edu
Phone Number: 9195155407
Principal: Y

Organization: **North Carolina State University**
Address: 2701 Sullivan Drive, Raleigh, NC 276957514
Country: USA

DUNS Number: 042092122 EIN: 566000756
Report Date: 31-Mar-2017 Date Received: 14-Jan-2019
Final Report for Period Beginning 25-Jun-2013 and Ending 31-Dec-2016
Title: Electron-Phonon Coupling in Atomic-Scale Two-Dimensional Chalcogenide Nanosheets
Begin Performance Period: 25-Jun-2013 **End Performance Period:** 31-Dec-2016
Report Term: 0-Other

Submitted By: Linyou Cao Email: lcao2@ncsu.edu
Phone: (919) 515-5407

Distribution Statement: 1-Approved for public release; distribution is unlimited.

STEM Degrees: 5 **STEM Participants:** 9

Major Goals: The main goal of this project is to study the synthesis and properties of two-dimensional (2D) layered chalcogenide materials and to develop process for the controlled scalable synthesis of these materials.

Accomplishments: 1. A US patent on the controlled scalable synthesis of 2D materials: 9,527,062 B2

2. Spun off a start-up company, Atomix Inc. (dba 2Dlayer, 2dlayer.com) based on the patented technique, which has already received $1 million angel investment

3. 30+ contributed and invited presentations

4. 14 peer-reviewed papers published , four of which are highly cited papers.

Alper Gurarslan, Shuping Jiao, Tai-De Li, Guoqing Li, Yiling Yu, Yang Gao, Elisa Riedo, Zhiping Linyou Cao, Van der Waals Force Isolation of Monolayer MoS2, Adv. Mater. 28, 10055(2016)

Lujun Huang, Guoqing Li, Yiling Yu, Linyou Cao, Atomically Thin MoS2 Narrowband and Broadband Light Superabsorbers, ACS Nano, 10, 7493, (2016)

Yifei Yu, Shi Hu, Liqin Su, Alexander A. Puretzky, David B. Geohegan, Yong Zhang, Linyou Cao, Equally Efficient Interlayer Excitonic Relaxation and Improved Absorption in Epitaxial and Non-epitaxial Monolayer MoS2/WS2 Heterostructures, Nano Lett. 15, 486-491 (2015). ESI Highly Cited Paper

Yifei Yu, Shengyang Huang, Yanpeng Li, Stephan Steinmann, Weitao Yang, Linyou Cao , Layer-dependent Electrocatalysis of MoS2 for Hydrogen Evolution, Nano Lett. 14, 553-558 (2014). ESI Highly Cited Paper

Cong Mai, Andrew Barrette, Yefei Yu, Yuriv Semenov, Ki Wook Kim, Linyou Cao, Kenan Gundogdu, Many Body Effects in Valleytronics: Direct Measurement of Valley Lifetimes in Single Layer MoS2, Nano Lett. 14, 202-206 (2014). ESI Highly Cited Paper

Yifei Yu, Chun Li, Yi Liu, Liqin Su, Yong Zhang, Linyou Cao, Controlled Scalable Synthesis of Uniform, High Quality Monolayer and Fewlayer MoS2 Films, Sci. Rep. 3, 1866 (2013) ESI Highly Cited Paper

Yiling Yu, Yifei Yu, Yongqing Cui, Wei Li, Alper Gurarslan, Hartwin Peelaers, David E. Aspnes, Chris G. Van de

Walle, Nhan V. Nguyen, Yong-Wei Zhang, Linyou Cao, Exciton-dominated Optical Functions of MoS2 Atomically Thin Films, Sci. Rep., 5, 16996 (2015)

Liang Huang, Yifei Yu, Chun Li, Linyou Cao, Substrate Mediation in Vapor Deposition Growth of Layered Chalcogenide Nanoplates: A Case Study of SnSe2, J. Phys. Chem. C 117, 6469-6475 (2013)

Alper Gurarslan, Yifei Yu, Liqin Su, Yiling Yu, Francisco Suarez, Shanshan Yao, Yong Zhu, Mehmet Ozturk, Yong Zhang, Linyou Cao, Surface Energy-Assisted Perfect Transfer of Centimeter-scale Monolayer and Fewlayer MoS2 Films onto Arbitrary Substrates, ACS Nano, 8, 11522-11528 (2014)

Chun Li, Yifei Yu, Miaofang Chi, Linyou Cao, Epitaxial Nanosheet - Nanowire Heterostructures, Nano Lett. 13, 948-953 (2013) .

E. M. Mannebach, S. Nah, Y. Kuo, Y. Yu, K. N. Duerloo, A. Marshall, E. J. Reed, L. Cao, A. M. Lindenberg, Ultrafast Nonlinear Optical Response of Monolayer MoS2 under Intense Photoexcitation Conditions, ACS Nano 8, 10734-10742 (2014)

Cong Mai, Yuriy G. Semenov, Andrew Barrette, Yifei Yu, Zhenghe Jin, Linyou Cao, Ki Wook Kim, Kenan Gundogdu, Exciton valley relaxation in a single layer of WS2 measured by ultrafast spectroscopy, Phys. Rev. B, 90, 041414(2014).

Liqin Su, Yong Zhang, Yifei Yu, Linyou Cao, Dependence of Coupling of Quasi 2-D MoS2 with Substrate on Substrate Type, Probed by Temperature Dependent Raman Scattering, Nanoscale , 6, 4920-4927 (2014).

Chun Li, Liang Huang, Gayatri Snyder, Yifei Yu, Linyou Cao, Role of Boundary Layer Diffusion in Vapor Deposition Growth of Chalcogenide Nanosheets: The Case of GeS, ACS Nano 6, 8868-8877 (2012) .

Training Opportunities: Multiple graduate, undergraduate, and high school students were involved in this project, receiving rigorous scientific training.
These include:
Graduate students: Alper Gurarslan, Yifei Yu, Yiling Yu, Lujun Huang
Undergraduate students: Thomas Payne , Brian Iezzi , Keith Vandegrift , Cody Heiman, Lin Zhu
High school students: Guy Blanc, Margaret Tian,Albert Feng , Ashley Yang,August Ning

RPPR Final Report
as of 15-Jan-2019

Results Dissemination: There results are reported in 3 dissertations, 13 peer-reviewed journal publications, 30+ invited and contributed presentations at major conferences, 18 invited seminars in world-class institutes, plus numerous news coverage by public and professional media worldwide.

Dissertations:

(2016) Yifei Yu: Two Dimensional Transition Metal Dichalcogenides: From Controlled Synthesis to Catalysis and Photonics
(2016) Yiling Yu: Engineering Light Matter Interaction of Atomically Thin Transition Metal Dichalcogenide Materials.
(2017) Lujun Huang: Engineering Optical and Thermal Properties of Two dimensional Transition Metal Dichalcogenide Monolayer

Journal Papers:

Alper Gurarslan, Shuping Jiao, Tai-De Li, Guoqing Li, Yiling Yu, Yang Gao, Elisa Riedo, Zhiping Linyou Cao, Van der Waals Force Isolation of Monolayer MoS2, Adv. Mater. 28, 10055(2016)

Lujun Huang, Guoqing Li, Yiling Yu, Linyou Cao, Atomically Thin MoS2 Narrowband and Broadband Light Superabsorbers, ACS Nano, 10, 7493, (2016)

Yifei Yu, Shi Hu, Liqin Su, Alexander A. Puretzky, David B. Geohegan, Yong Zhang, Linyou Cao, Equally Efficient Interlayer Excitonic Relaxation and Improved Absorption in Epitaxial and Non-epitaxial Monolayer MoS2/WS2 Heterostructures, Nano Lett. 15, 486-491 (2015). ESI Highly Cited Paper

Yifei Yu, Shengyang Huang, Yanpeng Li, Stephan Steinmann, Weitao Yang, Linyou Cao , Layer-dependent Electrocatalysis of MoS2 for Hydrogen Evolution, Nano Lett. 14, 553-558 (2014). ESI Highly Cited Paper

Cong Mai, Andrew Barrette, Yefei Yu, Yuriv Semenov, Ki Wook Kim, Linyou Cao, Kenan Gundogdu, Many Body Effects in Valleytronics: Direct Measurement of Valley Lifetimes in Single Layer MoS2, Nano Lett. 14, 202-206 (2014). ESI Highly Cited Paper

Yifei Yu, Chun Li, Yi Liu, Liqin Su, Yong Zhang, Linyou Cao, Controlled Scalable Synthesis of Uniform, High Quality Monolayer and Fewlayer MoS2 Films, Sci. Rep. 3, 1866 (2013) ESI Highly Cited Paper

Yiling Yu, Yifei Yu, Yongqing Cui, Wei Li, Alper Gurarslan, Hartwin Peelaers, David E. Aspnes, Chris G. Van de Walle, Nhan V. Nguyen, Yong-Wei Zhang, Linyou Cao, Exciton-dominated Optical Functions of MoS2 Atomically Thin Films, Sci. Rep., 5, 16996 (2015)

Liang Huang, Yifei Yu, Chun Li, Linyou Cao, Substrate Mediation in Vapor Deposition Growth of Layered Chalcogenide Nanoplates: A Case Study of SnSe2, J. Phys. Chem. C 117, 6469-6475 (2013)

Alper Gurarslan, Yifei Yu, Liqin Su, Yiling Yu, Francisco Suarez, Shanshan Yao, Yong Zhu, Mehmet Ozturk, Yong Zhang, Linyou Cao, Surface Energy-Assisted Perfect Transfer of Centimeter-scale Monolayer and Fewlayer MoS2 Films onto Arbitrary Substrates, ACS Nano, 8, 11522-11528 (2014)

Chun Li, Yifei Yu, Miaofang Chi, Linyou Cao, Epitaxial Nanosheet - Nanowire Heterostructures, Nano Lett. 13, 948-953 (2013) .

E. M. Mannebach, S. Nah, Y. Kuo, Y. Yu, K. N. Duerloo, A. Marshall, E. J. Reed, L. Cao, A. M. Lindenberg, Ultrafast Nonlinear Optical Response of Monolayer MoS2 under Intense Photoexcitation Conditions, ACS Nano 8, 10734-10742 (2014)

Cong Mai, Yuriy G. Semenov, Andrew Barrette, Yifei Yu, Zhenghe Jin, Linyou Cao, Ki Wook Kim, Kenan Gundogdu, Exciton valley relaxation in a single layer of WS2 measured by ultrafast spectroscopy, Phys. Rev. B, 90, 041414(2014).

Liqin Su, Yong Zhang, Yifei Yu, Linyou Cao, Dependence of Coupling of Quasi 2-D MoS2 with Substrate on Substrate Type, Probed by Temperature Dependent Raman Scattering, Nanoscale , 6, 4920-4927 (2014).

Chun Li, Liang Huang, Gayatri Snyder, Yifei Yu, Linyou Cao, Role of Boundary Layer Diffusion in Vapor Deposition Growth of Chalcogenide Nanosheets: The Case of GeS, ACS Nano 6, 8868-8877 (2012) .

Invited conference presentations:

1. “Extreme Manipulation of Light-matter Interactions in 2D TMDC Materials”, Micro- & Nano- Photonics Workshop, Fudan University, Shanghai, August 2016
2. “Extreme Manipulation of Light-matter Interactions in 2D TMDC Materials” PIERS conference, Shanghai, August 2016,
3. “Exciton dynamics engineering for high-luminescence efficiency of transition metal dichalcogenide monolayers ” SPIE Defense+Security Sensing Technology+Applications (SPIE DSS) conference, Baltimore, MD, April 2016,
4. “Engineering the Light-Matter Interactions at 2D TMDC Materials” Workshop on Science and Technology of 2D materials, University of Central Florida,, August 22, 2015
5. International Symposium on Physics and Device Applications of Two-dimensional Materials? Nanjing, China, July 13-15, 2015
6. NSF US-EU Workshop on 2D Layered Materials and Devices, Arlington,VA, April 22, 2015
7. Tutorial: 2D Transition Metal Dichalcogenide Materials: Syntheis, Properties, and Applications, MRS 2015 Spring Conference, San Francisco, April 6-10, 2015
8. 249th ACS meeting, Denver, CO, March 22-26, 2015.
9. MRS 2015 Spring Conference, San Francisco, April 6-10, 2015
10. GrapChina 2014, Ningbo, China, Sept. 1-3, 2014
11. 248th ACS National Meeting, San Francisco, CA, August 10-14, 2014.
12. Workshop on In Situ Probes for Investigating Solar Energy Conversion, Brookheaven National Lab, May 20, 2014
13. SPIE DSS14 Micro-Nanotechnology Sensors, Systems, and Applications Conference, Baltimore, MD, May 5-9, 2014
14. American Vacuum Society Annual Conference, Long Beach, California, Oct. 27, 2013

Invited Seminars:

1. Tutorial on 2D Transition Metal Dichalcogenide Materials, Center for the Computational Design of Functional Layered Materials, Temple University, Philadelphia, July 29, 2016
2. Department of Mechanical Engineering, Columbia University, Feb. 4, 2016
3. Duke Photonics Seminar, Duke University, September 15, 2015
4. Tutorial on 2D Transition Metal Dichalcogenide Materials, Center for the Computational Design of Functional Layered Materials, Temple University, Philadelphia, Oct. 2, 2015
5. Department of Materials Science and Engineering, University of Pennsylvania, October 1, 2015
6. Department of Physics, Fudan University, August 7, 2015
7. Joint School of Shanghai JiaoTong University and University of Michigan, August 2, 2015
8. Suzhou Institute of Nano-Tech and Nano-Bionics (SINANO), July 24, 2015
9. School of Materials Science and Engineering, Nanjing University of Science and Technology, July 15, 2015
10. Energy Science Institute, Yale University, April 27, 2015
11. Department of Physics, University of Kansas, Dec. 1, 2014
12. Department of Chemistry, Brown University, Oct. 30, 2014
13. Materials Research Lab, The University of California, Santa Barbara, Apr. 25, 2014
14. Materials Research Society Seminar, The University of North Carolina-Chapel Hill, Jan. 30, 2014
15. Joint School of Nanoscience and Nanoengineering, The University of North Carolina, Greensboro, Jan. 25, 2014
16. Department of Chemistry, Fudan University, China, Dec. 22, 2013
17. Department of Mechanical Engineering and Materials Science, Duke University, Nov. 18, 2013
18. Army Research Lab, Adelphi, MD, Sept. 14, 2013,

RPPR Final Report
as of 15-Jan-2019

Honors and Awards: Linyou Cao, CAREER award, National Science Foundation, 2014
Yifei Yu, MRS Graduate Student Award, 2015
Yifei Yu: Chinese Government Award for Outstanding Students Abroad, 2015
Yiling Yu: Chinese Government Award for Outstanding Students Abroad, 2015
Lujun Huang: Chinese Government Award for Outstanding Students Abroad, 2016
Alper Gurarslan, Marie Curie postdoc fellowship

Protocol Activity Status:

Technology Transfer: A US patent on the controlled scalable synthesis of 2D materials: 9,527,062 B2

Spun off a start-up company, Atomix Inc. (dba 2Dlayer, 2dlayer.com) based on the patented technique, which has already received $1 million angel investment

PARTICIPANTS:

Participant Type: PD/PI
Participant: Linyou Cao
Person Months Worked: 1.00 **Funding Support:**
Project Contribution:
International Collaboration:
International Travel:
National Academy Member: N
Other Collaborators:

Participant Type: Graduate Student (research assistant)
Participant: Yiling Yu
Person Months Worked: 6.00 **Funding Support:**
Project Contribution:
International Collaboration:
International Travel:
National Academy Member: N
Other Collaborators:

Participant Type: Graduate Student (research assistant)
Participant: Yifei Yu
Person Months Worked: 1.00 **Funding Support:**
Project Contribution:
International Collaboration:
International Travel:
National Academy Member: N
Other Collaborators:

Participant Type: Graduate Student (research assistant)
Participant: Lujun Huang
Person Months Worked: 15.00 **Funding Support:**
Project Contribution:
International Collaboration:
International Travel:
National Academy Member: N
Other Collaborators:

Participant Type: Graduate Student (research assistant)
Participant: Alper Gurarslan
Person Months Worked: 1.00 **Funding Support:**

RPPR Final Report
as of 15-Jan-2019

Project Contribution:
International Collaboration:
International Travel:
National Academy Member: N
Other Collaborators:

ARTICLES:

Publication Type: Journal Article Peer Reviewed: Y **Publication Status:** 1-Published
Journal: Nano Letters
Publication Identifier Type: Publication Identifier:
Volume: 0 Issue: 0 First Page #: 0
Date Submitted: 1/14/19 12:00AM Date Published:
Publication Location:
Article Title: Many-Body Effects in Valleytronics: Direct Measurement of Valley Lifetimes in Single-Layer MoS2
Authors: Cong Mai, Andrew Barrette, Yefei Yu, Yuriv Semenov, Ki Wook Kim, Linyou Cao, Kenan Gundogdu,
Keywords: Valley lifetime, many body, MoS2, monolayers, valleytronics
Abstract: Single layer MoS2 is an ideal material for the emerging field of “valleytronics” in which charge carrier momentum can be finely controlled by optical excitation. This system is also known to exhibit strong many-body interactions as observed by tightly bound excitons and trions. Here we report direct measurements of valley relaxation dynamics in single layer MoS2, by using ultrafast transient absorption spectroscopy. Our results show that strong Coulomb interactions significantly impact valley population dynamics. Initial excitation by circularly polarized light creates electron–hole pairs within the K-valley. These excitons coherently couple to dark intervalley excitonic states, which facilitate fast electron valley depolarization. Hole valley relaxation is delayed up to about 10 ps due to nondegeneracy of the valence band spin states. Intervalley biexciton formation reveals the hole valley relaxation dynamics. We observe that biexcitons form with more than an order of magnitude larger
Distribution Statement: 1-Approved for public release; distribution is unlimited.
Acknowledged Federal Support: **Y**

Publication Type: Journal Article Peer Reviewed: Y **Publication Status:** 1-Published
Journal: Nanoscale
Publication Identifier Type: Publication Identifier:
Volume: 0 Issue: 0 First Page #: 0
Date Submitted: 1/14/19 12:00AM Date Published:
Publication Location:
Article Title: Dependence of Coupling of Quasi 2-D MoS2 with Substrate on Substrate Type, Probed by Temperature Dependent Raman Scattering
Authors: Liqin Su, Yong Zhang, Yifei Yu, Linyou Cao
Keywords: MoS2, monolayers, Raman, substrates
Abstract: This work reports a study on the temperature dependence of in-plane E2g1 and out-of-plane A1g Raman modes of single-layer (1L) and bi-layer (2L) MoS2 films on sapphire (epitaxial) and SiO2 (transferred) substrates as well as bulk MoS2 single crystal in a temperature range of 25 – 500 °C. For the films on the transferred SiO2 substrate, the in-plane E2g1 mode is only weakly affected by the substrate, whereas the out-of-plane A1g mode is strongly perturbed, showing highly nonlinear, sometimes even non-monotonic, temperature dependence in the Raman peak shift and linewidth. In contrast, for the films on the epitaxial sapphire substrate, E2g1 is affected more significantly by the substrate than A1g. This study suggests that the 2-D film-substrate coupling depends sensitively on the preparation method, and in particular on the film morphology for the transferred film. These findings are vitally important for the fundamental understanding and application of this quasi 2-D material that is ex
Distribution Statement: 1-Approved for public release; distribution is unlimited.
Acknowledged Federal Support: **Y**

RPPR Final Report
as of 15-Jan-2019

Publication Type: Journal Article Peer Reviewed: Y **Publication Status:** 1-Published
Journal: Physical Review B, Rapid Communications
Publication Identifier Type: Publication Identifier:
Volume: 90 Issue: 0 First Page #: 041414(R)
Date Submitted: 1/14/19 12:00AM Date Published: 7/24/14 4:00AM
Publication Location:
Article Title: Exciton valley relaxation in a single layer of WS 2 measured by ultrafast spectroscopy
Authors: Cong Mai, Yuriy G. Semenov, Andrew Barrette, Yifei Yu, Zhenghe Jin, Linyou Cao, Ki Wook Kim, and K
Keywords: valley relaxation, WS2, 2D materials
Abstract: We measured the lifetime of optically created valley polarization in single-layer WS2 using transient absorption spectroscopy. The electron valley relaxation is very short (<1 ps). However, the hole valley lifetime is at least two orders of magnitude longer and exhibits a temperature dependence that cannot be explained by single-carrier spin/valley relaxation mechanisms. Our theoretical analysis suggests that a collective contribution of two potential processes may explain the valley relaxation in single-layer WS2. One process involves direct scattering of excitons from K to K' valleys with a spin flip-flop interaction. The other mechanism involves scattering through the spin-degenerate valley. This second process is thermally activated with an Arrhenius behavior due to theenergy barrier between the and K valleys.
Distribution Statement: 1-Approved for public release; distribution is unlimited.
Acknowledged Federal Support: **Y**

Publication Type: Journal Article Peer Reviewed: Y **Publication Status:** 1-Published
Journal: ACS Nano
Publication Identifier Type: DOI Publication Identifier: 10.1021/nn5044542
Volume: 8 Issue: 10 First Page #: 10743
Date Submitted: 1/14/19 12:00AM Date Published: 9/22/14 4:00AM
Publication Location:
Article Title: Ultrafast Electronic and StructuralResponse of Monolayer MoS2 underIntense Photoexcitation Conditions
Authors: Ehren M Mannebach, Karel-Alexander N Duerloo, Lenson A Pellouchoud, Meng-Ju Sher, Sanghee Nah
Keywords: molybdenum disulfide . MoS2 . second harmonic generation .ultrafast dynamics . monolayer . femtosecond
Abstract: We report on the dynamical response of single layer transition metal dichalcogenide MoS2 to intense above-bandgap photoexcitation using the nonlinear-optical second order susceptibility as a direct probe of the electronic and structural dynamics. Excitation conditions corresponding to the order of one electron ┌hole pair per unit cell generate unexpected increases in the second harmonic from monolayer films, occurring on few picosecond time-scales. These large amplitude changes recover on tens of picosecond time-scales and are reversible at megahertz repetition rates with no photoinduced change in lattice symmetry observed despite the extreme excitation conditions.
Distribution Statement: 1-Approved for public release; distribution is unlimited.
Acknowledged Federal Support: **Y**

RPPR Final Report
as of 15-Jan-2019

Publication Type: Journal Article Peer Reviewed: Y **Publication Status:** 1-Published
Journal: Nano Letters
Publication Identifier Type: DOI Publication Identifier: 10.1021/nl5038177
Volume: 15 Issue: 1 First Page #: 486
Date Submitted: 1/14/19 12:00AM Date Published: 12/1/14 5:00AM
Publication Location:
Article Title: Equally Efficient Interlayer Excitonic Relaxation and Improved Absorption in Epitaxial and Non-epitaxial Monolayer MoS2/WS2 Heterostructures
Authors: Yifei Yu, Shi Hu, Liqin Su, Alexander A. Puretzky, David B. Geohegan, Yong Zhang, Linyou Cao,
Keywords: Molybdenum disulfide, tungsten disulfide, van der Waals epitaxy, interlayer charge transfer,two-dimensional heterojunction
Abstract: Semiconductor heterostructures provide a powerful platform to engineer the dynamics of excitons for fundamental and applied interests. However, the functionality of conventional semiconductor heterostructures is often limited by inefficient charge transfer across interfaces due to the interfacial imperfection caused by lattice mismatch. Here we demonstrate that MoS2/WS2 heterostructures consisting of monolayer MoS2 and WS2 stacked in the vertical direction can enable equally efficient interlayer exciton relaxation regardless the epitaxy and orientation of the stacking. This is manifested by a similar 2 orders of magnitude decrease of photoluminescence intensity in both epitaxial and nonepitaxial MoS2/WS2 heterostructures. Both heterostructures also show similarly improved absorption beyond the simple superimposition of the absorptions of monolayer MoS2 and WS2. Our result indicates that 2D heterostructures bear significant implications for the development of photonic devices, in partic
Distribution Statement: 1-Approved for public release; distribution is unlimited.
Acknowledged Federal Support: **Y**

Publication Type: Journal Article Peer Reviewed: Y **Publication Status:** 1-Published
Journal: ACS Nano
Publication Identifier Type: DOI Publication Identifier: 10.1021/nn5057673
Volume: 8 Issue: 11 First Page #: 11522
Date Submitted: 1/14/19 12:00AM Date Published: 10/27/14 4:00AM
Publication Location:
Article Title: Surface Energy-Assisted Perfect Transfer of Centimeter-scale Monolayer and Fewlayer MoS2 Films onto Arbitrary Substrates
Authors: Alper Gurarslan, Yifei Yu, Liqin Su, Yiling Yu, Francisco Suarez, Shanshan Yao, Yong Zhu, Mehmet Oz
Keywords: molybdenum disulfide, 2D materials, tungsten disulfide, surface energy, large scale
Abstract: The transfer of synthesized 2D MoS2 films is important for fundamental and applied research. However, it is problematic to translate the well-established transfer processes for graphene to MoS2 due to different growth mechanisms and surface properties. Here we demonstrate a surface-energy-assisted process that can perfectly transfer centimeter-scale monolayer and few-layer MoS2 films from original growth substrates onto arbitrary substrates with no observable wrinkles, cracks, and polymer residues. The unique strategies used in this process include leveraging the penetration of water between hydrophobic MoS2 films and hydrophilic growth substrates to lift off the films and dry transferring the film after the lift off. This is in stark contrast with the previous transfer process for synthesized MoS2 films, which explores the etching of the growth substrate by hot base solutions to lift off the films. Our transfer process can effectively eliminate the mechanical force caused by bubble ge
Distribution Statement: 1-Approved for public release; distribution is unlimited.
Acknowledged Federal Support: **Y**

RPPR Final Report
as of 15-Jan-2019

Publication Type: Journal Article Peer Reviewed: Y **Publication Status:** 1-Published
Journal: Scientific Reports
Publication Identifier Type: Publication Identifier:
Volume: 3 Issue: 0 First Page #: 1866
Date Submitted: 1/14/19 12:00AM Date Published: 5/27/13 8:00AM
Publication Location:
Article Title: Controlled Scalable Synthesis of Uniform, High-Quality Monolayer and Few-layer MoS2 Films
Authors: Yifei Yu, Chun Li, Yi Liu, Liqin Su, Yong Zhang & Linyou Cao
Keywords: Molybdenum sulfide, centimeter-scale, self-limiting growth
Abstract: Two dimensional (2D) materials with a monolayer of atoms represent an ultimate control of material dimension in the vertical direction. Molybdenum sulfide (MoS2) monolayers, with a direct bandgap of 1.8 eV, offer an unprecedented prospect of miniaturizing semiconductor science and technology down to a truly atomic scale. Recent studies have indeed demonstrated the promise of 2D MoS2 in fields including field effect transistors, low power switches, optoelectronics, and spintronics. However, device development with 2D MoS2 has been delayed by the lack of capabilities to produce large-area, uniform, and high-quality MoS2 monolayers. Here we present a self-limiting approach that can grow high quality monolayer and few-layer MoS2 films over an area of centimeters with unprecedented uniformity and controllability. This approach is compatible with the standard fabrication process in semiconductor industry. It paves the way for the development of practical devices with 2D MoS2 and opens up new
Distribution Statement: 1-Approved for public release; distribution is unlimited.
Acknowledged Federal Support: **Y**

Publication Type: Journal Article Peer Reviewed: Y **Publication Status:** 1-Published
Journal: ACS Nano
Publication Identifier Type: DOI Publication Identifier: 10.1021/acsnano.6b02195
Volume: 10 Issue: 8 First Page #: 7493
Date Submitted: 1/14/19 12:00AM Date Published: 8/2/16 4:00AM
Publication Location:
Article Title: Atomically Thin MoS2 Narrowband and Broadband Light Superabsorbers
Authors: Lujun Huang, Guoqing Li, Alper Gurarslan, Yiling Yu, Ronny Kirste, Wei Guo, Junjie Zhao, Ramon Colla
Keywords: leaky mode; light absorption; MoS2; resonant photonics; two-dimensional materials;
Abstract: We present a combined theoretical and experimental effort to enable strong light absorption (>70%) in atomically thin MoS2 films (?4 layers) for either narrowband incidence with arbitrarily prespecified wavelengths or broadband incidence like solar radiation. This is achieved by integrating the films with resonant photonic structures that are deterministically designed using a unique reverse design approach based on leaky mode coupling. The design starts with identifying the properties of leaky modes necessary for the targeted strong absorption, followed by searching for the geometrical features of nanostructures to support the desired modes. This process is very intuitive and only involves a minimal amount of computation, thanks to the straightforward correlations between optical functionality and leaky modes as well as between leaky modes and the geometrical feature of nanostructures. The result may provide useful guidance for the development of high-performance atomic-scale photonic
Distribution Statement: 1-Approved for public release; distribution is unlimited.
Acknowledged Federal Support: **Y**

RPPR Final Report
as of 15-Jan-2019

Publication Type: Journal Article Peer Reviewed: Y **Publication Status:** 1-Published
Journal: Nano Letters
Publication Identifier Type: DOI Publication Identifier: 10.1021/nl303876a
Volume: 13 Issue: 3 First Page #: 948
Date Submitted: 1/14/19 12:00AM Date Published: 2/23/13 5:00AM
Publication Location:
Article Title: Epitaxial Nanosheet - Nanowire Heterostructures
Authors: Chun Li, Yifei Yu, Miaofang Chi, Linyou Cao
Keywords: epitaxial growth; germanium sulfide; Heterostructures; nanosheets; nanowires; three-dimensional nanostructures
Abstract: We demonstrate synthesis of a new type of heterostructures that comprise two-dimensional (2D) nanosheets (NSs) epitaxially grown at one-dimensional (1D) nanowires (NWs). The synthesis involves materials with a graphite-like layered structure in which covalently bonded layers are held by weak van der Waals forces. GeS was used as a prototype material in this work. The synthesis also involves a seeded-growth process, where GeS NWs are grown first as seeds followed by a seeded growth of NSs at the pre-grown NWs. We observe that exposing the pre-grown NWs to air prior to the seeded growth is critical for the formation of NSs to yield NS–NW heterostructures. Our experimental results suggest that this might be due to a mild oxidation at the NW surface caused by the air exposure, which could subsequently facilitate the nucleation of NSs at the NWs. It also suggests that the surface oxidation needs to be controlled in a proper range in order to achieve optimized NS growths. We believe that thi
Distribution Statement: 1-Approved for public release; distribution is unlimited.
Acknowledged Federal Support: **Y**

Publication Type: Journal Article Peer Reviewed: Y **Publication Status:** 1-Published
Journal: J. Phys. Chem. C
Publication Identifier Type: DOI Publication Identifier: 10.1021/jp400274a
Volume: 117 Issue: 12 First Page #: 6469
Date Submitted: 1/14/19 12:00AM Date Published: 2/28/13 5:00AM
Publication Location:
Article Title: Substrate Mediation in Vapor Deposition Growth of Layered Chalcogenide Nanoplates: A Case Study of SnSe2
Authors: Liang Huang, Yifei Yu, Chun Li, Linyou Cao
Keywords: Tin selenide, nanosheets, substrate interaction
Abstract: The two-dimensional (2D) nanostructure of layered chalcogenide materials (LCMs) is very interesting, but to make it a useful material platform necessiates the development of sophisticated synthetic control. We present the synthesis of single-crystalline SnSe2 nanoplates by a noncatalytic vapor deposition process and demonstrate that the growth is subject to strong influences from substrates. The effect of substrates is evidenced by a temperature-dependent morphological difference in the nanoplates grown on mica and silicon substrates. At a growth temperature of 280 °C, the diameter of the nanoplates grown on mica is larger than those grown on silicon by a ratio of 6.2. This ratio substantially decreases to be unity (1.04) at a higher temperature of 420 °C. Additionally, different from the nanoplates grown on silicon, which always show a well-defined hexagonal shape, the nanoplates grown on mica exhibit an irregular shape at low temperature and can gradually evolve into the hexagonal sh
Distribution Statement: 1-Approved for public release; distribution is unlimited.
Acknowledged Federal Support: **Y**

RPPR Final Report
as of 15-Jan-2019

Publication Type: Journal Article Peer Reviewed: Y **Publication Status:** 1-Published
Journal: ACS Nano
Publication Identifier Type: DOI Publication Identifier: 10.1021/nn303745e
Volume: Issue: First Page #:
Date Submitted: 1/14/19 12:00AM Date Published: 9/25/12 4:00AM
Publication Location:
Article Title: Role of Boundary Layer Diffusion in Vapor Deposition Growth of Chalcogenide Nanosheets: The Case of GeS
Authors: Chun Li, Liang Huang, Gayatri Snyder, Yifei Yu, Linyou Cao
Keywords: boundary layer; diffusion-limited; layered compound; nanosheets; vapor deposition
Abstract: We report a synthesis of single-crystalline two-dimensional GeS nanosheets using vapor deposition processes and show that the growth behavior of the nanosheet is substantially different from those of other nanomaterials and thin films grown by vapor depositions. The nanosheet growth is subject to strong influences of the diffusion of source materials through the boundary layer of gas flows. This boundary layer diffusion is found to be the rate-determining step of the growth under typical experimental conditions, evidenced by a substantial dependence of the nanosheet's size on diffusion fluxes. We also find that high-quality GeS nanosheets can grow only in the diffusion-limited regime, as the crystalline quality substantially deteriorates when the rate-determining step is changed away from the boundary layer diffusion. We establish a simple model to analyze the diffusion dynamics in experiments. Our analysis uncovers an intuitive correlation of diffusion flux with the partial pressure o
Distribution Statement: 1-Approved for public release; distribution is unlimited.
Acknowledged Federal Support: **Y**

Publication Type: Journal Article Peer Reviewed: Y **Publication Status:** 1-Published
Journal: Scientific Reports
Publication Identifier Type: Publication Identifier:
Volume: 5 Issue: First Page #: 16996
Date Submitted: 1/14/19 12:00AM Date Published: 11/1/15 4:00AM
Publication Location:
Article Title: Exciton-dominated Optical Functions of MoS2 Atomically Thin Films
Authors: Yiling Yu, Yifei Yu, Yongqing Cui, Wei Li, Alper Gurarslan, Hartwin Peelaers, David E. Aspnes, Chris G.
Keywords: molybdenum sulfide, dielectric function, layer dependence, excitonic effects
Abstract: We systematically measure the dielectric function of atomically thin MoS2 films with different layer numbers and demonstrate that excitonic effects play a dominant role in the dielectric function when the films are less than 5–7 layers thick. The dielectric function shows an anomalous dependence on the layer number. It decreases with the layer number increasing when the films are less than 5–7 layers thick but turns to increase with the layer number for thicker films. We show that this is because the excitonic effect is very strong in the thin MoS2 films and its contribution to the dielectric function may dominate over the contribution of the band structure. We also extract the value of layer-dependent exciton binding energy and Bohr radius in the films by fitting the experimental results with an intuitive model. The dominance of excitonic effects is in stark contrast with what reported at conventional materials whose dielectric functions are usually dictated by band structures. The kn
Distribution Statement: 1-Approved for public release; distribution is unlimited.
Acknowledged Federal Support: **Y**

RPPR Final Report
as of 15-Jan-2019

Publication Type: Journal Article Peer Reviewed: Y **Publication Status:** 1-Published
Journal: Adv. Mater.
Publication Identifier Type: DOI Publication Identifier: 10.1002/adma.201601581
Volume: 28 Issue: 45 First Page #: 10055
Date Submitted: 1/14/19 12:00AM Date Published: 9/30/16 4:00AM
Publication Location:
Article Title: Van der Waals Force Isolation of Monolayer MoS2
Authors: Alper Gurarslan, Shuping Jiao, Tai-De Li, Guoqing Li, Yiling Yu, Yang Gao, Elisa Riedo, Zhiping Linyou
Keywords: molybdenum sulfide, van der waals, contact angle, layer dependence, electrostatic screening
Abstract: Monolayer MoS2 can effectively screen the vdW interaction of underlying substrates with external systems by >90% because of the substantial increase in the separation between the substrate and external systems due to the presence of the monolayer. This substantial screening of vdW interactions by MoS2 monolayer is different from what reported at graphene
Distribution Statement: 1-Approved for public release; distribution is unlimited.
Acknowledged Federal Support: **Y**

WEBSITES:

URL: 2dlayer.com
Date Received: 14-Jan-2019
Title: 2Dlayer website
Description: This is the website of Atomic Inc. (dba 2Dlayer), which is spun off from the Cao lab based on the technical transfer of this project.

PATENTS:

Intellectual Property Type: Patent Date Received: **14-Jan-2019**
Patent Title: Process for scalable syntehsis of molybdenum disulfide monoalyers and few-layers films
Patent Abstract: The present disclosure relates to nanosheet synthesis. ore particularly, the present disclosure re
Patent Number: 9,527.062 B2
Patent Country: USA
Application Date: 01-May-2013 Application Status: 3
Date Issued: 27-Dec-2016

SCIENTIFIC REPORTS



OPEN

SUBJECT AREAS:
TWO-DIMENSIONAL MATERIALS
SYNTHESIS AND PROCESSING
SOLID-PHASE SYNTHESIS
ELECTRICAL AND ELECTRONIC ENGINEERING

Received
5 April 2013

Accepted
7 May 2013

Published
21 May 2013

Correspondence and requests for materials should be addressed to L.C. (lcao2@ncsu.edu)

Controlled Scalable Synthesis of Uniform, High-Quality Monolayer and Few-layer MoS_2 Films

Yifei Yu[1], Chun Li[1], Yi Liu[3], Liqin Su[4], Yong Zhang[4] & Linyou Cao[1,2]

[1]Department of Materials Science and Engineering, North Carolina State University, Raleigh NC 27695, [2]Department of Physics, North Carolina State University, Raleigh NC 27695, [3]Analytical Instrumentation Facility, North Carolina State University, Raleigh NC 27695, [4]Department of Electrical and Computer Engineering, The University of North Carolina at Charlotte, Charlotte, NC 28223.

Two dimensional (2D) materials with a monolayer of atoms represent an ultimate control of material dimension in the vertical direction. Molybdenum sulfide (MoS_2) monolayers, with a direct bandgap of 1.8 eV, offer an unprecedented prospect of miniaturizing semiconductor science and technology down to a truly atomic scale. Recent studies have indeed demonstrated the promise of 2D MoS_2 in fields including field effect transistors, low power switches, optoelectronics, and spintronics. However, device development with 2D MoS_2 has been delayed by the lack of capabilities to produce large-area, uniform, and high-quality MoS_2 monolayers. Here we present a self-limiting approach that can grow high quality monolayer and few-layer MoS_2 films over an area of centimeters with unprecedented uniformity and controllability. This approach is compatible with the standard fabrication process in semiconductor industry. It paves the way for the development of practical devices with 2D MoS_2 and opens up new avenues for fundamental research.

The significance of 2D materials has been manifested by a plethora of fascinating functionality demonstrated in graphene, a monolayer material of carbon atoms[1–4]. In contrast to graphene, which is a semi-metal with no bandgap by nature, MoS_2 monolayers offer an attractive semiconductor option due to a direct bandgap of 1.8 eV[5,6]. This non-trivial bandgap makes MoS_2 monolayers a better candidate than graphene to revolutionize many electronic and photonic devices that are currently dominated by traditional group IV or III–V semiconductor materials[7–23]. Considerable efforts have been dedicated to achieve scalable synthesis of high quality MoS_2 monolayers that is necessary for the development of practical devices. These include sulfurization of MoO_3 or Mo layers pre-deposited on substrates, or thermolysis of Mo compound $(NH_4)_2MoS_4$[24–31]. However, none of the existing processes provides the capability to exclusively produce uniform MoS_2 monolayers over a large area up to centimeters. Additionally, none of these processes is able to precisely control the layer number of MoS_2 films. For instance, MoS_2 monolayers resulted from these processes always co-exist with by-products of thicker layers. As the properties of MoS_2 materials strongly depend on the layer number, this unsatisfactory uniformity and controllability poses a formidable challenge for the improvement of device performance. Here we present a new, self-limiting chemical vapor deposition (CVD) approach that can exclusively grow high-quality monolayer or few-layer MoS_2 films over an area of centimeters on various substrates such as silicon oxide, sapphire, and graphite. The layer number of the MoS_2 films can be precisely controlled as 1, 2, 3, and beyond. The synthesized film shows unprecedented uniformity with no other layers found by thorough characterizations. It exhibits optical and electrical quality comparable to the MoS_2 exfoliated from bulk materials, and can be transferred to other arbitrary substrates.

Results

We grew MoS_2 films at high temperatures ($> 800^{\circ}C$) using $MoCl_5$ and sulfur as precursor materials (we found the quality of resulting thin films worse at lower growth temperatures). The precursor materials can react at elevated temperatures to produce MoS_2 species, which may subsequently precipitate onto receiving substrates to yield MoS_2 films (Fig. S1). The layer number of the resulting MoS_2 films can be very precisely controlled by controlling the amount of $MoCl_5$ used in experiments or the total pressure in the synthetic setup (details see Studies of growth mechanism in the Supplementary Information). We have successfully grown monolayer or few-layer MoS_2 films on various substrates including silicon oxide, sapphire, and graphite. Fig. 1 a–b show optical images of the MoS_2

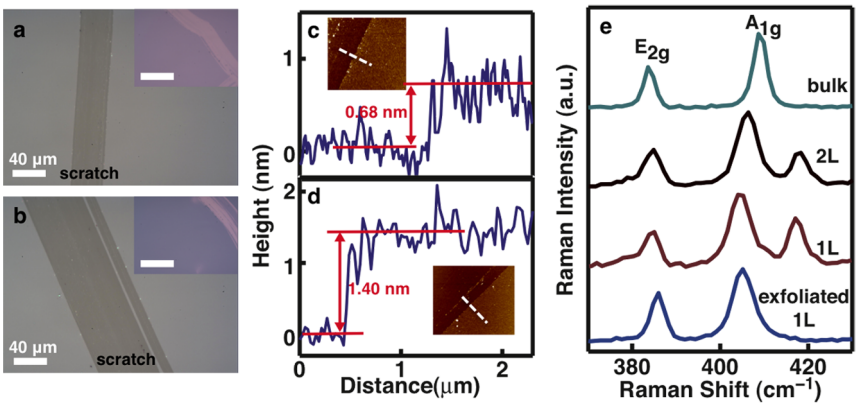


Figure 1 | Controlled synthesis of MoS_2 monolayer and bilayer films. (a) and (b), Optical images of the MoS_2 monolayer and bilayer films grown on sapphire substrates, respectively. The insets are optical images of the MoS_2 monolayer and bilayer films grown on SiO_2/Si substrates. The scale bars in the insets are 80 μm. (c) and (d), AFM height profiles for typical MoS_2 monolayer and bilayer films grown on sapphire, respectively. The insets show the AFM images from which the height profiles are extracted. A larger version of the AFM images is given in Fig.S3 of the Supplementary Information. (e), Raman spectra of the MoS_2 monolayer (1 L) and bilayer (2 L) films grown on sapphire. Also given are the Raman spectra of exfoliated MoS_2 monolayer and bulk MoS_2 dispersed on SiO_2/Si substrates. The two characteristic Raman modes are labeled. The peak at 418 cm^{-1} is from the sapphire substrate.

monolayer and bilayer films grown on sapphire substrates. The optical images of MoS_2 monolayer and bilayer films grown on silicon substrates with 280 nm thick silicon oxide (SiO_2/Si) are also given as insets. Scratches were intentionally introduced to show the color contrast between the thin film and the substrate (no MoS_2 film exists in the scratched area). We confirm the chemical composition of the thin films is MoS_2 using x-ray photoelectron spectroscopy (XPS) characterizations (Fig. S2). From the optical images, we can find that the thin films are continuous and uniform over a large area. We can also find that the color contrasts of MoS_2 monolayer and bilayer films bear little difference on sapphire but are substantially different on SiO_2/Si, the monolayer showing pink color while the bilayer more bluish. This substantial difference in color contrast may provide a facile approach to determine the thickness of 2D MoS_2 materials.

We characterized the synthesized thin films using atomic force microscope (AFM) and Raman spectroscopy. The thickness of the synthesized MoS_2 monolayers and bilayers are shown 0.68 nm and 1.40 nm (Fig. 1c–d), in consistence with exfoliated MoS_2 (Fig. S3–S5). Fig. 1e shows the Raman spectra collected from the as-grown MoS_2 thin films on sapphire with different layer numbers (the Raman spectra for the MoS_2 films grown on SiO_2/Si is given in Fig. S6). The Raman spectra of exfoliated MoS_2 monolayers and bulk MoS_2 materials are also given in Fig. 1e as references. Two characteristic Raman modes can be found in the spectra, the A_{1g} mode associated with the out-of-plane vibration of sulfur atoms and the E^1_{2g} mode related with the in-plane vibration of Mo and sulfur atoms[32–34]. The full width at half maximum (FWHM) of the E^1_{2g} peak may be used as an indicator for crystalline quality. The E^1_{2g} FWHM of the synthesized MoS_2 monolayer is 4.2 cm^{-1}, close to that of the exfoliated monolayer, 3.7 cm^{-1}. This suggests a good crystalline quality in the synthesized film. Additionally, the frequency difference (Δk) between the E^1_{2g} and A_{1g} modes has been known closely related with the layer number, and can be used to determine the thickness of MoS_2 materials[32–34]. We can find that the frequency difference Δk of the synthesized thin film increases with the thickness (Fig. 1e), consistent with what were observed on exfoliated MoS_2[32–34]. A systematic correlation between the value of Δk and the layer number of the synthesized film is given in Table S1 of the Supplementary Information. The Δk of the synthesized film is generally larger than that of exfoliated MoS_2. For example, the Δk of the synthesized monolayer is found around 20.4 cm^{-1}, different from that of the exfoliated monolayer, 19.4 cm^{-1}. This could be related with certain crystalline imperfection, for example, smaller crystalline grains in the synthesized thin film. Other groups also observed a larger Δk in synthesized MoS_2 materials than exfoliated counterparts[26].

The synthesized MoS_2 thin films show unprecedented uniformity. We can find the as-grown MoS_2 thin films continuous and uniform cross an area of centimeters under optical microscope or by eyes, as illustrated by Fig. 1a and 2a. To more quantitatively assess the uniformity over a large area, we divided the monolayer MoS_2 film grown on a typical sapphire substrate in size of 1 cm × 3 cm into eight areas (Fig. 2b inset). We measured numerous Raman spectra at each of the areas, and plotted the representative results in Fig. 2b. We can find that the peak positions of the E^1_{2g} and A_{1g} modes remain identical in all the spectra. The profile of the Raman peaks, such as the FWHM, shows negligible difference. This indicates that the synthesized thin film is indeed a homogeneous monolayer with similar crystalline quality across the entire substrate. We also performed Raman mapping over an area of 10 μm × 10 μm in the as-grown monolayer film, and plotted the measured frequency difference Δk in a 2D image (Fig. 2c). All the Δk are found in a range of 20.3 – 20.7 cm^{-1}, confirming the film a homogeneous monolayer. To further confirm the uniformity, we performed multiple AFM measurements at different areas on the film, and found similar thickness and surface topology in all the AFM images (Fig. S8). A typical AFM measurement (5 μm × 5 μm) is given in Fig. 2d. It shows a continuous and smooth surface (roughness < 0.2 nm) with no step and void observed. Similar uniformity can also be found at the synthesized bilayer MoS_2 film (Fig. S9–S10). We should note that the size of the synthesized thin film (1 cm × 3 cm) is limited by the size and temperature uniformity of our current synthetic setup. We believe that by optimizing the synthetic setup we can produce wafer-scale MoS_2 monolayer or few-layer films.

The synthesized MoS_2 films exhibit a very good crystalline quality as indicted by the Raman measurements (Fig. 1e and 2b). To further elucidate the crystalline structure, we characterized the thin film using aberration-corrected scanning transmission electron microscope (STEM). To do that, we transferred the synthesized film to TEM grids following a process reported in references[25]. The synthesized film is found as polycrystalline with crystalline grains varying from tens to hundreds of nanometers as indicated by selected area electron diffraction patterns (Fig. S11). We used high angle annular dark field (HAADF) imaging to investigate the atomic arrangement in the synthesized MoS_2 monolayer and bilayer films. The monolayer and the bilayer can be identified from the folding edge of the transferred thin film (Fig. 3a inset). Fig. 3a shows typical STEM high angle

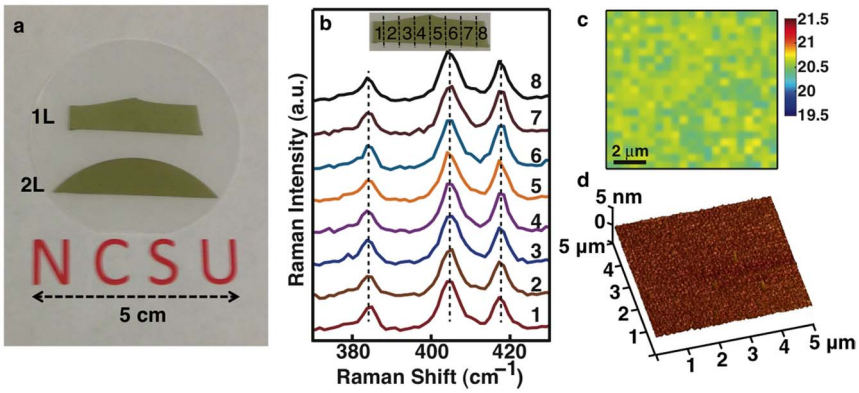


Figure 2 | Large-area uniformity of the synthesized MoS_2 monolayer and bilayer films. (a), A picture for as-grown MoS_2 monolayer (1 L) and bilayer (2 L) films, along with a NCSU logo. Underneath the films is a blank sapphire wafer, which is transparent and used as a refence. (b), Raman spectra collected from eight different areas of the MoS_2 monolayer film. The inset schematically illustrates how the eight areas distribute across the substrate. (c), Map of the Raman frequency difference Δk collected from an area of 10 μm × 10 μm in the MoS_2 monolayer film. All the measured Δk are in the range of 20.3 – 20.7 cm^{-1}. Mapping step: 0.5 μm. (d), Perspective view of a typical AFM image collected from the MoS_2 monolayer film. A topview of this AFM image is given as Fig. S7 in the Supplementary Information.

annular dark field (HAADF) image of synthesized monolayers and corresponding fast Fourier transformation (FFT) pattern. The hexagonal atomic arrangement shown in the STEM image and the FFT pattern indicate that the basal plane of the synthesized thin film is (001), i.e. the c-axis of MoS_2 materials perpendicular to the thin film. From the STEM image we can directly measure the lattice constant as $a = b = 0.32$ nm, consistent with bulk MoS_2 materials. As STEM-HAADF imaging is dependent on the atomic number, we can identify the positions of Mo and S atoms in the monolayer by the difference in image contrast (Mo atoms show much higher contrast than S atoms), as shown in Fig. 3b. Additionally, STEM-HAADF imaging provides a credible way to identify the stacking sequence in MoS_2 bilayers. We can find a substantial difference between the images of MoS_2 monolayer (Fig. 3b) and bilayer (Fig. 3c). This difference indicates an AB stacking sequence in the MoS_2 bilayer, where the Mo atoms of one layer overlap with the position of the sulfur atoms in the other layer (Fig. S13). The experimental observation matches the modeled image for the AB stacking very well (Fig. 3c).

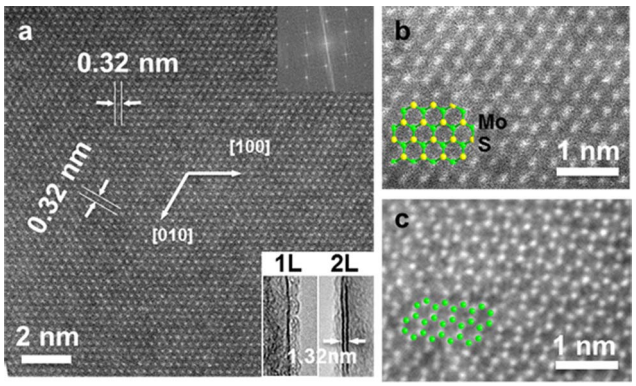


Figure 3 | Characterization of the crystal structure of synthesized MoS_2 monolayer and bilayer films. (a), High angle annular dark field (HAADF) image of typical MoS_2 monolayer film. Upper inset is the corresponding FFT pattern, which is not indexed for visual convenience (an indexed version is given in Fig. S12a). Lower inset shows the folded edges of MoS_2 monolayer and bilayer films. The lattice constant and important crystalline directions are given as shown. (b) and (c), HAADF of MoS_2 monolayer and bilayer films. The image of the bilayer film (c) is filtered and the original version is given in Fig. S12b. The insets show modeled crystal structures of MoS_2 monolayer and bilayer films with blue and yellow dots corresponding to Mo and S atoms, respectively. The sulfur atom in the inset of (c) is not given for visual convenience.

The synthesized thin films show excellent optical quality that is comparable to exfoliated MoS_2. Fig. 4a shows the PL spectra collected from exfoliated and synthesized MoS_2 monolayers. Raman peaks of the MoS_2 materials are also included, and the (photoluminescence) PL spectra are normalized to the intensity of corresponding Raman peaks. The normalization is to better correlate the measured PL intensity with the intrinsic luminescence efficiency of the materials[6]. Two peaks can be found in the PL spectra, ~ 620 nm and ~ 670 nm, and can be correlated to the B_1 and A_1 excitons of MoS_2, respectively[6]. We can find similar PL peaks from both synthesized and exfoliated MoS_2 monolayer. This suggests a comparable optical quality in the synthesized film with the exfoliated MoS_2. We should note that the synthesized monolayer for the PL measurement was grown on sapphire substrates. For the convenience of comparison with the exfoliated MoS_2, which were dispersed onto SiO2/Si substrates, the synthesized monolayer was transferred to SiO_2/Si substrates for the PL measurement (see the effect of substrates on PL in Fig. S14). We find that the PL from the MoS_2 monolayer film grown on SiO_2/Si substrates is much weaker than the films grown on sapphire (Fig. S15), probably due to a poorer crystalline quality in the films grown on SiO_2/Si substrates than those grown on sapphire as reported previously[25]. Additionally, the PL efficiency of exfoliated MoS_2 has been well known substantially decreasing with the increase in the layer number due to an evolution of the bandgap with the layer number. We can find that the PL efficiency of the synthesized MoS_2 bilayer is indeed substantially smaller than that of synthesized monolayers (Fig. S16). This suggests that the bandgap of the synthesized MoS_2 film bears a similar dependence on the layer number as exfoliated MoS_2. To illustrate the uniformity of the optical quality, we performed PL mapping over an area of 20 μm × 20 μm in the synthesized monolayer. The measurement demonstrates a uniform distribution in the PL intensity (Fig. 4a inset), confirming the uniformity as suggested by the Raman measurements shown in the preceding text.

We also evaluated the electrical quality of the synthesized MoS_2 monolayer film. We transferred the thin film grown on sapphire to degenerately doped silicon substrates covered with 280-nm-thick SiO_2, and fabricated bottom-gate transistors by evaporating 5 nm Ti/200 nm Au electrodes on top of the MoS_2 thin film. We performed electrical measurements at room temperature and in ambient environment using the degenerately doped silicon substrate as a back gate and deposited Au electrodes as the source and drain. Fig. 4b

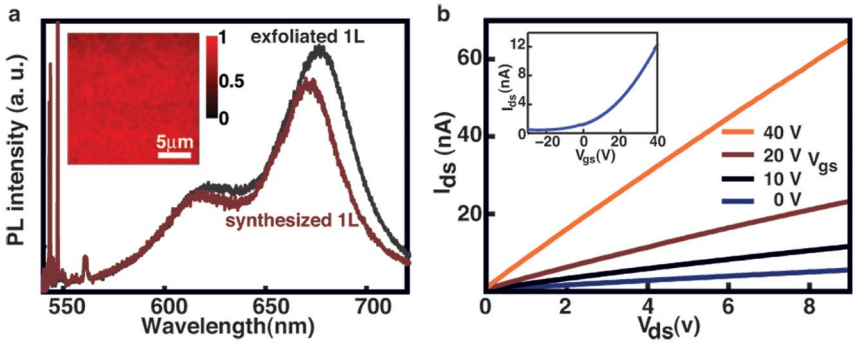


Figure 4 | Optical and electrical characterizations of the synthesized MoS_2 monolayer films. (a), Photoluminescence (PL) of the synthesized and exfoliated MoS_2 monolayers. Both were dispersed on SiO_2/Si substrates. The synthesized monolayer was grown on sapphire substrates and then transferred to SiO_2/Si substrates for the PL measurement. Using the sample substrate for the PL measurement is for the convenience of comparison. Our experimental results show the PL of MoS_2 films may be affected by the substrate (Fig. S14) (b), I_{ds}-V_{ds} curve for a field effect transistor (FET) made with the synthesized MoS_2 monolayer with gating voltages V_{gs} 0, 10, 20, 40 V. Inset, transfer characteristic for the FET with a source drain bias V_{ds} of 2 V.

shows typical output characteristic and transfer characteristic (inset) curves of the device. These results indicate that the device is an n-type channel field effect transistor, consistent with other works on exfoliated MoS_2[7,35,36]. The linear dependence of the current I_{ds} on the source-drain bias V_{ds} suggests that the contacts between the MoS_2 thin film and the electrodes are ohmic. This ensures that the observed field effect behavior is from the monolayer MoS_2 channel rather than Schottky barriers at the contact. From the measurements, we can derive the field-effect mobility of charge carriers in the device as 0.003–0.03 cm^2/V.s by using the expression $\mu = [dI_{ds}/dV_g] \times [L/(WC_iV_{ds})]$, where L and W is the length and width of the channel, respectively, C_i is the capacitance of the gating oxide, and V_g is the bias applied to the back gate. This is reasonably comparable to previous reports on exfoliated monolayers measured in similar conditions (ambient environment, back gating with silicon oxide as the gate oxide)[7,35,36]. We can thus conclude that the synthesized thin film has a reasonably comparable electrical quality with exfoliated MoS_2.

Discussion

The observed remarkable uniformity and controllability in the synthesized MoS_2 film strongly suggests that this synthetic process is self-limiting, i.e. the growth may be automatically stopped by some intrinsic factors of the synthetic process. Unlike the self-limiting mechanism for the growth of graphene[37], which is related with the limited solubility of carbon source in the catalyst of copper, our experimental results suggest that the partial pressure of gaseous MoS_2 species and the interaction of MoS_2 thin films with substrates play key roles in this self-limiting mechanism.

We found in experiments that the layer number of MoS_2 thin films increases with the amount of precursor materials (Table S1, Fig. S17–S18) and the total pressure in the synthetic setup (Fig. S19–S20). We can correlate this to the effect of the two parameters on the partial pressure of gaseous MoS_2 species P_{Mo}, which we find increasing with the amount of precursor materials and the total pressure (details see Supplementary Information). We believe that the partial pressure P_{Mo} plays an important role in control of the layer number.

To elucidate the role of P_{Mo}, we examine the dynamics of the synthetic process, and find that the precipitation reaction $MoS_2(g) \rightarrow MoS_2(s)$ is the rate-determining step, where g and s refer to gaseous and solid phases, respectively (details see Supplementary Information). The precipitation reaction is governed by two pressures, the partial pressure of gaseous MoS_2 species (P_{Mo}) and the equilibrium vapor pressure (referred as vapor pressure) of MoS_2 in solid phase (P^o_{Mo}). The role of P_{Mo} in control of the layer number is essentially rooted in its role in the thermodynamics and kinetics of the precipitation reaction. The difference between the partial pressure P_{Mo} and the vapor pressure P^o_{Mo} provides the thermodynamic driving force for the precipitation reaction. The partial pressure must be larger than the vapor pressure, i.e., $P_{Mo} > P^o_{Mo}$, to drive the precipitation of gaseous MoS_2 species. Additionally, based on the law of mass reaction, we know that the partial pressure P_{Mo} also dictates the rate of the precipitation, a larger P_{Mo} driving a faster precipitation.

The observed dependence of the layer number of MoS_2 films on experimental parameters (the amount of precursor materials and the total pressure) suggests that a larger partial pressure P_{Mo} tends to give rise to a thicker film (Fig. S21–S22). While a larger P_{Mo} can cause a larger precipitation rate, we do not think that this kinetic effect would be the major reason for the observed control of layer number. Should the precipitation rate be the major mechanism for the control, it would request a perfect control in timing to stop the precipitation right at the end of the formation of each individual layer, in order to produce the observed uniform MoS_2 films with precisely controlled layer number. This is most unlikely in our synthetic setup. The growth of large-area, highly uniform MoS_2 thin films in our experiments suggests that this precipitation is a self-limiting process, i.e. the precipitation automatically stops at the end of the formation of each individual layer.

We believe that the self-limiting mechanism may lie in a thermodynamic balance between the partial pressure of gaseous MoS_2 species (P_{Mo}) and the vapor pressure of MoS_2 thin films (P^o_{Mo}) on the substrate. The vapor pressure of MoS_2 thin films could depend on, more specifically, increase with the layer number. As P_{Mo} is requested larger than P^o_{Mo} to provide the thermodynamic driving force, the precipitation of gaseous MoS_2 species may be automatically stopped at a specific layer number by control of P_{Mo}. For instance, an exclusive growth of MoS_2 monolayer could be achieved by controlling the partial pressure P_{Mo} between the vapor pressures of MoS_2 monolayer ($P^o_{Mo,1}$) and bilayer ($P^o_{Mo,2}$) films as $P^o_{Mo,1} < P_{Mo} < P^o_{Mo,2}$. In this case, the larger vapor pressure of MoS_2 bilayers may automatically prevent the continuous growth once a MoS_2 monolayer film is formed, regardless a continuous supply of MoS_2 species. This indeed matches our observations that the lay number of MoS_2 films shows a step-function dependence on the amount of precursor materials (Table S1). Our hypothesis on the self-liming mechanism can also be supported by the observed dependence of the layer number on growth temperatures. We find that the layer number of MoS_2 film increases with the temperature of receiving substrates decreasing (Fig. S23). This can be understood that the vapor pressure of MoS_2 thin films P^o_{Mo} decreases with the temperature, and the same partial pressure P_{Mo} can drive a deposition of thicker films at lower temperatures.

The dependence of the vapor pressure of MoS_2 thin films on the layer number might be related with the interaction with substrates.

The vapor pressure indicates a capability of atoms escaping from solid phase into gas phase. The interaction of MoS_2 overlayers with substrates could substantially suppress the escaping of MoS_2 atoms, and subsequently cause a decrease in the vapor pressure. This interaction with substrates is expected to relax with the layer number (Fig. S24). As a result, the vapor pressure of MoS_2 thin film may increase with the layer number. Similar suppression effects of substrates on the vapor pressure have been well demonstrated in other materials adsorbed on substrates, for instance, polymers[38]. This dependence of vapor pressures on the layer number of MoS_2 films may provide the possibility of self-limiting growth. We also find in experiments that a precise control of the layer number generally tends to be more difficult for thicker films, for instance, larger than 4, often resulting a mixture of layer numbers. This suggests that the difference between the vapor pressures of MoS_2 films with neighboring layer number ($P^{o}_{Mo,n+1}$ - $P^{o}_{Mo,n}$, n refers to the layer number) tends to shrink with an increase in the layer number, which makes the selective growth more difficult.

To further examine the role of the interaction with substrates, we studied the growth on different receiving substrates, the traditional three-dimensional (3D) bonded materials such as sapphire (referred as 3D substrates) and highly ordered pyrolytic graphite (HOPG, from Ted Pella) that has a similar layered structure as MoS_2 (referred as 2D substrates). We grew MoS_2 films on these different substrates under identical experimental conditions (the different substrates were placed side by side in the tube furnace). We can find a substantial difference between the films grown on sapphire and HOPG (Fig. S25). With the same experimental conditions, while the film grown on sapphire substrates is monolayer (Δk 20.4 cm^{-1}), the one grown on HOPG is bilayer (Δk 22.4 cm^{-1}). We can exclude out the possibility that the observed difference in the Raman shifts is caused by the difference in substrates (see Supplementary Information). This result confirms that the interaction of MoS_2 films with substrates plays an important role in the self-limiting growth. The strength of the interaction of 2D material overlayer with conventional 3D substrates e.g. sapphire, is well known different from that with 2D substrates (such as HOPG). This difference has been extensively manifested by the van del Waals epitaxial growth of layered materials on 2D substrates[39]. In our experiment, the different interactions of MoS_2 films with sapphire and HOPG might cause different vapor pressures. Therefore, the same partial pressure of MoS_2 can give rise to a growth of thicker MoS_2 film on HOPG.

In conclusion, we demonstrate a new chemical vapor deposition (CVD) approach that can provide capabilities to produce large-area, high quality MoS_2 monolayer and few-layer films with unprecedented uniformity and controllability. While more studies would be necessary to better understand the growth mechanism, our experimental results strongly suggest that this synthetic process is self-limiting dictated by the balance between the equilibrium pressure of MoS_2 thin films and the partial pressure of MoS_2 species in the vapor phase. As a final note, this synthetic approach can be readily scaled up to produce wafer-scale 2D MoS_2 for the development of practical electronic and photonic devices. It is poised to enable 2D MoS_2 as a useful functional material to revolutionize a wide range of fields including information technology, optoelectronics, chemical/biological sensing, and spintronics.

Methods

MoS_2 thin films were synthesized in a tube furnace as illustrated in Fig. S1. In a typical growth, 1–50 mg of molybdenum chloride ($MoCl_5$) powder (99.99%, Sigma-Aldrich) was placed at the center of the furnace and 1 g of sulfur powder (Sigma-Aldrich) were placed at the upstream entry of the furnace. Receiving substrates were placed downstream in a distance of 1–7 centimeters away from the center of the furnace. In typical experiments, the furnace was heated up at a rate of 28°C/min under a flow of Ar gas, held at a setting temperature for 10 min, and then naturally cooled down to room temperature. Typical conditions for high-quality MoS_2 thin film growth include a temperature of 850°C (the temperature for sulfur source is estimated ~ 300°C), a flow rate of 50 sccm, and a pressure around 2 Torr. The layer number of the synthetic MoS_2 thin film can be controlled by control of the amount of $MoCl_5$ precursor or the total pressure in the synthetic setup (see Supplementary Information).

The crystal structure of the resulting products were analyzed with transmission electron microscope (TEM, JEOL-2010) and probe aberration-corrected scanning transmission electron microscope (STEM, FEI Titan 80–300 STEM) operated as 200 KV under STEM mode. The as-grown thin film was transferred to TEM grid for the structure characterization. The thickness and surface topology were measured using atomic force microscope (AFM, Veeco Dimension-3000). Raman mapping and photoluminescence (PL) measurements were carried out using Horiba Labram HR800 Raman Microscopy with an excitation wavelength of 532 nm. X-ray photoelectron spectroscopy were performed on SPECS XPS using an Mg Kα x ray source. The field-effect transistor device was fabricated by evaporating Ti/Au (5/200 nm) electrodes directly onto top of MoS_2 films transferred to degenerately doped Si substrates with 280 nm thick silicon oxide. A copper grid (100mesh, 30 micron spacing, Ted Pella) was placed on top of the thin film as mask for the electrode fabrication. This gives a relative large channel with a length L = 30 μm and a width W = 230 μm. The electrical measurements were performed in ambient conditions using a probe station (Karl Suss PSM6).

1. Novoselov, K. S. *et al.* Two-dimensional Gas of Massless Dirac Fermions in Graphene. *Nature* **438**, 197–200 (2005).
2. Berger, C. *et al.* Electronic Confinement and Coherence in Patterned Epitaxial Graphene. *Science* **312**, 1191–1196 (2006).
3. Huang, X., Qi, X. Y., Boey, F. & Zhang, H. Graphene-Based Composites. *Chem. Soc. Rev.* **41**, 666–686 (2012).
4. Huang, X. *et al.* Graphene-Based Materials: Synthesis, Characterization, Properties, and Applications. *Small* **7**, 1876–1902 (2011).
5. Mak, K. F., Lee, C., Hone, J., Shan, J. & Heinz, T. F. Atomically Thin MoS2: A New Direct-Gap Semiconductor. *Phys. Rev. Lett.* **105**, 136805 (2010).
6. Splendiani, A. *et al.* Emerging Photoluminescence in Monolayer MoS2. *Nano Lett.* **10**, 1271–1275 (2010).
7. Radisavljevic, B., Radenovic, A., Brivio, J., Giacometti, V. & Kis, A. Single-layer MoS2 Transistors. *Nat Nanotechnol* **6**, 147–150 (2011).
8. Wang, H. *et al.* Integrated Circuits Based on Bilayer MoS2 Transistors. *Nano Lett.* **12**, 4674–4680 (2012).
9. Yin, Z. Y. *et al.* Single-Layer MoS2 Phototransistors. *ACS Nano* **6**, 74–80 (2012).
10. Pu, J. *et al.* Highly Flexible MoS2 Thin-Film Transistors with Ion Gel Dielectrics. *Nano Lett.* **12**, 4013–4017 (2012).
11. Kim, S. *et al.* High-mobility and Low-power Thin-film Transistors Based on Multilayer MoS2 Crystals. *Nat. Comm.* **3**, 1011 (2012).
12. Yoon, Y., Ganapathi, K. & Salahuddin, S. How Good Can Monolayer MoS2 Transistors Be? *Nano Lett.* **11**, 3768–3773 (2011).
13. Cao, T. *et al.* Valley-selective Circular Dichroism of Monolayer Molybdenum Disulphide. *Nat. Comm.* **3**, 887 (2012).
14. Gunawan, O. *et al.* Valley Susceptibility of an Interacting Two-dimensional Electron System. *Phys. Rev. Lett.* **97**, 186404 (2006).
15. Lee, H. S. *et al.* MoS2 Nanosheet Phototransistors with Thickness-Modulated Optical Energy Gap. *Nano Lett* **12**, 3695–3700 (2012).
16. Mak, K. F. *et al.* Tightly Bound Trions in Monolayer MoS2. *Nat. Mater.* **12**, 207–211 (2012).
17. Mak, K. F., He, K., Shan, J. & Heinz, T. F. Control of Valley Polarization in Monolayer MoS2 by Optical Helicity. *Nat. Nanotechnol.* **7**, 494–498 (2012).
18. Xiao, D., Liu, G. B., Feng, W. X., Xu, X. D. & Yao, W. Coupled Spin and Valley Physics in Monolayers of MoS2 and Other Group-VI Dichalcogenides. *Phys. Rev. Lett.* **108**, 196802 (2012).
19. Zeng, H., Dai, J., Yao, W., Xiao, D. & Cui, X. Valley Polarization in MoS2 Monolayers by Optical Pumping. *Nat. Nanotechnol.* **7**, 490–493 (2012).
20. Chhowalla, M. *et al.* The Chemistry of Ultra-thin Transition Metal Dichalcogenide Nanosheets. *Nat. Chem.* **5** (2013).
21. He, Q. *et al.* Fabrication of Flexible MoS2 Thin-Film Transistor Arrays for Practical Gas-Sensing Applications. *Small* **8**, 2994–2999 (2012).
22. Huang, X., Zeng, Z. & Zhang, H. Metal Dichalcogenide Nanosheets: Preparation, Properties and Applications. *Chem. Soc. Rev.* **42**, 1934–1946 (2013).
23. Liu, J. *et al.* Preparation of MoS2-Polyvinylpyrrolidone Nanocomposites for Flexible Nonvolatile Rewritable Memory Devices with Reduced Graphene Oxide Electrodes. *Small* **8**, 3517–3522 (2012).
24. Lee, Y.-H. *et al.* Synthesis of Large-Area MoS2 Atomic Layers with Chemical Vapor Deposition. *Adv. Mater.* **24**, 2320–2325 (2012).
25. Etgar, L. *et al.* High Efficiency Quantum Dot Heterojunction Solar Cell Using Anatase (001) TiO2 Nanosheets. *Adv. Mater.* **24**, 2202–2206 (2012).
26. Zhan, Y., Liu, Z., Najmaei, S., Ajayan, P. M. & J, L. Large-Area Vapor-Phase Growth and Characterization of MoS2 Atomic Layers on a SiO2 Substrate. *Small* **8**, 966–971 (2012).
27. Lin, Y. C. *et al.* Wafer-scale MoS2 Thin Layers Prepared by MoO3 Sulfurization. *Nanoscale* **4**, 6637–6641 (2012).
28. Zhang, W. *et al.* Ultrahigh-Gain Phototransistors Based on Graphene-MoS2 Heterostructures. *arXiv:1302.1230* (2013).
29. Shi, Y. *et al.* van der Waals Epitaxy of MoS2 Layers Using Graphene As Growth Templates. *Nano Lett.* **12**, 2784–2791 (2012).
30. Najmaei, S. *et al.* Vapor Phase Growth and Grain Boundary Structure of Molybdenum Disulfide Atomic Layers. *arXiv 1301.2812* (2013).

31. Zande, A. M. v. d. *et al.* Grains and Grain Boundaries in Highly Crystalline Monolayer Molybdenum Disulfide. *arXiv 1301.1985* (2013).
32. Lee, C. *et al.* Anomalous Lattice Vibrations of Single- and Few-Layer MoS2. *ACS Nano* **4**, 2695–2700 (2010).
33. Li, H. *et al.* From Bulk to Monolayer MoS2: Evolution of Raman Scattering. *Adv. Func. Mater.s* **22**, 1385–1390 (2012).
34. Li, S.-L. *et al.* Quantitative Raman Spectrum and Reliable Thickness Identification for Atomic Layers on Insulating Substrates. *ACS Nano* **6**, 7381–7388 (2012).
35. Novoselov, K. S. *et al.* Two-dimensional Atomic Crystals. *Proc. Natl. Acad. Sci. USA* **102**, 10451–10453 (2005).
36. Li, H. *et al.* Fabrication of Single- and Multilayer MoS2 Film-Based Field-Effect Transistors for Sensing NO at Room Temperature. *Small* **8**, 63–67 (2012).
37. Li, X. *et al.* Large-Area Synthesis of High-Quality and Uniform Graphene Films on Copper Foils. *Science* **324**, 1312–1314 (2009).
38. Podgornik, P. & Parsegian, V. A. On a Possible Microscopic Mechansm Underlying the Vapor Pressure Paradox. *Biophys. J.* **72**, 942–952 (1997).
39. Ueno, K., Saiki, K., Shimada, T. & Koma, A. Epitaxial Growth of Transition Metal Dichalcogenides on Cleaved Faces of Mica. *J. Vac. Sci. Technol. A* **8**, 68 (1990).

Acknowledgments

The authors would like to thank Yuntian Zhu for providing access to a Raman spectrometer. L. C. acknowledges a Ralph E. Powe Junior Faculty Enhancement Award for Oak Ridge Associated Universities. Y. Z. acknowledges the support of Bissell Distinguished Professorship. Part of the work was supported by the Army Research Office (W911NF-11-1-0529).

Author contributions

Y.Y. and L.C. conceived the experiments. Y.Y. and C.L. perfermed the synthesis. Y.Y. performed most of the characterizations and device fabrications. Y.L. carried out the STEM characterization. L.S and Y.Z. performed the Raman and PL mapping. Y.Y. and L.C. analyzed the data. All authors were involved in writing the manuscript.

Additional information

Supplementary information accompanies this paper at http://www.nature.com/scientificreports

Competing financial interests: The authors declare no competing financial interests.

License: This work is licensed under a Creative Commons Attribution-NonCommercial-NoDerivs 3.0 Unported License. To view a copy of this license, visit http://creativecommons.org/licenses/by-nc-nd/3.0/

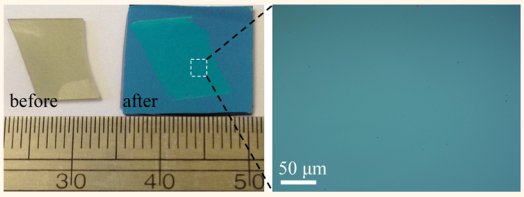
How to cite this article: Yu, Y. *et al.* Controlled Scalable Synthesis of Uniform, High-Quality Monolayer and Few-layer MoS_2 Films. *Sci. Rep.* **3**, 1866; DOI:10.1038/srep01866 (2013).

Surface-Energy-Assisted Perfect Transfer of Centimeter-Scale Monolayer and Few-Layer MoS_2 Films onto Arbitrary Substrates

Alper Gurarslan,[†,‡] Yifei Yu,[†] Liqin Su,[§] Yiling Yu,[∥] Francisco Suarez,[⊥] Shanshan Yao,[#] Yong Zhu,[#] Mehmet Ozturk,[⊥] Yong Zhang,[§] and Linyou Cao[*,†,∥]

[†]Department of Materials Science and Engineering and [‡]Department of Fiber and Polymer Science, North Carolina State University, Raleigh, North Carolina 27695, United States, [§]Department of Electrical and Computer Engineering, The University of North Carolina at Charlotte, Charlotte, North Carolina 28223, United States, and [∥]Department of Physics, [⊥]Department of Electrical and Computer Engineering, and [#]Department of Mechanical and Aerospace Engineering, North Carolina State University, Raleigh, North Carolina 27695, United States

ABSTRACT The transfer of synthesized 2D MoS_2 films is important for fundamental and applied research. However, it is problematic to translate the well-established transfer processes for graphene to MoS_2 due to different growth mechanisms and surface properties. Here we demonstrate a surface-energy-assisted process that can perfectly transfer centimeter-scale monolayer and few-layer MoS_2 films from original growth substrates onto arbitrary substrates with no observable wrinkles, cracks, and polymer residues. The unique strategies used in this process include leveraging the penetration of water between hydrophobic MoS_2 films and hydrophilic growth substrates to lift off the films and dry transferring the film after the lift off. This is in stark contrast with the previous transfer process for synthesized MoS_2 films, which explores the etching of the growth substrate by hot base solutions to lift off the films. Our transfer process can effectively eliminate the mechanical force caused by bubble generations, the attacks from chemical etchants, and the capillary force induced when transferring the film outside solutions as in the previous transfer process, which consists of the major causes for the previous unsatisfactory transfer. Our transfer process also benefits from using polystyrene (PS), instead of poly(methyl methacrylate) (PMMA) that was widely used previously, as the carrier polymer. PS can form more intimate interaction with MoS_2 films than PMMA and is important for maintaining the integrity of the film during the transfer process. This surface-energy-assisted approach can be generally applied to the transfer of other 2D materials, such as WS_2.



KEYWORDS: molybdenum disulfide · 2D materials · tungsten disulfide · surface energy · large scale

Two-dimensional (2D) transition metal dichalcogenide (TMDC) materials have recently emerged as a topical research area.[1−12] These materials present an attractive semiconductor option at the atomic scale that promises to scale all semiconductor devices including integrated circuits, lasers, light-emitting diodes, and photodetectors down to a truly atomic level. However, to fully explore the potential of 2D TMDC materials requires the ability to perfectly transfer synthesized 2D TMDC materials from the growth substrates onto other substrates without compromising the quality and properties. This is because the substrates used for the growth of 2D TMDC materials are often different from those required for fundamental or applied research. It has been demonstrated that centimeter-scale and high-quality 2D TMDC materials such as MoS_2 can be synthesized using chemical vapor deposition (CVD) processes that involve high temperature (usually >800 °C), corrosive vapor (sulfur vapor), and substrates with atomically smooth surfaces.[13,14] However, the substrates required for the research of 2D TMDC materials may not be able to survive the harsh environment of the growth process or to support the growth of high-quality 2D TMDC materials. One example is polymer substrates for the development of flexible devices.[15−17] Additionally, the capability of perfect transfer is necessary for the fabrication of 2D heterostructures that consist of dissimilar layers stacked in the vertical direction. The 2D heterostructures have

* Address correspondence to lcao2@ncsu.edu.

Received for review August 24, 2014 and accepted October 27, 2014.

Published online 10.1021/nn5057673

© XXXX American Chemical Society

been known to hold great promise to enable novel functionality that cannot be obtained with typical single-component 2D materials.[18−24]

However, the transfer of synthesized 2D materials is challenging due to the extreme mechanical delicacy of the atomically thin structure. While the transfer of graphene has been extensively studied,[1,25−30] simply translating the transfer processes for graphene to 2D TMDC materials such as MoS_2 is problematic because of the differences in the growth mechanism and surface properties.[13,14,31−33] The transfer process generally involves two steps, the lift off of 2D materials from the original growth substrates and the release of the lift 2D materials onto target substrates. It usually starts by coating a layer of polymer on top of the as-grown 2D materials to act as carrier polymers that help with the handling of the atomically thin materials. A perfect transfer would mean a complete lift off of the materials from the growth substrates and a complete release of the lift materials onto target substrates. Much of the difference between the transfer of graphene and that of 2D MoS_2 lies in the lift-off process. For graphene films, the lift off can be achieved by dissolving the growth substrate (*i.e.*, copper or nickel) into, for instance, $FeCl_3$ solutions.[26−30] In contrast, the lift off of MoS_2 films is more difficult because the growth substrate of MoS_2 films, which is typically ceramic materials like sapphire,[13,14,34] cannot be dissolved as easily. Current transfer processes for synthesized MoS_2 films predominantly use poly(methyl methacrylate) (PMMA) as the carrier polymer and leverage the etching of the growth substrate by a hot base (NaOH or KOH) solution bath to lift off the films.[13,34] However, the bubble generation in the hot solution may severely damage the film, and the capillary force induced when transferring the film out of the solution bath may cause wrinkles, wrapping, and cracks in the film. Recent studies also reported using polydimethylsiloxane (PDMS) (as the carrier polymer) and cold water to lift off synthesized MoS_2 films.[35] This requires the presence of a water-soluble layer underlying the as-grown films, which is not typical in the synthesis. Additionally, the removal of the PDMS from the MoS_2 film after the transfer relies on mechanical forces and may end up releasing only a part of the film onto the target substrates.[35]

Here we present a surface-energy-assisted process that can perfectly transfer centimeter-scale monolayer or few-layer MoS_2 films onto arbitrary substrates with no observable wrinkles, cracks, and polymer residues. This process is carefully designed to minimize the mechanical forces or chemical attacks experienced by the atomically thin MoS_2 film during the transfer. One key strategy is exploiting the penetration of water molecules between the synthesized MoS_2 film and the growth substrate to lift off the film at room temperature, which is different from what was used in the previous transfer methods that rely on the etching of growth

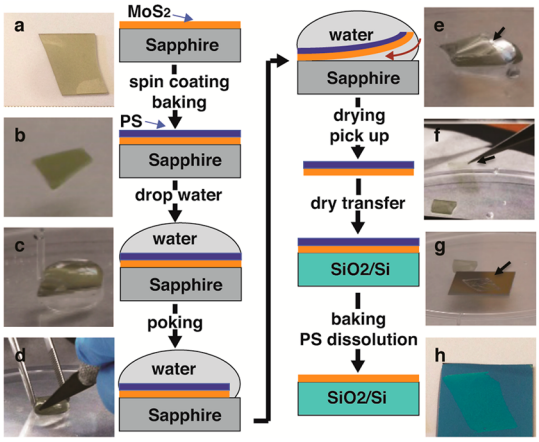


Figure 1. Illustration of the surface-energy-assisted transfer process. (a−h) Typical images of the transfer process. The arrows in (e−g) point toward the MoS_2 film for visual convenience.

substrates by hot base solutions for the lift off. We find that the synthesized MoS_2 film is hydrophobic, while the growth substrate (sapphire) is hydrophilic (see the contact angle measurement given in Supporting Information Figure S1). The different surface energies can drive water molecules to penetrate underneath the film, and this is why our process is termed surface-energy-assisted transfer. The mild lift off by water penetration at room temperatures eliminates the mechanical force caused by bubble generations and the attacks from chemical etchants as in the previous transfer process.[13,34] Other unique strategies used in this process include the use of polystyrene as the carrier polymer, instead of PMMA that was used previously,[13,34] and dry transfer of the film after the lift off.

RESULTS AND DISCUSSION

The transfer process is schematically illustrated in Figure 1 (see a video in the Supporting Information). We first spin-coat a layer of polystyrene (PS) onto as-grown MoS_2 films on sapphire substrates followed by a baking process at 80−90 °C for 15 min (Figure 1a,b). A water droplet is then dropped onto the PS layer (Figure 1c). While the water may have a natural tendency to penetrate between the MoS_2 film and the substrate due to different surface energies, the penetration actually cannot start by itself. This is because the intimate adhesion of the synthesized film with the substrate may effectively hinder the start of the penetration. We find that a gentle poking at the edge of the polymer/MoS_2 assembly with a sharp object, which might create cracks at the edge, is necessary to initiate the water penetration (Figure 1d). The polymer/MoS_2 assembly can be lifted off instantly after the poking (Figure 1e) and floats on top of the water droplet. The detached polymer−MoS_2 assembly can be dried by simply sucking the water droplet away with a paper towel. We can then readily pick the assembly using

tweezers (Figure 1f) and dry transfer it onto arbitrary target substrates (Figure 1g). After that, we bake the transferred assembly at 80 °C for 1 h to remove water residues and then at 150 °C for 30 min to spread the polymer for the elimination of possible wrinkles. The last step of the transfer process is dissolving the polymer with toluene (Figure 1h).

Our transfer process for the centimeter-scale synthesized MoS_2 films bear substantial difference from what was reported previously that employs the penetration of water between hydrophobic and hydrophilic surfaces to transfer small (micrometer-scale) exfoliated 2D materials.[36−38] The difference mainly lies in the lift off of the materials from the original substrate and is caused by the different sizes of the materials in the study as well as the different strengths of the interaction between the materials and the substrate. The previous works dealt with small (micrometer-scale) exfoliated 2D materials that had been predeposited onto substrates.[36−38] The exfoliated 2D materials were first coated by a carrier polymer, and the polymer-exfoliated 2D material assembly could then be lifted off from the original substrate by simply immersing the entire sample into water.[36−38] However, such a simple immersion into water cannot lift off our synthesized MoS_2 films from the growth substrate. Unlike the exfoliated 2D materials, which is much smaller than the polymer overlayer and its lift off actually relies on the penetration of water between the carrier polymer and the substrate, the synthesized film in our experiments covers the entire growth substrate and is the same size as the overlayer of the carrier polymer. As a result of the big size, to lift off the synthesized film requires the penetration of water molecules between the film and the substrate. This is more difficult because the synthesized film intimately adheres to the growth substrate, which may hinder the water penetration. External forces, such as poking, are necessary to initiate the water penetration underneath the synthesized film for the lift off, as we have demonstrated in the preceding text. The intimate adhesion of the synthesized film with the growth substrate also imposes additional requirements on the choice of the carrier polymer. To facilitate the lift off of 2D materials, ideally the adhesion between the carrier polymer and the 2D materials should be stronger than that between the substrate and the 2D materials. Unlike exfoliated 2D materials, which have relatively weaker adhesion with the substrate that can be easily overcome by the interaction with arbitrary polymers,[36−38] to successfully lift off the synthesized film requires the carrier polymer to form strong adhesion with the film in order to overcome the intimate adhesion of the film with the growth substrate. We find that PS is a better choice than PMMA as the carrier polymer to lift off the synthesized films as only part of the synthesized film may be lifted off and transferred when using PMMA as the carrier polymer (Figure S2). This is because PS can form stronger

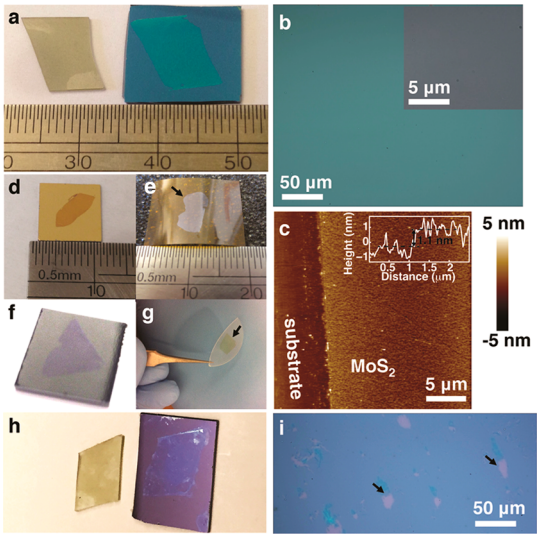


Figure 2. Transfer of MoS_2 films onto arbitrary substrates. (a) Monolayer MoS_2 film transferred onto a SiO_2/Si substrate and the sapphire substrate that the film was originally grown on. (b) Optical images of the transferred monolayer MoS_2. Inset: Optical image of the transferred monolayer with larger magnification. (c) Typical AFM image of the transferred monolayer MoS_2 film. Inset: Typical height profile showing the thickness of the film, and MoS_2 atomically thin films transferred onto various substrates including (d) gold, (e) kapton, (f) glassy carbon, and (g) quartz. The arrows serve to guide the eyes to the transferred film. (h) Monolayer MoS_2 film transferred onto a SiO_2/Si substrate by using the previous transfer process and the sapphire substrate that the film was originally grown on. (i) Optical images of the monolayer MoS_2 transferred by using the previous transfer process. The arrows indicate cracks/holes in the transferred film.

adhesion with the film than PMMA due to a larger hydrophobicity (Figure S3). As further evidence for the requirement of strong adhesion of the synthesized film with the polymer, we also find in experiments that it is difficult to lift off the film with a relatively rough surface, in which the rough surface could prevent strong interaction between the polymer and the film.

Our process can perfectly transfer centimeter-scale MoS_2 films onto arbitrary substrates. Without losing generality, we use the transfer of MoS_2 films onto SiO_2/Si substrates to illustrate this notion. Figure 2a shows a monolayer film transferred onto a SiO_2/Si substrate and the sapphire substrate that the film was originally grown on. The transferred MoS_2 film shows an identical size and shape as the growth substrate, indicating a perfect lift off and release. Under an optical microscope, the transferred film appears to be very uniform, continuous, and clean with no observable wrinkles, cracks, and polymer residues (Figure 2b). This remarkable uniformity is similar to what was observed on the as-grown MoS_2 films.[14] It is worthwhile to point out that the presence of wrinkles, cracks, or polymer residues, if any, can be easily identified under optical microscopes due to distinct contrast (Figure S4). The uniformity and cleanness of the transferred film can be further confirmed by AFM measurements. The surface roughness of the transferred

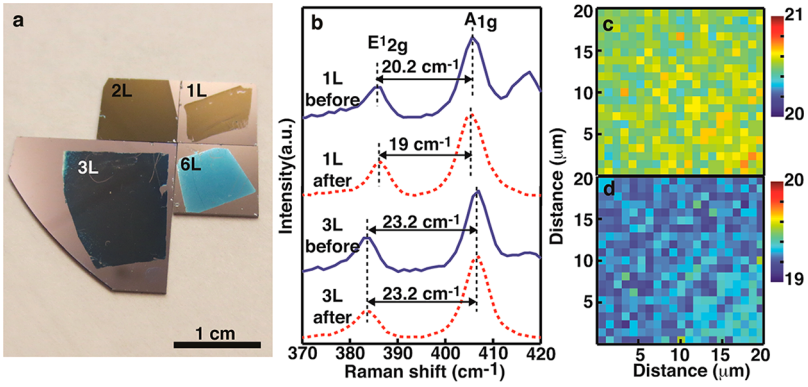


Figure 3. Unchanged layer number, crystalline quality, and uniformity of the transferred MoS_2 films. (a) MoS_2 films with different layer numbers transferred onto SiO_2/Si substrates. (b) Raman spectra of the as-grown MoS_2 films on sapphire substrates (before) and the transferred films on SiO_2/Si substrates. Only the results for monolayer (1L) and trilayer (3L) MoS_2 are given here. More can be seen in Figure S4. Mapped frequency differences between the characteristic Raman peaks A_{1g}, E_{2g}^1 for (c) as-grown monolayer MoS_2 on sapphire substrates and (d) monolayer MoS_2 transferred onto SiO_2/Si substrates.

monolayer film is measured to be around 0.4 nm (Figure 2c), comparable to what was previously observed with the as-grown MoS_2 films on sapphire substrates.[14] AFM measurements also indicate that the transferred film has a thickness of 1.1 nm. This is slightly larger than what was observed with as-grown monolayers,[14] likely due to a larger spatial separation between the film and the substrate after the transfer. The transfer process is very robust, and we have successfully used it to transfer MoS_2 films onto many different substrates, including gold (Figure 2d), kapton (Figure 2e), glassy carbon (Figure 2f), and quartz (Figure 2g).

To further illustrate the advantage of our process, we also transferred synthesized MoS_2 films from the growth substrate (sapphire) to SiO_2/Si substrates using the process widely used previously, in which the film was lifted off by etching the growth substrate with hot NaOH solution and PMMA used as the carrier polymer. The typical result is given in Figure 2h,i. Unlike the perfect transfer enabled by our process (Figure 2a,b), only part of the film can be lifted off and transferred from the original growth substrate to the target substrate by using the previous process,[13,34] as a substantial amount of voids may be found at the transferred film (Figure 2h) and MoS_2 materials at the original growth substrate after the transfer. This is likely due to the relatively weaker interaction of PMMA with the MoS_2 film compared to PS. The weaker interaction of PMMA with the hydrophobic MoS_2 film is supported by our contact angle measurements that show PMMA is less hydrophobic than PS (see the result in Figure S2). Additionally, we can find numerous micrometer-scale cracks/holes in the transferred films (Figure 2i). These cracks/holes are caused by bubbling in the hot solution and/or by the capillary force induced when transferring the film out of the solution. In contrast, our transfer process exploits the water penetration at room temperature to provide a mild lift off of the film. It eliminates the mechanical force generated by the bubbling and the possible attacks from chemical etchants as in the previous transfer process. Our transfer process also exploits the removal of the water droplet right after the lift off to make the subsequent transfer of the polymer−MoS_2 assembly essentially a dry process. This may minimize the capillary force experienced by the film. Capillary forces are well-known as a major cause of warping or wrinkles in the transferred atomically thin films and may trap a significant amount of water residue between the target substrate and the films, which may lead to the formation of cracks in the following baking step.

Our transfer process may maintain the layer number, crystalline quality, and uniformity of the MoS_2 films. Figure 3a shows the MoS_2 films with different layer numbers transferred onto SiO_2/Si substrates, whose strikingly different colors originate from optical interferences and depend on the thickness of the SiO_2 layer. All of these transferred films are in the same shapes and dimensions as the corresponding growth substrates (Figure S5). We have confirmed that no MoS_2 materials are left behind on the growth substrate after the transfer using an optical microscope imaging and Raman measurements. This indicates a complete lift off of the film from the growth substrate regardless of the layer number. Raman measurements also confirm that the layer number of the transferred film is the same as that of the as-grown one, indicating a complete release of the film onto the target substrate. Figure 3b shows the Raman spectra collected from as-grown MoS_2 films on sapphire substrates and the films transferred onto SiO_2/Si substrates (more results can be seen in Figure S6). The frequency difference Δk between the two characteristic peaks A_{1g} and E_{2g}^1, which has been widely used as an indicator for the layer number of MoS_2,[39] is essentially unchanged after the transfer. For instance, the Δk of trilayer MoS_2 films remains at 23.2 cm^{-1} before and after the transfer. Note that the Δk of the monolayer MoS_2 does show a slight change from 20.2 to ~19 cm^{-1} after the transfer, but this

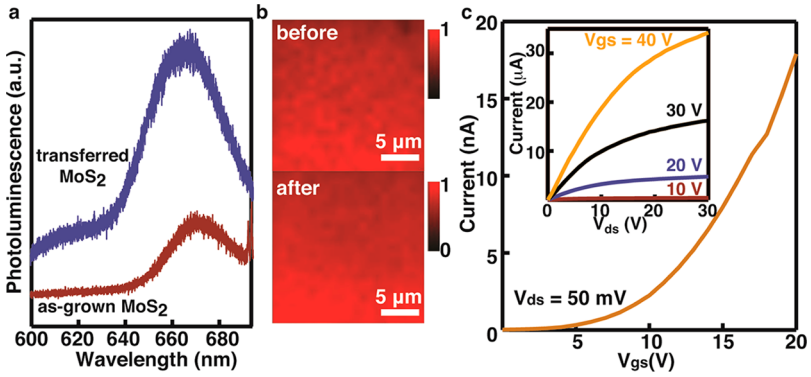


Figure 4. Optical and electrical qualities of transferred MoS_2 films. (a) Photoluminescence spectra and (b) mapped PL intensity (integrated over 650−670 nm) from an as-grown monolayer MoS_2 film on sapphire substrates (before) and the same film transferred onto SiO_2/Si substrates. (c) Transfer characteristic for a FET built upon monolayer MoS_2 transferred onto SiO_2/Si substrates with a source drain bias V_{ds} of 50 mV. Inset: $I_{ds}-V_{ds}$ curve for the FET with gating voltages V_{gs} of 10, 20, 30, and 40 V.

change is caused by changes in the interaction of the film with substrates rather than by a change in the layer number.[40] Our AFM measurement has already confirmed that the as-grown monolayer film remains as a monolayer after the transfer (Figure 2c). It has been well-known that the interaction with substrates may affect the Raman frequencies of MoS_2,[40] and the as-grown film may likely interact with substrates more strongly than the transferred film. Similar decrease of the Δk can also be seen in the monolayer film transferred from the original sapphire growth substrate to another bare sapphire substrate (Figure S7). Except for the Raman frequencies, the full width at half-maximum (fwhm) of the $E_{2g}{}^1$ peak, which may be used as an indicator for crystalline quality,[39] remains unchanged as well during the transfer process. For instance, the $E_{2g}{}^1$ fwhm is 5.2 cm^{-1} for both as-grown and transferred MoS_2 monolayers and 5.4 cm^{-1} for the trilayers.[39] This indicates that the transfer process does not compromise the crystalline quality of the films. Additionally, our optical microscope imaging indicates that the transfer films exhibit comparable uniformity as the as-grown counterpart (Figure 2b). This is further confirmed by Raman mapping measurements. For instance, the Raman mapping results of monolayer MoS_2 films show the Δk always in a narrow range before (20.2−20.8 cm^{-1}) and after (19.0−19.6 cm^{-1}) the transfer (Figure 3c,d).

The transferred films show good optical and electrical properties. The PL from the film transferred onto SiO_2/Si substrates can be found to be even stronger than that of the as-grown one on sapphire substrates (Figure 4a). This PL enhancement is caused by the optical interference effect in the SiO_2/Si substrates as reported previously.[40,41] We also observed similar enhancement in the Raman spectrum of the transferred monolayer on SiO_2/Si substrates (Figure S8). Nevertheless, the strong PL clearly indicates that the optical quality of the film is not compromised by the transfer process. The PL mapping results indicate comparable optical uniformity in the as-grown and transferred films (Figure 4b), consistent with the comparable structural uniformity illustrated in Figures 2 and 3. We also fabricated field-effect transistors (FETs) with transferred monolayer MoS_2 films to measure the mobility. The devices show clear current saturation due to the pinch-off of the channel, and the mobility is measured to be 0.03 $cm^2/V\cdot s$, reasonably consistent with the mobility measured at exfoliated monolayer MoS_2 with similar gating configuration and ambient environments.[42]

CONCLUSION

In conclusion, we have demonstrated a unique surface-energy-assisted transfer process that can perfectly transfer synthesized centimeter-scale MoS_2 films onto arbitrary substrates without compromising the crystalline/surface quality and properties. Although this work mainly focuses on the transfer of the MoS_2 films grown by using $MoCl_5$ as the precursor, the process can be applied to the transfer of MoS_2 materials synthesized using other methods, for instance, the CVD process with MoO_3 being the precursor (Figure S9). We believe that the key strategy of leveraging the difference in surface energies between the synthesized materials and the growth substrate can be generally applied to the transfer of other 2D materials. For instance, we have demonstrated a successful transfer of synthesized WS_2 films by using this transfer process (Figure S10).

METHODS

Synthesis of Centimeter-Scale MoS_2 Films. The centimeter monolayer and few-layer MoS_2 films were grown using a CVD process in a tube furnace that we have previously reported.[14] In a typical growth, 4−20 mg of molybdenum chloride ($MoCl_5$) powder (99.99%, Sigma-Aldrich) and 1 g of sulfur powder (Sigma-Aldrich) were placed upstream of the furnace. Receiving substrates (typically sapphire) were placed downstream of the tube.

Typical conditions for high-quality MoS_2 thin film growth include a temperature of 850 °C, a flow rate of 50 sccm, and a pressure around 2 Torr. During the synthesis, the vapor of the precursor materials reacted to produce gaseous molybdenum sulfide species, which could subsequently precipitate onto receiving substrates. The layer number was controlled by controlling the amount of precursors ($MoCl_5$) used in the synthesis (see the Supporting Information of ref 14).

Transfer of Centimeter-Scale MoS_2 Films. In a typical transfer process, 9 g of PS with a molecular weight of 280 000 g/mol was dissolved in 100 mL of toluene and then the PS solution was spin-coated (3500 rpm for 60 s) on as-grown MoS_2 films on sapphire substrates. This was followed by a baking at 80−90 °C for 15 min to facilitate intimate adhesion of the PS layer with the MoS_2 film. A water droplet was then dropped on top of the sample. To facilitate the penetration of water molecules, we poked the PS layer with a sharp object from the edge. Once the PS layer was scratched from the edge, water molecules could penetrate all the way through the MoS_2 film, resulting in the delamination of the PS−MoS_2 assembly. The water droplet was then removed from the detached PS−MoS_2 assembly with a paper towel. We could pick up the assembly with tweezers and transfer it onto the target substrate. To ensure the uniformity of the transferred MoS_2 film, we baked the transferred PS−MoS_2 assembly as follows: a mild baking at 80 °C for 1 h to remove the water residues and a final baking for 30 min at 150 °C to spread the polymer for the elimination of possible wrinkles. Finally, PS was removed by rinsing with toluene several times. The transfer using poly(methyl methacrylate) (950 K, Microchem) followed a previously report.[13] Briefly, a layer of PMMA was spin-coated onto the as-grown MoS_2 films on sapphire substrates first, and then the sample was immersed into hot (90 °C) NaOH solution for hours. After being lifted off from the original substrates, the polymer−MoS_2 assembly was fished out onto target substrates. This was followed by a baking process at 90 °C for 1 h, and the PMMA was dissolved by acetone afterward.

Characterizations of MoS_2 Films. The structure and composition of the as-grown and transferred MoS_2 were characterized by a variety of tools. The thickness and surface topology were measured using atomic force microscope (AFM, Veeco Dimension-3000). Raman measurements were typically performed witha Raman spectroscope (Renishaw-1000) with an excitation wavelength of 514.5 nm, except for the Raman mapping that was carried out using Horiba Labram HR800 Raman microscopy with an excitation wavelength of 532 nm. Photoluminescence (PL) measurements were also carried out with a Horiba Labram HR800 Raman microscope. The field-effect transistor device was fabricated by using standard photolithography, development, and metallization processes. Ti/Au (30/250 nm) was evaporated onto top of MoS_2 films transferred to degenerately doped Si substrates with 80 nm thick silicon oxide. Typical devices were features with a channel length of 5 μm and a width of 400 μm. The electrical measurements were performed in ambient conditions using a probe station (Karl Suss PSM6).

Conflict of Interest: The authors declare no competing financial interest.

Acknowledgment. This work was supported by a Young Investigator Award from the Army Research Office (W911NF-13-1-0201) and, partially, by a CAREER award from the National Science Foundation (DMR-1352028). Y.Z. acknowledges the support of the Bissell Distinguished Professorship. The authors acknowledge the use of the Analytical Instrumentation Facility (AIF) at North Carolina State University, which is supported by the State of North Carolina and the National Science Foundation.

Supporting Information Available: More results including a video for the transfer process. This material is available free of charge *via* the Internet at http://pubs.acs.org.

REFERENCES AND NOTES

1. Britnell, L.; Ribeiro, R. M.; Eckmann, A.; Jalil, R.; Belle, B. D.; Mishchenko, A.; Kim, Y. J.; Gorbachev, R. V.; Georgiou, T.; Morozov, S. V.; *et al.* Strong Light−Matter Interactions in Heterostructures of Atomically Thin Films. *Science* **2013**, *340*, 1311–1314.
2. Butler, S. Z.; Hollen, S. M.; Cao, L.; Cui, Y.; Gupta, J. A.; Gutiérrez, H. R.; Heinz, T. F.; Hong, S. S.; Huang, J.; Ismach, A. F.; *et al.* Progress, Challenges, and Opportunities in Two-Dimensional Materials Beyond Graphene. *ACS Nano* **2013**, *7*, 2898–2926.
3. Chhowalla, M.; Shin, H. S.; Eda, G.; Li, L.-J.; Loh, K. P.; Zhang, H. The Chemistry of Two-Dimensional Layered Transition Metal Dichalcogenide Nanosheets. *Nat. Chem.* **2013**, *5*, 263–275.
4. Jariwala, D.; Sangwan, V. K.; Lauhon, L. J.; Marks, T. J.; Hersam, M. C. Emerging Device Applications for Semiconducting Two-Dimensional Transition Metal Dichalcogenides. *ACS Nano* **2014**, *8*, 1102–1120.
5. Mai, C.; Barrette, A.; Yu, Y. F.; Semenov, Y. G.; Kim, K. W.; Cao, L. Y.; Gundogdu, K. Many-Body Effects in Valleytronics: Direct Measurement of Valley Lifetimes in Single-Layer MoS_2. *Nano Lett.* **2014**, *14*, 202–206.
6. Radisavljevic, B.; Radenovic, A.; Brivio, J.; Giacometti, V.; Kis, A. Single-Layer MoS_2 Transistors. *Nat. Nanotechnol.* **2011**, *6*, 147–150.
7. Wang, Q. H.; Kalantar-Zadeh, K.; Kis, A.; Coleman, J. N.; Strano, M. S. Electronics and Optoelectronics of Two-Dimensional Transition Metal Dichalcogenides. *Nat. Nanotechnol.* **2012**, *7*, 699–712.
8. Xu, X.; Yao, W.; Xiao, D.; Heinz, T. F. Spin and Pseudospins in Layered Transition Metal Dichalcogenides. *Nat. Phys.* **2014**, *10*, 343–350.
9. Yu, Y. F.; Huang, S. Y.; Li, Y. P.; Steinmann, S. N.; Yang, W. T.; Cao, L. Y. Layer-Dependent Electrocatalysis of MoS_2 for Hydrogen Evolution. *Nano Lett.* **2014**, *14*, 553–558.
10. Li, H.; Wu, J. M. T.; Yin, Z. Y.; Zhang, H. Preparation and Applications of Mechanically Exfoliated Single-Layer and Multilayer MoS_2 and WSe2 Nanosheets. *Acc. Chem. Res.* **2014**, *47*, 1067–1075.
11. Huang, X.; Tan, C. L.; Yin, Z. Y.; Zhang, H. 25th Anniversary Article: Hybrid Nanostructures Based on Two-Dimensional Nanomaterials. *Adv. Mater.* **2014**, *26*, 2185–2204.
12. Huang, X.; Zeng, Z. Y.; Zhang, H. Metal Dichalcogenide Nanosheets: Preparation, Properties and Applications. *Chem. Soc. Rev.* **2013**, *42*, 1934–1946.
13. Liu, K. K.; Zhang, W. J.; Lee, Y. H.; Lin, Y. C.; Chang, M. T.; Su, C.; Chang, C. S.; Li, H.; Shi, Y. M.; Zhang, H.; *et al.* Growth of Large-Area and Highly Crystalline MoS_2 Thin Layers on Insulating Substrates. *Nano Lett.* **2012**, *12*, 1538–1544.
14. Yu, Y. F.; Li, C.; Liu, Y.; Su, L. Q.; Zhang, Y.; Cao, L. Y. Controlled Scalable Synthesis of Uniform, High-Quality Monolayer and Few-Layer MoS_2 Films. *Sci. Rep.* **2013**, *3*, 1806.
15. Liu, J. Q.; Zeng, Z. Y.; Cao, X. H.; Lu, G.; Wang, L. H.; Fan, Q. L.; Huang, W.; Zhang, H. Preparation of MoS_2−Polyvinylpyrrolidone Nanocomposites for Flexible Nonvolatile Rewritable Memory Devices with Reduced Graphene Oxide Electrodes. *Small* **2012**, *8*, 3517–3522.
16. Salvatore, G. A.; Munzenrieder, N.; Barraud, C.; Petti, L.; Zysset, C.; Buthe, L.; Ensslin, K.; Troster, G. Fabrication and Transfer of Flexible Few-Layers MoS_2 Thin Film Transistors to Any Arbitrary Substrate. *ACS Nano* **2013**, *7*, 8809–8815.
17. He, Q. Y.; Zeng, Z. Y.; Yin, Z. Y.; Li, H.; Wu, S. X.; Huang, X.; Zhang, H. Fabrication of Flexible MoS_2 Thin-Film Transistor Arrays for Practical Gas-Sensing Applications. *Small* **2012**, *8*, 2994–2999.
18. Gao, G. H.; Gao, W.; Cannuccia, E.; Taha-Tijerina, J.; Balicas, L.; Mathkar, A.; Narayanan, T. N.; Liu, Z.; Gupta, B. K.; Peng, J.; *et al.* Artificially Stacked Atomic Layers: Toward New van der Waals Solids. *Nano Lett.* **2012**, *12*, 3518–3525.
19. Geim, A. K.; Grigorieva, I. V. van der Waals Heterostructures. *Nature* **2013**, *499*, 419–425.
20. Georgiou, T.; Jalil, R.; Belle, B. D.; Britnell, L.; Gorbachev, R. V.; Morozov, S. V.; Kim, Y.-J.; Gholinia, A.; Haigh, S. J.; Makarovsky, O.; *et al.* Vertical Field-Effect Transistor Based on Graphene−WS_2 Heterostructures for Flexible and Transparent Electronics. *Nat. Nanotechnol.* **2013**, *8*, 100–103.
21. Kośmider, K.; Fernández-Rossier, J. Electronic Properties of the MoS_2−WS_2 Heterojunction. *Phys. Rev. B* **2013**, *87*, 075451.

22. Yu, W. J.; Li, Z.; Zhou, H.; Chen, Y.; Wang, Y.; Huang, Y.; Duan, X. Vertically Stacked Multi-heterostructures of Layered Materials for Logic Transistors and Complementary Inverters. *Nat. Mater.* **2013**, *12*, 246–252.
23. Yu, Y.; Hu, S.; Su, L.; Huang, L.; Liu, Y.; Jin, Z.; Purezky, A. A.; Geohegan, D. B.; Kim, K. W.; Zhang, Y.; *et al.* Efficient Interlayer Relaxation and Transition of Excitons in Epitaxial and Non-epitaxial MoS_2/WS_2 Heterostructures. *arXiv:1403.6181* **2014**.
24. Terrones, H.; López-Urías, F.; Terrones, M. Novel Hetero-layered Materials with Tunable Direct Band Gaps by Sandwiching Different Metal Disulfides and Diselenides. *Sci. Rep.* **2013**, *3*, 1549.
25. Gao, L. B.; Ni, G. X.; Liu, Y. P.; Liu, B.; Neto, A. H. C.; Loh, K. P. Face-to-Face Transfer of Wafer-Scale Graphene Films. *Nature* **2014**, *505*, 190–194.
26. Li, X. S.; Zhu, Y. W.; Cai, W. W.; Borysiak, M.; Han, B. Y.; Chen, D.; Piner, R. D.; Colombo, L.; Ruoff, R. S. Transfer of Large-Area Graphene Films for High-Performance Transparent Conductive Electrodes. *Nano Lett.* **2009**, *9*, 4359–4363.
27. Lee, Y.; Bae, S.; Jang, H.; Jang, S.; Zhu, S.-E.; Sim, S. H.; Song, Y. I.; Hong, B. H.; Ahn, J.-H. Wafer-Scale Synthesis and Transfer of Graphene Films. *Nano Lett.* **2010**, *10*, 490–493.
28. Liang, X. L.; Sperling, B. A.; Calizo, I.; Cheng, G. J.; Hacker, C. A.; Zhang, Q.; Obeng, Y.; Yan, K.; Peng, H. L.; Li, Q. L.; *et al.* Toward Clean and Crackless Transfer of Graphene. *ACS Nano* **2011**, *5*, 9144–9153.
29. Suk, J. W.; Kitt, A.; Magnuson, C. W.; Hao, Y.; Ahmed, S.; An, J.; Swan, A. K.; Goldberg, B. B.; Ruoff, R. S. Transfer of CVD-Grown Monolayer Graphene onto Arbitrary Substrates. *ACS Nano* **2011**, *5*, 6916–6924.
30. Song, J.; Kam, F. Y.; Png, R. Q.; Seah, W. L.; Zhuo, J. M.; Lim, G. K.; Ho, P. K. H.; Chua, L. L. A General Method for Transferring Graphene onto Soft Surfaces. *Nat. Nanotechnol.* **2013**, *8*, 356–362.
31. Li, X.; Cai, W.; An, J.; Kim, S.; Nah, J.; Yang, D.; Piner, R.; Velamakanni, A.; Jung, I.; Tutuc, E.; *et al.* Large-Area Synthesis of High-Quality and Uniform Graphene Films on Copper Foils. *Science* **2009**, *324*, 1312–1314.
32. van der Zande, A. M.; Huang, P. Y.; Chenet, D. A.; Berkelbach, T. C.; You, Y. M.; Lee, G. H.; Heinz, T. F.; Reichman, D. R.; Muller, D. A.; Hone, J. C. Grains and Grain Boundaries in Highly Crystalline Monolayer Molybdenum Disulphide. *Nat. Mater.* **2013**, *12*, 554–561.
33. Najmaei, S.; Liu, Z.; Zhou, W.; Zou, X.; Shi, G.; Lei, S.; Yakobson, B. I.; Idrobo, J.-C.; Ajayan, P. M.; Lou, J. Vapour Phase Growth and Grain Boundary Structure of Molybdenum Disulphide Atomic Layers. *Nat. Mater.* **2013**, *12*, 754–759.
34. Lin, Y. C.; Zhang, W. J.; Huang, J. K.; Liu, K. K.; Lee, Y. H.; Liang, C. T.; Chu, C. W.; Li, L. J. Wafer-Scale MoS_2 Thin Layers Prepared by MoO_3 Sulfurization. *Nanoscale* **2012**, *4*, 6637–6641.
35. Lee, Y. H.; Yu, L. L.; Wang, H.; Fang, W. J.; Ling, X.; Shi, Y. M.; Lin, C. T.; Huang, J. K.; Chang, M. T.; Chang, C. S.; *et al.* Synthesis and Transfer of Single-Layer Transition Metal Disulfides on Diverse Surfaces. *Nano Lett.* **2013**, *13*, 1852–1857.
36. Li, H.; Wu, J.; Huang, X.; Yin, Z.; Liu, J.; Zhang, H. A Universal, Rapid Method for Clean Transfer of Nanostructures onto Various Substrates. *ACS Nano* **2014**, *8*, 6563–6570.
37. Schneider, G. F.; Calado, V. E.; Zandbergen, H.; Vandersypen, L. M. K.; Dekker, C. Wedging Transfer of Nanostructures. *Nano Lett.* **2010**, *10*, 1912–1916.
38. Sundaram, R. S.; Engel, M.; Lombardo, A.; Krupke, R.; Ferrari, A. C.; Avouris, P.; Steiner, M. Electroluminescence in Single Layer MoS_2. *Nano Lett.* **2013**, *13*, 1416–1421.
39. Lee, C.; Yan, H.; Brus, L. E.; Heinz, T. F.; Hone, J.; Ryu, S. Anomalous Lattice Vibrations of Single- and Few-Layer MoS_2. *ACS Nano* **2010**, *4*, 2695–2700.
40. Buscema, M.; Steele, G. A.; van der Zant, H. S. J.; Castellanos-Gomez, A. The Effect of the Substrate on the Raman and Photoluminescence Emission of Single-Layer MoS_2. *Nano Res.* **2014**, *7*, 561–571.
41. Li, S. L.; Miyazaki, H.; Song, H.; Kuramochi, H.; Nakaharai, S.; Tsukagoshi, K. Quantitative Raman Spectrum and Reliable Thickness Identification for Atomic Layers on Insulating Substrates. *ACS Nano* **2012**, *6*, 7381–7388.
42. Novoselov, K. S.; Jiang, D.; Schedin, F.; Booth, T. J.; Khotkevich, V. V.; Morozov, S. V.; Geim, A. K. Two-Dimensional Atomic Crystals. *Proc. Natl. Acad. Sci. U.S.A.* **2005**, *102*, 10451–10453.

ACSNANO

www.acsnano.org

ARTICLE

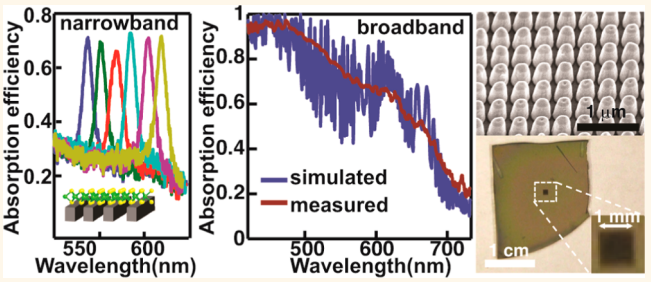
Atomically Thin MoS_2 Narrowband and Broadband Light Superabsorbers

Lujun Huang,[†] Guoqing Li,[†] Alper Gurarslan,[†] Yiling Yu,[‡] Ronny Kirste,[†] Wei Guo,[†] Junjie Zhao,[§] Ramon Collazo,[†] Zlatko Sitar,[†] Gregory N. Parsons,[§] Michael Kudenov,[∥] and Linyou Cao*[,†,‡]

Departments of [†]Materials Science and Engineering, [‡]Physics, [§]Chemical Engineering, and [∥]Electrical and Computer Engineering, North Carolina State University, Raleigh, North Carolina 27695, United States

Supporting Information

ABSTRACT: We present a combined theoretical and experimental effort to enable strong light absorption (>70%) in atomically thin MoS_2 films (≤4 layers) for either narrowband incidence with arbitrarily prespecified wavelengths or broadband incidence like solar radiation. This is achieved by integrating the films with resonant photonic structures that are deterministically designed using a unique reverse design approach based on leaky mode coupling. The design starts with identifying the properties of leaky modes necessary for the targeted strong absorption, followed by searching for the geometrical features of nanostructures to support the desired modes. This process is very intuitive and only involves a minimal amount of computation, thanks to the straightforward correlations between optical functionality and leaky modes as well as between leaky modes and the geometrical feature of nanostructures. The result may provide useful guidance for the development of high-performance atomic-scale photonic devices, such as solar cells, modulators, photodetectors, and photocatalysts.



KEYWORDS: *MoS_2, two-dimensional materials, light absorption, leaky mode, resonant photonics*

Two-dimensional (2D) transition-metal dichalcogenide (TMDC) materials such as monolayer or few layers MoS_2, WS_2, $MoSe_2$, and WSe_2 have recently emerged as a topical area of modern physical science and engineering.[1,2] One of the most appealing potentials of these materials is to enable the development of novel atomic-scale photonic devices owing to their semiconducting nature and remarkable excitonic properties.[1,3−8] However, the intrinsically weak light-matter interaction of these materials, which results from the atomically thin thickness, stands as a major challenge for the device development. For instance, monolayer MoS_2 or WS_2 may only absorb around 5−10% visible light.[9] In order to develop absorption-based photonic devices useful for practical applications, it is necessary to substantially improve the absorption efficiency. Ideally, the absorption efficiency would be engineered to be perfect for either narrowband incidence with arbitrarily prespecified wavelengths or broadband incidence. While recent studies have demonstrated enhancement for the light absorption in 2D TMDC materials, all of them fall short of providing satisfactory enhancement, spectral selectivity, or bandwidth tunability.[10−18]

Here we demonstrate the realization of strong light absorption (>70%) in atomically thin MoS_2 films (≤4 layers) for both narrowband and broadband incidences by integrating the films with resonant photonic structures. The resonant photonic structures are deterministically designed through a unique reverse design process built upon an intuitive theoretical model that we previously developed, coupled leaky mode theory (CLMT).[19,20] It starts with identifying the properties of leaky modes necessary for the targeted strong narrowband or broadband absorption and then searching for the geometrical dimension of the structures that can support the desired leaky modes. This reverse design process is very intuitive and only involves a minimal amount of computation, thanks to the straightforward correlation between optical functionality and leaky modes as well as between leaky modes and geometrical dimension of nanostructures. This design approach is in stark contrast with what was used in many previous works.[10,12,15,21−27] The previous works rely on directly surveying optical functionality as a function of physical features to design the photonic structures, which often involves heavy computation and may be time-consuming for the design of perfect absorbers at arbitrarily prespecified wavelengths.

RESULTS AND DISCUSSION

According to the CLMT model, regardless whatever morphological and compositional features, semiconductor nanostruc-

Received: March 31, 2016
Accepted: August 2, 2016

 © XXXX American Chemical Society

DOI: 10.1021/acsnano.6b02195
ACS Nano XXXX, XXX, XXX−XXX

tures can always be considered as leaky optical resonators and their optical responses as a result of the coupling between incident light and leaky modes of the structures.[19,28] Leaky modes are natural optical modes with propagating waves outside the structure and feature with a complex eigenvalue $N_{real} - N_{imag}i$ that can be readily calculated using analytical or numerical techniques.[19,20,29] The absorption efficiency Q_{abs} of one leaky mode in a planar structure such as an array of semiconductor nanostructures for a normal incidence λ may be written as

$$Q_{abs}(\lambda) = \frac{2N_{imag}/N_{real}\cdot n_{imag}/n_{real}}{(\alpha - 1)^2 + (N_{imag}/N_{real} + n_{imag}/n_{real})^2} \quad (1)$$

where n_{real} and n_{imag} are the real and imaginary parts of the refractive index of the materials involved, respectively, α represents the offset between the incident wavelength λ and the resonant wavelength of the leaky mode λ_0 as $\alpha = n_\lambda\lambda_0/n_0\lambda$ (n_λ and n_0 are the refractive index of the materials at λ and λ_0). The term $(\alpha - 1)^2$ in eq 1 vanishes on resonance as $\alpha = 1$. The resonant wavelength λ_0 is determined by the eigenvalue N_{real} and the characteristic size of the structure b as $N_{real} = 2\pi nb/\lambda_0$. Intuitively, N_{imag}/N_{real} and n_{imag}/n_{real} represent the radiative loss of the leaky mode and the intrinsic absorption loss of the materials involved, respectively. For the structure involving multiple leaky modes, the absorption is just a simple sum of the contribution from each mode. In previous studies we have extensively confirmed the accuracy of eq 1 for evaluating the absorptions of semiconductor structures.[19,29−31]

The perfect absorption for narrowband incidence can be realized under critical coupling,[32] in which the radiative loss of the leaky mode is equal to the intrinsic absorption loss of the materials $N_{imag}/N_{real} = n_{imag}/n_{real}$. According to eq 1, the on-resonance absorption by a single mode may reach a maximum of 50% at critical coupling. This maximum of 50% is rooted in the mismatch of channels for in-coupling (illumination) and out-coupling (reflection or transmission). As illustrated in Figure 1a, an array of single-mode nanostructures has two out-coupling channels located at the opposite sides (black arrows), while the in-coupling only occurs at one side (red arrows) in the typical one-side illumination configuration. The channel mismatch may be eliminated through either blocking one of the out-coupling channels with a mirror (Figure 1b) or illuminating the structure from both sides as reported previously.[25] By eliminating the channel mismatch, the on-resonance absorption at critical coupling can be improved to be 100%. It is worthwhile to point out that similar principles of critical coupling have previously been employed to enable strong absorption.[12,22,26,27,33] However, unlike the previous studies, which often rely on heavy computation to find out the proper structure for critical coupling, our CLMT model may enable a reverse design process to deterministically design the structures for critical coupling at arbitrarily prespecified wavelengths without involving much computation. This is rooted in a straightforward correlation between the eigenvalue of leaky modes and the physical features of nanostructures, as we will discuss in the following text.

We use the design for perfect absorption in atomically thin MoS_2 films at the wavelength of 600 nm as an example to illustrate the reverse design principle. The absorber consists of a MoS_2 film on top of an array of nonabsorbing dielectric nanostructures. Without losing generality, we use rectangular GaN nanowires as the nonabsorbing nanostructures and focus

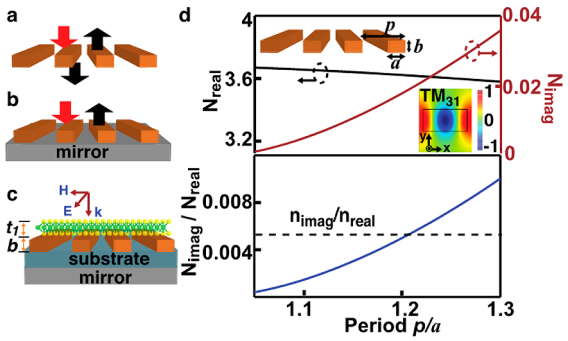


Figure 1. Reverse design for critical coupling based on the CLMT model. (a) Schematic illustration for the mismatch of in-coupling (red) and out-coupling (black) channels at an array of nanostructures. (b) Schematic illustration for the in-coupling and out-coupling channels at an array of nanostructures with mirror added at the backside. (c) Schematic illustration for the designed absorber under illumination of plane wave incidence with transverse magnetic (TM) polarization. The absorber consists of an atomically thin MoS_2 film (in thickness of t_1) on top of an array of nonabsorbing nanowires (in thickness of b). The nanowires are on sapphire substrates with a mirror coated at the backside. (d) (upper) Calculated N_{real}, and N_{imag} as well as (lower) radiative loss N_{imag}/N_{real} of the TM_{31} mode in an array of rectangular GaN nanowires as a function of the period p. The size ratio b/a of each individual nanowire is set to be 0.5. The upper inset schematically illustrates the nanowire array, and the lower inset shows the calculated electric field E_z of the TM_{31} mode. The dashed horizontal line in the lower panel indicates the estimated intrinsic absorption loss of the MoS_2/GaN assemble at an incidence of 600 nm.

on the absorption for incident plane waves with transverse magnetic (TM) polarization, in which the electric field of the incident light is parallel to the longitudinal direction of the nanowire as shown in Figure 1c. We can find out the intrinsic absorption loss of the structure from an effective refractive index, which can be estimated as $n_{eff} = (n_{MoS_2}t_1 + n_{GaN}b)/(t_1 + b)$ from the viewpoint of light propagation ($\exp[-2\pi (n_{MoS_2}t_1 + n_{GaN}b)/\lambda] = \exp[-2\pi n_{eff}(t_1 + b)/\lambda]$), where n_{MoS_2} and n_{GaN} are the refractive index of MoS_2 and GaN at 600 nm ($n_{MoS_2} = 4.02 + 0.96i$[5] and $n_{GaN} = 2.35$[34]), t_1 and b are the thickness of the MoS_2 film and the GaN nanowire array, respectively. For simplicity, the GaN nanowire array is approximately considered as a continuous slab in the evaluation of the effective refractive index because the interspacing between the nanowires is expected to be small in order to enable perfect absorption. The thickness t_1 and b can essentially be any arbitrary value. Just as an example, we set the MoS_2 film to be three layers (t_1 = 1.86 nm) and the thickness of GaN nanowires 140 nm (b = 140 nm). The effective refractive index can thus be estimated to be $n_{eff} = 2.37 + 0.0126i$, which means the absorption loss $n_{imag}/n_{real} = 0.0053$. Therefore, in order to achieve critical coupling at the wavelength of 600 nm, we need to design a structure supporting leaky modes in radiative loss N_{imag}/N_{real} of 0.0053 and resonant wavelength of 600 nm.

We can deterministically design GaN nanowire arrays featuring with the desired leaky mode by leveraging on a straightforward dependence of the modal eigenvalue on the geometrical features of nanostructures. We start by ensuring the designed structure has a resonant wavelength of 600 nm. The resonant wavelength is related with the real part of the

DOI: 10.1021/acsnano.6b02195
ACS Nano XXXX, XXX, XXX−XXX

eigenvalue N_{real} and the thickness of the nanowire as $N_{real} = 2\pi nb/\lambda_0$, where n is the refractive index of GaN. As the thickness b has already been arbitrarily set to be 140 nm, N_{real} is required to be around 3.44 for the resonant wavelength to be at 600 nm. We can make N_{real} to be around 3.44 by rationally designing the size ratio of the nanowire. Our previous study has demonstrated that the N_{real} of the leaky modes in individual rectangular nanowires bears a simple relationship with the size ratio R ($R = b/a$, a is the width of the nanowire) of the nanowire as $N_{real} \approx (m-1)\pi R + (l-1)\pi$, where m and l are the order number and mode number of the mode.[29] While m and l can, in principle, be any arbitrary integer number, the modes with lower number may provide some convenience in experimental fabrication. We use the TM_{31} mode ($m = 3$ and $l = 1$) as an example in this design. The size ratio R should be set to be around 0.5 for N_{real} to be around 3.44. In other words, rectangular GaN nanowires with a size ratio R around 0.5 and thickness of 140 nm are expected to have a leaky mode TM_{31} with resonant wavelength at 600 nm.

We can further optimize the design to ensure the radiative loss of the TM_{31} mode N_{imag}/N_{real} to be 0.0053. This can be realized by simply tuning the period of the nanowire array. Generally, the real part of the eigenvalue N_{real} shows mild dependence on the period of the array, while the imaginary part N_{imag} may substantially decrease with the interspacing between the nanowires decreasing (Figure 1d). This can be intuitively understood as the leaky mode tends to become more confined with the interspacing decreasing. Figure 1d shows the calculated N_{real} and N_{imag} of the TM_{31} mode in an array of rectangular GaN nanowires in size ratio R of 0.5 as a function of the period. The calculation indicates that the radiative loss N_{imag}/N_{real} is equal to the intrinsic absorption loss n_{imag}/n_{real} when the period is around $1.2a$ (Figure 1d, lower). This analysis does not consider the effect of the atomically thin MoS_2 film and the (sapphire) substrate underneath the GaN nanowire array. Nevertheless it provides reasonable accuracy because the effects of the film and the substrate are expected to be minor due to the atomically thin dimension of the film and the low refractive index of the substrate. To define the geometrical features more precisely, we numerically simulate the optical response of the structure in the parameter space around the estimated ones (size ratio $R = 0.5$, thickness $b = 140$ nm, and period $p = 1.2a$). Our simulation further confirms that a GaN nanowire array in thickness of 140 nm, size ratio b/a of ~0.5, and period p of $1.18a - 1.25a$ may enable reasonably perfect absorption in the three-layer MoS_2 film for an incidence of 600 nm. These parameters may tolerate ~5−10% deviation without significantly compromising the absorption capabilities. This is because the absorption loss and radiative loss involved are not very small and even a quasi-critical coupling may enable strong absorption.

The theoretical design can be validated with experimental measurements. We fabricate a GaN nanowire array following the theoretical design and transfer a centimeter-scale three-layer MoS_2 film onto the nanowire array using a surface-energy-assisted transfer technique that we previously developed (Figure 2a,b).[35] The centimeter-scale film is grown using a unique self-limiting chemical vapor deposition (CVD) process.[36] We have confirmed the layer number and high crystalline quality of the film with Raman and AFM measurements (Figures 2a and S1). We evaluate the absorption (A) of the film from the measurement of reflection (R) and transmission (T) as $A = 1 - R - T$ (Figure S2). We have

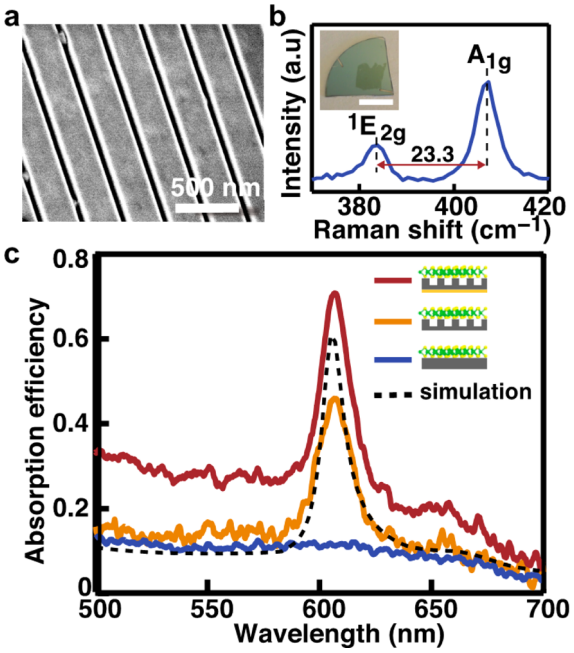


Figure 2. Strong absorption in atomically thin MoS_2 films for narrowband incidences. (a) SEM image of the designed GaN nanowire array on sapphire substrates. Each individual nanowire is 280 nm wide and 140 nm thick. The interspacing between neighboring nanowires is 50 nm. (b) Raman spectrum of the MoS_2 film transferred onto the GaN nanowire array. The two characteristic peaks A_{1g} and E^1_{2g} along with their frequency difference are labeled as shown. Inset is a picture of the transferred film with a scale bar of 1 cm. (c) Absorption spectra of the film on the GaN nanowire array (orange), the part of the film on the unpatterned substrate (blue), and the film on the GaN nanowire array after a mirror is coated at the backside of the substrate (red). Also plotted is the theoretical simulation for the absorption of the film on the GaN nanowire array with no mirror coated.

confirmed negligible scattering loss in the nanowire array (Figure S3). Our result indicates that the trilayer MoS_2 film on top of the nanowire array shows an absorption efficiency of 50% at around 600 nm (Figure 2c). This is significantly enhanced compared to the intrinsic absorption of the film on the unpatterned substrate and also reasonably matches what theoretically predicted. The absorption in the MoS_2 film can be further improved to 70% or higher by coating a silver mirror at the backside of the substrate. We have confirmed negligible absorption in the coated mirror itself (Figure S4). The improvement results from the absorption of the light reflected back at the mirror, which is less than the 2 times as predicted because the light loses coherence after interacting with the nanowire structures due to fabrication imperfection.

The resonant absorption peak of the MoS_2 film can be deterministically controlled by simply tuning the width of the nanowire due to a linear correlation between the resonant wavelength and the width. The resonant wavelength can be correlated to the real part of the eigenvalue as $\lambda_0 = 2\pi nb/N_{real}$, and N_{real} is dependent on the size ratio as $N_{real} \approx 2\pi R$ for the TM_{31} mode. Therefore, $\lambda_0 \approx nb/R \approx na$ as $R = b/a$. With a more precise evaluation for the eigenvalue of the TM_{31} mode, we find that the resonant wavelength $\lambda_0 = 0.8na = 1.88a$. Figure 3a shows the absorption spectra collected from the same trilayer MoS_2 film on top of nanowire arrays with different nanowire width. For all these nanowire arrays, the internano-

DOI: 10.1021/acsnano.6b02195
ACS Nano XXXX, XXX, XXX−XXX

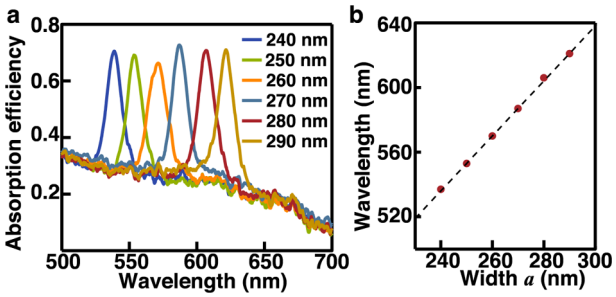


Figure 3. Precise control of the resonant absorption peak. (a) Absorption spectra of a three-layer MoS_2 film on top of GaN nanowire arrays with different width in the nanowires, including 240, 250, 260, 270, 280, and 290 nm. The interspacing between neighboring nanowires is always maintained to be 50 nm in all these arrays. (b) Linear dependence of the position of the resonant absorption peak on the width of the nanowire.

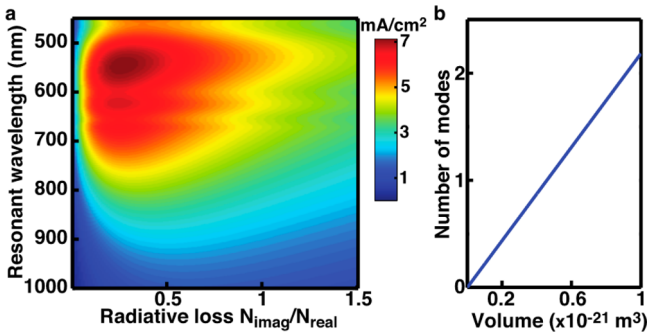


Figure 4. Design principle for solar super absorption in MoS_2. (a) Calculated single-mode solar absorption of in MoS_2 materials with 3D optical confinement as a function of radiative loss (horizontal axis) and resonant wavelength (vertical axis). (b) The number of leaky modes in the range of 500−600 nm that MoS_2 materials can support as a function of the volume of the materials.

wire spacing is maintained to be around 50 nm, and a mirror is coated at the backside. The film shows distinct resonant absorption peaks on the different nanowire arrays (Figure 3a), and the position of the peak linearly depends on the width of the nanowire by a slope of 1.77 (Figure 3b), reasonably matching what theoretically predicted. The peak absorptions of the film are all around 70−75%. By using the same design strategy, we can also enable strong absorption in atomically thin MoS_2 films on top of GaN nanowire arrays for incidence with transverse electric (TE) polarization (Figure S5a) or polarization-independent strong absorption using atomically thin MoS_2 films on top of an array of GaN nanoholes (Figure S5b).

Except the strong absorption for narrowband incidence, we can also design atomically thin MoS_2 superabsorbers for broadband incidence such as solar radiation. We start with examining the absorption of a single leaky mode in MoS_2 for solar radiation to gain insight into the modal properties that are ideal for solar absorption. The single-mode solar absorption can be calculated by integrating the single-mode absorption efficiency Q_{abs} over the spectral flux of solar radiation I_λ as

$$P_{solar} = \int_\lambda I_\lambda Q_{abs} d\lambda \quad (2)$$

As the solar flux and the refractive index are known, the only unknown variables in eq 2 are the resonant wavelength λ_0 and radiative loss N_{imag}/N_{real} of the leaky mode. We can evaluate the single-mode solar absorption P_{solar} as a function of the two variables in a 2D figure (Figure 4a). For the convenience of discussion, each of the absorbed photons is converted to one electron, which gives rise to a unit of current density (mA/cm^2) for the solar absorption. The calculation indicates that the solar absorption by a single leaky mode would have a maximum of 6−7 mA/cm^2 when the resonant wavelength of the mode is in the range of 500−600 nm and the radiative loss N_{imag}/N_{real} in the range of 0.15−0.4.

The calculation result provides useful guidance for the design of solar absorbers. As the solar energy above the bandgap of MoS_2 (<680 nm) amounts to 18 mA/cm^2 in total, one would expect a major part of the solar radiation available to be absorbed should a MoS_2 structure be designed to have two leaky modes with the maximal solar absorption capability, *i.e.*, with resonant wavelength in 500−600 nm and radiative loss in 0.15−0.4. The requirement of two leaky modes in the wavelength range of 500−600 nm actually imposes a fundamental limit on the volume of the MoS_2 materials that should be involved. Without losing generality, we assume the solar absorber to be an array of nanostructures with 3D optical confinement such as nanopillars. The density of leaky modes follows the well-established formalism of mode density in optical resonators.[37] It is $\rho(\lambda) = 8\pi n_0^3 V/\lambda^4$ for structures with 3D optical confinement, where n_0 and V are the refractive index and volume of MoS_2 materials.[30] We can find out the number of leaky modes in the wavelength range 500−600 nm by performing integration $\int_{500}^{600} \rho(\lambda) d\lambda$. The result is plotted as a function of the material volume V in Figure 4b. The calculation indicates that the volume of MoS_2 materials in the nanopillar should be no less than 1.0×10^{-21} m^3 in order to support two modes in the wavelength range of 500−600 nm. Our previous studies demonstrated that, while the calculation and analysis are for pure MoS_2 materials, the results may be applied to heterostructures that include nonabsorbing materials.[30,31] In brief, to maximize the solar absorption in MoS_2, the designed structures should involve MoS_2 materials in volume no less than 1.0×10^{-21} m^3 and have two leaky modes with resonant wavelength in the range of 500−600 nm and radiative loss in the range of 0.15−0.4.

We can deterministically design the nanostructures that may satisfy the requirements on material volume and modal properties. Just as an example, we design a structure that consists of a square array of rectangular GaN nanopillars conformally coated by a four-layer MoS_2 film as shown in Figure 5a, and the sides (a and b) in the lateral direction of the nanopillars are set to be the same. We can control the resonant wavelength of the leaky mode to be in the target range (500−600 nm) by rationally designing the lateral size of the structure. We use the 311 mode, *i.e.*, $m = 3$, $l = j = 1$, as an example to illustrate this notion. According to our previous studies,[29] the real part of the eigenvalue for the leaky modes in rectangle nanopillars can be written as $nkc \approx (m-1)\pi R_1 + (l-1)\pi R_2 + (j-1)\pi$, where $R_1 = c/a$ and $R_2 = c/b$, where c is the height of the nanopillar. For the 311 mode, $nkc \approx (m-1)\pi R_1$, which may give $2.35c \approx \lambda R_1$ or $2.35a \approx \lambda$. This indicates that the lateral side of the rectangular nanopillar should be in the range of 210−250 nm in order to make the resonant wavelength be in the range of 500−600 nm. Additionally, the lower limit of the volume (>1.0×10^{-21} m^3) of MoS_2 materials requires the height of the nanopillar to be at least 340−430 nm. The requirement for the radiative loss (0.15−0.4) can be readily

DOI: 10.1021/acsnano.6b02195
ACS Nano XXXX, XXX, XXX−XXX

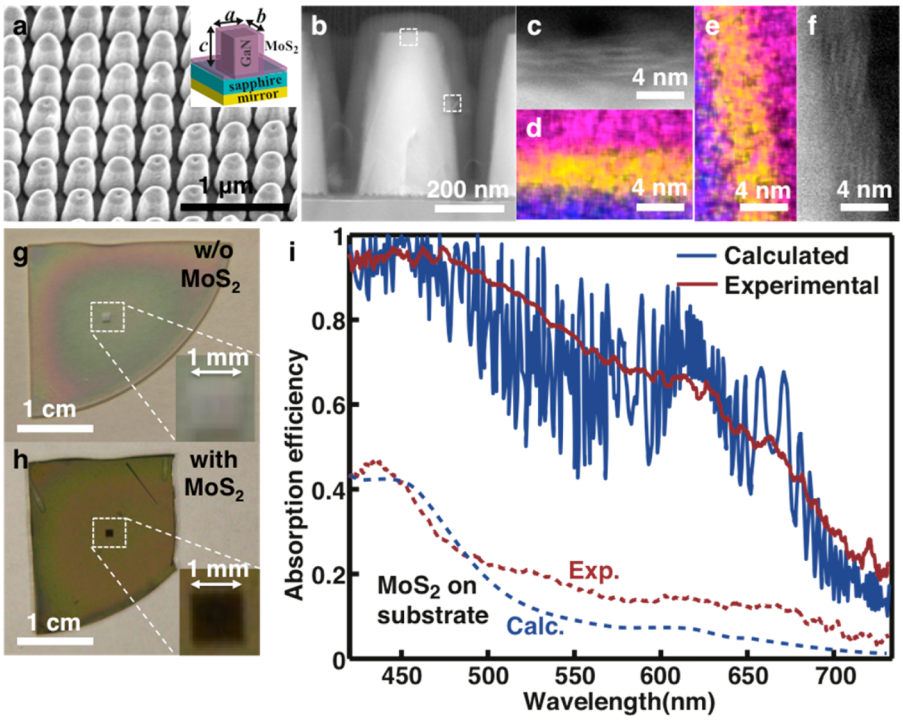


Figure 5. Strong solar absorption in four-layer MoS_2 films. (a) SEM image of an array of GaN nanopillars conformally coated with four-layer MoS_2. Inset, schematic illustration for the structure in which a mirror coated at the backside. (b) Cross-sectional TEM of the nanopillar coated with MoS_2. The TEM sample was extracted from the nanostructure array by using FIB. A layer of Al_2O_3 in thickness of 60 nm is coated on the top to protect the MoS_2 during the FIB processing. The two white dashed squares indicates where the images of (c,d) are taken from. (c) High-resolution TEM image and (d) EDAX mapping of the MoS_2 coated on the top of the nanopillar. The yellow part of the EDAX image is the signal from MoS_2. (e) High-resolution TEM image and (f) EDAX mapping of the MoS_2 coated at the side of the nanopillar. Image of the array of GaN nanopillars (g) before and (f) after the coating of the four-layer MoS_2. (i) Measured absorption spectra of the four-layer MoS_2 film coated on the nanopillar array (solid red) and on unpatterned substrates (dashed red). Also plotted are the corresponding simulation results.

satisfied by simply tuning the period of the nanopillars, just as what we did with the nanowire array in the design of narrowband absorbers. Our simulation indicates that the radiative loss N_{imag}/N_{real} would be in the targeted range when the period $p > 1.4a$ (Figure S6).

We fabricate the GaN nanopillar array following the theoretical prediction and conformally coated the array with a four-layer MoS_2 film using the self-limiting CVD processes we developed previously. The nanopillar is tapered a little bit due to fabrication imperfection, with the width of top and bottom surface 150 and 270 nm, height of 460 nm, and period of 360 nm (Figure 5b). The conformal growth and layer number of MoS_2 are confirmed by TEM characterizations (Figure 5c–f). We can find that the color of the fabricated structure under sunlight changes from white to black after the deposition of MoS_2, indicating a substantial absorption of solar light (Figure 5g,h). Figure 5i shows the absorption spectra of the structure measured using an integrating sphere system. The absorption may count for 13.5 mA/cm^2 if integrating it with solar flux and converting each absorbed photon to an electron. It is substantially improved compared to the absorption of the MoS_2 film deposited onto the unpatterned substrate. Note that the designed structure may maintain strong broadband in a large incident angle range from 0° to 60° (Figure S7), different from the broadband graphene absorber reported previously that may only show strong absorption in a very narrow range of incident angle (<1°).[24] The experimental result also reasonably matches the prediction obtained from FDTD simulation or analytic modeling. Modal analysis indicates that there are two modes in the ranges of 500–600 nm with resonant wavelengths at 579 and 525 nm and radiative loss of 0.194 and 0.179, respectively, indeed satisfying the requirements (Figure S8). It is worthwhile to point out that this design is not the only structure with capability to enable strong solar absorption in atomically thin MoS_2 materials. In principle any structures that that could satisfy the requirements on material volume and modal properties would provide strong solar absorption.

CONCLUSION

In conclusion, we have demonstrated the realization of strong absorption (>70%) in atomically thin MoS_2 films (≤4 layers) for narrowband incidence with arbitrarily prespecified wavelengths or broadband incidence like solar radiation by leveraging on resonant photonic structures. The resonant photonic structure may be deterministically designed with a reverse design approach based on an intuitive model that we previously developed, coupled leaky mode theory. We believe the absorption, in particular, the narrowband absorption, can be further improved to be close to perfect should the fabrication process be further optimized. While the focus is on MoS_2, the result of this work can be generally applied to the design of superabsorbers with other atomically thin 2D materials. This result may provide useful guidance for the development of high-performance absorption-based photonic devices with 2D TMDC materials, including solar cells, photodetectors, modulators, and photocatalysts. The designed structures, *i.e.*,

DOI: 10.1021/acsnano.6b02195
ACS Nano XXXX, XXX, XXX–XXX

a single layer of nanostructure arrays, can be readily scaled up using standard nanofabrication procedures that includes nanolithography (deep-UV or nanoimprinting) followed by dry etching. Electrical contacts may also be readily fabricated to extract photogenerated charge carriers. For instance, the electrical contact for the narrow-band absorbers may be made simply by depositing metallic structures on top of the MoS_2 film. For the broadband absorbers, we may use the substrate (with suitable doping) as one electrode and, if necessary, deposit a layer of ITO or other conductive materials on top of the MoS_2 film as the other electrode.

EXPERIMENTAL METHODS

Electromagnetic Simulation. The eigenvalues of GaN nanostructures were calculated using the commercial software package COMSOL Multiphysics. The simulated reflection and transmission were performed using both rigorous coupled wave analysis (RCWA) and finite-difference time-domain (FDTD) techniques.

Sample Preparation and Fabrication. GaN thin films with the thickness of 140 and 460 nm were grown on sapphire substrates using metal organic chemical vapor deposition (MOCVD). The GaN nanowire and nanoparticle array were patterned using standard procedures, including electron beam lithography (EBL) and reactive ion etching (RIE). 70 nm SiO_2 was deposited on the GaN film as a mask using plasma enhanced chemical vapor deposition (PECVD). 300 nm PMMA resist was spin coated on the top of SiO_2. The pattern was defined by Elionix ELS-7500 EX EBL System and transferred to SiO_2 layer by inductively coupled plasma RIE system with recipe of CHF_3 gas. After that, the pattern was further transferred to GaN layer with the combination recipe of $SiCl_4$ and Cl_2. Finally, the SiO_2 was removed by hydrogen fluoride (HF) acid.

The MoS_2 film was synthesized on sapphire substrates using a unique self-limiting CVD process we reported previously.[36] This process was performed in a tube furnace flown with Ar gas at high temperature (850 °C) and low pressure (2−3 Torr). $MoCl_5$ and sulfur were used as precursors. The transfer of the monolayers followed a surface-energy-assisted transfer approach that we have developed previously.[35] In a typical transfer process, a layer of of polystyrene (PS) was spin-coated on the as-grown film. After a baking at 80−90 °C for 1 h, a water droplet was then dropped on top of the monolayer. Water molecules could penetrate under the monolayer, resulting the delamination of the PS-monolayer assembly. We picked up the polymer/film assembly with a tweezers and transferred it to different substrates. After that, PS was removed by rinsing with toluene several times.

We used focused ion beam (FIB) to cut part of the nanopillar array coated by MoS_2 films for TEM characterizations and deposit a layer of Al_2O_3 to protect the films prior to the FIB processing. Al_2O_3 thin films were deposited using atomic layer deposition (ALD) in a viscous-flow hot-wall reactor at 100 °C. In an ALD Al_2O_3 cycle, trimethylaluminum (98%, STREM Chemicals) and deionized water were sequentially dosed to the reactor chamber with N_2 (99.999%, Airgas, further purified with an Entegris gatekeeper) purge steps between the precursor doses. 500 cycles of ALD Al_2O_3 were deposited onto MoS_2 for encapsulation, and the film thickness is ∼54 nm.

Structural and Optical Characterizations. Raman and AFM were used to characterize the synthesized and transferred films. The Raman measurement was carried out by Horiba Labram HR800 system with a 532 nm laser. AFM measurements were performed at a Veeco Dimension-3000 atomic force microscope.

The optical characterization for the narrowband absorbers were performed at a home-built setup that consists of a confocal microscope (Nikon Eclipse C1) connected with a monochromator (SpectraPro, Princeton Instruments) and a detector (Pixis, Princeton Instruments). A broadband Halogen lamp was used as light source for the reflection and transmission measurements. The reflected and transmitted light were collected by 2× objective lens, and a pinhole at the focal plane of the confocal microscope was used to collect signal from the area of our interest. The absorption of the broadband absorber was measured using an integrating sphere system that was specially designed to be capable of collecting signal from small areas.

ASSOCIATED CONTENT

Supporting Information

The Supporting Information is available free of charge on the ACS Publications website at DOI: 10.1021/acsnano.6b02195.

Experimental details and data (PDF)

AUTHOR INFORMATION

Corresponding Author

*Email: lcao2@ncsu.edu.

Notes

The authors declare no competing financial interest.

ACKNOWLEDGMENTS

This work was supported by a Young Investigator Award from the Army Research Office (W911NF-13-1-0201). The synthesis and transfer work is supported as part of a CAREER award from the National Science Foundation (DMR- 1352028). R.C. and Z.S. acknowledge the partial financial support from the National Science Foundation (DMR-1312582 and ECCS-1508854). The authors acknowledge the use of the Analytical Instrumentation Facility (AIF) at North Carolina State University, which is supported by the State of North Carolina and the National Science Foundation.

REFERENCES

(1) Cao, L. Two-Dimensional Transition-Metal Dichalcogenide Materials: Toward An Age of Atomic-scale Photonics. *MRS Bull.* **2015**, *40*, 592−599.

(2) Butler, S. Z.; Hollen, S. M.; Cao, L.; Cui, Y.; Gupta, J. A.; Gutiérrez, H. R.; Heinz, T. F.; Hong, S. S.; Huang, J.; Ismach, A. F.; Johnston-Halperin, E.; Kuno, M.; Plashnitsa, V. V.; Robinson, R. D.; Ruoff, R. S.; Salahuddin, S.; Shan, J.; Shi, L.; Spencer, M. G.; Terrones, M.; et al. Progress, Challenges, and Opportunities in Two-Dimensional Materials Beyond Graphene. *ACS Nano* **2013**, *7*, 2898−2926.

(3) Mak, K. F.; Lee, C.; Hone, J.; Shan, J.; Heinz, T. F. Atomically Thin MoS_2: A New Direct-Gap Semiconductor. *Phys. Rev. Lett.* **2010**, *105*, 136805.

(4) Splendiani, A.; Sun, L.; Zhang, Y.; Li, T.; Kim, J.; Chim, C.-Y.; Galli, G.; Wang, F. Emerging Photoluminescence in Monolayer MoS_2. *Nano Lett.* **2010**, *10*, 1271−1275.

(5) Yu, Y.; Yu, Y.; Cai, Y.; Li, W.; Gurarslan, A.; Peelaers, H.; Aspens, D. E.; Van de Walle, C. G.; Nguyen, N. V.; Zhang, Y.; Cao, L. Exciton-Dominated Dielectric Functions of Atomically Thin MoS_2 Films. *Sci. Rep.* **2015**, *5*, 16996.

(6) Britnell, L.; Ribeiro, R. M.; Eckmann, A.; Jalil, R.; Belle, B. D.; Mishchenko, A.; Kim, Y. J.; Gorbachev, R. V.; Georgiou, T.; Morozov, S. V.; Grigorenko, A. N.; Geim, A. K.; Casiraghi, C.; Castro Neto, A. H.; Novoselov, K. S. Strong Light-Matter Interactions in Heterostructures of Atomically Thin Films. *Science* **2013**, *340*, 1311−1314.

(7) Yu, Y.; Yu, Y.; Xu, C.; Cai, Y. Q.; Su, L.; Zhang, Y.; Zhang, Y.-W.; Gundogdu, K.; Cao, L. Engineering Substrate Interactions for High Luminescence Efficiency of Transition-Metal Dichalcogenide Monolayers. *Adv. Funct. Mater.* **2016**, *26*, 4733−4839.

(8) Yu, Y.; Yu, Y.; Xu, C.; Barrette, A.; Gundogdu, K.; Cao, L. Fundamental Limits of Exciton-Exciton Annihilation for Light Emission in Transition Metal Dichalcogenide Monolayers. *Phys. Rev. B: Condens. Matter Mater. Phys.* **2016**, *93*, 201111.

(9) Yu, Y.; Hu, S.; Su, L.; Huang, L.; Liu, Y.; Jin, Z.; Purezky, A. A.; Geohegan, D. B.; Kim, K. W.; Zhang, Y. Equally Efficient Interlayer Exciton Relaxation and Improved Absorption in Epitaxial and

DOI: 10.1021/acsnano.6b02195
ACS Nano XXXX, XXX, XXX−XXX

Nonepitaxial MoS_2/WS_2 Heterostructures. *Nano Lett.* **2015**, *15*, 486−491.
(10) Liu, J.-T.; Wang, T.-B.; Li, X.-J.; Liu, N.-H. Enhanced Absorption of Monolayer MoS_2 with Resonant back Reflector. *J. Appl. Phys.* **2014**, *115*, 193511.
(11) Liu, Y.; Chadha, A.; Zhao, D.; Piper, J. R.; Jia, Y.; Shuai, Y.; Menon, L.; Yang, H.; Ma, Z.; Fan, S.; Xia, F.; Zhou, W. Approaching Total Absorption at Near Infrared in a Large Area Monolayer Graphene by Critical Coupling. *Appl. Phys. Lett.* **2014**, *105*, 181105.
(12) Piper, J. R.; Fan, S. Total Absorption in a Graphene Monolayer in the Optical Regime by Critical Coupling with a Photonic Crystal Guided Resonance. *ACS Photonics* **2014**, *1*, 347−353.
(13) Akselrod, G. M.; Ming, T.; Argyropoulos, C.; Hoang, T. B.; Lin, Y. X.; Ling, X.; Smith, D. R.; Kong, J.; Mikkelsen, M. H. Leveraging Nanocavity Harmonics for Control of Optical Processes in 2D Semiconductors. *Nano Lett.* **2015**, *15*, 3578−3584.
(14) Zheng, J. B.; Barton, R. A.; Englund, D. Broadband Coherent Absorption in Chirped-Planar-Dielectric Cavities for 2D-Material-Based Photovoltaics and Photodetectors. *ACS Photonics* **2014**, *1*, 768−774.
(15) Song, H. M.; Jiang, S. H.; Ji, D. X.; Zeng, X.; Zhang, N.; Liu, K.; Wang, C.; Xu, Y.; Gan, Q. Q. Nanocavity Absorption Enhancement for Two-Dimensional Material Monolayer Systems. *Opt. Express* **2015**, *23*, 7120−7130.
(16) Miao, J. S.; Hu, W. D.; Jing, Y. L.; Luo, W. J.; Liao, L.; Pan, A. L.; Wu, S. W.; Cheng, J. X.; Chen, X. S.; Lu, W. Surface Plasmon-Enhanced Photodetection in Few Layer MoS_2 Phototransistors with Au Nanostructure Arrays. *Small* **2015**, *11*, 2392−2398.
(17) Mukherjee, B.; Simsek, E. Plasmonics Enhanced Average Broadband Absorption of Monolayer MoS_2. *Plasmonics* **2016**, *11*, 285−289.
(18) Sobhani, A.; Lauchner, A.; Najmaei, S.; Ayala-Orozco, C.; Wen, F. F.; Lou, J.; Halas, N. J. Enhancing the Photocurrent and Photoluminescence of Single Crystal Monolayer MoS_2 with Resonant Plasmonic Nanoshells. *Appl. Phys. Lett.* **2014**, *104*, 031112.
(19) Yu, Y.; Cao, L. Coupled Leaky Mode Theory for Light Absorption in 2D, 1D, and 0D Semiconductor Nanostructures. *Opt. Express* **2012**, *20*, 13847−13856.
(20) Yu, Y.; Cao, L. The Phase Shift of Light Scattering at Subwavelength Dielectric Structures. *Opt. Express* **2013**, *21*, 5957−5967.
(21) Furchi, M.; Urich, A.; Pospischil, A.; Lilley, G.; Unterrainer, K.; Detz, H.; Klang, P.; Andrews, A. M.; Schrenk, W.; Strasser, G.; Mueller, T. Microcavity-Integrated Graphene Photodetector. *Nano Lett.* **2012**, *12*, 2773−2777.
(22) Kats, M. A.; Byrnes, S. J.; Blanchard, R.; Kolle, M.; Genevet, P.; Aizenberg, J.; Capasso, F. Enhancement of Absorption and Color Contrast in Ultra-Thin Highly Absorbing Optical Coatings. *Appl. Phys. Lett.* **2013**, *103*, 101104.
(23) Thongrattanasiri, S.; Koppens, F. H. L.; García de Abajo, F. J. Complete Optical Absorption in Periodically Patterned Graphene. *Phys. Rev. Lett.* **2012**, *108*, 047401.
(24) Pirruccio, G.; Martin Moreno, L.; Lozano, G.; Rivas, J. G. Coherent and Broadband Enhanced Optical Absorption in Graphene. *ACS Nano* **2013**, *7*, 4810−4817.
(25) Chong, Y. D.; Ge, L.; Cao, H.; Stone, A. D. Coherent Perfect Absorbers: Time-Reversed Lasers. *Phys. Rev. Lett.* **2010**, *105*, 053901.
(26) Landy, N. I.; Sajuyigbe, S.; Mock, J. J.; Smith, D. R.; Padilla, W. J. Perfect Metamaterial Absorber. *Phys. Rev. Lett.* **2008**, *100*, 207402.
(27) Park, J.; Kim, S. J.; Brongersma, M. L. Condition for Unity Absorption in An Ultrathin and Highly Lossy Film in A Gires-Tournois Interferometer Configuration. *Opt. Lett.* **2015**, *40*, 1960−1963.
(28) Lin, J.; Huang, L.; Yu, Y.; He, S.; Cao, L. Deterministic phase engineering for optical Fano resonances with arbitrary lineshape and frequencies. *Opt. Express* **2015**, *23*, 19154−19165.
(29) Huang, L.; Yu, Y.; Cao, L. General Modal Properties of Optical Resonances in Subwavelength Nonspherical Dielectric Structures. *Nano Lett.* **2013**, *13*, 3559−3565.
(30) Yu, Y.; Huang, L.; Cao, L. Semiconductor Solar Superabsorbers. *Sci. Rep.* **2014**, *4*, 4107.
(31) Yu, Y.; Cao, L. Leaky Mode Engineering: A General Design Principle for Dielectric Optical Antenna Solar Absorbers. *Opt. Commun.* **2014**, *314*, 79−85.
(32) Yariv, A. Universal Relations for Coupling of Optical Power between Microresonators and Dielectric Waveguides. *Electron. Lett.* **2000**, *36*, 321.
(33) Liu, Y. H.; Chadha, A.; Zhao, D. Y.; Piper, J. R.; Jia, Y. C.; Shuai, Y. C.; Menon, L.; Yang, H. J.; Ma, Z. Q.; Fan, S. H.; Xia, F. N.; Zhou, W. D. Approaching Total Absorption at Near Infrared in A Large Area Monolayer Graphene by Critical Coupling. *Appl. Phys. Lett.* **2014**, *105*, 181105.
(34) Palik, E. D. *Handbook of Optical Constants of Solids*; Academic Press: Boston, 1998.
(35) Gurarslan, A.; Yu, Y.; Su, L.; Yu, Y.; Suarez, F.; Yao, S.; Zhu, Y.; Ozturk, M.; Zhang, Y.; Cao, L. Surface-Energy-Assisted Perfect Transfer of Centimeter-Scale Monolayer and Few-Layer MoS_2 Films onto Arbitrary Substrates. *ACS Nano* **2014**, *8*, 11522−11528.
(36) Yu, Y.; Li, C.; Liu, Y.; Su, L.; Zhang, Y.; Cao, L. Controlled Scalable Synthesis of Uniform, High-Quality Monolayer and Few-layer MoS_2 Films. *Sci. Rep.* **2013**, *3*, 1866.
(37) Saleh, B. E. A.; Teich, M. C. *Fundamentals of Photonics*; Wiley: New York, 2007.

DOI: 10.1021/acsnano.6b02195
ACS Nano XXXX, XXX, XXX−XXX

NANO LETTERS

Letter

pubs.acs.org/NanoLett

Equally Efficient Interlayer Exciton Relaxation and Improved Absorption in Epitaxial and Nonepitaxial MoS_2/WS_2 Heterostructures

Yifei Yu,[†] Shi Hu,[†] Liqin Su,[§] Lujun Huang,[†] Yi Liu,[∥] Zhenghe Jin,[⊥] Alexander A. Purezky,[#] David B. Geohegan,[#] Ki Wook Kim,[⊥] Yong Zhang,[§] and Linyou Cao*[,†,‡]

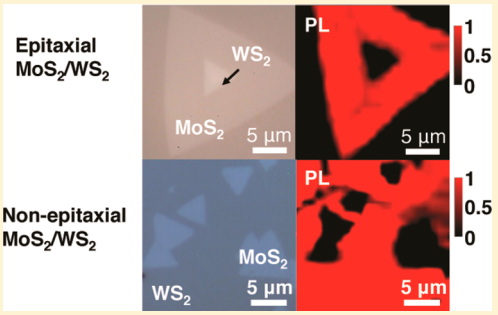
[†]Department of Materials Science and Engineering, [‡]Department of Physics, [∥]Analytical Instrumentation Facility, and [⊥]Department of Electrical and Computer Engineering, North Carolina State University, Raleigh, North Carolina 27695, United States

[§]Department of Electrical and Computer Engineering, The University of North Carolina at Charlotte, Charlotte, North Carolina 28223, United States

[#]Center for Nanophase Materials Sciences, Oak Ridge National Laboratory, Oak Ridge, Tennessee 37831, United States

Supporting Information

ABSTRACT: Semiconductor heterostructures provide a powerful platform to engineer the dynamics of excitons for fundamental and applied interests. However, the functionality of conventional semiconductor heterostructures is often limited by inefficient charge transfer across interfaces due to the interfacial imperfection caused by lattice mismatch. Here we demonstrate that MoS_2/WS_2 heterostructures consisting of monolayer MoS_2 and WS_2 stacked in the vertical direction can enable equally efficient interlayer exciton relaxation regardless the epitaxy and orientation of the stacking. This is manifested by a similar 2 orders of magnitude decrease of photoluminescence intensity in both epitaxial and nonepitaxial MoS_2/WS_2 heterostructures. Both heterostructures also show similarly improved absorption beyond the simple superimposition of the absorptions of monolayer MoS_2 and WS_2. Our result indicates that 2D heterostructures bear significant implications for the development of photonic devices, in particular those requesting efficient exciton separation and strong light absorption, such as solar cells, photodetectors, modulators, and photocatalysts. It also suggests that the simple stacking of dissimilar 2D materials with random orientations is a viable strategy to fabricate complex functional 2D heterostructures, which would show similar optical functionality as the counterpart with perfect epitaxy.



KEYWORDS: *Molybdenum disulfide, tungsten disulfide, van der Waals epitaxy, interlayer charge transfer, two-dimensional heterojunction*

Engineering the dynamics of excitons, including generation, dissociation, transfer, and recombination, by semiconductor heterostructures bears tremendous significance for fundamental and applied interests.[1,2] It stands as a major strategy for the development of all kinds of devices that involve photon-to-electron or electron-to-photon conversions, such as solar cells, LEDs, lasers, photodetectors, modulators, and photocatalysts. It also provides platforms with well-controlled excitons for the studies of fundamental physics. However, the capability of conventional semiconductor heterostructures to engineer excitons is often limited by the difficulty in developing high-quality interfaces for efficient interfacial charge transfer, a key step for the engineering of excitons. Typical heterostructures consist of two or more dissimilar semiconductor materials, and a nice match between the crystalline lattices of the semiconductor materials is required to yield high-quality interfaces. This requirement of lattice match imposes a fundamental constraint for the design of the conventional semiconductor heterostructures with increasing compositional and structural complexity to provide sophisticated control of excitons.

Two-dimensional (2D) transition metal dichalcogenide (TMDC) materials in forms of a monolayer or fewlayer of atoms promise to enable a new type of semiconductor heterostructures. These materials present an atomic-scale semiconductor with bandgap in amplitude comparable to those of conventional group IV, III−V semiconductor materials. The heterostructures that consist of dissimilar 2D materials stacked in the vertical direction would provide capabilities to engineer excitons from a truly atomic level. Most importantly, unlike the conventional semiconductor heterostructures, which request lattice match to ensure high-quality interfaces, 2D heterostructures may have high quality interfaces regardless substantial lattice mismatch.[3−10] This is because the interaction between 2D materials is van der Waals

Received: October 4, 2014
Revised: December 1, 2014

ACS Publications © XXXX American Chemical Society

dx.doi.org/10.1021/nl5038177 | *Nano Lett.* XXXX, XXX, XXX−XXX

(vdW) forces and the weak interaction can relax the requirement of lattice match. Numerous works have recently demonstrated the fabrication of 2D heterostructures with the presence of lattice mismatch and the capability of the 2D heterostructures to efficiently engineer excitons.[11−20] However, one very important question that has remained unanswered yet is how the excitonic properties of 2D heterostructures could depend on the epitaxy and orientation of the stacking. Knowledge of this question will provide useful guidance for the rational design of complex 2D heterostructures with desired exciton dynamics.

Here we have studied the excitonic properties of MoS_2/WS_2 heterostructures that consist of monolayer MoS_2 and WS_2 stacked either epitaxially or nonepitaxially in the vertical direction. Surprisingly, we demonstrate equally efficient interlayer relaxation of excitons in the heterostructures regardless the epitaxy and orientation of the stacking. This is manifested by a similar two-order magnitude decrease in the photoluminescence intensity of all of the heterostructures compared to that of separate monolayers. Additionally, both epitaxial and nonepitaxial MoS_2/WS_2 heterostructures show similarly improved absorption that is beyond the simple superimposition of the absorption of monolayer MoS_2 and WS_2, in particular for the incidence below the intrinsic bandgap of the monolayers. The nonepitaxial heterostructures are made by manually stacking single-crystalline monolayer MoS_2 and WS_2 pregrown separately with a chemical vapor deposition (CVD) process reported previously.[10,21−25] The epitaxial heterostructures, which are single crystalline as well, are synthesized by a CVD process that we have developed with a mixture of MoO_3 and WO_3 as the precursors (see Methods and Supporting Information). Our result indicates that 2D heterostructures bear significant implications for the development of photonic devices, particularly those requesting efficient exciton separation and strong light absorption, such as solar cells,[5,18−20] photodetectors, modulators, and photocatalysts. It also indicates that the simple stacking of dissimilar 2D materials with random stacking orientations may be a viable strategy to fabricate complex 2D heterostructures for the engineering of excitons.

We start the studies with epitaxial MoS_2/WS_2 heterostructures. Unlike nonepitaxial heterocturestures, whose band structure is difficult to theoretically predict due to the difficulty in building up unit cells in theoretical models, the band structure of epitaxial MoS_2/WS_2 heterostructures has been well-studied using first principle techniques.[11−14,26] This allows for synergistic studies from both experimental and theoretical sides to provide insights that are difficult to obtain from either perspective alone. The synthesized heterostructure consists of two concentric equilateral triangles in lateral size of tens of micrometers and well aligned in either the same or opposite directions (Figure 1a inset). Raman, STEM, and AFM characterizations indicate that the large triangle is single-crystalline monolayer MoS_2 while the small one single-crystalline monolayer WS_2, both continuous, smooth, and uniform (Figure 1a−b, and detailed characterizations seen in the Supporting Information). The STEM characterization also demonstrates that the MoS_2 and WS_2 monolayers, which have almost identical lattice constants,[27,28] are epitaxially stacked together in an A−B staking mode along the vertical direction (Figure1b and Figure S1−3).

We characterized the optical properties of the epitaxial MoS_2/WS_2 heterostructure at room temperatures. Figure 2a shows the mapping of photoluminescence (PL) from a typical as-grown heterostructure whose optical image is given in Figure 2b. The structure consists of a small WS_2 monolayer in lateral size of ~8 μm epitaxially stacked on the top of a big MoS_2 monolayer in lateral size of ~25 μm. We can immediately find that the PL from the edge region, which corresponds to monolayer MoS_2, is much stronger than that from the center where the MoS_2/WS_2 heterostructure is located. Representative PL spectra extracted from the mapping results are plotted in Figure 2c. The PL spectrum collected from the monolayer MoS_2 region (the big triangle) exhibits a strong peak at 1.87 eV, consistent with what was found for monolayer MoS_2 previously.[29] The PL collected from the MoS_2/WS_2 hetero-

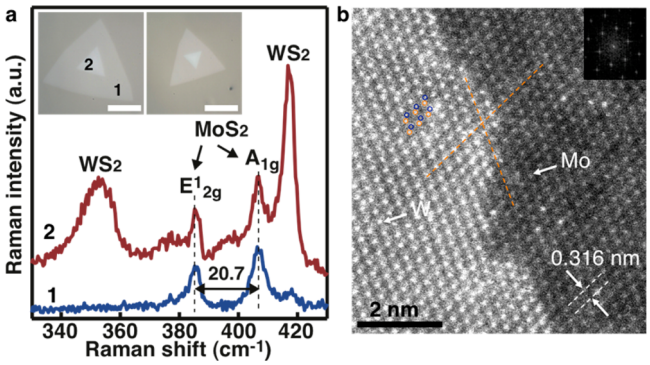


Figure 1. Characterizations of epitaxial MoS_2/WS_2 heterostructures. (a) Raman spectra collected from different areas (region 1 and 2) of the epitaxial heterostructure. The assignment for the Raman peaks is given as shown. Inset, optical images of two typical epitaxial MoS_2/WS_2 heterostructures with different relative orientations. The larger triangle is monolayer MoS_2, while the small one at the center is monolayer WS_2. Scale bar, 10 μm. (b) Scanning transmission electron microscope high-angle annular dark field image (STEM-HAADF) of the epitaxial heterostructure. The W and Mo atoms, which show different contrasts, are denoted in the figure. The lattice constant is measured in the figure as well. The dashed orange lines indicate the crystalline directions of the WS_2 layer. The circles in orange and blue represent W and Mo atoms, respectively, which are used to illustrate the offset of these atoms. Inset, the fast Fourier transformation pattern of the image.

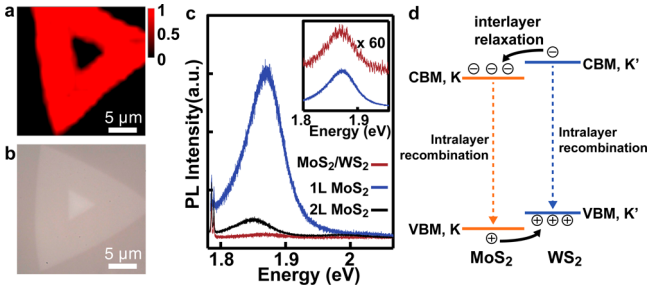


Figure 2. Low PL efficiency of epitaxial MoS_2/WS_2 heterostructures. (a) PL mapping of a typical epitaxial MoS_2/WS_2 heterostructure. (b) Optical image of the heterostructure mapped in (a). (c) Spectra PL collected from the monolayer (1L) MoS_2 area (red curve) and the MoS_2/WS_2 area (blue curve) of the heterostructure. The PL from a MoS_2 bilayer (2L) is also given (black curve). Inset, comparison of the PL from the MoS_2 area and the MoS_2/WS_2 area, where the PL from the MoS_2/WS_2 area scaled by a factor of 60 for visual convenience. (d) Schematic illustration for the bandstructure alignment of the heterostructure. The *K* point of MoS_2 coincides with the *K′* point of WS_2. The interlayer relaxations and intralayer recombination are illustrated.

dx.doi.org/10.1021/nl5038177 | *Nano Lett.* XXXX, XXX, XXX−XXX

structure region (the small triangle) shows a peak position similar to that of the MoS_2, but its intensity is smaller than that of the monolayer MoS_2 by 2 orders of magnitude (Figure 2c). To further illustrate the low PL efficiency of the heterostructure, the PL of bilayer MoS_2 collected under comparable conditions is given in Figure 2c as well (also see Figure S4). It has been well-known that bilayer MoS_2 shows weaker PL than monolayer MoS_2 because of the transition of the bandgap from direct to indirect.[29−32] However, the PL intensity of the MoS_2/WS_2 heterostructure can be found even much weaker than that of bilayer MoS_2. We would like to point out two differences of our results from one recent study[18] on similar epitaxial MoS_2/WS_2 heterostructures that was published during the review process of this work. First, the PL intensity of epitaxial MoS_2/WS_2 heterostructures in that study shows only three times smaller than that of monolayer MoS_2, instead of a 2 orders of magnitude decrease as we observed. Second, in that study, an additional PL peak at 1.4 eV was reported resulting from interlayer exciton transition, but we did not observe this PL peak in our materials even at a low temperature of 10 K (Figure S4). There are two possible reasons accounting for the differences. One could be the different synthetic processes, which might cause some differences in the resulting materials. Unlike that study, which used a mixture of element tungsten and tellurium as the precursor for WS_2, we used WO_3 instead. The other reason could be the difference in substrates, as sapphire substrates were used in our experiments while SiO_2/Si substrates were used in that study. It has been well-known that substrates could substantially affect the PL of 2D materials.[33]

The established theoretical calculations for the bandstructure of epitxial MoS_2/WS_2 heterostructures can provide useful insights into the fundamental physics underlying the observed low PL efficiency.[11−14,26] Theoretical calculations have indicated that the band structure of epitaxial MoS_2/WS_2 heterostructures at the *K*-point in the Brillouin zone is approximately a simple superposition of the states of monolayer MoS_2 and WS_2.[11,12,26] The MoS_2/WS_2 heterostructure essentially makes a type II heterojunction with the valence band maximum (VBM) completely localized to WS_2 and the conduction band minimum (CBM) to MoS_2.[11,12,26] Indeed, we observed similar PL peak positions in the heterostructure and monolayer MoS_2 in experiments (Figure 2c), and this supports the theoretical prediction that the bandstructures at the *K* point may not change much after the heterostructuring. As a result, we conclude that the observed low PL of the heterostructure is due to the interlayer relaxation (dissociation) of excitons as illustrated in Figure 2d. The band structure offset between the MoS_2 and WS_2 monolayers can facilitate the separation of photoexcited charges, electrons to MoS_2 and holes to WS_2. This separation in different monolayers decreases the spatial overlap between the wave functions of electrons and holes, which may subsequently lead to the decrease in PL efficiency.[34] The observed low PL efficiency also indicates that the interlayer relaxation (dissociation) is very fast. As illustrated in Figure 2d, the interlayer relaxation of the photoexcited charges at band edges competes with another relaxation pathway, intralayer recombination. Given the simple superposition of the band structure as theoretically predicted,[11,12,24] it is reasonable to assume that the intralayer recombination (at the *K* point) of the heterostructure is similar to that of standing-alone monolayers. The result that the PL of the heterostructure is 50−100 times weaker than that of monolayers MoS_2 implies that the interlayer relaxation process is 50−100 times faster than the intralayer recombination in monolayer MoS_2. We can further roughly estimate the interlayer relaxation to be in a time scale of 10−100 fs as the intralayer recombination of excitons in monolayer MoS_2 is reported in scale of around 1−5 ps.[35,36] This estimate is reasonably consistent with the result of another recent study[17] that was published during the review process of this work, in which the interlayer transfer process in MoS_2/WS_2 heterostructures is experimentally measured to be within 50 fs. Note that the dramatic decrease in the PL efficiency of epitaxial MoS_2/WS_2 heterostructures we observed in experiments is actually different from what predicted in theory. The theoretical calculation did not fully recognize how efficient the interlayer relaxation could be and predicted substantial PL signal in the heterostruecture due to the presence of direct transition at the *K* point.[11,12]

Very surprisingly, to achieve the efficient interlayer relaxation of excitons does not require the heterostructure to be epitaxially stacked. We observed similarly efficient interlayer relaxation of excitons in nonepitaxial MoS_2/WS_2 heterostructures as well. To make the nonepitaxial MoS_2/WS_2 heterostructure, we first grew single-crystalline MoS_2 and WS_2 monolayers separately on sapphire substrates using the CVD processes reported previously[23,37] and then transferred the monolayer MoS_2 onto the top of monolayer WS_2 using a unique surface energy-assisted transfer approach that we have recently developed[38] (see Methods and Figure S5). Different from the transfer techniques used in the previous works for the fabrication of heterostructures,[17,23,26] which involved chemical etchants and would most likely cause damages and leave organic residues at the transferred materials, our surface energy-assisted approach relies on room temperature water droplet to transfer the monolayers and are proved able to better protect the quality of the transferred materials with no damage and organic residues left behind.[38] After the transfer, we mildly annealed the heterostructure at 200−250 °C for 10−30 min under an Ar flow to remove solvent or water residues. We have confirmed that both MoS_2 and WS_2 monolayers are very stable and this mild annealing process cannot cause any change in the quality and crystalline structures of the materials.

Figure 3a−b shows the result of PL mapping for typical nonepitaxial MoS_2/WS_2 heterostructure and the optical image of the heterostructures mapped. The heterostructures consist of numerous small single-crystalline monolayer MoS_2 in the lateral size of ∼5 μm randomly stacked on top of a big single-crystalline WS_2 monolayer in size of ∼50 μm (also see Figure S6). Similar to what we find with the epitaxial MoS_2/WS_2 heterostructure, the PL of all the nonepitaxial MoS_2/WS_2 heterostructures is 2 orders of magnitude weaker than that of monolayer MoS_2 or WS_2, regardless the relative orientation of the monolayers (Figure 3b−c), indicating the general presence of efficiency interlayer exciton relaxation in all the heterostructures. The interlayer relaxation process is very sensitive to the surface quality of the heterostructures, which may affect the coupling between the MoS_2 and WS_2 monolayers. We find that the nonepitaxial MoS_2/WS_2 heterostructures, without being treated by the low temperature annealing (gray curve in Figure 3c), show a smaller decrease in PL intensity than the annealed one. The low-temperature annealing process may remove the residue of solvent and water molecules left between the two monolayers during the transfer process, which may subsequently facilitate the interlayer exciton relaxation. The independence of the efficient interlayer exciton relaxation in MoS_2/WS_2 heterostructures on the epitaxy and orientation of

dx.doi.org/10.1021/nl5038177 | *Nano Lett.* XXXX, XXX, XXX−XXX

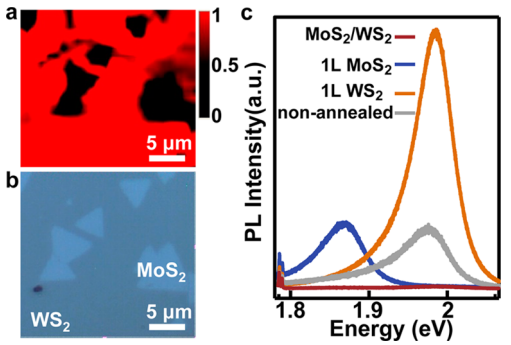


Figure 3. Low PL efficiency of nonepitaxial MoS_2/WS_2 heterostructures. (a) PL mapping of typical nonepitaxial MoS_2/WS_2 heterostructures. (b) Optical image of the heterostructure mapped in (a). It consists of multiple monolayer MoS_2 (small triangles) randomly distributed on top of a big monolayer WS_2. This can be seen more clearly in the image given in Figure S6 that shows the edge of the monolayer WS_2. (c) Spectra PL collected from the nonepitaxial MoS_2/WS_2 heterostructure (red curve), monolayer (1L) MoS_2 (blue curve), and monolayer (1L) WS_2 (brown curve). The PL from the nonepitaxial MoS_2/WS_2 heterostructure without being annealed is also given (gray curve).

the stacking suggests a strong electron−phonon coupling in 2D materials.[39] The electron-phonon coupling could be so strong that able to efficiently compensate whatever momentum mismatch for the charge transfer between the monolayers. A full-fledged study on the electron−phonon coupling is beyond the scope of this work.

To further understand our conclusion, we compare our results with what have been recently published during the review of this work.[17,18,26] The 2 orders of magnitude decrease in PL intensity we observed is substantially greater than what reported by the other groups for nonepitaxial MoS_2/WS_2 heterostructures,[17,18,26] which typically see a decrease of less than 3 times. The difference could be due to the different transferring processes used in the fabrication of the heterostructure. The unique surface energy-assisted transfer we used[38] can better protect the quality of the transferred monolayer with no organic residue and damage left than the approach used by the other groups.[17,18,26] This could result in better coupling between the two monolayers involved and hence higher efficiency of interlayer exciton relaxation in the nonepitaxial heterostructure we made. Another possible reason could be related with the substrates. The two-order magnitude decreases in PL intensities we observed is from the nonepitaxial MoS_2/WS_2 heterostructures on sapphire substrates, while the nonepitaxial MoS_2/WS_2 heterostructures studied in some of the previous works[18,26] were fabricated on SiO_2/Si substrates. We did observe a lesser decrease in PL at the nonepitaxial MoS_2/WS_2 heterostructures made on SiO_2/Si substrates (Figure S7). Nevertheless, the different decrease in the PL caused by using different substrates does not affect the generality of our conclusion. For instance, the decrease in PL that we observed at the nonepitaxial MoS_2/WS_2 heterostructures made on SiO_2/Si substrates (Figure S7) is very similar to the PL decrease recently observed at the epitaxial MoS_2/WS_2 heterostructures grown on SiO_2/Si substrates.[18] This suggests that our conclusion for the independence of the interlayer exciton relaxation on the stacking epitaxy and orientation can be generally applied to the MoS_2/WS_2 heterostructures on other substrates, although using different substrates might lead to different absolute amplitudes of the decrease in PL

Whereas the PL is dramatically suppressed due to efficient interlayer exciton relaxation, MoS_2/WS_2 heterostructures show improved absorption that is beyond a simple superimposition of the absorptions of monolayer MoS_2 and WS_2. The absorption improvement is particularly prominent for the incidence below the intrinsic band gap of the monolayers. The absorption spectra measured from epitaxial, annealed nonepitaxial, and nonannealed nonepitaxial MoS_2/WS_2 heterostructures are plotted in the upper panels of Figure 4 along with

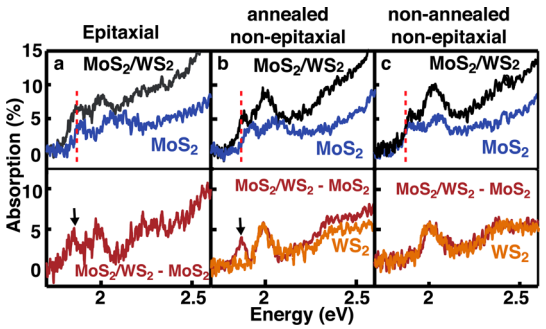


Figure 4. Improved absorption of MoS_2/WS_2 heterostructures. Absorption spectra collected from the MoS_2 area (blue curve) and the MoS_2/WS_2 area (black curve) for (a) epitaxial MoS_2/WS_2 heterostructures, (b) annealed nonepitaxial MoS_2/WS_2 heterostructures, and (c) nonepitaxial MoS_2/WS_2 heterostructure without being annealed. The dashed red lines indicate the boundary where the epitaxial and annealed nonepitaxial heterostructures show obvious higher absorption for the incidence to the left than the monolayer MoS_2. The difference between the two absorption spectra (MoS_2/WS_2 − MoS_2) is given in the corresponding lower panel (red curve). For the nonepitaxial heterostructures, the absorption spectrum of monolayer WS_2 (brown curve) is also given in the lower panel as a reference. The black arrows point toward the peaks indicating the improved absorption of the heterostructures.

the absorption spectra of corresponding monolayer MoS_2. We can find that the epitaxial and annealed nonepitaxial heterostructures exhibit substantially higher absorption efficiencies than monolayer MoS_2 for the incidence below the bandgap of MoS_2, which is to the left of the dashed red lines (Figure 4a−b, upper panels). But similar absorption improvement for the sub-bandgap incidence cannot be found in the nonepitaxial heterostructure without being annealed (Figure 4c, upper panel). To further illustrate the relationship between the absorptions of the heterostructure and the monolayers involved, we subtract the absorption spectra of monolayer MoS_2 from those of MoS_2/WS_2 heterostructures. For the nonannealed nonepitaxial heterostructures, the spectrum resulted from the subtraction is identical to the absorption spectrum of monolayer WS_2 (Figure 4c, lower panel), indicating the absorption of the heterostructure is a simple superposition of separate monolayer MoS_2 and WS_2. But for the epitaxial and annealed nonepitaxial heterostructures, the subtraction gives rise to a peak at 1.84 eV along with the features resulting from the absorption of monolayer WS_2 (Figure 4a−b, lower panels). Intuitively, this extra peak, which indicates improved absorption in the heterostructure for the low energy incidence, results from the red-shift of exciton peaks due to the reduction of dielectric screening in the heterostructure, similar to what observed in bilayer MoS_2 and bilayer WS_2 (Figure S8).[40]

dx.doi.org/10.1021/nl5038177 | Nano Lett. XXXX, XXX, XXX−XXX

Our result indicates that 2D heterostructures present a useful platform for the engineering of excitons at the atomic level. For instance, it provides the capabilities to efficiently dissociate the excitons in 2D materials that would otherwise be difficult to separate and tend to radiatively recombine due to extraordinarily strong excitonic binding energy.[41,42] The combination of efficient exciton dissociation and improved absorption make 2D heterostructures particularly useful for the absorption-based photonic devices, such as photovoltaics, solar fuels, photodetectors, optical modulators, and photocatalysts. Additionally, the independence of the interlayer exciton relaxation on the stacking epitaxy and orientation clearly points out that the simple stacking of 2D materials in the vertical direction with random orientations is a viable strategy for the fabrication of functional 2D heterostructures. Complex 2D heterostructures fabricated by manually stacking dissimilar 2D materials with a random orientation may show equal optical functionality as the counterpart with perfect epitaxy.

Methods. *Synthesis of Epitaxial MoS_2/WS_2 Heterostructures.* The epitaxial heterostructures were synthesized by using a chemical vapor deposition process that we have developed by adapting what was previously reported for the synthesis of monolayer MoS_2 and WS_2.[23,37] Briefly, the synthesis was performed in a tube furnace with sulfur (typically 1.0 g) and a mixture of MoO_3 and WO_3 (typically 80 mg with the weight percent of MoO_3 1% and WO_3 99%) as the precursors. The sulfur was placed at the upstream of the tube furnace and the mixed MoO_3/WO_3 at the center. Sapphire substrates were placed at the downstream in the tube. Other typical experimental conditions including a temperature of 950 °C and a flow of Ar gas in a rate of ~100 sccm. In a typical synthetic process, the temperature was ramped to 950 °C in 35 min and kept 950 °C for 2 h. After that, the whole system was cooled down to room temperature naturally.

Fabrication of Nonepitaxial MoS_2/WS_2 Heterostructures. The nonexpitaxial heterostructures were made by manually stacking monolayer MoS_2 and WS_2 that were grown using the chemical vapor deposition process reported previously.[23,37] The process is similar to what was used for the synthesis of heterostructures, but only either MoO_3 or WO_3 instead of the mixture was used for the synthesis of MoS_2 or WS_2. The typical temperatures used for the synthesis are 750 °C for MoS_2 and 900 °C for WS_2. Ar was used as the carrier gas for the synthesis of MoS_2 and forming gas (5% H_2 in Ar) for WS_2 with a flux rate of 100 sccm in both cases.

To make the nonepitaxial heterostructure, we first lifted off the synthesized MoS_2 from the growth substrate using a surface energy-assisted transfer process that we have recently developed.[38] Briefly, in a typical transfer process, 9 g of polystyrene (PS) with a molecular weight of 280 000 g/mol was dissolved in 100 mL of toluene, and then the PS solution was spin-coated (3500 rpm for 60 s) on the as-grown MoS_2 on sapphire substrates. This was followed by a baking at 80−90 °C for 15 min. A water droplet was then dropped on top of the sample. To facilitate the penetration of water molecules, we poked the PS layer with a sharp object from the edge. Once the PS layer was scratched from the edge, water molecules could penetrate through all the way under MoS_2, resulting the delamination of the PS-MoS_2 assembly. The water droplet was then removed away with paper towel. We could pick up the polymer/MoS_2 assembly with a tweezers and transferred it onto as-grown WS_2 monolayers. To ensure the uniformity of the transferred MoS_2, we baked the transferred PS-MoS_2 assembly at 80 °C for 1 h and performed a final baking for 30 min at 150 °C. Finally, PS was removed by rinsing with toluene several times. After that, the stacked heterostructure was annealed at 200−250 °C for 10−30 min under an Ar environment.

Characterizations of MoS_2 Films. High-resolution STEM images were taken using the FEI Titan 80-300 probe aberration corrected and monochromated scanning transmission electron microscope (STEM) operated at 200 kV. In STEM mode, *Z*-contrast images were taken using a high-angle annular dark-field (HAADF) detector (Fischione Instrument), and elemental mapping was performed using the "Super X" energy dispersive spectrometric (EDS) system. We transferred the synthesized materials to TEM grids following a surface energy-assisted transfer approach that we have recently developed.[38] The convergence angle was set at 21 mrad, and probe current was about 110 pA, at which, we found that the beam damage on the MoS_2 sample can be controlled to the minimum within a reasonable period of time for imaging. The thickness and surface topology were measured using an atomic force microscope (AFM, Veeco Dimension-3000). Raman and photoluminescence (PL) measurements were carried out using Horiba Labram HR800 system using a 532 nm laser.

A home-built setup that consists of a confocal microscope (Nikon Eclipse C1) connected with a monochromator (SpectraPro, Princeton Instruments) and a detector (Pixis, Princeton Instruments) was used to perform the absorption measurement. In a typical measurement, we collected the white light transmitted through the sample using a 100× objective with a numerical aperture of 0.9 (Nikon). The light was from a halogen lamp and was broadly cast onto the samples with no focusing. We obtained the spectral absorption efficiency by normalized the transmitted light with I_1 and without the sample I_0 as $(I_0 - I_1)/I_0$. A focal plane aperture at the confocal scanning head installed with the microscope allows us to define the sample area to be measured with a spatial resolution of 300 nm.

■ ASSOCIATED CONTENT

Supporting Information

(1) Detailed experimental results on the synthesis and compositional and structural characterizations of the synthesized epitaxial MoS_2/WS_2 heterostructures; (2) more Raman and optical measurements for bilayer MoS_2, bilayer WS_2, and MoS_2/WS_2 heterostructures. This material is available free of charge via the Internet at http://pubs.acs.org.

■ AUTHOR INFORMATION

Corresponding Author

*E-mail: lcao2@ncsu.edu.

Author Contributions

Y.Y., S.H., and L.S. contributed equally.

Notes

The authors declare no competing financial interest.

■ ACKNOWLEDGMENTS

This work was supported by a Young Investigator Award from the Army Research Office (W911NF-13-1-0201) and, partially, by a CAREER award from the National Science Foundation (DMR 1352028). K.W.K. acknowledges the support from FAME (one of six centers of STARnet, a SRC program sponsored by MARCO and DARPA). Y.Z. acknowledges the support of the Bissell Distinguished Professorship. The authors

acknowledge the use of the Analytical Instrumentation Facility (AIF) at North Carolina State University, which is supported by the State of North Carolina and the National Science Foundation. Part of the Raman and PL work was conducted at the Center for Nanophase Materials Sciences, which is sponsored at Oak Ridge National Laboratory by the Scientific User Facilities Division, Office of Basic Energy Sciences, U.S. Department of Energy..

REFERENCES

(1) Weisbuch, G.; Vinter, B. *Quantum Semiconductor Sturctures: Fundamentals and Applications*; Academic Press: San Diego, 1991.
(2) Piprek, J. *Semiconductor Optoelectronic Devices*; Academic Press: San Diego, 2003.
(3) Gao, G. H.; Gao, W.; Cannuccia, E.; Taha-Tijerina, J.; Balicas, L.; Mathkar, A.; Narayanan, T. N.; Liu, Z.; Gupta, B. K.; Peng, J.; Yin, Y. S.; Rubio, A.; Ajayan, P. M. *Nano Lett.* **2012**, *12*, 3518−3525.
(4) Geim, A. K.; Grigorieva, I. V. *Nature* **2013**, *499*, 419−425.
(5) Britnell, L.; Ribeiro, R. M.; Eckmann, A.; Jalil, R.; Belle, B. D.; Mishchenko, A.; Kim, Y. J.; Gorbachev, R. V.; Georgiou, T.; Morozov, S. V.; Grigorenko, A. N.; Geim, A. K.; Casiraghi, C.; Neto, A. H. C.; Novoselov, K. S. *Science* **2013**, *340*, 1311−1314.
(6) Shi, Y. M.; Zhou, W.; Lu, A. Y.; Fang, W. J.; Lee, Y. H.; Hsu, A. L.; Kim, S. M.; Kim, K. K.; Yang, H. Y.; Li, L. J.; Idrobo, J. C.; Kong, J. *Nano Lett.* **2012**, *12*, 2784−2791.
(7) Georgiou, T.; Jalil, R.; Belle, B. D.; Britnell, L.; Gorbachev, R. V.; Morozov, S. V.; Kim, Y.-J.; Gholinia, A.; Haigh, S. J.; Makarovsky, O.; Eaves, L.; Ponomarenko, L. A.; Geim, A. K.; Novoselov, K. S.; Mishchenko, A. *Nat. Nanotechnol.* **2013**, *8*, 100−103.
(8) Yu, W. J.; Li, Z.; Zhou, H.; Chen, Y.; Wang, Y.; Huang, Y.; Duan, X. *Nat. Mater.* **2013**, *12*, 246−252.
(9) Zhang, W.; Chuu, C.-P.; Huang, J.-K.; Chen, C. H.; Tsai, M.-L.; Chang, Y.-H.; Liang, C.-T.; He, J.-H.; Chou, M.-Y.; Li, L.-J. *Sci. Rep.* **2013**, *4*, 3826.
(10) Ji, Q. Q.; Zhang, Y. F.; Gao, T.; Zhang, Y.; Ma, D. L.; Liu, M. X.; Chen, Y. B.; Qiao, X. F.; Tan, P. H.; Kan, M.; Feng, J.; Sun, Q.; Liu, Z. F. *Nano Lett.* **2013**, *13*, 3870−3877.
(11) Komsa, H.-P.; Krasheninnikov, A. V. *Phys. Rev. B* **2013**, *88*, 085318.
(12) Kośmider, K.; Fernández-Rossier, J. *Phys. Rev. B* **2013**, *87*, 075451.
(13) Terrones, H.; López-Urías, F.; Terrones, M. *Sci. Rep.* **2013**, *3*, 1549.
(14) Kang, J.; Tongay, S.; Zhou, J.; Li, J. B.; Wu, J. Q. *Appl. Phys. Lett.* **2013**, 102.
(15) Fang, H.; Battaglia, C.; Carraro, C.; Nemsak, S.; Ozdol, B.; Kang, J. S.; Bechtel, H. A.; Desai, S. B.; Kronast, F.; Unal, A. A.; Conti, G.; Conlon, C.; Palsson, G. K.; Martin, M. C.; Minor, A. M.; Fadley, C. S.; Yablonovitch, E.; Maboudian, R.; Javey, A. *Proc. Natl. Acad. Sci. U.S.A.* **2014**, 6198−6202.
(16) Rivera, P.; Schaibley, J. R.; Jones, A. M.; Ross, J. S.; Wu, S.; Aivazian, G.; Klement, P.; Ghimire, N. J.; Yan, J.; Mandrus, D. G.; Yao, W.; Xu, X. *arXiv*:1403.4985 **2014**.
(17) Hong, X.; Kim, J.; Shi, S.-F.; Zhang, Y.; Jin, C.; Sun, Y.; Tongay, S.; Wu, J.; Zhang, Y.; Wang, F. *Nat. Nanotechnol.* **2014**, *9*, 682−686.
(18) Gong, Y.; Lin, J.; Wang, X.; Shi, G.; Lei, S.; Lin, Z.; Zou, X.; Ye, G.; Vajtai, R.; Yakobson, B. I.; Terrones, H.; Terrones, M.; Tay, B. K.; Lou, J.; Pantelides, S. T.; Liu, Z.; Zhou, W.; Ajayan, P. M. *Nat. Mater.* **2014**, *13*, 1135−1142.
(19) Pospischil, A.; Furchi, M. M.; Mueller, T. *Nat. Nanotechnol.* **2014**, *9*, 257−261.
(20) Lee, C.-H.; Lee, G.-H.; Zande, A. M. v. d.; Chen, W.; Li, Y.; Han, M.; Cui, X.; Arefe, G.; Nuckolls, C.; Heinz, T. F.; Guo, J.; Hone, J.; Kim, P. *Nat. Nanotechnol.* **2014**, *9*, 676−681.
(21) Najmaei, S.; Liu, Z.; Zhou, W.; Zou, X. L.; Shi, G.; Lei, S. D.; Yakobson, B. I.; Idrobo, J. C.; Ajayan, P. M.; Lou, J. *Nat. Mater.* **2013**, *12*, 754−759.
(22) van der Zande, A. M.; Huang, P. Y.; Chenet, D. A.; Berkelbach, T. C.; You, Y. M.; Lee, G. H.; Heinz, T. F.; Reichman, D. R.; Muller, D. A.; Hone, J. C. *Nat. Mater.* **2013**, *12*, 554−561.
(23) Lee, Y. H.; Zhang, X. Q.; Zhang, W.; Chang, M. T.; Lin, C. T.; Chang, K. D.; Yu, Y. C.; Wang, J. T. W.; Chang, C. S.; Li, L. J. *Adv. Mater.* **2012**, *24*, 2320−2325.
(24) Butler, S. Z.; Hollen, S. M.; Cao, L.; Cui, Y.; Gupta, J. A.; Gutiérrez, H. R.; Heinz, T. F.; Hong, S. S.; Huang, J.; Ismach, A. F.; Johnston-Halperin, E.; Kuno, M.; Plashnitsa, V. V.; Robinson, R. D.; Ruoff, R. S.; Salahuddin, S.; Shan, J.; Shi, L.; Spencer, M. G.; Terrones, M.; Windl, W.; Goldberger, J. E. *ACS Nano* **2013**, *7*, 2898−2926.
(25) Lee, Y.-H.; Yu, L.; Wang, H.; Fang, W.; Ling, X.; Shi, Y.; Lin, C.-T.; Huang, J.-K.; Chang, M.-T.; Chang, C.-S. *Nano Lett.* **2013**, *13*, 1852−1857.
(26) Tongay, S.; Fan, W.; Kang, J.; Park, J.; Koldemir, U.; Suh, J.; Narang, D. S.; Liu, K.; Ji, J.; Li, J.; Sinclair, R.; Wu, J. *Nano Lett.* **2014**, *14*, 3185−3190.
(27) Schonfeld, B.; Huang, J.; Moss, S. *Acta Crystallogr., Sect. B: Struct. Sci.* **1983**, *39*, 404−407.
(28) Schutte, W.; De Boer, J.; Jellinek, F. *J. Solid State Chem.* **1987**, *70*, 207−209.
(29) Yu, Y. F.; Li, C.; Liu, Y.; Su, L. Q.; Zhang, Y.; Cao, L. Y. *Sci. Rep.* **2013**, *3*, 1866.
(30) Mak, K. F.; Lee, C.; Hone, J.; Shan, J.; Heinz, T. F. *Phys. Rev. Lett.* **2010**, *105*, 136805.
(31) Splendiani, A.; Sun, L.; Zhang, Y. B.; Li, T. S.; Kim, J.; Chim, C. Y.; Galli, G.; Wang, F. *Nano Lett.* **2010**, *10*, 1271−1275.
(32) Cheiwchanchamnangij, T.; Lambrecht, W. R. L. *Phys. Rev. B* **2012**, *85*, 205302.
(33) Buscema, M.; Steele, G. A.; Zant, H. S. J. v. d.; Castellanos-Gomez, A. *Nano Res.* **2014**, *7*, 561−571.
(34) Miller, D. A. B. *Quantum Mechanics for Scientists and Engineers*; Cambridge University Press: New York, 2008.
(35) Korn, T.; Heydrich, S.; Hirmer, M.; Schmutzler, J.; Schuller, C. *Appl. Phys. Lett.* **2011**, *99*, 102109.
(36) Mai, C.; Barrette, A.; Yu, Y. F.; Semenov, Y. G.; Kim, K. W.; Cao, L. Y.; Gundogdu, K. *Nano Lett.* **2014**, *14*, 202−206.
(37) Gutierrez, H. R.; Perea-Lopez, N.; Elias, A. L.; Berkdemir, A.; Wang, B.; Lv, R.; Lopez-Urias, F.; Crespi, V. H.; Terrones, H.; Terrones, M. *Nano Lett.* **2013**, *13*, 3447−3454.
(38) Gurarslan, A.; Yu, Y.; Su, L.; Yu, Y.; Suarez, F.; Yao, S.; Zhu, Y.; Ozturk, M.; Zhang, Y.; Cao, L. *ACS Nano* **2014**, *8*, 11522−11528.
(39) Fivaz, R.; Mooser, E. *Phys. Rev.* **1964**, *136*, A833.
(40) Consadori, F.; Frindt, R. *Phys. Rev. B* **1970**, *2*, 4893.
(41) Mak, K. F.; He, K. L.; Lee, C.; Lee, G. H.; Hone, J.; Heinz, T. F.; Shan, J. *Nat. Mater.* **2013**, *12*, 207−211.
(42) Ramasubramaniam, A. *Phys. Rev. B* **2012**, *86*, 115409.

NANO LETTERS

Letter

pubs.acs.org/NanoLett

Layer-Dependent Electrocatalysis of MoS_2 for Hydrogen Evolution

Yifei Yu,[†,#] Sheng-Yang Huang,[†,#] Yanpeng Li,[†] Stephan N. Steinmann,[§] Weitao Yang,[§] and Linyou Cao*[,†,‡]

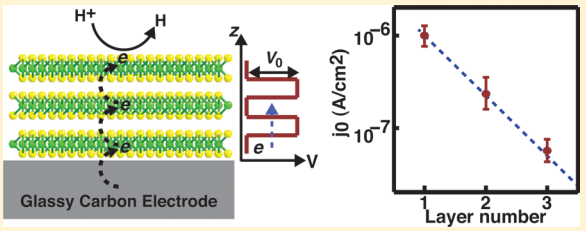
[†]Department of Materials Science and Engineering, North Carolina State University, Raleigh, North Carolina 27695, United States

[‡]Department of Physics, North Carolina State University, Raleigh, North Carolina 27695, United States

[§]Department of Chemistry, Duke University, Durham, North Carolina 27708, United States

Supporting Information

ABSTRACT: The quantitative correlation of the catalytic activity with the microscopic structure of heterogeneous catalysts is a major challenge for the field of catalysis science. It requests synergistic capabilities to tailor the structure with atomic scale precision and to control the catalytic reaction to proceed through well-defined pathways. Here we leverage on the controlled growth of MoS_2 atomically thin films to demonstrate that the catalytic activity of MoS_2 for the hydrogen evolution reaction decreases by a factor of ~4.47 for the addition of every one more layer. Similar layer dependence is also found in edge-riched MoS_2 pyramid platelets. This layer-dependent electrocatalysis can be correlated to the hopping of electrons in the vertical direction of MoS_2 layers over an interlayer potential barrier. Our experimental results suggest the potential barrier to be 0.119 V, consistent with theoretical calculations. Different from the conventional wisdom, which states that the number of edge sites is important, our results suggest that increasing the hopping efficiency of electrons in the vertical direction is a key for the development of high-efficiency two-dimensional material catalysts.



KEYWORDS: *MoS_2, monolayers, few layers, layer dependence, electrocatalyst, hydrogen evolution*

Seeking high-efficiency, cost-effective catalysts for the mass production of hydrogen gas is critical for the utilization of hydrogen energy. The existing catalysts of Pt-group metals for the hydrogen evolution reaction (HER) are highly efficient but too expensive and rare to be useful for mass production. Molybdenum disulfide (MoS_2) promises an earth-abundant, low-cost alternative to the precious metals.[1] Considerable efforts have been dedicated to investigating and optimizing the catalytic activities of various MoS_2 materials, including nanoparticles,[2−4] mesopores,[5] nanowires,[6] amorphous and doped MoS_2,[7−9] thin films,[10] MoS_2/graphene heterostructures,[11] and chemically exfoliated MoS_2 layers.[12−15] It was suggested that the edge site and metallic 1T polymorph of MoS_2 materials are catalytically active.[2,14−17] However, despite the remarkable progress, the rational design of MoS_2 structures with optimal catalytic activities has remained elusive due to limited quantitative understanding on the correlation between the catalytic activity and the microscopic structure of MoS_2 materials.

To quantitatively correlate the catalytic activity with microscopic structure requests capabilities to tailor the structure with atomic scale precision and to control the catalytic reaction to proceed in well-defined pathways. Most of the MoS_2 materials studied to date involve a wide dispersion in size, morphology, surface texture, and crystalline structure. This makes it difficult to quantitatively assess the role of structural parameters in the catalytic performance. Here we demonstrate a layer-dependent electrocatalysis of MoS_2 for the HER by leveraging on a unique synthetic capability that can grow large-area, uniform, and high-quality MoS_2 atomically thin films with precisely controlled layer numbers. The well-defined physical features make the film an ideal platform for studies of the structure−catalysis correlation. We find that the catalytic activity, indicated by the exchange current density, of the MoS_2 film decreases by a factor of about 4.47 for the addition of each additional layer. Similar layer dependence is also found in the electrocatalysis of edge-riched MoS_2 pyramid platelets. This layer-dependent electrocatalysis can be correlated to the hopping of electrons in the vertical direction of MoS_2 layers over an interlayer potential barrier, which is found to be 0.119 V and consistent with theoretical calculations.

We grew MoS_2 thin films on glassy carbon substrates following a chemical vapor deposition (CVD) process that we have previously developed.[18] The layer number was controlled by control of the amount of precursors ($MoCl_5$).[18] The composition of the film was confirmed as MoS_2 by X-ray photoelectron spectroscopy (XPS) characterizations (Figure S1 of the Supporting Information). The synthesized films are continuous, uniform, and of high crystalline quality, similar to the films we previously grew on sapphire substrates.[18] It can be seen uniformly covering the entire substrate under optical microscopes (Figure 1a and Figure S2). Atomic force

Received: September 27, 2013
Revised: January 3, 2014
Published: January 7, 2014

ACS Publications © 2014 American Chemical Society

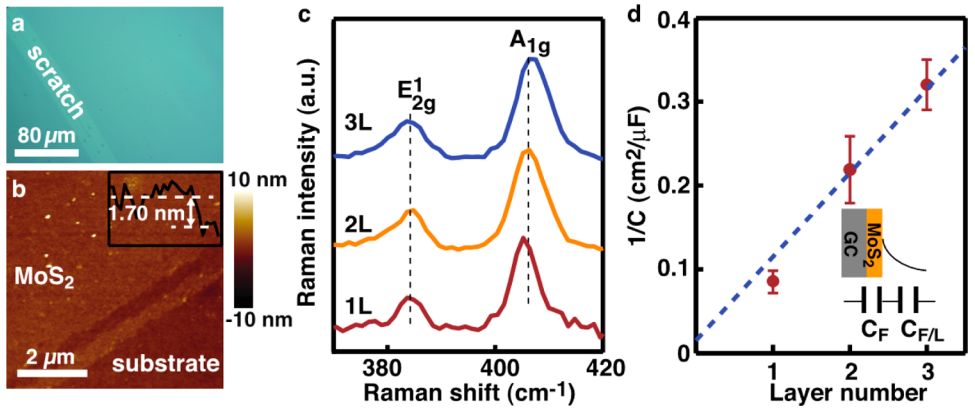


Figure 1. Structure characterizations of synthesized MoS_2 films. (a) Optical image and (b) AFM image of a bilayer MoS_2 film (monolayer and trilayer, see Figures S1 and S3). A scratch is intentionally made in the film to show the contrast between the substrate and the film and for the convenience of characterizing the height of the film. The inset of b is a typical height profile of the film. (c) Raman spectra of the synthesized monolayer (1L), bilayer (2L), and trilayer (3L) MoS_2 films. The dashed lines serve to visualize the layer-dependent Raman shift. The characteristic Raman modes are labeled as shown. (d) The reciprocal of measured capacitances of the films as a function of the layer number. The inset is a schematic illustration for the model of two capacitors in series.

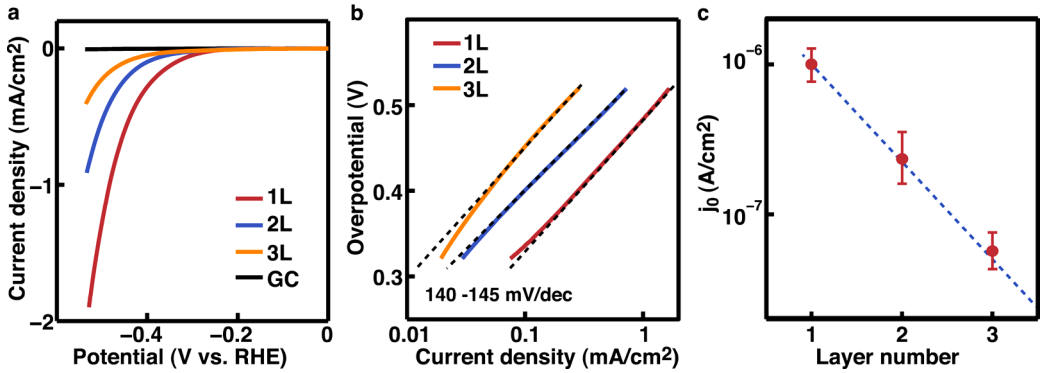


Figure 2. Layer dependence of the catalytic activities of MoS_2 films. (a) Polarization curves of the synthesized monolayer (red, 1L), bilayer (blue, 2L), and trilayer (orange, 3L) MoS_2 films. The curve of bare glass carbon substrates is also given (black). (b) Tafel plots of the MoS_2 films. The dashed lines indicate linear fitting for the plots. (c) The exchange current density of the MoS_2 film as a function of the layer number. The current density is plotted in a logarithmic scale. The dashed line is a fitting of $\log y = -0.65x - 5.35$.

microscope (AFM) characterizations identify the synthesized monolayer, bilayer, and trilayer MoS_2 films in thickness of 0.90, 1.70, and 2.15 nm, respectively (Figure 1b and Figure S3). These measured results are slightly larger than those of the MoS_2 films grown on sapphire,[18] which may be related to the relatively larger surface roughness of the glassy carbon substrate (~1 nm) than that of sapphire. Raman measurements further confirm the layer number. The frequency differences (Δk) of the two characteristic Raman modes (A_{1g} and E^1_{2g}), which is widely used to identify the layer number,[19] of the synthesized monolayer, bilayer, and trilayer MoS_2 films are 20.5, 22.4, and 23 cm^{-1} (Figure 1c), respectively, consistent with previous results.[18,19] The AFM and Raman characterizations also confirm the large-area continuity and uniformity of the synthesized films. No substantial voids, steps, and edges were found in the films through numerous AFM measurements. The frequency difference Δk remains reasonably constant during extensive Raman characterizations across the films (Figure S4). Additionally, the crystalline quality of the synthesized films is reasonably high, as evidenced by the full width at half-maximum (fwhm) of the E^1_{2g} mode that is known related with crystalline quality.[19] The E^1_{2g} fwhm of these MoS_2 films is comparable with the MoS_2 films grown on sapphire, which we previously demonstrated in high crystalline quality by electron microscope and electrical/optical characterizations (Figure S5).[18]

The layer number of the film is equally confirmed by capacitance measurements. The reciprocal of the measured capacitance ($1/C$) of the film is found linearly dependent on the layer number (Figure 1d). This linear dependence can be accounted for by a model of two capacitors in series, the film with a capacitance of C_F and the double-layer at the film/liquid interface with a capacitance of $C_{F/L}$, $1/C = 1/C_F + 1/C_{F/L}$ (Figure 1d inset). C_F is dependent on the thickness d and dielectric constant of the MoS_2 film ε_r, $C_F = \varepsilon_r\varepsilon_0/d$ (ε_0 is the vacuum permittivity). By linearly fitting the measured capacitance with the model, we can find out the double-layer capacitance $C_{F/L}$ as 66.7 $\mu F/cm^2$, similar to the typical double-layer capacitances previously reported.[5] We can also find the capacitance of monolayer MoS_2 C_F as 10 $\mu F/cm^2$. This suggests the dielectric constant of MoS_2 monolayers ε_r to be 7.63, consistent with the result in ref 20.

The electrocatalysis of the MoS_2 film strongly depends on the layer number. Figure 2a–b shows the polarization curves and corresponding Tafel plots of the synthesized monolayer, bilayer, and trilayer films. The polarization curve of bare glassy carbon electrodes is also given in Figure 2a, whose trivial current indicates that the glassy carbon is catalytically inactive

dx.doi.org/10.1021/nl403620g | Nano Lett. 2014, 14, 553−558

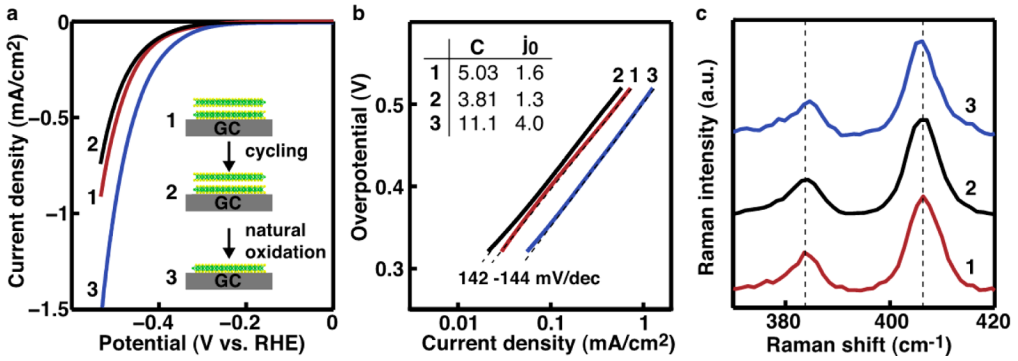


Figure 3. Improvement in the electrocatalysis of MoS_2 films after the stripping. (a) Polarization curves of a bilayer MoS_2 film recorded at the different stages in the stripping process: 1, as-grown; 2, after cyclic voltammetry; and 3, after oxidation and dissolution. Inset, schematic illustration for the stripping process. (b) Tafel plots corresponding to the results in a. The dashed lines indicate the linear fitting for the slope. The inset lists the capacitance (C, $\mu F/cm^2$) and exchange current density (j_0, 10^{-7} A/cm^2) of the bilayer film at the different stages. (c) Raman spectra of the bilayer MoS_2 film at the different stages. The dashed lines serve to visualize the change in the Raman spectra.

for the HER. From these results we deduce that the cathodic current of the film monotonically decreases with the layer number increasing.

The observed layer dependence can be linked to exchange current densities. By fitting the Tafel plots to the equation of $\eta = \rho \log j + \log j_0$ (overpotential η, current density j, and exchange current density j_0), we can find that all of the films have a similar slope ρ in the range of 140−145 mV/decade, while the exchange current density j_0 substantially decreases with the layer number increasing. We repeated the electrocatalytic characterization with numerous MoS_2 films (>15 films in total). The results reproducibly show a constant ρ in the range of 140−145 mV/decade and a layer-dependent j_0 (Figure 2c). Interestingly, j_0 decreases by a factor of ∼4.47 for the addition of every one more layer. Note that the observed Tafel slope is larger than typical results on MoS_2 materials. This may be related with the high temperature (850 °C) used in the synthetic process. Other groups reported a slope of ∼120 mV/decade in the MoS_2 materials processed at a temperature of ∼500 °C,[10,14,15] and it has been well-known that a processing of MoS_2 materials at a higher temperature can result in a higher Tafel slope.[10,14−16,21] As will be shown later (Figure 4), similar Tafel slopes (∼140 mV/decade) can be found in the other MoS_2 structures (i.e., edge-riched pyramid platelets) synthesized at the same temperature (850 °C). This indicates that the Tafel slope is not related with the structure of the film that is of our major interest in this work.

The layer-dependent electrocatalysis can be confirmed by a substantial improvement in the catalytic activities of bilayer and trilayer MoS_2 films after a stripping process. The stripping process is designed to selectively remove the outmost layer of the film (Figure 3 and Figure S6). It involves procedures of cyclic voltammetry (CV), natural oxidation, and dissolution. We first performed multiple (>1000 times) CV with the film in a potential range (+0.2 to −0.3 V) smaller than the range for the electrocatalysis measurement (+0.2 to −0.6 V) and then naturally exposed the CV-processed film to air for weeks (typically one month), which was followed by an immersion of the film into electrolyte solutions. We believe that the outmost layer of the CV-processed film can be gradually oxidized to Mo^{6+} (for instance, MoO_3) by the exposure to air and that the oxidized layer can be dissolved in aqueous solutions to expose the layer underneath due to a weak solubility of MoO_3 in water. This stripping mechanism is confirmed by our XPS characterizations throughout the process. The XPS characterization shows no oxidation (Mo^{6+}) in the film right after the CV processing, but substantial oxidation (Mo^{6+}) can be found after the CV-processed film being exposed to air for one month. The oxidation (Mo^{6+}) peak can be found disappearing again after the oxidized film being immersed into the electrolyte solution (Figure S7). This indicates that the CV processing does not oxidize the film but may somehow cause it easier to be oxidized by air. The XPS results also indicate that the ratios of Mo^{6+} and Mo^{4+} are around 1:0, 1:1, and 1:2 in the monolayer, bilayer, and trilayer films, respectively, after the natural oxidation (Figure S8). This suggests that the electrochemical reaction only occurs at the outmost layer, which subsequently limits the oxidation at that layer.

Figure 3a−b shows the polarization currents and corresponding Tafel plots of a bilayer film recorded through the stripping process (results for the other films, see Figure S6). The current slightly decreases after the CV processing (curve 2 in Figure 3a) but turns to be much stronger than the initial value after the stripping (curve 3 in Figure 3a). While the Tafel slope remains pretty much constant through the process, the exchange current density substantially increases from 1.6×10^{-7} to 5×10^{-7} A/cm^2 after the stripping (Figure 3b). Capacitance and Raman measurements both confirm that the bilayer film indeed becomes a monolayer after the stripping, the capacitance changing from 5.08 to 11.1 $\mu F/cm^2$ (Figure 3b inset) and the frequency Δk from 22.4 cm^{-1} (curve 1 in Figure 3c) to 20.5 cm^{-1} (curve 3 in Figure 3c). It is worthwhile to note that no obvious change is obtained in the Raman spectrum collected right after the CV processing (curve 2 in Figure 3c). This confirms that the electrochemical process does not cause substantial changes in the structure and composition of the film. A similar increase in the catalytic activity after the stripping process can also be found in trilayer MoS_2 films, but understandably not in monolayer MoS_2 films (Figure S6).

It is important to understand the mechanism underlying the observed layer-dependent exchange current density. We can reasonably exclude differences in the composition (i.e., stoichiometry) and crystalline quality (i.e., defects) of the MoS_2 films, which might cause a difference in electrocatalysis, because all of them were grown under highly comparable conditions. Additionally, previous studies show that the exchange current density of MoS_2 materials linearly depends on the number of edge sites.[16] However, we can exclude the

dx.doi.org/10.1021/nl403620g | Nano Lett. 2014, 14, 553−558

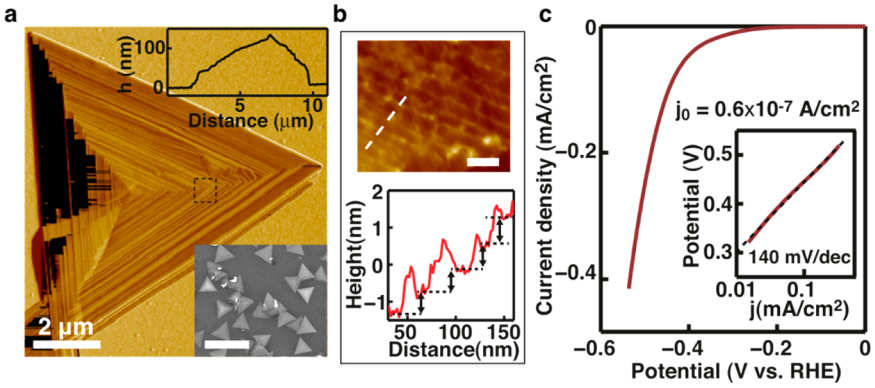


Figure 4. Poor electrocatalytic performance of edge-riched MoS_2 pyramid platelets. (a) AFM image of a typical pyramid. Low inset, SEM image of the platelets on glassy carbon substrates with a scale bar of 20 μm; upper inset, a typical height profile for the platelet. (b) A magnified image of the area indicated by the dashed square in part a as well as the height profile for the given dashed white line. The arrows shown in the height profile indicate that the step is one layer. Scale bar, 100 nm. (c) Polarization curve and Tafel plot of the MoS_2 pyramid platelet. The given current density considers is normalized to the area of the platelets by considering the partial coverage (60%) of the platelets on the substrate. The Tafel slope and exchange current density are noted as shown.

difference in the number of edge sites as the cause for the layer-dependent exchange current densities. The synthesized MoS_2 films are continuous, uniform, and show reasonably high crystalline quality (Figure 1). It is safe to conclude that there is no substantial amount of edge sites in the synthesized films and the observed layer dependence is related with the MoS_2 atoms in the basal plane.

To further support that the number of edge sites is not the cause, we grew MoS_2 pyramid platelets on glassy carbon substrates using temperatures similar to what were used for the synthesis of the film and tested the electrocatalytic performance of the platelets. The synthesized platelets show a monodisperse distribution in size (Figure 4a, lower inset). Different from the film, in which no obvious edges can be found, the pyramid platelet consists of a large number of gradually shrinking monolayers stacking in the vertical direction with a rich amount of edge sites exposed (Figure 4a–b). We can find that the pyramid platelets show a very poor electrocatalytic performance (Figure 4c). The Tafel slope, ~140 mV/decade, is similar to what was observed in the film. As discussed in the preceding text, this is related with the synthetic temperature and is not our interest here. The exchange current density, 0.6×10^{-7} A/cm^2, is barely comparable to those of trilayer thin films. The poor performance of the edge-riched platelets indicates that the number of edge sites is not the cause for the observed layer dependence. Otherwise, we would expect a high exchange current density in the platelets.

Our experimental results also suggest a layer dependence in the electrocatalysis of the edge-riched platelets. We observed the catalytic performance of the pyramid platelets increasing with the size decreasing (Figure S9). The ratio between the size and height of the pyramid platelet always remains to be constant around 60 (Figure S9). This constant size/height ratio enables comparable number of edge sites in unit area among the platelets in different sizes. Therefore, the observed size-dependent electrocatalysis of the platelet can be ascribed to a dependence on the layer number (height), instead of the density of edge sites. The layer dependence can account for the poorer performance observed in the platelets with a larger height (Figure 4c). Only the part close to the substrate electrode can effectively participate in the catalytic reaction.

We find that the layer-dependent exchange current density can be correlated to the hopping of electrons in the vertical direction of MoS_2 layers. As discussed in the preceding text, our results indicate that the electrochemical reaction only occurs at the outmost layer of the film. Electrons have to transfer from the glassy carbon electrode to the outmost layer to drive the HER (Figure 4). It is known that the electron transfer in the direction perpendicular to the basal plane of MoS_2 materials is through hopping,[22] because potential barriers exist in the interlayer gap. We can build up a quantum-tunneling model for the hopping process (Figure 5). The hopping efficiency is

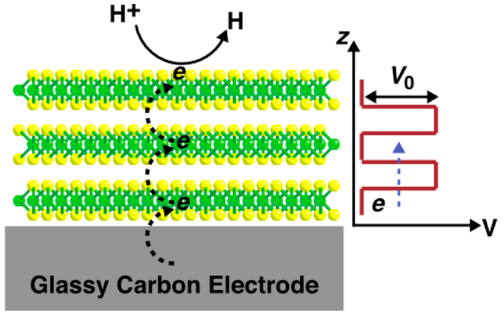


Figure 5. Hopping of electrons in the vertical direction of MoS_2 layers. The right side illustrates the potential distribution in the multilayer film and the hopping of electrons through the potential barrier in the interlayer gap.

dictated by the interlayer distance L and the potential barrier V_o as $T = e^{-2kL}$, and $k = (2m_eV_o)^{1/2}/\hbar$, where m_e is the effective mass of electrons and $\hbar$ is the Planck's constant. Our results, the exchange current density decreasing by a factor of 4.47 for the addition of every one more layer, suggest $T = e^{-2kL} = 1/4.47$. By substituting the values of L (0.62 nm) and m_e ($0.48m_o$, $m_o = 9.11 \times 10^{-31}$ kg) in MoS_2 atomic films,[23] we can get $V_o = 0.119$ V. This value is in excellent agreement with a recent theoretical calculation, which predicts that the hopping potential in the vertical direction of MoS_2 layers is 0.123 V.[24] The nice consistency suggests a dominant role of the electron hopping in the layer-dependent electrocatalysis of MoS_2.

We have quantitatively demonstrated the layer-dependent electrocatalysis of MoS_2 materials and elucidated that the layer dependence is rooted in the interlayer hopping of electrons. Different from conventional wisdom, which believes that the

dx.doi.org/10.1021/nl403620g | Nano Lett. 2014, 14, 553–558

edge site is catalytically active, our results suggest that the atoms in the basal plane can be active sites as well. The reportedly better catalytic performance of the edge sites could be because the edge site may provide an easier path for the hopping of electrons than the atoms in the basal plane. The result points out that increasing the hopping efficiency of electrons is a key for the rational design of MoS_2 materials with optimal catalytic activities. The efficiency of hopping is determined by the interlayer coupling of electron orbitals.[24] Therefore, strategies that can increase the interlayer coupling, such as intercalation of metal ions or atoms, are expected able to enhance the electrocatalytic performance of MoS_2 materials.

Methods. *1. Synthesis of MoS_2 Atomic Films with a Controlled Layer Number.* MoS_2 thin films were synthesized in a tube furnace following a chemical vapor deposition process we have recently developed.[18] In a typical growth, 1−50 mg of molybdenum chloride ($MoCl_5$) powder (99.99%, Sigma-Aldrich) was placed at the center of the furnace, and 1 g of sulfur powder (Sigma-Aldrich) was placed at the upstream entry of the furnace. Receiving substrates (glassy carbon) were placed in the downstream of the tube. Typical conditions for MoS_2 thin film growth included a temperature of 850 °C, a flow rate of 50 sccm, and a pressure around 2 Torr. The precursors were subjected to evaporation at elevated temperatures. The vapor of the precursor materials reacted to produce gaseous MoS_2 species, which subsequently precipitates onto receiving substrates at downstream to yield MoS_2 films. The layer number of the synthetic MoS_2 thin film can be controlled by control of the amount of $MoCl_5$ precursor. More details can be found in ref 18. MoS_2 pyramid platelets were grown under similar conditions as for the growth of thin films. The only difference lies in the pressure. 760 Torr was used for the growth of the pyramid platelets.

2. Structure and Electrochemical Characterizations. The structure and composition of the synthesized films were characterized by tools including an optical microscope, atomic force microscope (AFM), Raman spectroscope, and X-ray photoelectron spectroscope (XPS). AFM measurements were performed with a Veeco Dimension-3000 AFM. Raman spectra were collected on a Renishaw-1000 Raman spectroscopy with an excitation wavelength of 514.5 nm. XPS were performed on a SPECS System with PHOIBOS 150 analyzer using an Mg Kα X-ray source.

The electrochemical characterization of the MoS_2 films were performed in 0.5 M H_2SO_4 using a CH Instrument electrochemical analyzer (model CHI604D), a Pt-wire counter electrode, a saturated calomel reference electrode (SCE), and a glassy carbon (0.785 cm^2) working electrode. Nitrogen gas was bubbled into the electrolyte throughout the experiment. While all of the electrochemical characterization studies were performed using a saturated calomel reference electrode (SCE), the potential values mentioned in the electrochemical study are referred to a reversible hydrogen electrode (RHE). Calibration of the reference electrode for the reversible hydrogen potential was performed using a platinum (Pt) disk as a working electrode and a Pt wire as a counter electrode in 0.5 M H_2SO_4. The electrolyte was purged with ultrahigh purity hydrogen (Airgas) during the measurement. The potential shift of the SCE is −0.262 V vs RHE. The electrocatalysis was measured using linear sweeping from +0.2 to −0.6 V (vs RHE) with a scan rate of 5 mV/S. The cycling voltammetry was performed in a range of +0.2 to −0.3 V (vs RHE) at a scan rate of 50 mV/s.

The capacitance of the film was characterized using electrochemical impedance spectroscopy (EIS). The AC impedance is measured within the frequency range of 10^5 to 1 Hz with perturbation voltage amplitude of 5 mV. An equivalent Randles circuit model was fit to the data with ZSimpWin software to determine the system resistance and the capacitance.

■ ASSOCIATED CONTENT

Ⓢ Supporting Information

XPS of the synthesized MoS_2 films, optical images of monolayer and bilayer MoS_2 films grown on glassy carbon substrates, AFM characterizations, Raman spectra collected from numerous locations of the MoS_2 film and of the monolayer MoS_2 films grown on the substrates of glassy carbon and sapphire, polarization curves of the MoS_2 films in the stripping test, XPS characterization of the MoS_2 films through the stripping test and of the oxidation in MoS_2 films, and characterizations of MoS_2 pyramid platelets grown on glassy carbon substrates. This material is available free of charge via the Internet at http://pubs.acs.org.

■ AUTHOR INFORMATION

Corresponding Author

*E-mail: lcao2@ncsu.edu.

Author Contributions

Y.Y. and S.H. contributed equally. Y.Y. and L.C. conceived the experiments. Y.Y., S.H., and Y.L. performed the experiments. Y.Y., S.H., and L.C. analyzed the data. S.S., W.Y., and L.C. came up with the mechanism. All authors were involved in writing the manuscript.

Author Contributions

#These authors contributed equally to this work.

Notes

The authors declare no competing financial interest.

■ ACKNOWLEDGMENTS

L.C. acknowledges a Young Investigator Award from the Army Research Office (W911NF-13-1-0201). W.Y. acknowledges the support from National Science Foundation (CHE-09-11119). The authors acknowledge the use of the Analytical Instrumentation Facility (AIF) at North Carolina State University, which is supported by the State of North Carolina and the National Science Foundation. L.C. is grateful for the useful discussion with Dr. Zhebo Chen at the beginning of this project.

■ REFERENCES

(1) Laursen, A. B.; Kegnaes, S.; Dahl, S.; Chorkendorff, I. Molybdenum sulfides-efficient and viable materials for electro- and photoelectrocatalytic hydrogen evolution. *Energy Environ. Sci.* **2012**, *5*, 5577−5591.

(2) Hinnemann, B.; Moses, P. G.; Bonde, J.; Jorgensen, K. P.; Nielsen, J. H.; Horch, S.; Chorkendorff, I.; Norskov, J. K. Biornimetic hydrogen evolution: MoS2 nanoparticles as catalyst for hydrogen evolution. *J. Am. Chem. Soc.* **2005**, *127*, 5308−5309.

(3) Vrubel, H.; Merki, D.; Hu, X. L. Hydrogen evolution catalyzed by MoS_3 and MoS_2 particles. *Energy Environ. Sci.* **2012**, *5*, 6136−6144.

(4) Bonde, J.; Moses, P. G.; Jaramillo, T. F.; Norskov, J. K.; Chorkendorff, I. Hydrogen evolution on nano-particulate transition metal sulfides. *Faraday Discuss.* **2008**, *140*, 219−231.

(5) Kibsgaard, J.; Chen, Z. B.; Reinecke, B. N.; Jaramillo, T. F. Engineering the surface structure of MoS_2 to preferentially expose active edge sites for electrocatalysis. *Nat. Mater.* **2012**, *11*, 963−969.
(6) Chen, Z. B.; Cummins, D.; Reinecke, B. N.; Clark, E.; Sunkara, M. K.; Jaramillo, T. F. Core-shell MoO_3-MoS_2 Nanowires for Hydrogen Evolution: A Functional Design for Electrocatalytic Materials. *Nano Lett.* **2011**, *11*, 4168−4175.
(7) Merki, D.; Fierro, S.; Vrubel, H.; Hu, X. L. Amorphous molybdenum sulfide films as catalysts for electrochemical hydrogen production in water. *Chem. Sci.* **2011**, *2*, 1262−1267.
(8) Merki, D.; Vrubel, H.; Rovelli, L.; Fierro, S.; Hu, X. L. Fe, Co, and Ni ions promote the catalytic activity of amorphous molybdenum sulfide films for hydrogen evolution. *Chem. Sci.* **2012**, *3*, 2515−2525.
(9) Benck, J. D.; Chen, Z.; Kuritzky, L. Y.; Forman, A. J.; Jaramillo, T. F. Amorphous Molybdenum Sulfide Catalysts for Electrochemical Hydrogen Evolution: Insights into the Origin of their Catalytic Activity. *ACS Catal.* **2012**, *2*, 1916−1923.
(10) Kong, D. S.; Wang, H. T.; Cha, J. J.; Pasta, M.; Koski, K. J.; Yao, J.; Cui, Y. Synthesis of MoS_2 and $MoSe_2$ Films with Vertically Aligned Layers. *Nano Lett.* **2013**, *13*, 1341−1347.
(11) Li, Y. G.; Wang, H. L.; Xie, L. M.; Liang, Y. Y.; Hong, G. S.; Dai, H. J. MoS_2 Nanoparticles Grown on Graphene: An Advanced Catalyst for the Hydrogen Evolution Reaction. *J. Am. Chem. Soc.* **2011**, *133*, 7296−7299.
(12) Huang, X.; Zeng, Z. Y.; Bao, S. Y.; Wang, M. F.; Qi, X. Y.; Fan, Z. X.; Zhang, H. Solution-phase epitaxial growth of noble metal nanostructures on dispersible single-layer molybdenum disulfide nanosheets. *Nat. Commun.* **2013**, *4*, 1444.
(13) Chhowalla, M.; Shin, H. S.; Eda, G.; Li, L. J.; Loh, K. P.; Zhang, H. The chemistry of two-dimensional layered transition metal dichalcogenide nanosheets. *Nat. Chem.* **2013**, *5*, 263−275.
(14) Lukowski, M. A.; Daniel, A. S.; Meng, F.; Forticaux, A.; Li, L.; Jin, S. Enhanced Hydrogen Evolution Catalysis from Chemically Exfoliated Metallic MoS2 Nanosheets. *J. Am. Chem. Soc.* **2013**, *135*, 10274−10277.
(15) Voiry, D.; Yamaguchi, H.; Li, J.; Silva, R.; Alves, D. C. B.; Fujita, T.; Chen, M.; Asefa, T.; Shenoy, V. B.; Eda, G.; Chhowalla, M. Enhanced catalytic activity in strained chemically exfoliated WS_2 nanosheets for hydrogen evolution. *Nat. Mater.* **2013**, *12*, 850−855.
(16) Jaramillo, T. F.; Jorgensen, K. P.; Bonde, J.; Nielsen, J. H.; Horch, S.; Chorkendorff, I. Identification of active edge sites for electrochemical H-2 evolution from MoS_2 nanocatalysts. *Science* **2007**, *317*, 100−102.
(17) Karunadasa, H. I.; Montalvo, E.; Sun, Y. J.; Majda, M.; Long, J. R.; Chang, C. J. A Molecular MoS_2 Edge Site Mimic for Catalytic Hydrogen Generation. *Science* **2012**, *335*, 698−702.
(18) Yu, Y. F.; Li, C.; Liu, Y.; Su, L. Q.; Zhang, Y.; Cao, L. Y. Controlled Scalable Synthesis of Uniform, High-Quality Monolayer and Few-layer MoS_2 Films. *Sci. Rep.* **2013**, *3*, 1866.
(19) Lee, C.; Yan, H.; Brus, L. E.; Heinz, T. F.; Hone, J.; Ryu, S. Anomalous Lattice Vibrations of Single- and Few-Layer MoS_2. *ACS Nano* **2010**, *4*, 2695−2700.
(20) Frindt, R. F.; Yoffe, A. D. Physical Properties of Layer Structures - Optical Properties and Photoconductivity of Thin Crystals of Molybdenum Disulphide. *Proc. R. Soc. A* **1963**, *273*, 69−83.
(21) Chang, Y.-H.; Lin, C.-T.; Chen, T.-Y.; Hsu, C.-L.; Lee, Y.-H.; Zhang, W.; Wei, K.-H.; Li, L.-J. Highly Efficient Electrocatalytic Hydrogen Production by MoSx Grown on Graphene-Protected 3D Ni Foams. *Adv. Mater.* **2012**, *25*, 756−760.
(22) Tang, H.; Morrison, S. R. Optimization of the Anisotropy of Composite MoS_2 Films. *Thin Solid Films* **1993**, *227*, 90−94.
(23) Cheiwchanchamnangij, T.; Lambrecht, W. R. L. Quasiparticle band structure calculation of monolayer, bilayer, and bulk MoS_2. *Phys. Rev. B* **2012**, *85*, 205302.
(24) Cappelluti, E.; Roldan, R.; Silva-Guillen, J. A.; Ordejon, P.; Guinea, F. Tight-binding model and direct-gap/indirect-gap transition in single-layer and multi-layer MoS_2. *arXiv*: 1304.4831, **2013**.

Van der Waals Force Isolation of Monolayer MoS_2

*Alper Gurarslan, Shuping Jiao, Tai-De Li, Guoqing Li, Yiling Yu, Yang Gao, Elisa Riedo, Zhiping Xu, and Linyou Cao**

Van der Waals (vdW) interactions play an important role in many interfacial processes such as wetting, lubrication, adhesion, and adsorption, but the understanding has remained relatively limited. 2D materials present an unprecedented platform for the studies of interfacial vdW interactions due to the atomically thin dimension and perfect surface passivation.[1] The atomically thin dimension may allow to study interfacial vdW interactions as a function of physical features engineered with atomic-scale precision. The perfect surface passivation can ensure that the interaction at the interface is predominantly van der Waals in nature, which is difficult to realize at conventional material systems as the interfacial dangling bonds may invoke strong chemical bonding. A common strategy to study interfacial vdW interactions is to examine the process of water wetting.[2,3] Previous studies on the wetting of graphene have indicated that graphene may partially transmit the vdW interaction from the underlying substrate to the water droplet.[4–7] However, little has been known for how nongraphene 2D materials, like transition metal dichacolgenide (TMDC) materials, may affect interfacial vdW interactions. While recent studies on the wetting of 2D TMDC materials provide some useful information,[8–10] the inferior surface quality and structural uniformity of the materials used in those studies essentially prevents the possibility of precisely evaluating the interfacial vdW interaction and its correlation with physical features. For instance, it is not clear how the interfacial vdW interaction may depend on the layer number of MoS_2 and the surface properties of underlying substrates.

Here, we have demonstrated that monolayer MoS_2 can efficiently screen the vdW interaction of the underlying substrate with external systems by >90% because of the substantial increase in the physical separation between the substrate and the external systems by the presence of the monolayer. This is evidenced by a negligible dependence of the water contact angle of MoS_2 films on the layer number and on the hydrophilicity of the substrate. It is also supported by a constant vdW force between atomic force microscope (AFM) tips and the MoS_2 films with different layer numbers. The experimental observation is consistent with theoretical simulations based on an analytic model and molecular dynamic techniques. The quantitative correlation we have derived for the changes in physical separation and vdW interactions can also be generally applied to other 2D materials, such as the partial wetting transmission at graphene. Additionally, our preliminary result indicates that this efficient screening of vdW interactions by atomically thin MoS_2 monolayer bears significant implications for the dynamic control of interfacial processes.

Compared to the previous studies on the wetting of 2D TMDC materials,[9,10] in which the 2D TMDC materials used bear relatively poor surface quality and structural uniformity due to the synthetic approach, this work benefits from a unique self-limiting chemical vapor deposition technique that we developed for the synthesis centimeter-scale high-quality uniform MoS_2 films with precisely controlled layer numbers.[11] It also benefits from a surface-energy-assisted transfer technique that we developed that may perfectly transfer the synthesized film onto arbitrary substrates without compromising the quality and uniformity.[12] We have confirmed the layer number and surface roughness of all the as-grown films studied in this work, the latter of which is as low as 0.2 to 0.3 nm (Figures S1–S3, Supporting Information). We have also confirmed the high surface quality and uniformity of the transferred films (Figures S4–S6, Supporting Information). As further evidence for the superior surface quality and uniformity of our materials, the static and advancing contact angles show a difference of less than 2° (Figure S7, Supporting Information). By contrast, the wetting hysterysis is reported to be 20–30° in the previous studies.[10]

Figure 1 shows the water contact angle measured at as-grown MoS_2 films with different layer numbers on sapphire substrates. The contact angle of bare sapphire substrates is also given as a reference. To reflect the possible effect of the high-temperature synthetic process, the bare substrate was annealed under the

Dr. A. Gurarslan, G. Li, Prof. Dr. L. Cao
Department of Materials Science and Engineering
North Carolina State University
Raleigh, NC 27695, USA
E-mail: lcao2@ncsu.edu
Dr. A. Gurarslan, G. Li
Department of Fiber and Polymer Science
North Carolina State University
Raleigh, NC 27695, USA
S. Jiao, Prof. Dr. Z. Xu
Department of Mechanical Engineering
Tsinghua University
Beijing 100084, China
Dr. T.-D. Li, Y. Gao, Prof. Dr. E. Riedo
CUNY-Advanced Science Research Center
New York, NY 10031, USA
Y. Yu, Prof. Dr. L. Cao
Department of Physics
North Carolina State University
Raleigh, NC 27695, USA
Dr. T.-D. Li, Y. Gao, Prof. Dr. E. Riedo
School of Physics
Georgia Institue of Technology
Atlanta, GA 30332, USA
Prof. Dr. E. Riedo
Department of Physics
CUNY-City College of New York
New York, NY 10031, USA
Prof. Dr. E. Riedo
Phyics Program
CUNY-The Graduate Center
New York, NY 10016, USA

DOI: 10.1002/adma.201601581

© 2016 WILEY-VCH Verlag GmbH & Co. KGaA, Weinheim

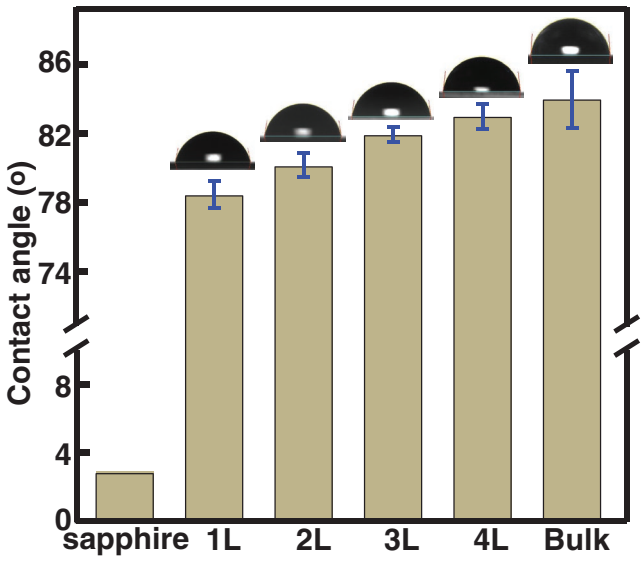


Figure 1. Mild dependence of the water contact angle of MoS_2 films on the layer number. The bar diagrams indicate the contact angles of as-grown MoS_2 films with different layer numbers on sapphire substrates. At the top of the bar the standard deviation of the measured contact angles is shown. Also given are the contact angles of bulk MoS_2 and the bare sapphire substrate. The plotted contact angle of the bare sapphire substrate does not represent the measured result, but just serves to illustrate that the contact angle is very small, <5°.

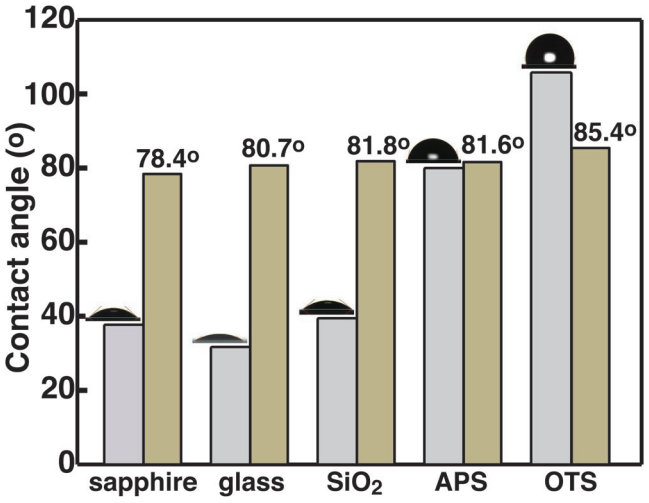


Figure 2. Minor dependence of the water contact angle of monolayer MoS_2 on the underlying substrates. The bar diagrams indicate the contact angles of the monolayer MoS_2 on different substrates (yellow) as well as the contact angles of bare substrates (grey). At the top of the bar the standard deviation of the measured contact angles of the monolayer is shown, which is usually less than 1°, and the number given is the mean value of the measured contact angle at corresponding monolayers. The substrates include sapphire (as-grown), glass, SiO_2/Si (300 nm thermally grown oxide on silicon substrates), SiO_2/Si substrates functionalized with self-assembled APTMS, and OTS.

same condition as what used for the synthesis except involving the precursors. The contact angle shows minor change with the layer number increasing, being 78.4° ± 0.8°, 80.1 ± 0.7°, 81.9°° ± 0.3°, 83.0°° ± 0.7°, and 83.9°° ± 1.6° for monolayer (1L), bilayer (2L), trilayer (3L), tetralayer (4L), and bulk MoS_2, respectively. Very interestingly, this mild layer dependence is different from what is reported with graphene.[4–7] The contact angle of graphene on hydrophilic substrates may be smaller than that of bulk graphite and increases with the layer number, which is ascribed to the capability of monolayer graphene to partially transmit the vdW interaction from the underlying substrate to the water droplet.[4–7] The minor layer-number dependence in the contact angle of MoS_2 films strongly suggests that monolayer MoS_2 may efficiently screen the interaction of the substrate with water molecules. In other words, it suggests that the wetting of the MoS_2 films is dominated by the intrinsic surface properties of MoS_2.

To further confirm the wetting screening, we transferred the synthesized centimeter-scale monolayer MoS_2 from the growth substrate (sapphire) onto other substrates, and monitored the contact angle of the transferred films as a function of the surface properties of the substrates. **Figure 2** shows the contact angles collected from the monolayer MoS_2 on different substrates, including sapphire (as-grown), glass, silicon substrates with thermally grown SiO_2 (SiO_2/Si), and SiO_2/Si substrates functionalized with self-assembled monolayers of octadecyltrichlorosilane (OTS) or 3-aminopropyltrimethoxysilane (APTMS). The contact angles of bare substrates are also plotted as reference. While the bare substrates show contact angles substantially varying from 0° to 110°, the contact angle of the supported monolayer MoS_2 maintains to be in a narrow range of 80°–86°. This again indicates that monolayer MoS_2 can efficiently screen the effect of underlying substrates in wetting, regardless of how hydrophilic the substrate is.

We can obtain quantitative understanding for the wetting screening by examining the interfacial interactions involved. According to the Young-Dupré equation, the water contact angle θ of an object is determined by the interaction potential (adhesion energy) of the object with water W versus the surface energy of water γ_w as $cos\theta = W/\gamma_w - 1$. Generally, the stronger the interaction, the smaller the contact angle. **Figure 3**a schematically illustrates the system studied in this work, in which a water droplet sits on top of monolayer MoS_2 supported by substrates. The total adhesion energy of the water droplet W_{tot} may be considered as a simple sum of the interaction potentials contributed by both the monolayer MoS_2 (W_{MoS2}) and the substrate (W_{Sub}), $W_{tot} = W_{MoS2} + W_{Sub}$.

The interaction potential (adhesion energy) contributed by the monolayer MoS_2 and the substrate may be quantitatively evaluated from water contact angles. W_{MoS2} is related with the contact angle of free-standing monolayer MoS_2 with no substrate support. While there is no way to experimentally measure the contact angle of free-standing monolayer MoS_2, we can make a reasonable estimate based on the experimental results and molecular dynamic simulation. The contact angle of free-standing monolayer MoS_2 is expected to be close to that of the monolayer on the OTS substrate, because OTS is highly hydrophobic and contributes less adhesion energy than the other substrates. Based on the experimental result, we estimate the contact angle of free-standing monolayer MoS_2 to be in the range of 85°–87°. This is also reasonably consistent with the prediction of our molecular dynamic simulations (Figures S8–S11, Supporting Information). As a result, the adhesion energy

© 2016 WILEY-VCH Verlag GmbH & Co. KGaA, Weinheim
Adv. Mater. 2016,
DOI: 10.1002/adma.201601581

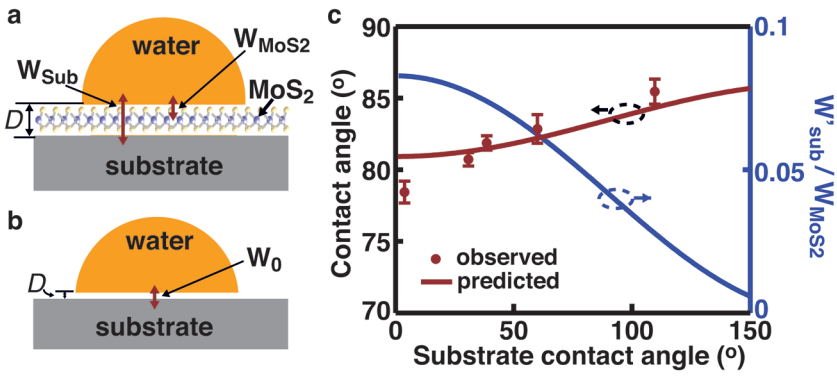


Figure 3. vdW interaction of the substrate with the water droplet. Schematic illustration for the wetting of a) monolayer MoS_2 films on substrates and b) bare substrates. The vertical red arrows indicate the vdW interactions. *D* represents the separation between the substrate and the water droplet. c) Predicted vdW interactions of the substrate with the water droplet in the presence of monolayer MoS_2 (blue curve) and contact angle of the supported monolayer as a function of the contact angle of the bare substrate. The measured contact angles of the monolayer MoS_2 on different substrates are given as red dots.

contributed by the monolayer W_{MoS2} can be estimated to be in the range of 0.0758–0.0783 J m^{-2} using the Young-Dupré equation (γ_w set to be 0.072 J m^{-2}). We can also evaluate the total adhesion energy W_{tot} from the contact angles measured at the supported monolayers, and then find out what is contributed by the substrate W_{Sub} as $W_{Sub} = W_{tot} - W_{MoS2}$. The result is given in **Table 1**. Indeed, the substrate contribution W_{Sub} only makes less than 10% of the total adhesion energy W_{tot}.

We can correlate the trivial contribution of the substrate in adhesion energy in the presence of monolayer MoS_2 to the increase in the separation between the substrate and the water. The experimental result can be nicely explained by a model based on the pairwise additivity treatment of van der Waals (vdW) interactions. According to the well-established hard-sphere model for vdW interactions, the adhesion energy can be written as a function of the separation *D* and a Hamaker constant *A* as $W = -A/(12\pi D^{[2]})$.[13] The Hamaker constant *A* is related with the density and the polarizability of the materials involved, and has been always considered to be a constant for given materials in the pairwise additivity treatment of vdW interactions.[13] The interfacial separation *D* is not the distance between neighboring atomic centers but an effective "cut-off" distance, in which the discrete and bumpy features of surface atoms are artificially "smeared out".[13] For simplicity, we can set the interfacial separation *D* to be a constant of 1.65 Å, which has been widely used as a reasonable approximation for the interfacial separation in vdW interactions.[13] The value of 1.65Å is also reasonably consistent with the prediction of our molecular dynamic simulations (Table S1, Supporting Information) and with the separations previously reported for copper-water and graphite-water systems.[5] The insertion of a MoS_2 monolayer (in thickness of 6.2 Å) may increase the substrate-water separation up to 7.85 Å. Therefore, the vdW interaction of the substrate with the water droplet in the presence of monolayer MoS_2 may dramatically decrease compared to that of the bare substrate as $W'_{Sub} = W_0\ (1.65/7.85)^{[2]} = 0.0442\ W_0$, where W_0 is the vdW interaction of the bare substrate with water and can be evaluated from the bare substrate's contact angle (Figure 2). As shown in Table 1, the predicted vdW interaction of the substrate W'_{Sub} is reasonably consistent with the W_{Sub} that is derived from the experimental measurements. This consistence indicates that the wetting screening of monolayer MoS_2 is mainly due to the screening of the vdW interaction between the substrate and water as the substrate-water separation is substantially increased.

Table 1. vdW interactions contributed by monolayer MoS_2 and the substrates.

	θ [°]	W_{tot} [J m^{-2}]	W_{sub} [J m^{-2}]	W'_{sub} [J m^{-2}]	W_0 [J m^{-2}]	θ [°]	Bare substrate
MoS_2/sapphire	78.4	0.0865	0.0082–0.0107	0.0064	0.1440	0	Sapphire
MoS_2/glass	80.7	0.0837	0.0054–0.0079	0.0059	0.1337	31	Glass
MoS_2/SiO_2	81.8	0.0823	0.0040–0.0065	0.0057	0.1282	38.7	SiO_2
MoS_2/APTMS	82.8	0.0811	0.0027–0.0053	0.0048	0.1077	60.3	APTMS
MoS_2/OTS	85.4	0.0782	–0.0001–0.0024	0.0021	0.0533	110	OTS

We can predict the water contact angle of monolayer MoS_2 on an arbitrary substrate using the model. The vdW interaction contributed by an arbitrary substrate underlying monolayer MoS_2 can be written as a function of the contact angle of the bare substrate θ_S as $W'_{Sub} = \gamma_w(1 + cos\theta_S)\ (1.65/7.85)$.[2] We can derive the water contact angle of the supported monolayer MoS_2 using $\theta = arcos[(W'_{Sub} + W_{MoS2})/\gamma_w - 1]$. The predicted contact angle θ (red curve) and vdW interaction W'_{Sub} (blue curve) are plotted as a function of the contact angle θ_S of the bare substrate in Figure 3c. The experimental results of this work are also plotted (red dots) to show the consistence between the predicted and experimental results. We can find that the predicted vdW interaction contributed by the substrate W'_{Sub} is always less than 10% of the contribution of the monolayer W_{MoS2} regardless of how hydrophilic the substrate is. We have also performed molecular dynamic simulation for the contact angle of monolayer MoS_2 supported by substrates and the simulation results confirm that the contact angle shows very mild dependence on the hydrophilicity of the substrate (Figure S9, Supporting Information).

To further illustrate the capability of monolayer MoS_2 to screen the vdW interaction of underlying substrates, we performed force-distance measurements at as-grown MoS_2 films with different layer numbers as well as bare sapphire substrates. This measurement allows us to directly evaluate the effect of MoS_2 films on the vdW interaction of underlying substrates with external systems, although the external system here is the AFM tip instead of water droplets. The force-distance curves measured by approaching the tip to the MoS_2 films are given in **Figure 4**. The maximum attractive force, which appears at "snap-in" when the tip jumps into contact with the sample, indicates the tip-sample vdW interaction when they are in touch. The interaction of the tip with the bare substrate is apparently stronger than that with the MoS_2 films. And the

© 2016 WILEY-VCH Verlag GmbH & Co. KGaA, Weinheim

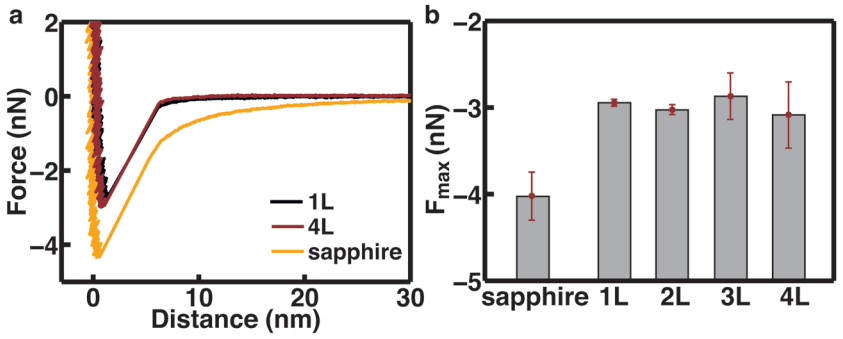


Figure 4. Force–distance relationship of the substrate with and without the presence of monolayer MoS_2. a) Measured force–distance curves for as-grown monolayer MoS_2 (black curve), tetra-layer MoS_2 (red curve), and the bare sapphire substrate (yellow curve). b) The maximum force, where the tip is in contact with the surface of the sample and corresponds to the valley in the curve given in (a) as function of the layer number of the film. At the top of the bar the standard deviation of the measured results is indicated.

interaction with the films shows negligible dependence on the layer number. This measurement provides corroborating evidence for the vdW screening of monolayer MoS_2.

As a matter of fact, we observed obvious effects of air-borne contaminants in the wetting of MoS_2, which is similar to what was previously reported for WS_2[4]. This is indicated by an increase of the contact angle with the time of being exposed to ambient environment (**Figure 5**). The adsorption of air-borne contaminant like hydrocarbon on the surface of newly made MoS_2 films has previously been confirmed by X-ray photoelectron spectroscopy and Auger electron spectroscopy.[14] However, the effect of the air-borne contamination does not affect our conclusion and analysis for the vdW screening. The contact angles of freshly made MoS_2 films or newly cleaved bulk MoS_2 materials show minor dependence on the layer number as well, all in the range of 65–69° (Figure 5 inset). This indicates that the wetting isolation is intrinsic to monolayer MoS_2, instead of the effect of air-borne contamination. Additionally, we did not observe any substantial change in the surface smoothness and thickness of the film with the exposure time with AFM and elliposometry measurements (Figures S12,S13, Supporting Information). Previous studies demonstrated that the air-borne contaminant adsorbed on SiO_2 surfaces might be in thickness of only 1–2 Å.[15] Given the lower surface energy of MoS_2, the air-borne contaminant on our materials is expected to be even less and thus might be difficult to be convincingly resolved by AFM and ellipsometry measurements. Therefore, the increase in the substrate-water separation is mainly dictated by the thickness of the monolayer MoS_2 even with the presence of adsorbed air-borne contaminants.

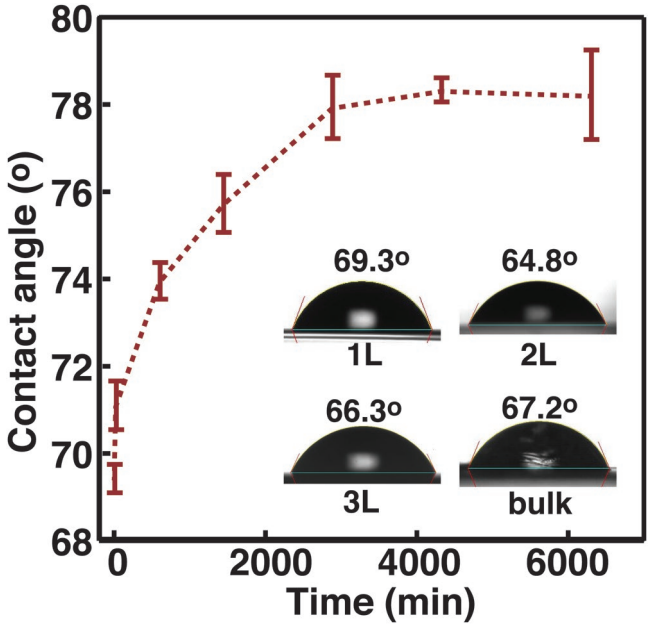


Figure 5. Evolution of the contact angle of as-grown monolayer MoS_2 as a function of the exposure time to ambient environment. The time is counted starting from when the monolayer is taken out of the synthetic setup. Insets are the images for the contact angle measured at MoS_2 films and bulk MoS_2 materials with exposure time less than 5 min.

The difference between the wetting isolation of monolayer MoS_2 and the partial wetting transmission previously reported with graphene can be correlated to the different thickness of the two materials. Monolayer graphene is reportedly able to partially transmit the vdW interaction of underlying substrates as its contact angle is subject to the strong influence of the substrate.[4–7] We can perform similar analysis for graphene as what we did for monolayer MoS_2 (for details see the Supporting Information). As the measured contact angles for graphene vary substantially in the literature.[4–7,16] here we focus on analyzing the results measured at freshly made graphene and newly cleaved highly ordered pyrolytic graphic (HOPG).[4] The contact angles are 51°, 59°, and 64° for fresh monolayer graphene on copper, —two to three layer graphene on nickel, and newly cleaved HOPG, respectively.[4] From the observed contact angles, the vdW interaction contributed by the copper substrate W_{Sub} can be estimated to be 0.0248 J m^{-2}. By contrast, the counterpart W'_{Sub} is predicted to be 0.0154 J m^{-2} by considering the effect of increased separation (from 1.65 to 5.05 Å). By the same token, the observed and predicted vdW interactions from the nickel substrate in the 2–3 layer grpahene grown on nickel can be found to be 0.0038 J m^{-2} and 0.0028–0.0055 J m^{-2}, respectively. The reasonable consistence between W_{Sub} and W'_{Sub} suggests that, similar to monolayer MoS_2, the role of graphene is just increasing the substrate-water separation. The partial wetting transmission at monolayer graphene reported in previous studies is simply because graphene may not increase the substrate-water separation as much as monolayer MoS_2 due to its smaller thickness (3.4 Å vs 6.2 Å).

In conclusion, we have demonstrated that monolayer MoS_2 can efficiently screen the vdW interaction from the underlying substrates to external systems by >90 due to the substantial increase in the separation between the substrate and the external system by the presence of the MoS_2 monolayer. This means that the wettability of an object covered by MoS_2

© 2016 WILEY-VCH Verlag GmbH & Co. KGaA, Weinheim
Adv. Mater. **2016**,
DOI: 10.1002/adma.201601581

monolayer is dominated by the intrinsic surface properties of the monolayer. As monolayer MoS_2 also features with excellent electrical, optical, and catalytic properties,[17–20] its dominance in interfacial vdW interactions may enable capabilities to dynamically manipulate the interfacial process through electrical, optical, or chemical ways. For instance, we have observed that the contact angle of monolayer MoS_2 can be tuned by applying a gating voltage (Figure S14, Supporting Information).

Experimental Section

Synthesis, Transfer, and Characterization of Centimeter-Scale MoS_2 Films: The centimeter monolayer and fewlayer MoS_2 films were grown using a chemical vapor deposition process in a tube furnace that we have previously reported.[11] Molybdenum chloride ($MoCl_5$) (99.99%, Sigma-Aldrich) and sulfur powder (Sigma-Aldrich) were used as precursors and sapphire as growth substrates. Typical conditions for high-quality MoS_2 thin film growth include a temperature of 850 °C and a pressure around 2 Torr. The layer number was controlled by controlling the amount of precursors ($MoCl_5$) used in the synthesis.

The transfer of the synthesized film was performed using a surface-energy-assisted transfer process that we have previously developed.[12] This process leverages on the different surface properties of MoS_2 films and the growth substrates. Basically, a layer of polystyrene (PS) was spin coated on as-grown MoS_2 films, followed by dropping a water droplet on the top. Driven by the different surface energies of the hydrophobic MoS_2 film and the hydrophilic substrate, water molecules could penetrate underneath the MoS_2 film to lift the film off the growth substrate. After removing the water droplet with paper towel, we could pick up the assembly with a pair of tweezers and transferred onto target substrate. The PS was removed by rinsing with toluene several times.

The uniformity, layer number, and crystalline quality of the as-grown and transferred MoS_2 were characterized by a variety of tools, including atomic force microscope (AFM, Veeco Dimension-3000), Raman spectroscope (Renishaw-1000), and optical microscope.

Contact Angle Measurements of Centimeter-Scale MoS_2 Films: The contact angle measurements were conducted on a First Ten Angstroms (FTA) 1000 C Class goniometer equipped with a dispensing needle and an HD camcorder (Canon VIXIA HF S20) mounted on a microscope (Olympus SZ-61l). 1 µL deionized water droplet generated with the automatic dispenser was gently brought in contact with the sample surface and then a snapshot was taken after separating the droplet from the needle for the static contact angle. Then static contact angle calculated from the tangent of the water droplet at the intersection of the air/drop surface using the spherical fit option on the FTA 32 software. For advancing and receding contact angles measurements, water droplet was placed on the sample surface and the volume of the droplet increased and then decreased gradually.

Force-Distance Measurements of As-Grown MoS_2 Films: The force-distance measurements were performed with a Multimode AFM while approaching a conductive tip to MoS_2 films deposited on double side-polished sapphire samples. The humidity was controlled and kept at 38–40%. A conductive tip (Pt/Ir) attached to a cantilever with force constant of 0.49 N m^{-1} was used. For each sample different measurements on three different positions were repeated, showing reproducibility of the data. The data were acquired with a scanner z-range of 100 nm at approaching speeds of 20 nm s^{-1}. Only the range 3–30 nm is shown because the force at longer distances doesn't show any variation. The MoS_2 films are grounded with cooper double side tape that will ground the substrate from the bottom side of the sample. Around the edges of the sample, a silver paste that grounds the MoS_2 layers on top of the substrate is used. For the calibration of the spring constant and force-distance curves see previous works.[21,22]

Molecular Dynamics Simulations: MD simulations were carried out by using the large-scale atomic/molecular massively parallel simulator. All equilibrium simulations were performed at a constant temperature of 300 K by using the Nosé-Hoover thermostat. The time step for integrating equations of motion was set to be 1 fs. The rigid SPC/E model was used for water molecules. The SHAKE algorithm was applied for the stretching terms between oxygen and hydrogen atoms to reduce high-frequency vibrations that require a shorter time step for numerical integration. The interaction between water and MOS_2 includes both van der Waals and electrostatic terms and the parameters are listed in the Table S1 (Supporting Information), which are taken from Ref. [2]. The van der Waals forces calculated in the Lennard-Jones 12–6 form $V(r) = 4\varepsilon[(\sigma/r)^{12} - (\sigma/r)^6]$ are truncated at 2.0 nm, and the long-range Coulomb interactions are computed by using the particle–particle particle-mesh algorithm with an accuracy of 10^{-4}. A droplet consisting of 1588 water molecules was involved in the simulation. More detailed information about the MD simulation can be found in the Supporting Information.

Supporting Information

Supporting Information is available from the Wiley Online Library or from the author.

Acknowledgements

The synthesis and transfer work was supported by a Young Investigator Award from the Army Research Office (W911NF-13-1-0201). The work of contact angle measurement, data analysis, and theoretical modeling was supported part of the Center for the Computational Design of Functional Layered Materials, an Energy Frontier Research Center funded by the U.S. Department of Energy, Office of Science, Basic Energy Sciences under Award # DE-SC0012575. E. R., T.-D. L., and Y. G. performed the AFM measurement and thank the support of the Office of Basic Energy Sciences of the Department of Energy (DE 0000224414). The authors thank D. Brenner, E. Reed, and J. Miller for useful discussion, and M. Dickey for providing access to the goniometer, and acknowledge the use of the Analytical Instrumentation Facility (AIF) at North Carolina State University, which is supported by the State of North Carolina and the National Science Foundation.

Received: March 22, 2016
Revised: July 7, 2016
Published online:

[1] S. Z. Butler, S. M. Hollen, L. Cao, Y. Cui, J. A. Gupta, H. R. Gutierrez, T. F. Heinz, S. S. Hong, J. Huang, A. F. Ismach, E. Johnston-Halperin, M. Kuno, V. V. Plashnitsa, R. D. Robinson, R. S. Ruolff, S. Salahuddin, J. Shan, L. Shi, M. G. Spencer, M. Terrones, W. Windl, J. E. Goldberger, *ACS Nano* **2013**, *7*, 2898.
[2] D. Bonn, J. Eggers, J. Indekeu, J. Meunier, E. Rolley, *Rev. Mod. Phys.* **2009**, *81*, 739.
[3] P. G. de Gennes, *Rev. Mod. Phys.* **1985**, *57*, 827.
[4] Z. Li, Y. Wang, A. Kozbial, G. Shenoy, F. Zhou, R. McGinley, P. Ireland, B. Morganstein, A. Kunkel, S. P. Surwade, L. Li, H. Liu, *Nat. Mater.* **2013**, *12*, 925.
[5] J. Rafiee, X. Mi, H. Gullapalli, A. V. Thomas, F. Yavari, Y. Shi, P. M. Ajayan, N. A. Koratkar, *Nat. Mater.* **2012**, *11*, 217.
[6] C. J. Shih, M. S. Strano, D. Blankschtein, *Nat. Mater.* **2013**, *12*, 866.
[7] C. J. Shih, Q. H. Wang, S. Lin, K. C. Park, Z. Jin, M. S. Strano, D. Blankschtein, *Phys. Rev. Lett.* **2012**, *109*, 176101.
[8] A. Kozbial, X. Gong, H. Liu, L. Li, *Langmuir* **2015**, *31*, 8429.
[9] A. P. S. Gaur, S. Sahoo, M. Ahmadi, M. J. Guinel, R. S. Katiyar, *Nano Lett.* **2014**, *14*, 4314.
[10] P. K. Chow, E. Singh, B. C. Viana, J. Gao, J. Luo, J. Lin, A. L. Elias, Y. Shi, Z. Wang, M. Terrones, N. Koratkar, *ACS Nano* **2015**, *9*, 3023.

© 2016 WILEY-VCH Verlag GmbH & Co. KGaA, Weinheim

[11] Y. Yu, Y. C. Li, Y. Liu, L. Su, Y. Zhang, L. Cao, *Sci. Rep.* **2013**, *3*, 1866.
[12] A. Gurarslan, Y. Yu, L. Su, Y. Yu, F. Suarez, S. Yao, Y. Zhu, M. Ozturk, Y. Zhang, L. Cao, *ACS Nano* **2014**, *8*, 11522.
[13] J. N. Israelachvili, *Intermolecular and Surface Forces*, 3rd Ed., Academic Press, San Diego, CA, USA **2011**.
[14] K. Miyoshi, *Solid Lubrication Fundamentals and Applications*, Marcel Dekker, New York, NY, USA **2001**.
[15] A. Shinozaki, K. Arima, M. Morita, I. Kojima, Y. Azuma, *Anal. Sci.* **2003**, *19*, 1557.
[16] R. Raj, S. C. Maroo, E. N. Wang, *Nano Lett.* **2013**, *13*, 1509.
[17] Q. H. Wang, K. Kalantar-Zadeh, A. Kis, J. N. Coleman, M. S. Strano, *Nat. Nanotech.* **2012**, *7*, 699.
[18] M. Chhowalla, H. S. Shin, G. Eda, L. J. Li, K. P. Loh, H. Zhang, *Nat. Chem.* **2013**, *5*, 263.
[19] Y. Li, Y. Yu, Y. Huang, R. A. Nielsen, W. A. Goddard III, Y. Li, L. Cao, *ACS Catal.* **2015**, *5*, 448.
[20] Y. Yu, S.-Y. Huang, Y. Li, S. N. Steinmann, W. Yang, L. Cao, *Nano Lett.* **2014**, *14*, 553.
[21] D. Ortiz-Young, H.-C. Chiu, S. Kim, K. Voïtchovsky, E. Riedo, *Nat. Commun.* **2013**, *4*, 2482.
[22] H. C. Chiu, D. Ortiz-Young, E. Riedo, *Rev. Sci. Instrum.* **2014**, *85*, 123707.

© 2016 WILEY-VCH Verlag GmbH & Co. KGaA, Weinheim
Adv. Mater. **2016**,
DOI: 10.1002/adma.201601581

NANO LETTERS

Letter

pubs.acs.org/NanoLett

Many-Body Effects in Valleytronics: Direct Measurement of Valley Lifetimes in Single-Layer MoS_2

Cong Mai,[†] Andrew Barrette,[†] Yifei Yu,[‡] Yuriy G. Semenov,[§] Ki Wook Kim,[§] Linyou Cao,*[,‡] and Kenan Gundogdu*[,†]

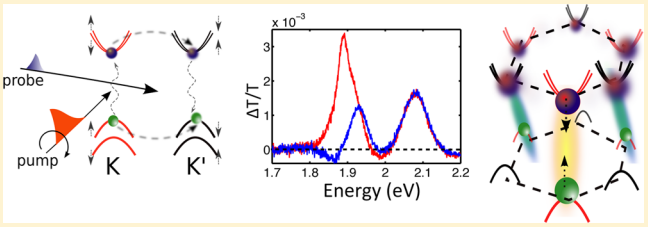
[†]Department of Physics, North Carolina State University, Raleigh, North Carolina 27695, United States

[‡]Department of Material Science and Engineering, North Carolina State University, Raleigh, North Carolina 27695, United States

[§]Department of Electrical and Computer Engineering, North Carolina State University, Raleigh, North Carolina 27695, United States

Supporting Information

ABSTRACT: Single layer MoS_2 is an ideal material for the emerging field of "valleytronics" in which charge carrier momentum can be finely controlled by optical excitation. This system is also known to exhibit strong many-body interactions as observed by tightly bound excitons and trions. Here we report direct measurements of valley relaxation dynamics in single layer MoS_2, by using ultrafast transient absorption spectroscopy. Our results show that strong Coulomb interactions significantly impact valley population dynamics. Initial excitation by circularly polarized light creates electron−hole pairs within the K-valley. These excitons coherently couple to dark intervalley excitonic states, which facilitate fast electron valley depolarization. Hole valley relaxation is delayed up to about 10 ps due to nondegeneracy of the valence band spin states. Intervalley biexciton formation reveals the hole valley relaxation dynamics. We observe that biexcitons form with more than an order of magnitude larger binding energy compared to conventional semiconductors. These measurements provide significant insight into valley specific processes in 2D semiconductors. Hence they could be used to suggest routes to design semiconducting materials that enable control of valley polarization.



KEYWORDS: *MoS_2, valley relaxation, transient absorption, many-body interactions, transition metal dichalcogenides, two-dimensional materials*

Carriers in semiconductors are located in band minima that are also known as valleys formed as a consequence of specific symmetry and electronic properties of crystalline periodic potential. Optical absorption, carrier mobility, effective mass, and momentum all depend on the valley in which the carrier is located. Hence control of valley polarization could provide a capability of tuning optical and electronic processes in semiconductors in an unprecedented way. Single-layer MoS_2, similar to many transition-metal dichalcogenides, is a 2D semiconducting system that has potential for such valleytronic applications. Its electronic structure exhibits two degenerate valleys, K and K′, at the band edges for both electrons and holes. Spin−orbital splitting of valence band lifts the spin degeneracy that leads to possibility of selective excitation of carriers in only one of these valleys depending on helicity of circularly polarized light.[1−4] Therefore, it provides with an ideal system to study semiconductor valley physics and poses significant potential for development of valleytronic applications.[1−8]

An initially excited valley population in MoS_2 eventually relaxes over both valleys. Since the durations of valley population provide the time window in which valley specific processes take place, it is an essential parameter for developing valleytronic applications. Here we present the relaxation dynamics of an initially excited valley population in single layer MoS_2, directly measured by transient absorption spectroscopy. Figure 1a shows the electronic band structure at the K and K′ valleys and the transient absorption experimental scheme. Upon excitation of one of the valleys with circularly polarized pump pulses, the measurement of the transmission of the same circularly polarized probe (SCP) pulses at different time delays reveals the decay of the excited valley polarization, whereas the measurement of opposite circularly polarized (OCP) probe pulses reveals the rise of the population in the other valley.

Figure 1b shows the absorption spectra. In the K-point the spin states are degenerate in the conduction band and are split by 160 meV in the valence band.[4,9−11] The transitions from the lower and higher energy valence bands in the same valley are known to be associated with A and B excitons, which differ by the spin orientation of the electron and hole pairs. In the other valley the corresponding spin orientations are reversed.

Received: October 8, 2013
Revised: December 10, 2013
Published: December 10, 2013

ACS Publications © 2013 American Chemical Society

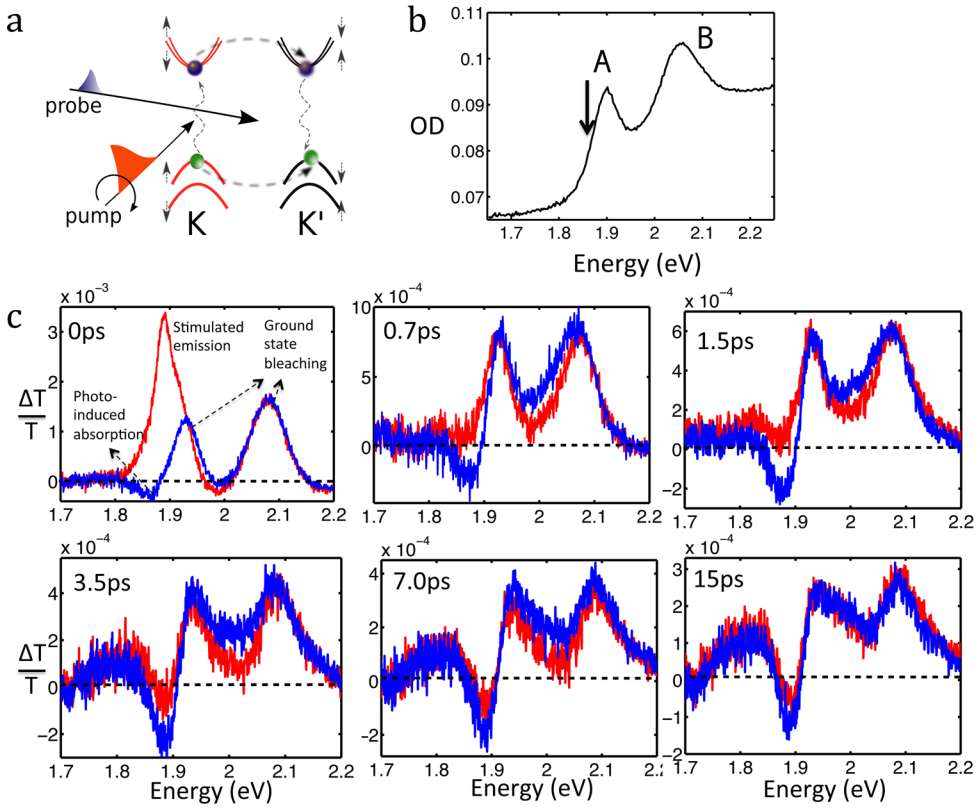


Figure 1. (a) Circularly polarized beam σ^- excite the K valley, and the same and oppositely circularly polarized probe measures the population in K and K′ valleys. (b) Absorbance of monolayer MoS_2 at 74 K. The arrow shows our excitation energy. (c) Transient absorption spectra of monolayer MoS_2 at 74 K with various delays between pump and probe beams. SCP (red line) and OCP (blue line) are shown, with PIA, SE, and GSB peaks labeled. The decay of PIA polarization anisotropy over time is apparent.

In the time-resolved experiments, left circularly polarized pump pulses tuned to the bottom of the lower energy A exciton create spin-down electrons in the conduction band and spin-up holes at the top of the upper valence band of the K-valley. By using broadband probe pulses, we measure the spectral evolutions in both A and B transitions. The presence of either an electron or a hole population in a band increases the probe transmission due to ground state bleaching (GSB). If both electrons and holes are present in the same valley, the probe field can stimulate the emission (SE) to further increase the signal. In case new optical transitions arise due to existence of the excited-state population, the transmission of probe pulses reduces due to photoinduced absorption (PIA). Hence the evolutions of GSB, SE, and PIA features provide a convenient means to measure electron and hole dynamics in both valleys simultaneously.

A number of interesting results are apparent in the data. First, the spectral features evolve quickly that the overall signal decays to 10% of its initial value within the first 20 ps (Supporting Information SI1). This suggests that both radiative and nonradiative relaxation rates are very large.[12−15] Second, even at the time overlap of pump and probe pulses (0 fs), the OCP spectra show GSB for both A and B excitonic transitions. This suggests that the two valleys are not completely uncoupled. Third, in the SCP experiment the B excitonic transition exhibits strong GSB response despite initial excitation of the A exciton, which suggests very fast electron spin relaxation within the K valley. Finally the SE signal decays quickly in the first few hundreds of femtoseconds in the SCP experiment, and the polarization anisotropy in the A transition is completely lost in about 400 fs. However, the total spin/valley polarization does not completely relax for about 10 ps. This follows because the polarization anisotropy persists in the PIA features at 1.87 and 2 eV.

These results imply the impact of strong many-body correlations on spin and valley dynamics in these 2D systems. Unlike bulk MoS_2, the transitions in monolayers are excitonic with an exciton binding energy of 500−900 meV, which is about half of its band gap.[9−18] Because excitons in many-valley semiconductors are formed as the coherent compounds of all $N_h \times N_e$ possible states of coupled pairs of electrons located in N_e valleys and holes located in N_h valleys,[19] dark excitonic states that involve intervalley K−K′ Coulomb interactions exist but cannot be directly excited. In such a multivalley system, excited eigenstates will be formed of linear combinations of these bright and dark excitons. As a result, although optical fields only couple transitions in individual valleys, the resulting excitons interact coherently with dark excitons involving electrons and holes in both valleys.

Figure 2a illustrates these dark and bright excitons and resulting population evolution. Specifically, the electron part of the exciton wave function coherently couples to the other valley because of the energy degeneracy of the spin states. This is similar to the observation of coherent superposition of degenerate electronic quantum states in correlated electron materials.[20] This electronic electronic coherence collapses into a population state in both valleys. Such a coherent coupling does not exist for holes due to the orthogonal K and K′ spin states. Therefore, the hole population collapses into the original valley of excitation. The electron population in the K′ valley

dx.doi.org/10.1021/nl403742j | Nano Lett. 2014, 14, 202−206

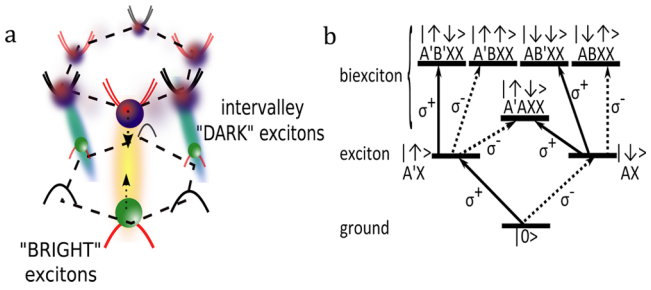


Figure 2. (a) Upon optical excitation intravalley "bright excitons" form. Because of Coulomb coupling the excited eigenstate is a super position of intervalley "dark excitons" and bright excitons. The electron part of the excitation immediately redistributes over the conduction bands in both K and K′ valleys. But the hole is located in K because it has to flip spin to coherently couple to the K′ valley. (b) The optical transitions and biexcitonic pathways that result in intervalley and intravalley biexcitons. The arrows in the kets are the hole spin orientation.

causes bleaching of the transitions as observed by a strong B′ exciton GSB signal of OCP spectra even at 0 fs (Figure 1).

In addition to the valley relaxation, electrons also lose their spin orientation rather quickly. The SCP spectra exhibit bleaching of B exciton transition in the K valley, and OCP spectra exhibit A′ exciton transitions in the K′ valley. Both of these transitions involve oppositely spin-polarized electrons compared to the initial excitation. Unlike electrons, hole spin relaxation is slower due to the fact that the spin states of the valence bands are nondegenerate. Since electrons lose their spin orientations but holes preserve it for longer time, the OCP signal does not exhibit SE. This explains the large photoluminescence (PL) helicity observed by the previous studies.[1−3]

To extract the hole valley/spin lifetime, we look at the overall spectral polarization anisotropy. The SCP and OCP spectra exhibit clear differences at probe energies near 1.87 eV, 70 meV lower than the A exciton transition and at 1.98 eV, about 70 meV lower than the B exciton transition. This anisotropy lasts longer than the SE lifetime. At 1.87 eV the SCP signal is higher, whereas at 1.98 eV the OCP signal is higher. Photoinduced absorption at these spectral positions has previously been observed for mono and bilayers of MoS_2 and has been attributed to carrier-induced peak broadening[14] similar to those observed in carbon nanotubes.[21] However the polarization dependence indicate these are spectral signatures of biexcitonic transitions.

Figure 2b shows the potential biexciton pathways that could be excited with a 660 nm pump and white-light-continuum probe pulses. Because of the distinct optical transitions allowed in the monolayer and single-spin occupation of each band in the K and K′ valley, only two biexcitons are allowed; an intervalley biexciton formed of A excitons (|AA′>), and an intra and intervalley biexciton formed of A and B excitons (|AB>, |AB′>, and |A′B′>). With these in mind, in the presence of an A exciton in the K valley, the reduced transmission of OCP probe pulses at 1.85 eV could be explained by absorption due to |A> to |AA′> exciton−biexciton transitions. Because of Pauli blocking, SCP pulses cannot induce such transitions without valley relaxation of the hole in K valley. Therefore the decay of polarization anisotropy and |AA′> biexciton formation with SCP pulses offer an effective means to monitor hole spin/valley polarization dynamics. The difference of the SCP and OCP spectra in Figure 1 clearly shows that most of the valley polarization decays within the first 10 ps.

It is important to note that 70 meV is an unusually strong biexciton binding energy when compared to conventional semiconductors. Reduced dielectric screening and large electron and hole effective masses together with the very large exciton binding energy contribute to such strong biexciton binding in single layer MoS_2 (Supporting Information SI2).

To isolate the effect of valley/spin coupling, we measured the spin relaxation in a bilayer structure in which inversion symmetry imposes doubly degenerate valence and conduction bands in both valleys. As a result, circularly polarized pulses create a net spin polarization but no valley polarization. Bilayers also form an excitonic system with about 500 meV binding energy.[9,16] Here both intra-and intervalley |AA> and |AB> biexciton transitions are allowed. Figure 3 shows the

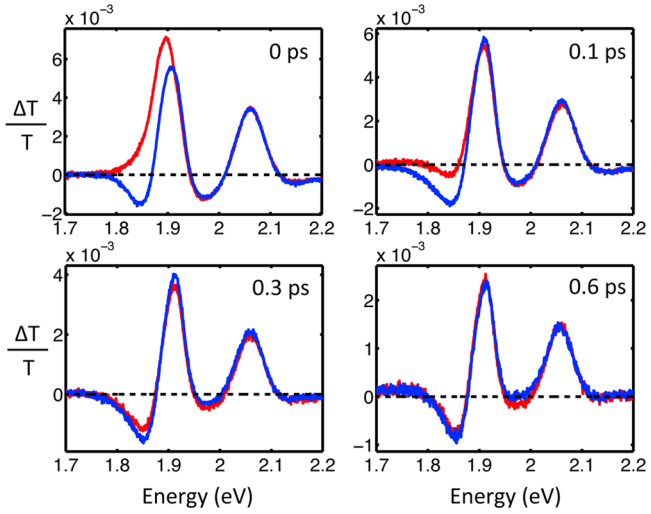


Figure 3. In bilayers the helicity of PIA at 1.85 eV decays completely within 600 fs.

experimental results. Both SCP and OCP spectra show the same PIA for the |AB> biexciton transition. In the OCP experiment a very strong |AA> biexciton PIA is observable at 0 fs. In the SCP spectra the same PIA features of the |AA> biexcitons are observable in the first 100 fs with the quick loss of SE. The polarization anisotropy in the |AA> biexciton region is lost in about 600 fs, much faster compared to the monolayer structure, suggesting very fast electron and hole spin relaxation.

Our results clearly show that the monolayer spin lifetime is about an order of magnitude longer compared to that of the bilayer. In the monolayer, the hole spin can only relax by switching valleys. One potential mechanism for hole valley relaxation is therefore to exchange the spin polarization with an oppositely spin-polarized electron in the other valley through electron−hole exchange mechanism as illustrated in Figure 4a. In this process, momentum is conserved because of the similar effective mass of electrons and holes.[22] Figure 4b illustrates another potential mechanism that involves the Γ valley, which falls in the energy range of valence K-valley in monolayer MoS_2.[10,23] Spin degeneracy in the Γ valley enables incoherent two-step transitions. After the transition from K to Γ and following spin relaxation, the Γ to K′ transition looks like a net K−K′ intervalley spin relaxation.

Previous steady-state PL helicity measurements suggest nanosecond hole valley lifetimes, which is 2 orders of

dx.doi.org/10.1021/nl403742j | Nano Lett. 2014, 14, 202−206

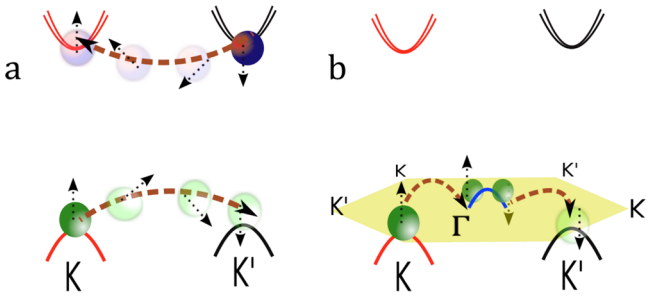


Figure 4. (a) Electron–hole exchange interaction leads to valley relaxation of initially excited holes by exchanging spin and momentum with an electron in the other valley. (b) Valley relaxation of holes via scattering through the Γ valley.

magnitude larger than our results.[2] The difference could be understood as the PL helicity measures the hole spin relaxation only indirectly, using the 50 ps PL lifetime as a parameter.[12] Our studies show that SE relaxes much faster. This could originate from the differences in substrates. Nevertheless, our results also show that many-body correlations dominate the ultrafast processes in this system, and biexciton formation reveals the valley/spin relaxation time.

In conclusion, control of valley polarization in semiconductors and investigation of valley specific processes is an active field, and 2D semiconductors, specifically single-layer MoS_2 and similar transition metal dichalcogenides, are emerging materials for such applications as they enable valley population control via circularly polarized light. These systems also exhibit strong many-body interactions due to reduced dielectric screening of Coulomb interactions. The effect of these Coulomb effects in valley dynamics was ambiguous. In this work we present the direct measurements of valley relaxation dynamics for the first time by polarization resolved transient absorption spectroscopy. The significance of the many-body dynamics is evident in mediating valley relaxation processes in these materials. We observed that coupling to intervalley dark excitonic states facilitates electron valley relaxation. Furthermore hole valley relaxation is measured through loss of polarization anisotropy in the exciton–biexciton transitions. Our results clearly show that Coulomb effects needs to be taken into account in designing optoelectronic applications based on 2D materials based on transition metal dichalcogenides.

Methods. *Optical Experiments.* All time-resolved measurements are performed at 74 K. In the pump probe experiments we used the output of an optical parametric amplifier to excite the sample. Pump pulses are 60 fs and centered at 660 nm. They have energy of 3 nJ per pulse. The spot size at the sample is 200 μm. White light continuum pulses, generated by focusing amplified 800 nm laser pulses on a 2 mm sapphire window, measure the resulting dynamics. The chirp in the white light continuum limits the time resolution of the experiment. We measured the chirp with a cross-correlation experiment. Between 1.9 and 2.32 eV the white light pulses have a 200 fs temporal duration. A CCD/spectrometer combination detects the transmitting probe pulses. To avoid scattered pulses and to reduce shot-to-shot noise, we used full phase cycling using a Dazzler pulse shaper. The CCD is triggered to detect every pulse at the 1 kHz repetition rate of the laser.

The absorption spectrum is measured using a Varian 50 UV/vis spectrometer.

Sample Preparation. The synthesis of monolayer and bilayer MoS_2 films is done by following a unique chemical vapor deposition process that we have recently developed. Briefly, we used $MoCl_5$ (1–25 mg) and sulfur (~1 g) as precursor materials and performed the synthesis in a tube furnace with flowing Ar gas (50 sccm). Key experimental parameters include high temperature (>800 °C) and low pressure (2–3 Torr). The precursor materials were separately placed at upstream in the tube and subjected to sublimation at elevated temperatures. The vapor of the precursor materials reacted to produce gaseous MoS_2, which subsequently precipitated onto receiving substrates downstream in the tube to yield MoS_2 films. The amount of $MoCl_5$ used in experiments determines the number of layers in a MoS_2 thin film. Our thorough characterizations with atomic force microscopy (AFM), Raman, and photoluminescence have demonstrated that the synthesized film shows remarkable uniformity over an area in the scale of centimeters[24] (Supporting Information SI3).

■ ASSOCIATED CONTENT

Ⓢ Supporting Information

Time-resolved absorption spectra for various delays between 0 and 20 ps; biexciton binding energy calculation; AFM, PL, and Raman spectroscopy measurements on single layer and bilayer samples. This material is available free of charge via the Internet at http://pubs.acs.org.

■ AUTHOR INFORMATION

Corresponding Authors

*E-mail: kenan_gundogdu@ncsu.edu.
*E-mail: lcao2@ncsu.edu.

Notes

The authors declare no competing financial interest.

■ ACKNOWLEDGMENTS

L.C. acknowledges the support of a Young Investigator Award from the Army Research Office (W911NF-13-1-0201). K.W.K acknowledges the support from the Army Research Office and SRC/NRI SWAN.

■ REFERENCES

(1) Cao, T.; Wang, G.; Han, W.; Ye, H.; Zhu, C.; Shi, J.; Niu, Q.; Tan, P.; Wang, E.; Liu, B.; Feng, J. Valley-selective circular dichroism of monolayer molybdenum disulphide. *Nat. Commun.* **2012**, *3*, 887.
(2) Zeng, H.; Dai, J.; Yao, W.; Xiao, D.; Cui, X. Valley polarization in MoS_2 monolayers by optical pumping. *Nat. Nanotechnol.* **2012**, *7*, 490–493.
(3) Mak, K. F.; He, K.; Shan, J.; Heinz, T. F. Control of valley polarization in monolayer MoS_2 by optical helicity. *Nat. Nanotechnol.* **2012**, *7*, 494–498.
(4) Xiao, D.; Liu, G. B.; Feng, W.; Xu, X.; Yao, W. Coupled spin and valley physics in monolayers of MoS_2 and other group-VI dichalcogenides. *Phys. Rev. Lett.* **2012**, *108*, 196802.
(5) Rycerz, A.; Tworzydlo, J.; Beenakker, C. W. J. Valley filter and valley valve in graphene. *Nat. Phys.* **2007**, *3*, 172–175.
(6) Xiao, D.; Yao, W.; Niu, Q. Valley-contrasting physics in graphene: magnetic moment and topological transport. *Phys. Rev. Lett.* **2007**, *99*, 236809.
(7) Zhu, Z.; Collaudin, A.; Fauque, B.; Kang, W.; Behnia, K. Field-induced polarization of Dirac valleys in bismuth. *Nat. Phys.* **2012**, *8*, 89–94.
(8) Yao, W.; Xiao, D.; Niu, Q. Valley-dependent optoelectronics from inversion symmetry breaking. *Phys. Rev. B* **2008**, *77*, 235406.

(9) Cheiwchanchamnangij, T.; Lambrecht, W. R. L. Quasiparticle band structure calculation of monolayer, bilayer, and bulk MoS_2. *Phys. Rev. B* **2012**, *85*, 205302.
(10) Splendiani, A.; Sun, L.; Zhang, Y.; Li, T.; Kim, J.; Chim, C.-Y.; Galli, G.; Wang, F. Emerging photoluminescence in monolayer MoS_2. *Nano Lett.* **2010**, *10*, 1271−75.
(11) Zhu, Z. Y.; Cheng, Y. C.; Schwingenschlogl, U. Giant spin-orbit-induced spin splitting in two-dimensional transition-metal dichalcogenide semiconductors. *Phys. Rev. B* **2011**, *84*, 153402.
(12) Korn, T.; Heydrich, S.; Hirmer, M.; Schmutzler, J.; Schuller, C. Low-temperature photocarrier dynamics in monolayer MoS_2. *Appl. Phys. Lett.* **2011**, *99*, 102109.
(13) Wang, R.; Ruzicka, B. A.; Kumar, N.; Bellus, M. Z.; Chiu, H.-Y.; Zhao, H. Ultrafast and spatially resolved studies of charge carriers in atomically thin molybdenum disulfide. *Phys. Rev. B* **2012**, *86*, 045406.
(14) Shi, H.; Yan, R.; Bertolazzi, S.; Brivio, J.; Gao, B.; Kis, A.; Jena, D.; Xing, H. G.; Huang, L. Exciton dynamics in suspended mono layer and few-layer MoS_2 2D crystals. *ACS Nano* **2013**, *7*, 1072−1080.
(15) Sim, S.; Park, J.; Song, J.-G.; In, C.; Lee, Y.-S.; Kim, H.; Choi, H. Exciton dynamics in atomically thin MoS_2: Interexcitonic interaction and broadening kinetics. *Phys. Rev. B* **2013**, *88*, 075434.
(16) Mak, K. F.; Lee, C.; Hone, J.; Shan, J.; Heinz, T. F. Atomically thin MoS_2: A new direct-gap semiconductor. *Phys. Rev. Lett.* **2010**, *105*, 136805.
(17) Schuller, J. A.; Karaveli, S.; Schiros, T.; He, K.; Yang, S.; Kymissis, I.; Shan, J.; Zia, R. Orientation of luminescent excitons in layered nanomaterials. *Nat. Nanotechnol.* **2013**, *8*, 271−276.
(18) Jones, A. M.; Yu, H.; Ghimire, N. J.; Wu, S.; Aivazian, G.; Ross, J. S.; Zhao, B.; Yan, J.; Mandrus, D. G.; Xiao, D.; Yao, W.; Xiaodong, X. Optical generation of excitonic valley coherence in monolayer WSe_2. *Nat. Nanotechnol.* **2013**, *8*, 634−638.
(19) Bir, G. L.; Pikus, G. E. *Symmetry and Strain-induced Effects in Semiconductors*; Wiley Press: New York, 1974.
(20) Li, T. Q.; Patz, A.; Mouchliadis, L.; Yan, J.; Lograsso, T. A.; Perakis, I. E.; Wang, J. Femtosecond switching of magnetism via strongly correlated spin-charge quantum excitations. *Nature* **2013**, *496*, 69.
(21) Ostojic, G. N.; Zaric, S.; Kono, J. Stability of high-density one-dimensional excitons in carbon nanotubes under high laser excitation. *Phys. Rev. Lett.* **2005**, *94*, 097401.
(22) Mak, K. F.; He, K.; Lee, C.; Lee, G. H.; Hone, J.; Heinz, T. F.; Shan, J. Tightly bound trions in monolayer MoS_2. *Nat. Mater.* **2013**, *12*, 207−211.
(23) Kadantsev, E.; Hawrylakb, P. Electronic structure of a single MoS_2 monolayer. *Solid State Commun.* **2012**, *152*, 909.
(24) Yu, Y.; Li, C.; Su, L.; Zhang, Y.; Cao, L. Controlled Scalable Synthesis of Uniform, High-Quality Monolayer and Few-layer MoS_2 Films. *Sci. Rep.* **2013**, *3*, 1866.

SCIENTIFIC REPORTS

OPEN

Exciton-dominated Dielectric Function of Atomically Thin MoS_2 Films

Received: 08 July 2015
Accepted: 22 October 2015
Published: 24 November 2015

Yiling Yu[2], Yifei Yu[1], Yongqing Cai[3], Wei Li[4], Alper Gurarslan[1,5], Hartwin Peelaers[6], David E. Aspnes[2], Chris G. Van de Walle[6], Nhan V. Nguyen[4], Yong-Wei Zhang[3] & Linyou Cao[1,2]

We systematically measure the dielectric function of atomically thin MoS_2 films with different layer numbers and demonstrate that excitonic effects play a dominant role in the dielectric function when the films are less than 5–7 layers thick. The dielectric function shows an anomalous dependence on the layer number. It decreases with the layer number increasing when the films are less than 5–7 layers thick but turns to increase with the layer number for thicker films. We show that this is because the excitonic effect is very strong in the thin MoS_2 films and its contribution to the dielectric function may dominate over the contribution of the band structure. We also extract the value of layer-dependent exciton binding energy and Bohr radius in the films by fitting the experimental results with an intuitive model. The dominance of excitonic effects is in stark contrast with what reported at conventional materials whose dielectric functions are usually dictated by band structures. The knowledge of the dielectric function may enable capabilities to engineer the light-matter interactions of atomically thin MoS_2 films for the development of novel photonic devices, such as metamaterials, waveguides, light absorbers, and light emitters.

Two-dimensional (2D) transition metal dichalcogenide (TMDC) materials have been known exhibiting strong exciton binding energy that may be one order of magnitude larger than conventional semiconductor materials[1–6]. However, how the extraordinarily strong exciton binding energy could affect the light-matter interactions such as dielectric functions of the materials has remained unexplored. The lack of knowledge about the dielectric function has significantly limited the application of 2D TMDC materials in many exciting photonic fields such as metamaterials[7], which relies on the sophisticated manipulation of effective dielectric functions to enable novel optical functionalities. In this work we have measured the dielectric function of atomically thin MoS_2 films and discovered that it is dominated by the effect of the tightly bound excitons, as evidenced by an anomalous dependence of the dielectric function on the layer number. The dielectric function decreases with the layer number increasing when the MoS_2 films are less than 5 layers thick, but turn to increase with the layer number for thicker. We also quantitatively evaluate the exciton binding energy and Bohr radius of the thin films by fitting the experimental results with an intuitive model. The observed dominance of excitonic effects in the dielectric function is in stark contrast with what expected at conventional materials, whose dielectric functions are usually dictated by band structures[8,9]. Our success in this discovery is built upon a unique self-limiting chemical vapor deposition (CVD) process that we have recently developed[10]. The self-limiting CVD process can

[1]Department of Materials Science and Engineering, North Carolina State University, Raleigh, NC 27695, USA. [2]Department of Physics, North Carolina State University, Raleigh, NC 27695, USA. [3]Institute of High Performance Computing, A*STAR, Singapore 138632. [4]Semiconductor and Dimensional Metrology Division, National Institute of Standards and Technology, Gaithersburg, Maryland 20899, USA. [5]Department of Fiber and Polymer Science, North Carolina State University, Raleigh, NC 27695, USA. [6]Materials Department, University of California, Santa Barbara, CA 93106, USA. Correspondence and requests for materials should be addressed to L.C. (email: lcao2@ncsu.edu)

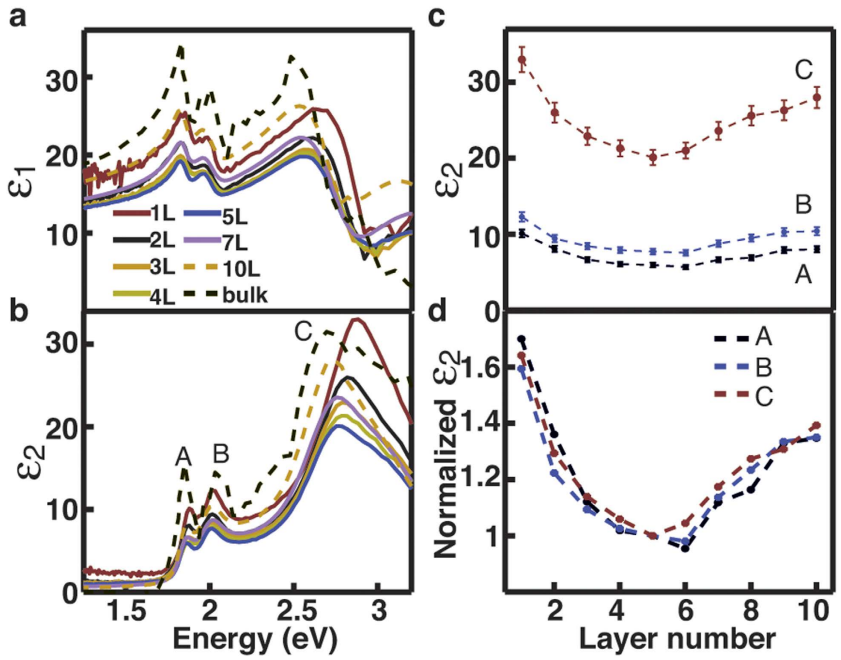


Figure 1. Anomalous layer-dependence of the dielectric function of 2D MoS_2. (**a**,**b**) Real and imaginary parts of the dielectric function of 2D MoS_2 vs. layer number. Also given is the dielectric function of bulk MoS_2. The three peaks can be assigned to *A*, *B*, and *C* excitons as labeled. Corresponding refractive indexes of the films are given in Fig. S6 and Table S1 of the Supplementary Information. (**c**) The dependence of the imaginary part ε_2 of the dielectric function at the *A*, *B*, and *C* peaks on layer number. The error bar is 5% and estimated from the measurement results of multiple samples. (**d**) Normalized ε_2 at the *A*, *B*, and *C* peaks vs. layer number. The normalization is performed with respect to the corresponding value of each peak in the 5-layer MoS_2. Error bar is ignored for visual convenience.

be used to grow centimeter-scale, uniform, and high quality atomically thin MoS_2 films with controlled layer numbers and remarkable uniformity (Figs S1–S5). This allows us to examine the dielectric function of MoS_2 films as a function of well-defined layer numbers. Our work is different from earlier research for the dielectric function of MoS_2 films[11,12], whose results are likely inaccurate due to the lack of satisfactory uniformity or precise control of the layer number.

We measured the dielectric function ($\varepsilon_1 + i\varepsilon_2$) of as-grown MoS_2 films on sapphire substrates using spectroscopic ellipsometry[13]. Figure 1a,b shows the real ε_1 and imaginary ε_2 parts of the dielectric function in the visible range that are derived from experimental measurements (see Figs S7,S8 for the fit between experimental and simulated results). Owing to the extreme geometrical anisotropy of the film, what we obtained is actually the in-plane component of the dielectric tensor because the out-of-plane dielectric function may only contribute trivially to the optical response due to the difficulty in exciting the vertical dipole of the atomically thin film[13]. As further evidence for the measured in-plane dielectric function, we performed the spectroscopic ellipsometry at different incident angles (40°–75°), and all of them ended up with giving very similar dielectric functions. The dielectric function of bulk MoS_2 is also measured and plotted in Fig. 1a,b as a reference, the result of which is consistent with what reported previously[14]. The three peaks in the spectral dielectric function can be assigned to *A*, *B*, and *C* from low to high energies, respectively[15–18]. The *A* and *B* peaks are related with the transition from the spin-orbit split valence bands to the lowest conduction band at the *K* and *K'* points, while the *C* peak is associated with the transition from the valence band to the conduction band at the part of the Brillouin zone between the Λ and Γ point[16,17].

The measured dielectric function is not sensitive to the synthetic process or the substrate. The dielectric functions measured from the MoS_2 grown by using $MoCl_5$ and S as the precursors[10] and by using MoO_3 and S as the precursors[19] are essentially identical (Fig. S9a). We also find that the dielectric functions of the as-grown MoS_2 films on sapphire substrates and those transferred onto SiO_2/Si substrates are identical (Fig. S9b). Additionally, the dielectric function of the film is stable under ambient environment. We monitored the dielectric function of the as-grown MoS_2 films on sapphire substrates as a function of the time for the films to be exposed to ambient environment. We monitored the dielectric function of the films exposed to ambient environment for more than one week and found no change in the measured result (Fig. S10). The result we measured for the monolayer MoS_2 film is consistent with what previously measured using spectroscopic ellipsometry[20] but is 10–15% less than the results derived from absorption spectra[21]. We do like to point out some difference in the spectroscopic ellipsometry used by us as well as

ref. 20 and the spectroscopic absorption technique used in ref. 21. Spectroscopic ellipsometry is the most established technique for the measurement of dielectric functions, in which two parameters are measured at each wavelength and the dielectric function can be uniquely determined in any spectrum range with the thickness information of the film indepedently determined by AFM. The dielectric function may be derived from spectroscopic reflection using the Kramer-Kronig relationship as well. But to precisely find out the dielectric function using the Kramer-Kronig relationship requires information of the absorption in the entire spectral range. In ref. 21 the absorption of the monolayer in the range higher than 3 eV, whose value is not experimentally available, is assumed to be equal to that of the bulk counterpart. This assumption might overestimate the dielectric function to some degree. We believe this is likely the reason why our result is around 10–15% less than the result reported in ref. 21.

Significantly, the measured dielectric function shows an anomalous dependence on the layer number (Fig. 1a,b). It decreases with the layer number increasing when the film is less than 5–7 layers thick and then turns to increase with the layer for thicker films. We were very careful to ensure no artifact introduced in the measurement. More specifically, we performed extensive AFM for each of the films studied prior to the ellipsometry measurement and confirmed the atomic-scale smoothness (roughness usually < 0.5 nm except the 8L, 9L and 10L films, whose roughness is a little bit larger in the range of 0.7–0.9 nm, see Figs S1–S5) and excellent uniformity of the film. Additionally, for the result of each layer number, we measured at least three different sets of samples and observed only minor variation (5%) in the resulting dielectric function. To further illustrate this anomalous layer-dependence, we extract the imaginary part of the dielectric functions at the *A*, *B*, and *C* peaks from Fig. 1b and plot it as a function of the layer number (Fig. 1c). The result clearly shows a decrease and then an increase in the dielectric function with the layer number continuously increasing from one. The layer dependence is similar for all the *A*, *B*, and *C* peaks (Fig. 1d). Given the similarity in the layer dependence, we only focus on the *C* peak in the following discussion.

To obtain physical insights into the observed layer dependence, we examine the dielectric function from the perspective of quantum mechanics. We only focus on the imaginary part ε_2 because the real part ε_1 can be deterministically correlated to ε_2 by the well-established Kramer-Kronig equation[22]. Fundamentally, ε_2 is related with interband transitions as[8,22,23]

$$\varepsilon_2(\omega) = \frac{4\pi^2 e^2}{m_0^2 \omega^2} J_{cv} |p_{cv}|^2 |U(0)|^2 \frac{\Gamma/2}{(E_{cv} - \hbar\omega)^2 + (\Gamma/2)^2} \quad (1)$$

where ω is the frequency, $\hbar$ is the Planck's constant, e and m_0 are the charge and mass of free electrons, J_{cv} is the joint density of the initial (valence band) and final (conduction band) states involved in the transition. p_{cv} is an optical matrix element indicating the probability of the transition from the initial to final states. It consists of an integral over a unit cell that involves the momentum operator as well as the unit cell wavefunctions in the conduction and valence bands. $|U(0)|^2$ represents the effect of excitons on the oscillator strength of the interband transition, where U is the relative motion wavefunction of the eletrons and holes bound by Coulomb interactions and 0 indicates the physical overlap of the electron and hole wavefunctions. E_{cv} is the optical energy gap between the conduction and valence bands involved and Γ is a damping constant determining the bandwidth of the interband transition.

For simplicity, we only focus on the dielectric function at the peak position (on-resonance) as shown in Fig. 1c,d, where $E_{cv} - \hbar\omega = 0$ and eq.(1) can be simplified as

$$\varepsilon_2(\omega) = \frac{4\pi^2 e^2}{m_0^2 \omega^2} J_{cv} |p_{cv}|^2 |U(0)|^2 \frac{2}{\Gamma} \quad (2)$$

Physically, Γ represents the width of the peak. From Fig. 1b the peak can be found phenomenally remaining to be similar in the films with different layer numbers. Therefore, it is reasonable to consider that Γ is independent of the layer number. The optical matrix element p_{cv} is also independent of the layer number because it is only related with unit cells and unit cell wavefunctions, both of which are not dependent on the layer number. The independence of p_{cv} on geometrical features has previously been demonstrated at quantum wells[24]. Therefore, eq. (2) can be further simplified as

$$\varepsilon_2(\omega) = A_0 J_{cv} |U(0)|^2 \quad (3)$$

where A_0 includes all the terms independent of the layer number. Eq. (3) indicates that the layer dependence of the dielectric function may result from only two parameters: the joint density of states J_{cv} and the excitonic effect $|U(0)|^2$.

We can get more insight by further examining the specific layer dependence of the two parameters J_{cv} and $|U(0)|^2$. The joint density of states J_{cv} is determined by the band structure and expected to monotonically increase with the layer number. This is because the density of states in 2D materials is well known to be smaller than that in 3D materials[8,22] and the increase of the layer number in effect enables a continuous evolution from two dimensions (monolayers) to three dimensions (bulk). To quantitatively elucidate the layer dependence of J_{cv}, we calculate the ε_2 of MoS_2 films using density functional theory

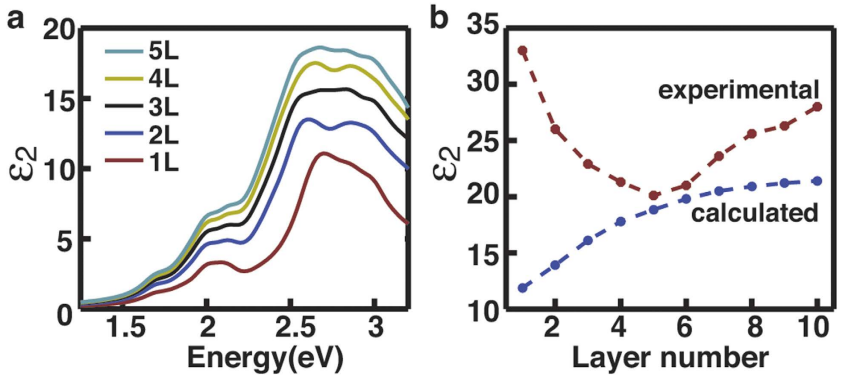


Figure 2. Comparison of the measured and calculated dielectric function of 2D MoS_2. (**a**) Calculated imaginary part ε_2 of the dielectric function of MoS_2 with different thickness. (**b**) Comparison of experimental and calculated results for ε_2 at the *C* peak as a function of the layer number. The error bar in the experimental result is ignored for visual convenience.

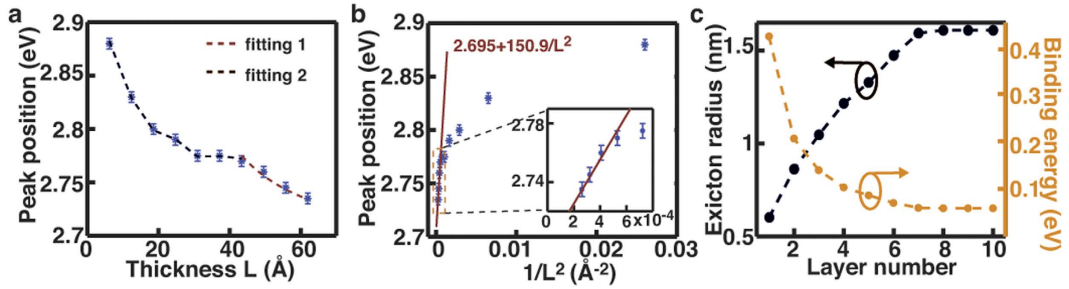


Figure 3. Strong, layer-dependent excitonic effects in atomically thin MoS_2 films. (**a**) The position of the *C* peak in MoS_2 films as a function of the thickness of the film *L*. The error bar ± 0.005 eV results from the possible errors in determining the peak position. The dashed lines are the fitting results using the model of infinite quantum wells (fitting 1) and the quantum well in fraction space (fitting 2) (**b**) The position of the *C* peak in MoS_2 films as a function of $1/L^2$, where *L* is the thickness of the film. The red line is the fitting results using the model of infinite quantum well with the fitting equation given as shown. The inset is a magnified version of the area indicated by the dashed yellow rectangle. (**c**) The dependence of the binding energy and exciton radius in MoS_2 films on the layer number.

(DFT) techniques without considering excitonic effects[18]. The calculation result is given in Fig. 2a and essentially represents the density of states J_{cv}. It reproduces the major spectral features of the experimental results and indeed shows a monotonic increase with the layer number. For the convenience of comparison, we plot the calculated and measured dielectric functions at the *C* peak as a function of the layer number in Fig. 2b. The calculated results are understandably smaller than the experimental results due to the exclusion of excitonic effects. Of our interest is to compare the layer dependence in the calculated and experimental results. The similarity of the two results for the films >5L suggests that the observed layer-dependent increase in the dielectric function in the relatively thicker films may be correlated to the effect of the density of states J_{cv}. However, for the films less than 5 layers thick the calculated layer-dependence is opposite to the experimental observation (Fig. 2b). This can be correlated to the other parameter not considered in the calculation, the excitonic effect $|U(0)|^2$. The excitonic effect is expected to be strong and to quickly decrease with the layer number due to the well known layer-dependent exponential decrease of exciton binding energy[15].

The layer-dependent excitonic effect can be understood more quantitatively by examining the excitonic peak position with an intuitive model that involves quantum confinement and exciton binding energy. Of our interest is to quantitatively evaluate the layer dependence of the exciton binding energy from the observed evolution of the *C* exciton peak position with the layer number (Fig. 3a). The excitonic peak position (i.e. optical bandgap) is equal to the electronic bandgap minus the exciton binding energy, and its layer dependence originates from the layer dependence of both components. Should the layer dependence of the electronic bandgap be found out, we would be able to figure out the layer dependence of the exciton binding energy from the measured excitonic peak position. It is actually very difficult to experimentally or theoretically evaluate the electronic bandgap of MoS_2 with different layer

numbers. However, we find out that the layer dependence of the electronic bandgap may be reasonably correlated to quantum confinement effects. The peak position of the *C* exciton E_C in the films thicker than 7 layers shows a linear dependence on $1/L^2$ (Fig. 3b), and can be fitted by the conventional model of infinite quantum wells as $E_C = E_g + R_y + \pi^2\hbar^2/2m_{eff}L^2 - R_y$, where E_g is the position (optical bandgap) of the *C* peak in bulk MoS_2 materials ($E_g = 2.695$ eV as measured in Fig. 1b), R_y is the exciton binding energy and assumed not changing with the thickness in the model of infinite quantum wells, and m_{eff} is the reduced electron-hole effective mass of the film. The introduction of R_y in the equation is to illustrate that the optical bandgap is equal to the electronic bandgap (the first three terms) minus the exciton binding energy (the last term). The fitting to the experimental results (the red lines in Fig. 3a,b) gives $E_C = 2.695\,\text{eV} + 150.9/L^2$, from which we can derive the reduced effective mass $m_{eff} = 0.250\ m_0$ for the *C* extions in bulk MoS_2 and the films thicker than 7 layers. We can also derive the exciton binding energy $R_y = 58.9$ meV and Bohr radius $a_b = 1.61$ nm in bulk MoS_2 and thick films, in which the static dielectric constant is set to be 7.6 as measured for bulk MoS_2 previously[25].

The peak position E_C in the films thinner than 5–7 layers shows apparent deviation from the model of infinite quantum wells (Fig. 3b). Instead, we can fit the experimental results with a model of quantum wells in fractional dimensional space as[26,27]

$$E_C = E_g + R_y + \frac{\pi^2\hbar^2}{2m_{eff}L^2}[(D-1)/2]^2 - \frac{R_y}{[(D-1)/2]^2} \quad (4)$$

where *D* is the effective dimensionality that is defined by the ratio of the exciton binding energy R_y^* in the films and that of bulk MoS_2 R_y as $[(D-1)/2]^2 = R_y/R_y^*$. Again, the first three terms of eq. (4) represent the electronic bandgap and the last term indicates the exciton binding energy. The factor of $[(D-1)/2]^2$ in the third term originates from the change in the effective mass associated with the effective dimensionality. For the films thicker than 7 layers, *D* is 3 and eq. (4) is then reduced to the equation for infinite quantum wells. By fitting the experimental results with eq. (4), we can have the effective dimensionality *D* as 1.75, 2.07, 2.30, 2.51, 2.65, and 2.83 for the films in layer number of 1, 2, 3, 4, 5, and 6, respectively. We can then derive the corresponding exciton binding energies using $R_y^* = R_y/[(D-1)/2]^2$ as 0.421 eV, 0.206 eV, 0.139 eV, 0.103 eV, 0.0865 eV, and 0.0704 eV; we can also derive the corresponding Bohr radius of excitons from $a_b^* = a_b(D-1)/2$[26,27] as 0.602 nm, 0.861 nm, 1.04 nm,1.22 nm,1.33 nm, and 1.47 nm, respectively. These results are plotted in Fig. 3c.

The model we used to fit the experimental result is based on an assumption that the layer dependence of the electronic bandgap can be ascribed to the effect of quantum confinement. This is supported by our experimental results, in particular, the consistence between the observed peak position of the films thicker than 7 layers and what predicted from the model of infinite quantum wells. However, more theoretical and experimental studies would be necessary to provide more rigorous support, which is to our best knowledge expected to very difficult. Nevertheless, the result we obtained by fitting the experimental results using this model seems to be reasonable when compared to the limited number of studies on the exciton binding eerngy and Bohr radisu available in the literature. There is not study that would allow us to systematically crosscheck all of our results. For instance, the binding energy $R_y = 58.9$ meV and Bohr radius $a_b = 1.61$ we derived for the *C* exciton in bulk MoS_2 and thick films is reasonably consistent with the binding energy and Bohr radius reported for the *A* exciton in bulk MoS_2, which are 87.2 meV and 1.11 nm, respectively[28]. Additionally, the Bohr radius (0.602 nm) we derived for the *C* exciton in monolayer MoS_2 nicely matches the theoretical prediction, ~0.5 nm[17]. The derived binding energy (0.421 eV) is reasonable compared with what reported for the *A* exciton, which is believed to be 0.4–0.6 eV in monolayer MoS_2[18,29].

With the information of the exciton binding energy and radius, the observed layer dependence of the dielectric function can be intuitively understood from a perspective of geometric confinement. Figure 4 shows the comparison between the size of excitons and the thickness of the film. While the film is highly anisotropic, the size of the exciton is schematically illustrated by the diameter of a sphere anyway. This is because eq. (4), which we used to derive the exciton radius, treats the excitons as spheres in an isotropic space by converting the geometrical anisotropy into fractional dimensionality[26,27]. The size of the exciton in bulk MoS_2, 3.22 nm, is close to the thickness of the 5L film, 3.10 nm (Fig. 4a). Therefore, the exciton in MoS_2 films is expected to start experiencing substantial geometrical confinement when the layer number of the film is decreased to 5, which may lead to decrease in the exciton size. Intuitively, a smaller exciton radius can better facilitate the spatial overlap of the electron and hole wavefunctions and subsequently cause larger amplitude in $|U(0)|^2$. The layer-dependent decrease of the dielectric function is expected when the layer-dependent decrease of the excitonic effect offsets or even exceeds the layer-dependent increase of the join density of states.

The main conclusion we draw from the analysis of the *C* exciton, i.e. the dominance of excitonic effects in the dielectric function, can be applied to the *A* and *B* excitons as well due to the similar layer dependence in corresponding dielectric functions (Fig. 1c,d). However, it is difficult to quantitatively extract the binding energy and Bohr radius for the *A* and *B* excitons as what we did for the *C* exciton. This is because that the positions of the *A* and *B* excitons do not show substantial layer dependence as what observed as the *C* exciton, which makes the fitting by the intuitive model difficult. One reason for

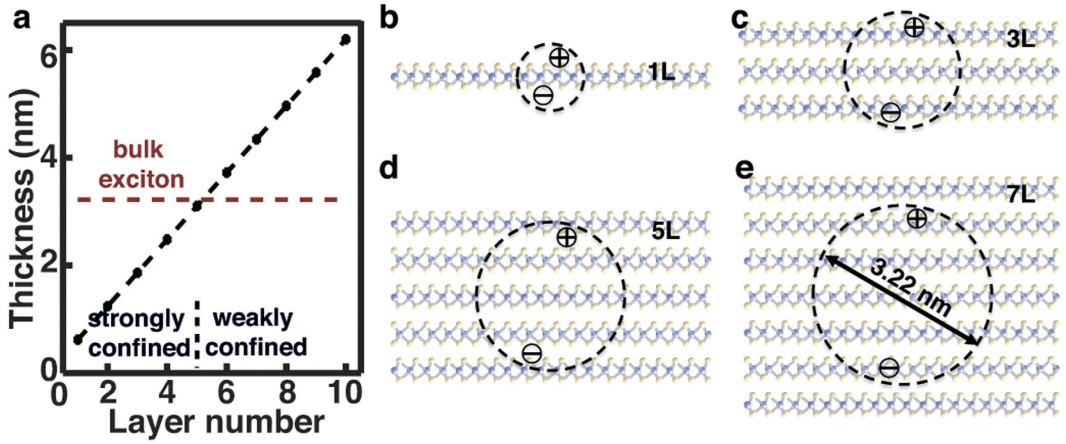


Figure 4. Geometric confinement of excitons in MoS_2 films. (**a**) Comparison of the size of the exciton in bulk MoS_2 with the thickness of MoS_2 films. The regime where the film is thinner than the exciton size is categorized as strong confinement. (**b–e**) Schematic illustration of the size of excitons in the films with different layer numbers.

the less layer dependence observed at the *A* and *B* excitons could be related with the random variation of the position of the *A* and *B* excitons due to local doping effect from the substrate, which may be as large as ~10 meV[30]. Another reason could be related with the better localization of the A and B excitons in the plane of the film, which may lead to a less dependence on interlayer interactions[31].

While our work mainly focuses on MoS_2, we believe that similar dominance of excitonic effects in the dielectric function could generally exist in all the atomically thin semiconducting TMDC materials. Our result bears significant implications for the development of photonics devices with 2D TMDC materials. The obtained dielectric function and refractive index (Table S1) for the MoS_2 with different layer numbers can be immediately useful for the rational design of photonic devices. In particular, as excitons are subject to influence of electric or magnetic fields, the dominance of excitonic effects in the dielectric function makes atomically MoS_2 films an unprecedented platform that may enable the development of field-effect photonics, whose optical functionalities would be tuned by external electric or magnetic fields.

References

1. Cao, L. Y. Two-dimensional transition-metal dichalcogenide materials: Toward an age of atomic-scale photonics. *MRS Bull* **40,** 592–599 (2015).
2. Mak, K. F. *et al.* Tightly bound trions in monolayer MoS2. *Nat Mater* **12,** 207–211 (2013).
3. Mak, K. F., Lee, C., Hone, J., Shan, J. & Heinz, T. F. Atomically Thin MoS2: A New Direct-Gap Semiconductor. *Phys Rev Lett* **105** (2010).
4. Splendiani, A. *et al.* Emerging Photoluminescence in Monolayer MoS2. *Nano Lett* **10,** 1271–1275 (2010).
5. Wang, Q. H., Kalantar-Zadeh, K., Kis, A., Coleman, J. N. & Strano, M. S. Electronics and optoelectronics of two-dimensional transition metal dichalcogenides. *Nat. Nanotech.* **7,** 699–712 (2012).
6. Xu, X., Yao, W., Xiao, D. & Heinz, T. F. Spin and Pseudospins in Layered Transition Metal Dichalcogenides. *Nature Physics* **10,** 343–350 (2014).
7. Smith, D. R., Pendry, J. B. & Wiltshire, M. C. K. Metamaterials and negative refractive index. *Science* **305,** 788–792 (2004).
8. Miller, D. A. B. *Quantum Mechanics for Scientists and Engineer.* (Cambridge University Press, New York, NY; 2008).
9. Palik, E. D. *Handbook of Optical Constants of Solids.* (Acadmic Press, London, 1985).
10. Yu, Y. F. *et al.* Controlled Scalable Synthesis of Uniform, High-Quality Monolayer and Few-layer MoS2 Films. *Sci. Rep.* **3,** 1866 (2013).
11. Yim, C. *et al.* Investigation of the optical properties of MoS2 thin films using spectroscopic ellipsometry. *Appl. Phys. Lett.* **104,** 103114 (2014).
12. Liu, H.-L. *et al.* Optical properties of monolayer transition metal dichalcogenides probed by spectroscopic ellipsometry. *Appl. Phys. Lett.* **105,** 201905 (2014).
13. Tompkins, H. G. & Irene, E. A. *Handbook of Ellipsometry.* (William Andrew, Norwich, NY, 2005).
14. Beal, A. R. & Hughes, H. P. Kramers-Kronig Analysis of the Reflectivity Spectra of 2h-Mos2, 2h-Mose2 and 2h-Mote2. *J Phys C Solid State* **12,** 881–890 (1979).
15. Komsa, H.-P. & Krasheninnikov, A. V. Effects of confinement and environment on the electronic structure and exciton binding energy of MoS2 from first principles. *Phys. Rev. B* **86,** 241201 (2012).
16. Kozawa, D. *et al.* Photocarrier relaxation pathway in two-dimensional semiconducting transition metal dichalcogenides. *Sci. Rep.* **5,** 4543 (2014).
17. Qiu, D. Y., Jornada, F. H. D. & Louie, S. G. Optical Spectrum of MoS2: Many-Body Effects and Diversity of Exciton States. *Phys. Rev. Lett.* **111,** 216805 (2013).
18. Shi, H. L., Pan, H., Zhang, Y. W. & Yakobson, B. I. Quasiparticle band structures and optical properties of strained monolayer MoS2 and WS2. *Phys. Rev. B* **87,** 155304 (2013).
19. Lee, Y. H. *et al.* Synthesis of Large-Area MoS2 Atomic Layers with Chemical Vapor Deposition. *Adv Mater* **24,** 2320–2325 (2012).
20. Li, W. *et al.* Broad Band Optical Properties of Large Area Monolayer CVD Molybdenum Disulfide. *Phys. Rev. B* **90,** 195434 (2014).

21. Li, Y. *et al.* Measurement of the optical dielectric function of monolayer transition-metal dichalcogenides: MoS2, MoSe2, WS2, and WSe2. *Phys. Rev. B* **90,** 205422 (2014).
22. Chuang, S. L. *Physics of Photonic Devices*. (John Wiley & Sons, New York, NY, 1995).
23. Miller, D. A. B., Weiner, J. S. & Chemla, D. S. Electric-Field Dependence of Linear Optical-Properties in Quantum-Well Structures - Wave-Guide Electroabsorption and Sum-Rules. *Ieee J Quantum Elect* **22,** 1816–1830 (1986).
24. Weisbuch, C. & Vinter, B. *Quantum Semiconductor Structures: Fundamentals and Applications* (Academic Press, San Diego, 1991).
25. Evans, B. L. & Young, P. A. Optical absorption and dispersion in molybdenum disulphide. *Proc. R. Soc. Lond. A* **284,** 402–422 (1965).
26. He, X. F. Fractional dimensionality and fractional derivative spectra of interband optical transitions. *Phys. Rev. B* **42,** 11751–11756 (1990).
27. He, X. F. Excitons in anisotropic solids: The model of fractional-dimensional space. *Phys. Rev. B* **43,** 2063–2069 (1991).
28. Fortin, E. & Raga, F. Excitons in molybdenum disulphifle. *Phys. Rev. B* **11,** 905–912 (1965).
29. Klots, A. R. *et al.* Probing excitonic states in suspended two-dimensional semiconductors by photocurrent spectroscopy. *Sci. Rep.* **4,** 6608 (2014).
30. Buscema, M., Steele, G. A., Zant, H. S. J. v. d. & Castellanos-Gomez, A. The effect of the substrate on the Raman and photoluminescence emission of single layer MoS2. *Nano Res.*, doi: 10.1007/s12274-12014-10424-12270 (2014).
31. Gurarslan, A. *et al.* Surface Energy-Assisted Transfer of Centimeter-Scale Monolayer and Fewlayer MoS2 Films onto Arbitrary Substrates. *ACS Nano* **8,** 11522–11528 (2014).

Acknowledgements

This work was supported by a Young Investigator Award from the Army Research Office (W911NF-13-1-0201). Y.C. and Y.Z. gratefully acknowledge the use of computing resources at the A*STAR Computational Resource Centre, Singapore. H.P. and C.G.V.d.W. were supported by the U.S. Department of Energy, Office of Science, Basic Energy Sciences, under Award DE-FG02-07ER46434.

Author Contributions

L.Y. conceived the idea. Y.Y. performed most of the elliposometry measurements and other characterizations of the films, Y.Y. synthesized the films. A.G. performed the transfer of the film and some of the AFM measurements. W.L. and N.V.N. helped with part of the ellipsometry measurements. Y.C. and Y.Z. conducted the theoretical calculations. H.P. and C.G.V.d.W. also contributed to the theoretical calculations. L.Y., Y.Y. and D.E.A. analyzed the results. L.Y. and Y.Y. wrote the paper. All the people were involved in reviewing the paper.

Additional Information

Supplementary information accompanies this paper at http://www.nature.com/srep

Competing financial interests: The authors declare no competing financial interests.

How to cite this article: Yu, Y. *et al.* Exciton-dominated Dielectric Function of Atomically Thin MoS_2 Films. *Sci. Rep.* **5**, 16996; doi: 10.1038/srep16996 (2015).

This work is licensed under a Creative Commons Attribution 4.0 International License. The images or other third party material in this article are included in the article's Creative Commons license, unless indicated otherwise in the credit line; if the material is not included under the Creative Commons license, users will need to obtain permission from the license holder to reproduce the material. To view a copy of this license, visit http://creativecommons.org/licenses/by/4.0/

THE JOURNAL OF PHYSICAL CHEMISTRY C

Article

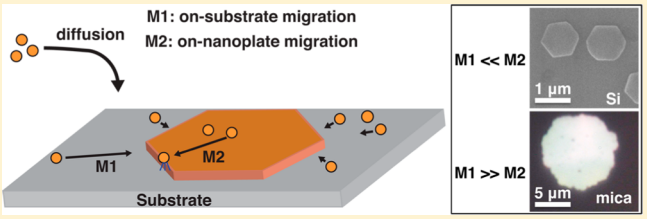
pubs.acs.org/JPCC

Substrate Mediation in Vapor Deposition Growth of Layered Chalcogenide Nanoplates: A Case Study of $SnSe_2$

Liang Huang,[†] Yifei Yu,[†] Chun Li,[†] and Linyou Cao*[,†,‡]

[†]Department of Materials Science and Engineering, and [‡]Department of Physics, North Carolina State University, Raleigh, North Carolina 27695, United States

ABSTRACT: The two-dimensional (2D) nanostructure of layered chalcogenide materials (LCMs) is very interesting, but to make it a useful material platform necessiates the development of sophisticated synthetic control. We present the synthesis of single-crystalline $SnSe_2$ nanoplates by a noncatalytic vapor deposition process and demonstrate that the growth is subject to strong influences from substrates. The effect of substrates is evidenced by a temperature-dependent morphological difference in the nanoplates grown on mica and silicon substrates. At a growth temperature of 280 °C, the diameter of the nanoplates grown on mica is larger than those grown on silicon by a ratio of 6.2. This ratio substantially decreases to be unity (1.04) at a higher temperature of 420 °C. Additionally, different from the nanoplates grown on silicon, which always show a well-defined hexagonal shape, the nanoplates grown on mica exhibit an irregular shape at low temperature and can gradually evolve into the hexagonal shape with increasing temperature. Our dynamics analysis suggests that the observed temperature-dependent morphological difference can be specifically correlated to the migration of $SnSe_2$ adatoms on the surface of substrates. $SnSe_2$ adatoms may migrate on mica more easily than on silicon substrates because of the presence of dangling bonds at the surface of silicon. The role of the facile migration on mica in the nanoplate growth may be further confirmed by a correlation between the nanoplate diameter and the distance between neighboring nanoplates. While the focus is on $SnSe_2$, we believe that this understanding can apply to the growth of two-dimensional (2D) nanostructures of other layered chalcogenide materials (LCMs). It may pave the way for the development of a general synthetic paradigm that leverages the effect of substrates to control the growth of 2D LCM nanostructures.



1. INTRODUCTION

The two-dimensional (2D) structures of layered chalcogenide materials (LCMs) are emerging as a new frontier of modern materials science. Originally inspired by the spectacular success of graphene,[1,2] interest in the 2D LCM nanostructure is poised to extend well beyond the territory of graphene. LCMs have graphite-like structures, consisting of covalently bonded layers held together by weak van der Waals forces.[3] But unlike graphite whose constituent is limited to be carbon atoms, LCMs comprise cations, which can be semiconductors (like Ge and Sn) or transition metals (such as Mo and W), and anions that can be either of −S, −Se, or −Te.[4,5] This richer variety in compositions can provide the 2D LCM nanostructure new functionality that cannot be obtained from graphene, for instance, bandgap and strong spin−orbital coupling.[6−11] Indeed, recent studies have demonstrated that 2D LCM nanostructures are promising for fields ranging from topological insulators[12] to solar energy conversion,[13] field effect transistors,[14−19] novel optoelectronic devices,[20−22] spintronics,[9−11] and energy storage.[23,24]

Developing sophisticated synthetic capabilities is important for exploring the full potential of 2D LCM nanostructures. Compared to the traditional approaches, which rely on exfoliation from bulk materials to prepare the 2D structures, synthetic techniques can provide better controllability, scalability, and reproducibility that are necessary for both fundamental and applied interest. Vapor deposition stands as a particularly appealing, versatile synthetic strategy. It has a proven track record in enabling control of the physical features of nanomaterials with atomic precision.[25−27] However, the development of controlled synthesis of 2D LCM nanostructures by vapor deposition techniques necessitates a better understanding of the fundamentals involved. While the technique of vapor deposition has been extensively studied in the growth of thin films and nanomaterials such as nanowires, nanotubes, and graphene, knowledge obtained from these materials may not simply apply to the growth of the 2D LCM nanostructure.

One key issue for the development of synthetic control of 2D LCM nanostructures lies in the effect of substrates. Vapor deposition growth constitutes of a precipitation of source material vapor at receiving substrates. Unlike typical nanomaterials such as graphene and nanowires, whose growth involves catalysts and is primarily governed by the catalyst,[25−28] the vapor deposition growth of 2D LCM nanostructures is noncatalytic.[29−32] Without the dominance of catalysts, noncatalytic vapor deposition growth is known subject to influences of the interaction between the deposited overlayer and the

Received: January 9, 2013
Revised: February 27, 2013
Published: February 28, 2013

 © 2013 American Chemical Society dx.doi.org/10.1021/jp400274a | J. Phys. Chem. C 2013, 117, 6469−6475

substrate. For instance, thin films of typical semiconductor materials such as Si can grow in a mode of either layer-by-layer or layer-plus-island depending on the interaction with the substrate.[33] However, the effect of substrates for the growth of 2D LCM nanostructures is expected substantially different from those reported for conventional thin films. The difference can be best manifested by the epitaxial growth of LCMs on substrates that are similarly two-dimensionally bonded, regardless dramatic lattice mismatch. This is referred as van der Waals epitaxy (vdWE) growth.[34] For instance, $MoSe_2$ materials may epitaxially grown on mica despite a 58% lattice mismatch .[35] In contrast, the epitaxial growth of conventional thin films requests a much smaller lattice misfit, typically <4%.[33] This is because the interaction of LCMs with two-dimensionally bonded substrates is weak van der Waals forces due to the absence of dangling bonds at the surfaces. The weak interaction may drastically relax the requirement of lattice match for epitaxial growth.

A fundamental understanding of the effect of substrates can pave the way toward leveraging the substrate as a useful channel to control the growth of 2D LCM nanostructures. For instance, it has been recently demonstrated that by controlling the wetting properties of the substrate surface can achieved patterned deposition of $SnSe_2$ materials.[36] However, much of the substrate effect on the growth of 2D LCM nanostructures has remained unknown. For example, how may the weak van der Waals interaction with the substrate affect the growth dynamics of 2D LCM nanostructures? How would the growth of 2D LCM nanostructures be different on two-dimensionally bonded (such as mica) and conventional three-dimensionally bonded substrates (such as silicon)? The growth on conventional three-dimensionally bonded substrates like silicon is more appealing, because it provides a way to directly prepare as-grown 2D LCM nanostructures for applications in integrated devices.

Here we demonstrate the synthesis of single crystalline 2D $SnSe_2$ nanoplates with a noncatalytic vapor deposition process and elucidate that the growth process is strongly mediated by substrates. This is evidenced by a temperature-dependent morphological difference in the nanoplates grown on mica and silicon substrates. At relatively low temperature, for instance, 280 °C, the nanoplates grown on mica are substantially larger than those grown on silicon, and show an irregular shape, in contrast with the nanoplates on silicon that are in well-defined hexagonal shapes. The morphological difference decreases with the growth temperature increasing. Our dynamic analysis indicates that the rate-determining step of the nanoplate synthesis is the growth reaction, and suggests that the observed temperature-dependent morphological difference can be specifically ascribed to one step involved in the growth reaction, the surface migration of $SnSe_2$ adatoms. This migration strongly depends on the temperature and the surface state of substrates. The absence of dangling bonds at the surface of mica can enable a facile migration of $SnSe_2$ adatoms. The role of the facile surface migration on mica in the nanoplate growth is further confirmed by a correlation of the nanoplate diameter with the distance between neighboring nanoplates.

2. EXPERIMENTAL SECTION

Nanoplate Synthesis. The synthesis of nanoplates was performed in a home-built CVD reactor comprised of a fused silica tube (in diameter of 1 in. and length of 24 in.) and a horizontal single-zone tube furnace (Lindberg/Blue M TF55035A). In a typical growth, a quartz boat loaded with ~25 mg of SnSe powder (99.99%, Sigma-Aldrich) was placed at the center of the tube furnace and another quartz boat loaded with ~45 mg of Se powder at the upstream entry of the furnace. Multiple nondoped Si (100) substrates (in thickness of 500 μm and lateral dimension of 4 × 10 mm) with native oxide (University Wafer) were placed 12−15 cm downstream from the center of the furnace. Prior to being placed in the tube furnace, these substrates were treated with piranha solutions, a mixture of 98% sulfuric acid and 30% hydrogen peroxide in a ratio 3:1 by volume, for 10 min. An identical number of freshly cleaved mica substrates (Pelco Mica sheets, Ted Pella) in a thickness <0.03 mm and with lateral dimension similar to the silicon substrates were placed side by side along with the silicon substrates. Typical experimental conditions for the nanoplate growth include 550 °C at the center, ~350 °C at the Se powder, 10−30 sccm of carrier gas flow (Ar gas), and 20−40 Torr in total pressure. The local deposition temperatures of the substrates are in a range of 280−420 °C depending on the specific position of the substrate. No catalysts were used in experiments.

Nanoplate Characterizations. The morphology and crystal structure of the resulting products were analyzed with a JEOL-6400 high resolution field-emission scanning electron microscope (SEM) and a JEOL-2010 transmission electron microscope (TEM, operated at 200 kV) with an energy-dispersive X-ray (EDX) detector. Samples for TEM imaging were prepared by scratching the as-synthediameterd products from the substrate onto Formvar film (Ted Pella) copper grids. The thickness of the nanoplates was characterized using atomic force microscope (AFM, Veeco Dimension-3000). The nanoplates were also characterized with X-ray diffraction (XRD) using a Rigaku X-ray diffractometer with a Cu Kα radiation source. Raman spectra of the nanoplates were collected at a Renishaw 1000 Raman spectrometer.

3. RESULTS AND DISCUSSION

We grew $SnSe_2$ nanoplates using a noncatalytic vapor deposition process that is similar to what was used for the growth of GeS nanosheets previously.[30,37] The precursor material (SnSe and Se) vapor generated by the sublimation of solid powders can react at elevated temperatures to produce gaseous $SnSe_2$ species. In typical experiments, the temperatures of the precursor materials Se (350 °C) and SnSe (550 °C) were designed to make the sublimation flux of Se (melting point, 217 °C) much bigger than that of SnSe (melting point, 861 °C). This is to ensure the complete reaction of SnSe vapor. The gaseous $SnSe_2$ species may be transferred downstream by the flow of carrier gas to precipitate at receiving substrates with lower temperatures (Figure 1a). This process can produce high quality $SnSe_2$ nanoplates. Figure 1b shows a scanning electron microscope (SEM) image of as-grown nanoplates on silicon substrates. We can find that most of the nanoplates grow horizontally on the substrate (Figure 1b, inset) with few out-of-plane growth (indicated by the white arrows). Raman (Figure 1c) and energy-dispersive X-ray spectroscopy (not shown) results indicate that the composition of the nanoplate is tin diselenide, $SnSe_2$, instead of SnSe. The peak at 185 cm^{-1} in the Raman spectrum correpsonds to the A_{1g} phonon mode of $SnSe_2$ materials.[38,39] Unlike SnSe, which is a cubic crystal, $SnSe_2$ has a layered structure with a hexagonal symmetry in space group of $P\bar{3}m1$(Figure 1c, inset).[40] The hexagonal shape of the nanoplate matches the equilibrium shape of the crystal

dx.doi.org/10.1021/jp400274a | J. Phys. Chem. C 2013, 117, 6469−6475

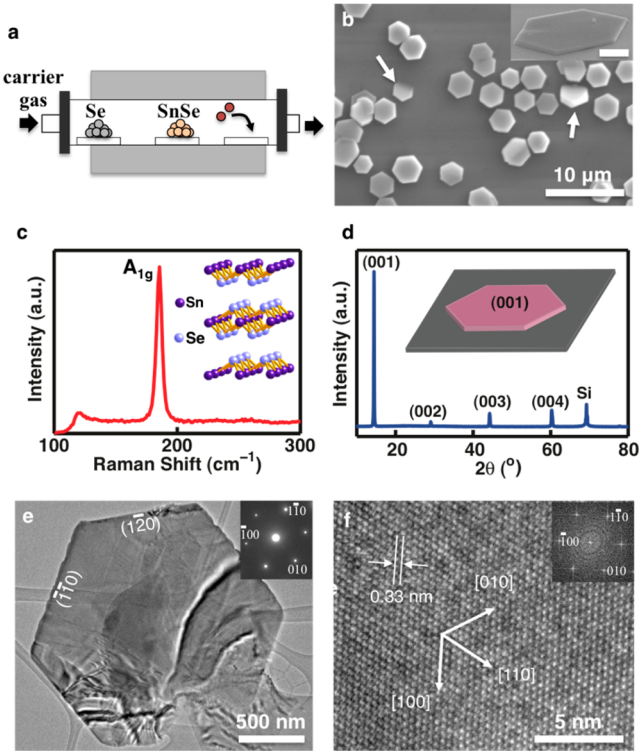


Figure 1. Synthesis and characterizations of $SnSe_2$ nanoplates. (a) Schematic illustration of the synthetic setup used in experiments. (b) SEM image of as-grown $SnSe_2$ nanoplates on silicon substrates. The white arrows indicate the nanoplates growing out of the plane of the substrate surface. Inset is a side-viewed SEM image showing the in-plane growth of the nanoplate. Scale bar: 1 μm. (c) Raman spectrum of $SnSe_2$ nanoplates. Inset is a structure model for $SnSe_2$ materials. (d) XRD characterization of as-grown nanoplates on silicon substrates. Inset is a schematic illustration for the geometry of the nanoplates on the substrate. (e) TEM image of a representative nanoplate and corresponding SAED pattern (inset). The crystalline planes enclosing the hexagonal plate are labeled as shown. (f) HRTEM image of a typical $SnSe_2$ nanoplate. Inset is the corresponding FFT pattern. Important crystalline directions are given in the figure.

structure, suggesting that the basal plane of the nanoplate is (001), the most energetically stable plane. The dominance of (00*l*) peaks in the XRD result collected from as-grown nanoplates confirms that most of the nanoplates grow in the z direction with (001) as the basal plane (Figure 1d). From the XRD results we can also derive the lattice constant of the nanoplate as $a = b = 3.80$ Å and $c = 6.14$ Å, consistent with that of bulk $SnSe_2$.[40,41] It is worthy to note that we can not find any obvious strain in the nanoplates from the XRD measurement. This is expected because the interaction between the substrate and the nanoplate would be weak van der Waals forces due to the absence of dangling bond at the surface of the nanoplate (we will discuss it more later). The synthediameterd nanoplate exhibits high crystalline quality. Figure 1e shows a transmission electron microscope (TEM) image and selected area electron diffraction (SAED) pattern of a typical nanoplate. Part of the nanoplate was broken in the process of preparing samples for the TEM characterization. A representative high-resolution TEM image is given in Figure 1f. These results indicate that the nanoplate is single crystalline. They also confirm that the basal plane is (001) and that the lattice constant is 0.381 nm.

Significantly, we find the growth of the nanoplate is subject to strong influences from the substrate. A substantial difference can be found in the morphology of the nanoplates grown on mica and silicon substrates. The experimental conditions for the growths on both substrates were controlled comparable by placing the two substrates side by side in the tube perpendicular to the direction of gas flow (Figure 2a). This configuration can

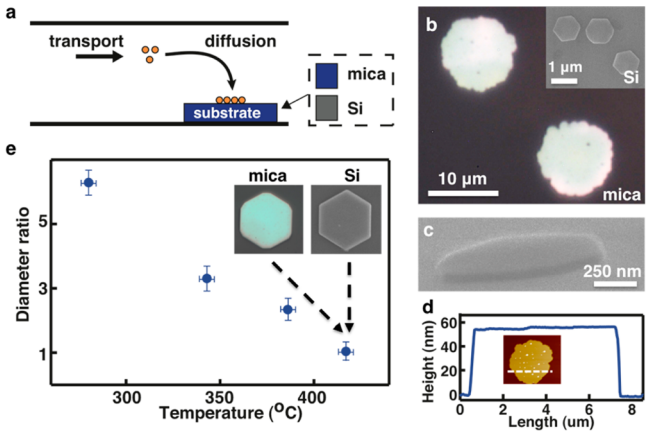


Figure 2. Morphological difference of $SnSe_2$ nanoplates grown on mica and silicon substrates. (a) Schematic illustration of the synthetic geometry in experiments. The two substrates were placed side by side perpendicular to the direction of the gas flow. (b) Optical image of as grown $SnSe_2$ nanoplates on mica. Inset, SEM image of $SnSe_2$ nanoplates grown on silicon substrates. (c) Side-viewed SEM image of a typical nanoplate grown on silicon. (d) A height profile from the AFM characterization of a representative nanoplate grown on mica. Inset, the AFM image from which the height profile is collected from as indicated by the white dashed line. (e) The diameter ratio of the nanoplates grown on mica and silicon substrates as a function of growth temperature. Inset shows the optical (mica) and SEM (silicon) images of typical nanoplates grown on the two substrates at a temperature of 420 °C. Both nanoplates are in a diameter of around 16 μm.

ensure the temperatures of both substrates similar. The diameter of the nanoplates grown on mica can be substantially larger than those grown on silicon (Figure 2b). But the thickness of the nanoplates on both substrates is similar (for example, 58 nm on mica vs 54 nm on silicon in Figure 2c,d). Additionally, unlike the nanoplates grown on silicon substrates, which always show a well-defined hexagonal shape, those grown on mica exhibit irregular shapes (Figure 2b). The morphological difference is found decreasing with the growth temperature increasing. The diameter ratio of the nanoplates grown on the two substrates, S_M/S_S (S_M and S_S are the diameter of the nanoplates grown on mica and silicon, respectively), shrinks to be unity (1.04) at a high growth temperature of 420 °C from 6.2 at a lower temperature of 280 °C (Figure 2e). Meanwhile, the shape of the nanoplates grown on mica evolves to be more similar to those on silicon with increase in the temperature. We can see that the nanoplates grown on mica are also in a well-defined hexagonal shape at the growth temperature of 420 °C (Figure 2e, inset).

To understand the observed morphological difference, we examine the dynamics behavior of the synthetic process. As illustrated in Figure 3a, three major steps are involved in the synthesis: (1) diffusion of source material vapor onto substrates, (2) growth reaction in which adsorbed source material species migrate to growth sites (typically at the edge of the nanoplate) and are incorporated into crystal lattice, and (3) desorption of excess adsorbed species. Of the most importance

dx.doi.org/10.1021/jp400274a | J. Phys. Chem. C 2013, 117, 6469−6475

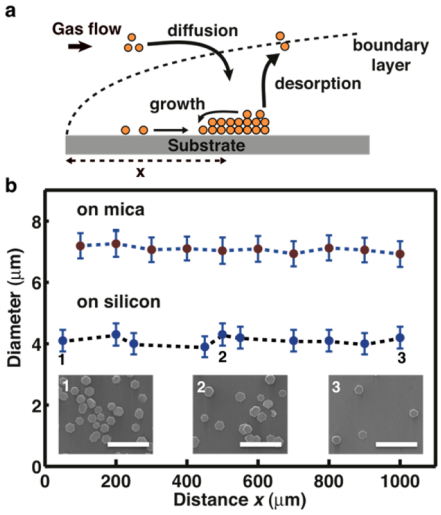


Figure 3. Reaction-limited growth of $SnSe_2$ nanoplates. (a) Schematic illustration for the dynamics behavior involved in the synthetic process. The synthesis includes three major steps: diffusion of source material vapor onto receiving substrates, growth reaction in which source material adatoms migrate to growth sites to be incorporated into crystal lattice, and desorption of excessive source material adatoms. The dashed curve indicates the boundary layer that source material vapor diffuse through to arrive at the substrate. The dashed line x below the substrate indicates the distance of growth locations away from the upstream edge of the substrate. (b) The diameter of nanoplates plotted as a function of the distance x. The given results are for typical growths on mica and silicon substrates. Inset are SEM images of the nanoplates grown at three different positions 1, 2, and 3 on the silicon substrate. The positions of 1, 2, and 3 are in a distance of 50, 500, and 1000 μm from the upstream edge of the substrate, respectively.

is the rate-determining step that dictates the growth rate of the nanoplate. Generally, the rate-determining step of vapor deposition growths could be either the diffusion (step 1) or the growth reaction (step 2), which is referred as diffusion-limited or reaction-limited growth, respectively.

The growth of $SnSe_2$ nanoplates is found to be reaction-limited. In another word, the rate-determining step is the grow reaction. This is concluded based on analysis of the diameter of the nanoplates. It has been well-known that a diffusion-limited growth is featured with a decrease in the diameter S of resulting nanostructures as a function of the lateral distance x of growth locations from the upstream edge of the substrate as $S \propto 1/\sqrt{x}$, as what we previously demonstrated in the synthesis of GeS nanosheets.[31] This is because the thickness of the gas flow boundary layer which the source material vapor need diffuse through to arrive at the substrate increases with the lateral distance, giving rise to a lower diffusion flux at the position further away from the edge (Figure 3a). However, our experimental results indicate that the diameter of $SnSe_2$ nanoplates grown on both substrates of silicon and mica remains largely independent of the lateral distance x (Figure 3b). This strongly suggests that the rate-determining step for this nanoplate synthesis is the growth reaction rather than the diffusion. It is worthwhile to briefly note that the density of nanoplates can be found decreasing with increase of the distance x (Figure 3b, inset). The density can be correlated to the nucleation rate of nanoplates. This distance-dependent density suggests that the very early phase of the synthesis, i.e., the nucleation phase, seems to be diffusion-limited. In this work, our main focus is on the phase of growth.

As this growth is reaction-limited,, the observed morphological difference indicates that the dynamics of the growth reaction is different on the substrates of silicon and mica. As illustrated in Figure 4, the growth reaction actually includes

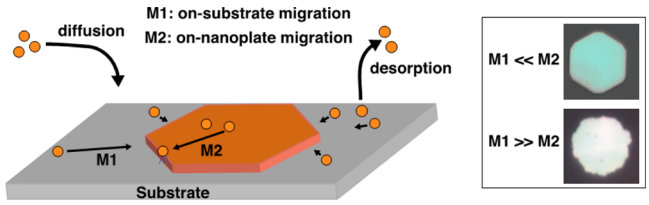


Figure 4. Schematic illustration for the effect of surface migrations on the nanoplate growth. Two migration processes, on the substrate surface (M1) and on the nanoplate surface (M2), are involved in the growth. The inset indicates the morphological difference of resulting nanoplates due to different rates of the two migrations.

three processes, migration of $SnSe_2$ species adsorbed on substrates to growth sites that are typically at the edge of nanoplates (referred as M1), migration of the $SnSe_2$ species adsorbed on nanoplates to the growth sites (referred as M2), incorporation of the $SnSe_2$ adatoms into crystal lattice at the growth sites. The migrations and the incorporation are in series, whichever slower determines the rate of the growth reaction. Because the only difference between the growth reactions on mica and silicon lies in the migration on substrates (M1), the observed morphological difference suggests that the migrations rather than the incorporation determines the growth rate. More specifically, the growth rate of nanoplates depends on the supply flux of $SnSe_2$ adatoms toward the growth sites (at the edge of the nanoplate) *via* the two migration processes, on-substrate migration M1 and on-nanoplate migration M2. We neglect the direct impingement of source material atoms on the growth sites from the vapor phase, whose flux can be reasonably considered much smaller than the flux supplied by the migrations.[33] Therefore, the observed morphological difference can be specifically correlated to the migration processes of $SnSe_2$ adatoms.

We can get more insights into the morphological difference by further examining the dynamics of the migrations. Surface migration is known driven by a concentration gradient of adatoms on the adsorbent surface, and its rate can be generally written as $J = D \cdot \nabla C$, where D is the migration coefficient of the adatom and ∇C is the concentration gradient. The difference in ∇C on the substrates of mica and silicon is expected to be minor, because the concentration gradient heavily depends on the diffusion flux of gaseous $SnSe_2$ species from the vapor phase,[33] which would be similar for both substrates given their comparable experimental conditions. However, the migration coefficient D is well-known depending on the nature of adsorbates and adsorbents. It is dictated by a migration barrier energy E_m and temperature T as $D \propto e^{-E_m/kT}$ (k is the Boltzmann constant). The migration barrier energy is the required energy for the adatoms to move from a site to other site. The amplitude of the energy E_m relies on the interaction of $SnSe_2$ adatoms with the substrate and on the surface state of the substrate..

The observed morphological difference can be reasonably correlated to the different migration energy of $SnSe_2$ adatoms on the substrates. While no quantitative information for the

dx.doi.org/10.1021/jp400274a | J. Phys. Chem. C 2013, 117, 6469−6475

migration energies is available, we can make a qualitative comparison between them. It has been documented that the migration energy may linearly increase with the number of dangling bonds.[42] In contrast with silicon, which is three-dimensionally bonded and has dangling bonds at the surface, the surface of the two-dimensionally bonded materials, such mica or $SnSe_2$, is completely passivated with no dangling bonds, as illustrated in Figure 5. Therefore, the migration barrier

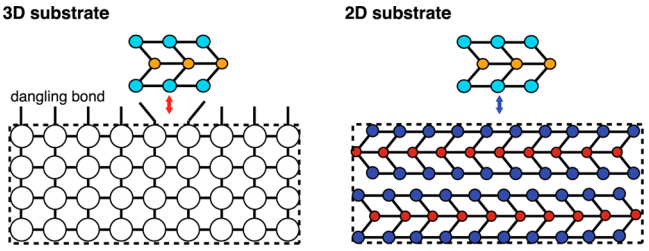


Figure 5. Schematic illustration for the interactions of layered chalcogenide materials with (left) three-dimensionally bonded and (right) two-dimensionally bonded substrates.

energy on the silicon substrate is expected to be larger than that on the mica substrate or on the $SnSe_2$ nanoplate. As a result, the migration rate on the silicon substrate is expected smaller than that on the nanoplate, $M1_{Si} \ll M2$. In this case, the on-nanoplate migration M2 is the dominant pathway to supply $SnSe_2$ adatoms for the nanoplate growth. This is consistent with our experimental observations. We find that the nanoplates grown on silicon substrates always show a hexagonal shape that is a thermodynamic equilibrium shape for the crystal structure in space group of $P\bar{3}m1$. The yield of the equilibrium shape suggests that the nanoplate growth is governed by intrinsic thermodynamic factors of $SnSe_2$ materials. This can be possible only if the on-nanoplate migration M2 dominates the growth. The substantially larger diameter of the nanoplates grown on mica suggests that the migration of $SnSe_2$ adatoms on mica is much faster than that on the nanoplate surface, $M1_{mica} \gg M2$. This gives rise to a larger flux of source material adatoms than the growth on silicon, which only rely on the on-nanoplate migration for adatom supply. This also suggests that the migration on mica has a smaller barrier energy E_m than the one for the on-nanoplate migration. The observed irregular shape of the nanoplates grown on mica provides corroborating evidence for the substantial contribution of the on-mica migration $M1_{mica}$. The irregular shape suggests that the migration process involved in the growth is subject to influences of random factors that are extrinsic to $SnSe_2$ materials. In our experiments, these factors are the surface state of the mica susbtrate.

The observed temperature dependence of the morphological difference (Figure 2e) can be ascribed to the dependence of the migrations on temperature. The migration coefficient D depends on the temperature as $D \propto e^{-E_m/kT}$. It increases faster with the temperature for the migration on the nanoplate, which has a larger migration barrier energy, than that on mica. Therefore, the difference in the supply flux of $SnSe_2$ adatoms for the growths on mica (by the migrations $M1_{mica}$ and M2) and on silicon (by the migration M2) tends to decrease with the temperature. This is consistent with experimental observations (Figure 2e). The well-defined hexagonal shape of the nanoplates grown on mica at a relatively high temperature (420 °C) strongly indicates that, at this temperature, the on-nanoplate migration M2 may overtake the on-mica migration $M1_{mica}$ as the dominant pathway to supply $SnSe_2$ adatoms. The similar diameter of the nanoplates grown on both mica and silicon also supports the dominance of the on-nanoplate migration at 420 °C (Figure 2e inset).

The facile migration of $SnSe_2$ adatoms on mica and its important role in the growth can be confirmed by a dependence of the nanoplate diameter on the distance between neighboring nanoplates. We found in experiments that the diameter of nanoplates decreases with increase in the density of the nanoplates on mica. Figure 6a–c gives SEM images of the

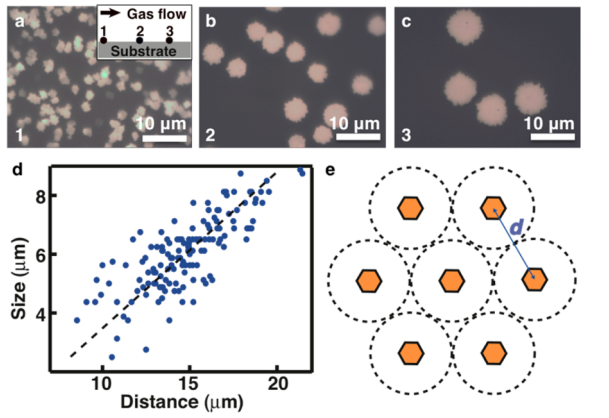


Figure 6. Effect of the on-substrate migration on the nanoplate growth. (a–c) SEM images of $SnSe_2$ nanoplates grown at different locations on a typical mica substrate. The locations of 1, 2, and 3 on the substrate are schematically illustrated in the inset of (a). (d) Correlation of the diameter of the nanoplate with the internanoplate distance d. The dashed black line serves to guide the vision of the relationship between the diameter and the distance (e) A simplified model to illustrate the coupling of migration fields between neighboring nanoplates. The dashed line indicates the boundary of the migration field of individual nanoplate.

nanoplates grown at different locations of a typical mica substrate. The location 1 is the closest to the upstream edge of the substrate (~100 μm), and has the highest density of nanoplates, followed by the locations of 2 and 3 with larger distances (~3.5 and 5.5 mm, respectively) and lower nanoplate densities. The decrease in the nanoplate density with the distance can be related with the nucleation phase of nanoplates, which is diffusion limited as discussed in preceding text. We can see a very obvious tendency that the nanoplate diameter decreases with increase in the nanoplate density (Figure 6a–c). To more quantitatively demonstrate this tendency, we measured the diameter of each nanoplate and the (center-to-center) distances of the nanoplate with its three-closest neighbors, which were then averaged as the internanoplate distance. Figure 6d shows a plot of the nanoplate diameter as a function of the internanoplate distance. The nanoplate diameter can be reasonably considered as linearly correlated with the distance.

This correlation suggests that the nanoplate growth is indeed limited by the migration of $SnSe_2$ materials on the substrate. When the nanoplates are well separated, the supply flux F of source material adatoms for the growth is dependent on a characteristic migration length λ, which is the distance the adatom can migrate during its lifetime, $F \propto \lambda^2$. However, for an ensemble of nanoplates that are closely packed with internanoplate distances smaller than the migration length λ,

dx.doi.org/10.1021/jp400274a | J. Phys. Chem. C 2013, 117, 6469–6475

the migration field (areas covered by the characteristic migration length) of neighboring nanoplates may interfere each other (Figure 6e). Therefore, the supply flux F turns to depend on the interplate distance d as $F \propto d^2$ instead. The total amount of adatoms N_{total} supplied for the growth of each individual nanoplate can be linked to the distance d as $N_{total} \propto d^2$. N_{total} can be related with the dimension of the nanoplate as $N_{total} = \pi r^2 h \rho N_A$, where r and h is the radius and height of the nanoplate, respectively, ρ is the molar density of the materials, and N_A is the Avogadro's constant. Therefore, we may have $\pi r^2 h \rho N_A \propto d^2$. By assuming an identical thickness h for all the nanoplates, which is a reasonable approximation for our experiments, we can see that a linear relationship between the diameter of the nanoplate r and the internanoplate distance d is indeed expected.

4. CONCLUSION

This work presents the synthesis of single-crystalline $SnSe_2$ nanoplates by a noncatalytic vapor deposition process and demonstrates a strong mediation effect of the substrate for the growth. The effect of substrates is evidenced by a temperature-dependent morphological difference in the nanoplates grown on mica and silicon substrates. Our analysis indicates that the observed temperature-dependent morphological difference can be specifically linked to the surface migration of $SnSe_2$ adatoms. The migration depends on the temperature and the interaction of the adatoms with substrates. Due to the absence of dangling bonds, $SnSe_2$ adatoms can migrate on mica more easily, which can result in a larger supply of adatoms for the nanoplate growth. The role of the facile migration on mica in the nanoplate growth is further confirmed by a correlation of the nanoplate diameter with the distance between neighboring nanoplates. While the focus is on $SnSe_2$, this understanding can generally apply to the growth of two-dimensional (2D) nanostructures of many other layered chalcogenide materials (LCMs). It paves the way for leveraging the substrate to control the growth of 2D LCM nanostructures.

AUTHOR INFORMATION

Corresponding Author

*E-mail: lcao2@ncsu.edu.

Notes

The authors declare no competing financial interest.

ACKNOWLEDGMENTS

The authors thank Yuntian Zhu for providing access to the Raman spectrometer. The authors acknowledge support from the Army Research Office (W911NF-11-1-0529). L.C. acknowledges a Ralph E. Powe Junior Faculty Enhancement Award from Oak Ridge Associated Universities.

REFERENCES

(1) Novoselov, K. S.; Geim, A. K.; Morozov, S. V.; Jiang, D.; Katsnelson, M. I.; Grigorieva, I. V.; Dubonos, S. V.; Firsov, A. A. Two-dimensional Gas of Massless Dirac Fermions in Graphene. *Nature* **2005**, *438*, 197−200.

(2) Zhang, Y. B.; Tan, Y. W.; Stormer, H. L.; Kim, P. Experimental Observation of The Quantum Hall Effect and Berry's Phase in Graphene. *Nature* **2005**, *438*, 201−204.

(3) Matte, H. S. S. R.; Gomathi, A.; Manna, A. K.; Late, D. J.; Datta, R.; Pati, S. K.; Rao, C. N. R. MoS2 and WS2 Analogues of Graphene. *Angew Chem. Int. Ed.* **2010**, *49*, 4059−4062.

(4) Auerbach, S. M.; Carrado, K. A.; Dutta, P. K. *Handbook of Layered Materials*; CRC Press: New York, 2004.

(5) Zhao, W.; Ghorannevis, Z.; Chu, L.; Toh, M.; Kloc, C.; Tan, P.-H.; Eda, G. Evolution of Electronic Structure in Atomically Thin Sheets of WS2 and WSe2. *ACS Nano* **2013**, *7*, 791−797.

(6) Han, S. W.; Kwon, H.; Kim, S. K.; Ryu, S.; Yun, W. S.; Kim, D. H.; Hwang, J. H.; Kang, J. S.; Baik, J.; Shin, H. J.; et al. Band-gap Transition Induced by Interlayer van der Waals Interaction in MoS2. *Phys. Rev. B* **2011**, *84*, 045409.

(7) Coehoorn, R.; Haas, C.; Degroot, R. A. Electronic-Structure of Mose2, Mos2, and Wse2 0.2. The Nature of the Optical Band-Gaps. *Phys. Rev. B* **1987**, *35*, 6203−6206.

(8) Mak, K. F.; Lee, C.; Hone, J.; Shan, J.; Heinz, T. F. Atomically Thin MoS2: A New Direct-Gap Semiconductor. *Phys. Rev. Lett.* **2010**, *105*, 136805.

(9) Xiao, D.; Liu, G. B.; Feng, W. X.; Xu, X. D.; Yao, W. Coupled Spin and Valley Physics in Monolayers of MoS2 and Other Group-VI Dichalcogenides. *Phys. Rev. Lett.* **2012**, *108*, 196802.

(10) Zeng, H. L.; Dai, J. F.; Yao, W.; Xiao, D.; Cui, X. D. Valley Polarization in MoS2Monolayers by Optical Pumping. *Nat. Nanotechnol.* **2012**, *7*, 490−493.

(11) Mak, K. F.; He, K. L.; Shan, J.; Heinz, T. F. Control of Valley Polarization in Monolayer MoS2 by Optical Helicity. *Nat. Nanotechnol.* **2012**, *7*, 494−498.

(12) Peng, H. L.; Lai, K. J.; Kong, D. S.; Meister, S.; Chen, Y. L.; Qi, X. L.; Zhang, S. C.; Shen, Z. X.; Cui, Y. Aharonov-Bohm Interference in Topological Insulator Nanoribbons. *Nat. Mater.* **2010**, *9*, 225−229.

(13) Zhou, W.; Yin, Z.; Du, Y.; Huang, X.; Zeng, Z.; Fan, Z.; Liu, H.; Wang, J.; Zhang, H. Synthesis of Few-Layer MoS2 Nanosheet-Coated TiO2 Nanobelt Heterostructures for Enhanced Photocatalytic Activities. *Small* **2013**, *9*, 140−147.

(14) Radisavljevic, B.; Radenovic, A.; Brivio, J.; Giacometti, V.; Kis, A. Single-layer MoS2 Transistors. *Nat. Nanotechnol.* **2011**, *6*, 147−150.

(15) Osada, M.; Sasaki, T. Two-Dimensional Dielectric Nanosheets: Novel Nanoelectronics From Nanocrystal Building Blocks. *Adv. Mater.* **2012**, *24*, 210−228.

(16) Kim, S.; Konar, A.; Hwang, W.-S.; Lee, J. H.; Lee, J.; Yang, J.; Jung, C.; Kim, H.; Yoo, i.-B.; Choi, J.-Y.; et al. High-Mobility and Low-Power Thin-Film Transistors Based on Multilayer MoS2 Crystals. *Nat. Commun.* **2012**, *3*, 1011.

(17) Pu, J.; Yomogida, Y.; Liu, K. K.; Li, L. J.; Iwasa, Y.; Takenobu, T. Highly Flexible MoS2 Thin-Film Transistors with Ion Gel Dielectrics. *Nano Lett.* **2012**, *12*, 4013−4017.

(18) Wang, H.; Yu, L.; Lee, Y.-H.; Shi, Y.; Hsu, A.; Chin, M. L.; Li, L.-J.; Dubey, M.; Kong, J.; Palacios, T. Integrated Circuits Based on Bilayer MoS2 Transistors. *Nano Lett.* **2012**, *12*, 4674−4680.

(19) Fang, H.; Chuang, S.; Chang, T. C.; Takei, K.; Takahashi, T.; Javey, A. High-Performance Single Layered WSe2 p-FETs with Chemically Doped Contacts. *Nano Lett.* **2012**, *12*, 3788−3792.

(20) Splendiani, A.; Sun, L.; Zhang, Y.; Li, T.; Kim, J.; Chim, C.-Y.; Galli, G.; Wang, F. Emerging Photoluminescence in Monolayer MoS2. *Nano Lett.* **2010**, *10*, 1271−1275.

(21) Yin, Z. Y.; Li, H.; Li, H.; Jiang, L.; Shi, Y. M.; Sun, Y. H.; Lu, G.; Zhang, Q.; Chen, X. D.; Zhang, H. Single-Layer MoS2 Phototransistors. *ACS Nano* **2012**, *6*, 74−80.

(22) Lee, H. S.; Min, S. W.; Chang, Y. G.; Park, M. K.; Nam, T.; Kim, H.; Kim, J. H.; Ryu, S.; Im, S. MoS2 Nanosheet Phototransistors with Thickness-Modulated Optical Energy Gap. *Nano Lett.* **2012**, *12*, 3695−3700.

(23) Liu, J.; Liu, X.-W. Two-Dimensional Nanoarchitectures for Lithium Storage. *Adv. Mater.* **2012**, *24*, 4097−4111.

(24) Chang, K.; Chen, W. X. In situ Synthesis of MoS2/Graphene Nanosheet Composites with Extraordinarily High Electrochemical Performance for Lithium Ion Batteries. *Chem. Commun.* **2011**, *47*, 4252−4254.

(25) Cui, Y.; Lauhon, L. J.; Gudiksen, M. S.; Wang, J.; Lieber, C. M. Diameter-controlled Synthesis of Single-crystal Silicon Nanowires. *Appl. Phys. Lett.* **2001**, *78*, 2214.

(26) Kong, J.; Cassell, A. M.; Dai, H. J. Chemical Vapor Deposition of Methane for Single-walled Carbon Nanotubes. *Chem. Phys. Lett.* **1998**, *292*, 567−574.
(27) Li, X. S.; Cai, W. W.; An, J. H.; Kim, S.; Nah, J.; Yang, D. X.; Piner, R.; Velamakanni, A.; Jung, I.; Tutuc, E.; et al. Large-Area Synthesis of High-Quality and Uniform Graphene Films on Copper Foils. *Science* **2009**, *324*, 1312−1314.
(28) Hu, J. T.; Odom, T. W.; Lieber, C. M. Chemistry and Physics in One Dimension: Synthesis and Properties of Nanowires and Nanotubes. *Acc. Chem. Res.* **1999**, *32*, 435−445.
(29) Kong, D.; Dang, W.; Cha, J. J.; Li, H.; Meister, S.; Peng, H.; Liu, Z.; Cui, Y. Few-Layer Nanoplates of Bi2Se3 and Bi2Te3 with Highly Tunable Chemical Potential. *Nano Lett.* **2010**, *10*, 2245−2250.
(30) Lee, Y.-H.; Zhang, X.-Q.; Zhang, W.; Chang, M.-T.; Lin, C.-T.; Chang, K.-D.; Yu, Y.-C.; Wang, J. T.-W.; Chang, C.-S.; Li, L.-J.; et al. Synthesis of Large-Area MoS2 Atomic Layers with Chemical Vapor Deposition. *Adv. Mater.* **2012**, *24*, 2320−2325.
(31) Li, C.; Huang, L.; Snigdha, G. P.; Yu, Y.; Cao, L. Role of Boundary Layer Diffusion in Vapor Deposition Growth of Chalcogenide Nanosheets: The Case of GeS. *ACS Nano* **2012**, *6*, 8868−8877.
(32) Shi, Y.; Zhou, W.; Lu, A. Y.; Fang, W.; Lee, Y. H.; Hsu, A. L.; Kim, S. M.; Kim, K. K.; Yang, H. Y.; Li, L. J.; et al. van der Waals Epitaxy of MoS2 Layers Using Graphene as Growth Templates. *Nano Lett.* **2012**, *12*, 2784−2791.
(33) Markov, I. V. *Crystal Growth for Beginners: Fundamentals of Nucleation, Crystal Growth and Epitaxy*; World Scientific: Singapore, 1995.
(34) Koma, A. Van der Waals Epitaxy for Highly Lattice-Mismatched Systems. *J. Cryst. Growth* **1999**, *201*, 236−241.
(35) Ueno, K.; Saiki, K.; Shimada, T.; Koma, A. Epitaxial Growth of Transition Metal Dichalcogenides on Cleaved Faces of Mica. *J. Vac. Sci. Technol. A* **1990**, *8*, 68.
(36) Groot, C. H. d.; Gurnani, C.; Hector, A. L.; Huang, R.; Jura, M.; Levason, W.; Reid, G. Highly Selective Chemical Vapor Deposition of Tin Diselenide Thin Films onto Patterned Substrates via Single Source Diselenoether Precursors. *Chem. Mater.* **2012**, *24*, 4442−4449.
(37) Li, C.; Yu, Y.; Chi, M.; Cao, L., Epitaxial Nanosheet−Nanowire Heterostructures. *Nano Lett.* **2013**, *13*, 10.1021/nl303876a.
(38) Smith, A. J.; Meek, P. E.; Liang, W. Y. Raman Scattering Studies of SnS2 and SnSe2. *J. Phys. C: Solid State Phys.* **1977**, *10*, 1321−1333.
(39) Mead, D. G.; Irwin, J. C. Raman Spectra of SnS2 and SnSe2. *Solid State Commun.* **1976**, *20*, 885−887.
(40) Bhatt, V. P.; Gireesan, K.; Pandya, G. R. Growth and Characterization of SnSe and SnSe2 Single-Crystals. *J. Cryst. Growth* **1989**, *96*, 649−651.
(41) Trifonova, E.; Yanchev, I. Y.; Manou, P.; Kambas, K.; Anagnostopoulos, A. N. Growth and Characterization of SnSe2. *J. Mater. Sci.* **1996**, *31*, 3647−3649.
(42) Furukawa, Y.; Nakajima, K. *Advances in Crystal Growth Research*; Elsevier: Amsterdam, The Netherlands, 2001.

NANO LETTERS

Letter

pubs.acs.org/NanoLett

Epitaxial Nanosheet−Nanowire Heterostructures

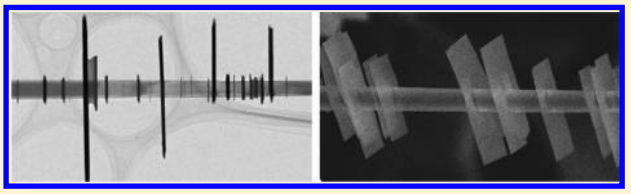
Chun Li,[†,∥] Yifei Yu,[†,∥] Miaofang Chi,[§] and Linyou Cao*[,†,‡]

[†]Department of Materials Science and Engineering, [‡]Department of Physics, North Carolina State University, Raleigh, North Carolina 27695, United States

[§]Materials Science and Technology Division, Oak Ridge National Laboratory, Oak Ridge, Tennessee 37831, United States

Supporting Information

ABSTRACT: We demonstrate synthesis of a new type of heterostructures that comprise two-dimensional (2D) nanosheets (NSs) epitaxially grown at one-dimensional (1D) nanowires (NWs). The synthesis involves materials with a graphite-like layered structure in which covalently bonded layers are held by weak van der Waals forces. GeS was used as a prototype material in this work. The synthesis also involves a seeded-growth process, where GeS NWs are grown first as seeds followed by a seeded growth of NSs at the pre-grown NWs. We observe that exposing the pre-grown NWs to air prior to the seeded growth is critical for the formation of NSs to yield NS−NW heterostructures. Our experimental results suggest that this might be due to a mild oxidation at the NW surface caused by the air exposure, which could subsequently facilitate the nucleation of NSs at the NWs. It also suggests that the surface oxidation needs to be controlled in a proper range in order to achieve optimized NS growths. We believe that this synthetic strategy may generally apply to the growth of NS−NW heterostructures of other layered chalcogenide materials. NS−NW heterostructures provide capabilities to monolithically integrate the functionality of 1D NWs and 2D NSs into a 3D space. It holds great potential in applications that request complex nanomaterials with multiple functionality, high surface area, and efficient charge transport, such as energy storage, chemical sensing, solar energy conversion, and 3D electric and photonic devices.



KEYWORDS: *Heterostructures, epitaxial growth, nanosheets, nanowires, germanium sulfide, three-dimensional nanostructures*

Epitaxial heterostructures with modulated topologies or compositions are interesting for fundamental and applied interest.[1−6] These structures can provide an appealing platform with well-defined structures and interfaces for the studies of fundamental physics. For instance, heterogeneous quantum wells have historically enabled the discovery of numerous exotic phenomena like quantum spin Hall effects in two-dimensional electron gases.[7,8] The heterostructures also present a natural way to monolithically integrate multiple functional components into one system, which may enable novel functions that cannot be obtained from each of the components separately. One example is semiconductor nanowire (NW) heterostructures.[1,3,4,9] It has been well documented that branched, core−shell, and kinked NWs exhibit substantial advantages for applications in electronics, photonics, energy storage, and biosensing over homogeneous NWs.[4,10−15]

Existing efforts have overwhelmingly focused on the epitaxial heterostructures that comprise materials with similar dimensionalities. These include two-dimensional (2D) layered quantum wells,[6] one-dimensional (1D) branched NWs,[4] and zero-dimensional (0D) core−shell quantum dots.[5] In stark contrast, studies for heterostructures made of components in dissimilar dimensionalities (referred to as dimensional heterostructure) have remained limited.[2,16] Dimensional heterostructure is nevertheless very interesting due to its potential to open up new opportunities. Materials in different dimensionalities bear genetic advantages and disadvantages in terms of fundamental properties and technological applications. Integrating materials with dissimilar dimensionalities promises to combine the advantages and to mitigate the disadvantages, which may not be possible with conventional heterostructures. For example, in heterostructures made of 1D nanorods and 0D quantum dots, the nanorods can provide a unique way to tune the electrical coupling between the quantum dots.[16]

One key issue for the studies of dimensional heterostructures lies in the synthesis. Typical synthetic approaches for heterogeneous materials rely on a process of seeded growth. This process involves two steps, an initial growth of one material to act as seeds and a subsequent growth of another material on the pre-grown seed. Central to this synthesis is to control the second growth to only occur at the seed materials. For most of the existing heterostructures, the growth of seeds and the subsequent seeded growth both yield materials with similar dimensionalities. As a result, the seeded growth can be readily initiated by mildly modifying the experimental conditions used for the initial growth of seeds, such as loading new catalysts or lowering growth temperatures.[1,4,5] However, dimensional heterostructures necessitate a different paradigm in which the two growths are requested to produce materials in different dimensionalities. This is challenging because the growth of materials in different dimensionalities involves

Received: October 22, 2012
Revised: December 12, 2012

 © XXXX American Chemical Society dx.doi.org/10.1021/nl303876a | *Nano Lett.* XXXX, XXX, XXX−XXX

distinct growth behaviors/mechanisms and may request dramatically different experimental conditions. For instance, a nanowire−nanosheet (NW−NS) heterostructure would involve a unidirectional growth of NWs and a two-dimensional growth of nanosheets (NSs). It is very difficult to integrate the two distinct growths at one single structure.

Here we present a strategy to synthesize a new type of heterostructure that consists of 2D NSs and 1D NWs. This NS−NW heterostructure is made by an epitaxial growth of NSs at pre-grown NWs. It exhibits a shish-kebab-like structure with thin NWs as the backbone and large NSs as the branches. The key issue for this synthesis is to control the growth at the pre-grown NWs to yield nanowire−nanosheet (NS−NW) heterostructures, instead of core−shell NWs as previous studies did (Figure 1).[1] We find that this can be achieved by exposing

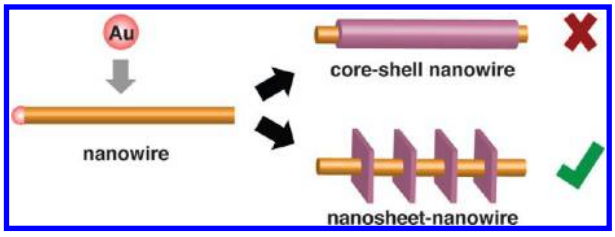


Figure 1. Schematic illustration of the synthetic strategy for nanosheet−nanowire heterostructures. First, the nanowire is grown using a gold-catalyzed vapor deposition process, and then, the nanowire is used as seeds for a second growth. The second growth must be controlled yield nanosheet−nanowire heterostructures instead of core−shell nanowires.

the pre-grown NWs to air prior to the NS growth. The role of this air exposure might be ascribed to a mild oxidation caused by the exposure at the surface of the NW, which may subsequently facilitate the nucleation of NSs. In this work, the NW and the NS both are GeS, a layered chalcogenide material with covalently bonded layers held by weak interlayer van der Waals forces that is promising for energy storage, solar energy conversion,[17] nonvolatile memory,[18] and photonics.[19] However, we believe that this synthetic strategy for NS−NW heterostructures may generally apply to other layered chalcogenide materials.

Our strategy for the development of NS−NW heterostructures builds upon the success in synthesis of both NWs and NSs with GeS materials. We find that the growth of GeS NWs can be realized using a gold-catalyzed vapor deposition process. Briefly, Si(100) substrates covered with a thin (5 nm) film of gold were placed downstream (local temperature ∼270−310 °C) in a tube furnace flowed with GeS vapor (total pressure 30 Torr). The GeS vapor was generated by sublimation of GeS powder loaded at the center of the tube furnace with elevated temperatures (∼450−490 °C), and was forced to flow toward downstream by carrier gas (5% H_2/Ar, ∼10−30 sccm). The growth of GeS NWs is via the well-established vapor−liquid−solid mechanism,[20] as evidenced by the presence of spherical catalyst particles at the end of the NW (Figure 2b). It is rooted in a larger accommodation coefficient for source material vapor at the liquid surface that makes the catalyst droplet a preferred site for deposition. Structural characterizations indicate that the resulting NW is single crystalline, typically grows along the direction of [100], and exhibits a smooth surface (Figure 2b and Figure S1, Supporting Information). Additionally, we have previously demonstrated the successful growth of GeS NSs using a noncatalyzed vapor deposition process.[21] Dictated by the nature of the layered structure, the deposition of GeS vapor in the absence of catalysts genetically tends to drive a two-dimensional growth to yield NSs. The basal plane of resulting GeS NSs is found always to be (100) (Figure 2b).

The coincidental crystalline structures of GeS NWs (the axial direction is [100]) and NSs (the basal plane is (100)) suggest a possibility of epitaxial growth of the NS at the radial direction of the NW, as illustrated in Figure 2b. However, to achieve this epitaxial growth requires activation of the surface of the NW. The smooth surface of as-grown GeS NWs indicates that the crystal growth at the radial direction of the NW (in the (100) plane) is effectively turned off. Because (100) is the most energetically stable plane of GeS materials, the radial growth of GeS materials is actually thermodynamically favorable. The observed turn-off suggests that this growth is kinetically hindered at the NW surface. Therefore, to realize the epitaxial growth of NSs at the radial direction of NWs requires activation of the NW surface, i.e., overcoming the kinetic hindrance for the NS growth. We found that the NW surface can be activated by exposing the NW to air.

We performed experiments to synthesize heterostructures with and without the exposure to air. Figure 3 shows the experimental processes and corresponding results. The experimental process includes two steps: a gold-catalyzed vapor deposition step to grow GeS NWs and a second deposition step with presence of the pre-grown NWs. The

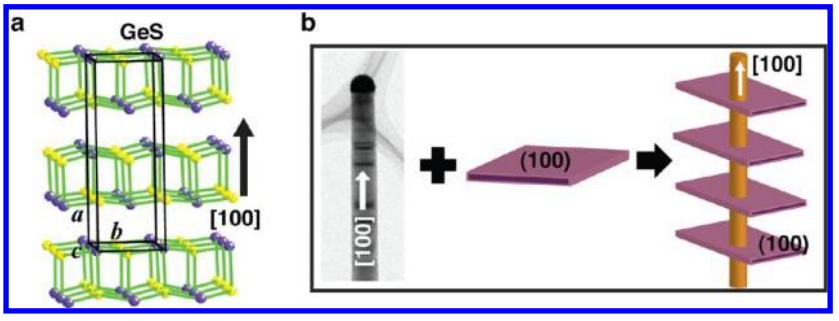


Figure 2. Epitaxial growth of two-dimensional (2D) GeS nanosheets at one-dimensional (1D) GeS nanowires. (a) Structural model for GeS that is a layered compound. GeS shows a rhombohedra structure with lattice constants a = 10.48 Å, b = 3.65 Å, and c = 4.30 Å. The unit cell is also shown in the figure. The black arrow indicates the direction of [100]. (b) Schematic illustration for the proposed epitaxial growth of 2D nanosheets with a basal plane of (100) at 1D nanowires with axis in the [100] direction. The image of the nanowire was collected using a transmission electron microscope (TEM), and the diameter of the nanowire is 210 nm.

dx.doi.org/10.1021/nl303876a | *Nano Lett.* XXXX, XXX, XXX−XXX

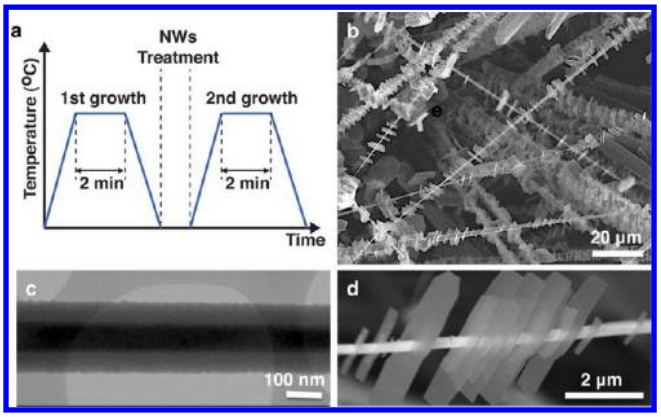


Figure 3. Seeded growth of GeS heterostructures. (a) Schematic illustration of the experimental processes. Two different ways were used to treat the as-grown NWs prior to the second growth, the NWs left inside the synthetic setup without exposure to air or taken out for air exposure and then replaced back. (b, d) Scanning electron microscope (SEM) images of the NS−NW heterostructures grown at the NWs exposed to air. (c) TEM image of core−shell nanowires grown from the NWs not exposed to air. The structure consists of a crystalline core coated by an amorphous shell.

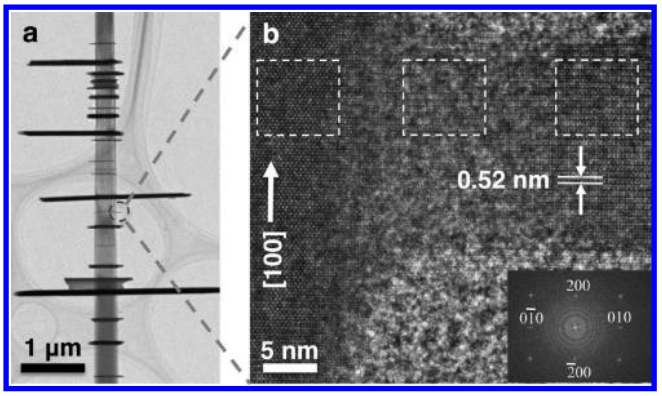


Figure 4. Structural characterization of nanosheet−nanowire heterostructures. (a) Low resolution TEM image of a nanosheet−nanowire heterostructure. (b) HRTEM image from a typical nanosheet−nanowire structure shown in part a. The growth direction of [100] and the thickness of each layer are marked in the figure. The three white dashed squares denote the three areas we performed FFT, all resulting in an identical pattern as shown in the inset.

synthetic setup was cooled in a flow of carrier gas down to room temperature after the first step. This is to deactivate the gold catalyst in order to minimize catalyzed growth in the second step. After the NWs were cooled down, we treated the as-grown NWs using two different methods: leaving the NWs inside the furnace with carrier gas continuously flowing or taking the NWs out for an exposure to air (typically for days) and then replacing them back (Figure 3a). The second deposition was initiated on these treated NWs separately by resuming the flow of GeS vapor and elevating the temperature. The experimental conditions in the second step were similar to what had been used for the catalyzed growth of GeS NWs (sublimation temperature ∼450−490 °C, deposition temperature ∼270−310 °C, flow rates of carrier gas 30 sccm, total pressure ∼10−30 Torr). The conditions are also comparable to what we previously used for the growth of standalone GeS NSs.[21]

We find that the two different treatments to the NWs can give rise to different morphologies in the structures yielded from the second growth. Using the NWs not exposed to air produces core−shell NWs consisting of a crystalline core NW coated by an amorphous shell (Figure 3c). The second step only causes a conformal deposition of amorphous GeS on the pre-grown crystalline NWs. In striking contrast, using the NWs exposed to air prior to the second growth can produce nanosheet−nanowire (NS−NW) heterostructures (Figure 3b). The heterostructure shows a shish-kebab-like structure with a backbone NW branched by NSs (Figure 3d). These on-wire NSs show a truncated rectangular shape, similar to the standalone GeS NSs that were grown previously.[21] The lateral size of the NSs varies in a broad range from hundreds of nanometers to micrometers. However, all of the NSs show similar length/width ratios.

Structural characterizations indicate that the growth of the on-wire NS is epitaxial from the NW. The high resolution TEM (HRTEM) image shows lattice planes nicely extend from the NW to the branched NS (Figure 4). We performed FFT (fast Fourier transform) on selected areas in the HRTEM image as indicated by the dashed white squares, all giving identical patterns (inset of Figure 4b). The FFT pattern also indicates the growth direction of the NW is [100]. As the NSs are perpendicular to the NW axis, this confirms that the basal plane of the branched NS is (100), which is again similar to the standalone GeS NSs that were grown previously and matches our expectation for the seeded growth of GeS NSs at GeS NWs (Figure 2). At the HRTEM image, we can measure the interspacing between (200) planes as 0.52 nm, consistent with the crystal lattice of GeS materials (rhombohedra structure, a = 10.48 Å, b = 3.65 Å, c = 4.30 Å).[22] On the basis of the characterization results, we can conclude that the branched NSs epitaxially grow from the NW along the (100) plane.

The epitaxial growth can also be seen at another type of NS−NW heterostructures found in experiments, as shown in Figure 5. Instead of being perpendicular to the NW axis, the NSs in this structure obliquely grow in a constant angle of 56° with the NW axis (Figure 5a and f). This angle of 56° is due to an epitaxial growth of NSs from twinned NWs. The NW in the oblique NS−NW heterostructure can be found as a twin crystal (Figure 5a,b). High resolution electron microscope images (Figure 5b) and corresponding FFT patterns (Figure S4, Supporting Information) indicate that the twin boundary plane is $(\bar{2}10)$ and the axis of the NW is along the [120] direction. They also indicate that the (100) plane of each domain of the twin forms an angle of 56° with the boundary plane (Figure 5b). This angle is consistent with the observed angle between the NW axis and the NS, suggesting that the growth of the NS is epitaxial along the (100) plane. To further confirm the epitaxial growth, we took selected area electron diffraction at the NS (red circle in Figure 5a) and the two domains of the NW (blue and orange circles in Figure 5a). We can find that the SAED pattern from the NS is identical to one of the domain. Analysis of the diffraction patterns also indicates that the epitaxial growth of the NS is indeed along the (100) plane, the same as the perpendicular NS−NW structures. This epitaxial growth of NSs from the twinned NWs to yield oblique NS−NW heterostructures can be illustrated by the structure model shown in Figure 5g.

The difference in the morphology of resulting heterostructures depending on the exposure to air (Figure 3) indicates that the air exposure can activate the surface of NWs for the growth of NSs. Exposing the NW to air may result in

dx.doi.org/10.1021/nl303876a | Nano Lett. XXXX, XXX, XXX−XXX

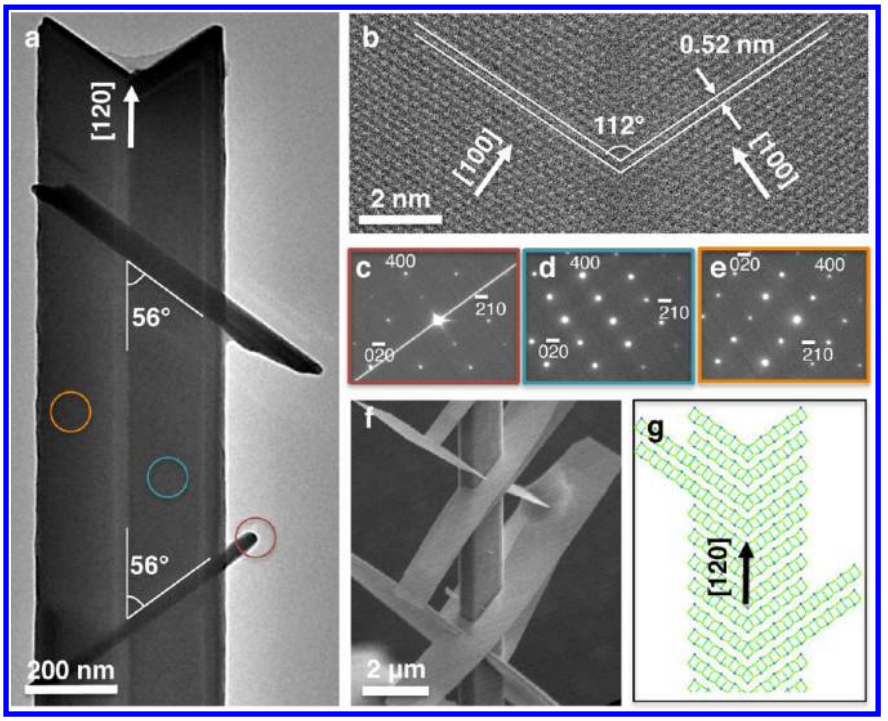


Figure 5. Structural characterization of oblique nanosheet−nanowire heterostructures. (a) Low resolution TEM image of the oblique nanosheet−nanowire heterostructure. The constant angle of 56° between the NS and the NW axis is marked as shown. The crystal directions parallel and perpendicular to the twin boundary plane are given in the figure. The three circles with different colors indicate the location where electron diffractions were collected from. (b) An atomic-resolution HAADF image of the twin boundary in the nanowire. The white lines indicate (100) planes in each of the two domains. The angle of 112° between the (100) planes, the interspacing between (200) planes, and the [100] directions are given in the figure. (c−e) Electron diffraction patterns taken from the different areas marked with different colorized circles in part a, the NS (red), the right part of the twin NW (blue), and the left side of the NW (orange). (f) SEM image of the oblique NS−NW heterostructures. (g) Structural model for the oblique NS−NW heterostructures.

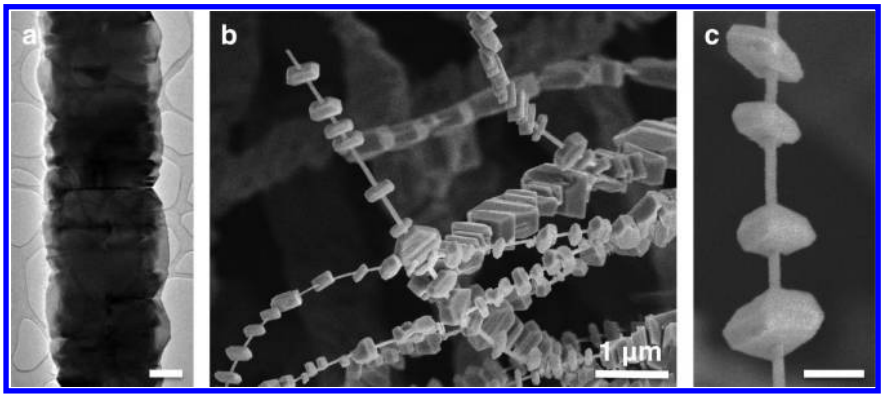


Figure 6. SEM images of heterogeneous structures grown at pre-grown NWs treated with different degrees of oxidation. (a) structures yielded from the deposition on pre-grown NWs under a carrier gas of Ar. The pre-grown NW was not exposed to air prior to the second growth.. Scale bar: 500 nm. (b) heterostructures grown on the NWs treated with O_2 plasma prior to the second growth. (b) A magnified SEM image of the heterostructures shown in (b). Scale bar: 500 nm.

modification of the NW surface, which may subsequently help overcome the kinetic hindrance for the NS growth at the surface. Without the activation, the deposition of GeS materials on the pre-grown NWs cannot yield NSs, just resulting in an amorphous shell. More specifically, the activation role of the air exposure can be correlated to its effect on the nucleation of NSs at the NW surface. Similar to typical crystal synthesis, the synthesis of the on-wire NSs includes two phases, nucleation and growth. As discussed in preceding texts, the on-wire NSs bear similar morphological features as standalone NSs and show a constant length/width ratio regardless of the size (Figure 4). These suggest that the growth of the on-wire NSs is mainly governed by the intrinsic thermodynamics factors of GeS materials, and imply that the surface of the NW treated with air exposure does not substantially affect the growth phase. Since we can exclude a substantial role of the NW surface in the phase of growth, it is reasonable to conclude that the activation role of the air exposure mainly lies in facilitating the nucleation of NSs at the NW surface.

We believe that the air exposure facilitates the nucleation of NSs by modifying the surface of the NW. The exposure to air could modify the NW surface through multiple ways, for

dx.doi.org/10.1021/nl303876a | *Nano Lett.* XXXX, XXX, XXX−XXX

instance, introduction of moisture or dust. However, our experimental results seem to suggest that a mild oxidation at the NW surface caused by the exposure plays an important role in activating the on-wire growth of NSs. It has been known that germanium sulfide can be gradually oxidized into germanium oxide by the oxygen in air, in particular, with the presence of moisture.[23] The oxidized part of the NW surface, which could bear different surface properties (e.g., defects, surface energy, strain energy) from those of pristine NW surfaces, may serve as favorite nucleation sites for the growth of NSs. In contrast, the nucleation at the pristine surface of as-grown NWs may need to overcome a larger energy barrier due to, for example, a close-to-perfect atomic arrangement that provides fewer nucleation sites. It has been well-known that in the vapor deposition process imperfect substrates with defects at the surface can better facilitate the nucleation than perfect crystals.[20,24] As corroborating evidence, we found in experiments that the NWs with longer exposure time to air, for instance, 1 week, typically had a better chance to yield NS−NW heterstructures than the NWs with a shorter exposure time, e.g., a couple of minutes (Figure S3, Supporting Information).

To further support the role of oxidation in the activation of the NW surface for crystal growth, we performed the synthesis of heterostructures using two other processes that were designed to introduce different degrees of oxidation. In one process, we changed the carrier gas from 5% H_2/Ar to pure Ar and kept the NWs not exposed to air (similar to the process described in Figure 3a except the carrier gas). Unlike the amorphous shell yielded under H_2/Ar (Figure 3c), we can find that the deposition on the pre-grown NWs under the gas of Ar may give rise to a growth of crystalline GeS in the radial direction of the NW, which leads to a substantial increase in the radius (the size of pre-grown NWs is typically in a range from tens to hundreds of nanometers, but the NW after the second deposition under Ar can be around 2 μm, as shown in Figure 6a). As a result of the crystal growth in the radial direction, the surface of the resulting NW is very rough, but no well-defined NSs can be found (Figure 6a). This radial growth may be ascribed to an oxidation of the NW surface caused by a trace amount of O_2 residue in the synthetic setup. The oxidation effect of the O_2 residue was suppressed when using H_2/Ar as a carrier gas. In the other process, we took the pre-grown NWs out of the synthetic setup for oxygen plasma treatment prior to initiating the second growth (similar to the process described in Figure 3b except the way to treat the NWs). We can find very bulky crystals with faceted planes grown at the NW (Figure 6b,c), which is substantially different from the on-wire NSs grown at the NWs treated by natural air exposure. For example, the ratio of its lateral size (the dimension perpendicular to the NW axis) to thickness (the dimension parallel to the NW axis) is around 1, in orders of magnitude less than that of typical on-wire NSs. The morphological difference is reminiscent of the different growth modes (epitaxial growth and island growth) in conventional thin film depositions caused by the lattice mismatch degree between overlayers and substrates.[25] This growth of bulky crystals might be related with the greater oxidation of the NW by oxygen plasma treatment, which may cause a substantial change in the crystal lattice of the NWs and thus makes the epitaxial growth of NSs from the NW difficult. These results further confirm that oxidation plays a critical role in activating the NW surface for crystal growth. It also indicates that a proper degree of oxidation is necessary to achieve optimized growth of thin NSs at the NWs. Over-oxidizing the NWs could compromise the epitaxial growth of NSs. While to quantitatively understand the right range of oxidation for optimized growth of on-wire NSs necessitates more studies, our experiments demonstrate that natural exposure to air can give rise to oxidation in the right range.

In conclusion, we demonstrate a strategy to synthesize a new type of heterostructure that consists of branched 2D nanosheets (NSs) epitaxially growing at 1D nanowires (NWs). Our strategy involves using materials with layered structures, which is GeS in this study. It also involves a process of seeded growth where NWs were grown first as seeds followed by an epitaxial growth of NSs at the pre-grown NWs. We demonstrate that exposing the pre-grown NWs to air plays a critical role in the seeded growth. This might be due to the fact that the exposure to air can cause a mild degree of oxidation at the NW surface, which can subsequently facilitate the nucleation of the NSs. We also find that the surface oxidation needs to be controlled in a proper range in order to achieve optimized NS growths. For instance, a heavier oxidation may compromise the NS growth at the NW surface. While the focus of this work is on GeS, we believe that this strategy can generally apply to the synthesis of NS−NW heterostructures of many other layered chalcogenide materials, including structures with different materials in the NW and the NS. The NS−NW heterostructure provide an architecture to integrate the extraordinary properties of 1D NWs and 2D NSs into a 3D space. It holds great potential in applications that request complex nanomaterials with multiple functionality, high surface area, and efficient charge transport. For instance, this heterostructure can be useful for solar energy as photovoltacis and energy storage such as super capacitor and lithium ion battery. The backbone NW can provide an efficient channel for transport of charge carriers, and the 2D nanosheets can provide a large area that cannot be obtained with NWs. The epitaxial NS−NW heterostructure can also be very useful for other important fields, such as 3D optoelectronics and sensing.

■ ASSOCIATED CONTENT

Ⓢ Supporting Information

Figures showing structure characterizations of GeS NWs grown by gold-catalyzed vapor deposition and twinned GeS NWs and SEM images of the resulting structures grown at the pre-grown NWs that were naturally exposed to air. This material is available free of charge via the Internet at http://pubs.acs.org.

■ AUTHOR INFORMATION

Corresponding Author

*E-mail: lcao2@ncsu.edu.

Author Contributions

‖These authors contributed equally to this work.

Notes

The authors declare no competing financial interest.

■ ACKNOWLEDGMENTS

The authors acknowledge support from the Army Research Office (W911NF-11-1-0529). L.C. acknowledges a Ralph E. Powe Junior Faculty Enhancement Award for Oak Ridge Associated Universities. Part of the TEM work was performed at ShaRE user facility at ORNL, which is sponsored by the Office of Basic Energy Sciences, U.S. Department of Energy.

REFERENCES

(1) Lauhon, L. J.; Gudiksen, M. S.; Wang, D.; Lieber, C. M. *Nature* **2002**, *420* (6911), 57−61.
(2) Milliron, D. J.; Hughes, S. M.; Cui, Y.; Manna, L.; Li, J. B.; Wang, L. W.; Alivisatos, A. P. *Nature* **2004**, *430* (6996), 190−195.
(3) Tian, B.; Xie, P.; Kempa, T. J.; Bell, D. C.; Lieber, C. M. *Nat. Nanotechnol.* **2009**, *4* (12), 824−829.
(4) Wang, D.; Qian, F.; Yang, C.; Zhong, Z. H.; Lieber, C. M. *Nano Lett.* **2004**, *4* (5), 871−874.
(5) Dabbousi, B. O.; RodriguezViejo, J.; Mikulec, F. V.; Heine, J. R.; Mattoussi, H.; Ober, R.; Jensen, K. F.; Bawendi, M. G. *J. Phys. Chem. B* **1997**, *101* (46), 9463−9475.
(6) Weisbuch, C.; Vinter, B. *Quantum Semiconductor Structures: Fundamentals and Applications*; Academic Press: San Diego, CA, 1991.
(7) Ando, T.; Fowler, A. B.; Stern, F. *Rev. Mod. Phys.* **1982**, *54* (2), 437−672.
(8) Kosterlitz, J. M.; Thouless, D. J. *J. Phys. C: Solid State Phys.* **1973**, *6* (7), 1181−1203.
(9) Zhu, J.; Peng, H.; Marshall, A. F.; Barnett, D. M.; Nix, W. D.; Cui, Y. *Nat. Nanotechnol.* **2008**, *3* (8), 477−481.
(10) Jiang, Z.; Qing, Q.; Xie, P.; Gao, R. X.; Lieber, C. M. *Nano Lett.* **2012**, *12* (3), 1711−1716.
(11) Lu, W.; Xiang, J.; Timko, B. P.; Wu, Y.; Lieber, C. M. *Proc. Natl. Acad. Sci. U.S.A.* **2005**, *102* (29), 10046−10051.
(12) Shi, J.; Hara, Y.; Sun, C. L.; Anderson, M. A.; Wang, X. D. *Nano Lett.* **2011**, *11* (8), 3413−3419.
(13) Sun, K.; Jing, Y.; Li, C.; Zhang, X. F.; Aguinaldo, R.; Kargar, A.; Madsen, K.; Banu, K.; Zhou, Y. C.; Bando, Y.; Liu, Z. W.; Wang, D. L. *Nanoscale* **2012**, *4* (5), 1515−1521.
(14) Tang, J. Y.; Huo, Z. Y.; Brittman, S.; Gao, H. W.; Yang, P. D. *Nat. Nanotechnol.* **2011**, *6* (9), 568−572.
(15) Cho, I. S.; Chen, Z. B.; Forman, A. J.; Kim, D. R.; Rao, P. M.; Jaramillo, T. F.; Zheng, X. L. *Nano Lett.* **2011**, *11* (11), 4978−4984.
(16) Dorfs, D.; Salant, A.; Popov, I.; Banin, U. *Small* **2008**, *4* (9), 1319−1323.
(17) Antunez, P. D.; Buckley, J. J.; Brutchey, R. L. *Nanoscale* **2011**, *3*, 2399−2411.
(18) Kato, N.; Fukano, T.; Takeda, Y.; Takeichi, A.; Motohiro, T.; Kawai, S. *J. Appl. Phys.* **2006**, *100*, 113115.
(19) Huang, C. C.; Hewak, D. W.; Badding, J. V. *Opt. Express* **2004**, *12*, 2501−2506.
(20) Levitt, A. P. *Whisker Technology*; Wiley: New York, 1970.
(21) Li, C.; Huang, L.; Snigdha, G.; Yu, Y.; Cao, L. *ACS Nano* **2012**, *6*, 8868−8877.
(22) Wiedemeier, H.; Schnering, H. G. V. *Z. Kristallogr.* **1978**, *148*, 295−303.
(23) Kalebailaa, K. K.; Georgievb, D. G.; Brock, S. L. *J. Non-Cryst. Solids* **2006**, *352*, 232−240.
(24) Pierson, H. O. *Handbook of Chemical Vapor Deposition: Principles, Technology and Applications*; William Andrew: Norwich, NY, 1999.
(25) Venables, J. A.; Spiller, G. D. T.; Hanbucken, M. *Rep. Prog. Phys.* **1984**, *47* (4), 399.

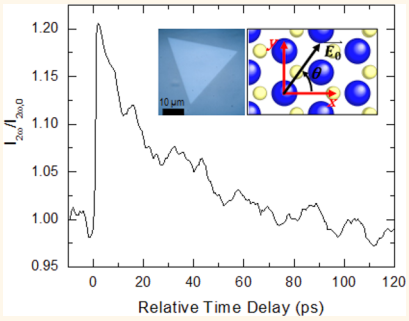
dx.doi.org/10.1021/nl303876a | *Nano Lett.* XXXX, XXX, XXX−XXX

Ultrafast Electronic and Structural Response of Monolayer MoS_2 under Intense Photoexcitation Conditions

Ehren M. Mannebach,[†] Karel-Alexander N. Duerloo,[†] Lenson A. Pellouchoud,[†] Meng-Ju Sher,[‡] Sanghee Nah,[†,‡] Yi-Hong Kuo,[§] Yifei Yu,[⊥] Ann F. Marshall,[∥] Linyou Cao,[⊥] Evan J. Reed,[†] and Aaron M. Lindenberg[*,†,‡,#]

[†]Department of Materials Science and Engineering, Stanford University, Stanford, California 94305, United States, [‡]Stanford Institute for Materials and Energy Sciences, SLAC National Accelerator Laboratory, Menlo Park, California 94025, United States, [§]Department of Electrical Engineering, Stanford University, Stanford, California 94305, United States, [⊥]Department of Materials Science and Engineering, North Carolina State University, Raleigh, North Carolina 27695, United States, [∥]Stanford Nanocharacterization Laboratory, Stanford University, Stanford, California 94305, United States, and [#]PULSE Institute, SLAC National Accelerator Laboratory, Menlo Park, California 94025, United States

ABSTRACT We report on the dynamical response of single layer transition metal dichalcogenide MoS_2 to intense above-bandgap photoexcitation using the nonlinear-optical second order susceptibility as a direct probe of the electronic and structural dynamics. Excitation conditions corresponding to the order of one electron–hole pair per unit cell generate unexpected increases in the second harmonic from monolayer films, occurring on few picosecond time-scales. These large amplitude changes recover on tens of picosecond time-scales and are reversible at megahertz repetition rates with no photoinduced change in lattice symmetry observed despite the extreme excitation conditions.



KEYWORDS: molybdenum disulfide · MoS_2 · second harmonic generation · ultrafast dynamics · monolayer · femtosecond

Intense efforts in the past few years have focused on the novel electronic, optical, and structural properties exhibited by molybdenum disulfide and related two-dimensional transition metal dichalcogenides. These include the emergence of a direct band gap,[1,2] strong light-matter interactions,[3,4] enhanced catalytic activity,[5,6] unique semiconducting and metallic structural phases controllable by strain,[5,7−10] and the ability to withstand extreme strains without plastic deformations.[11−14] 2D transition metal dichalcogenides typically consist of two hexagonal planes of chalcogen atoms separated by a hexagonal layer of metal atoms with trigonal prismatic coordination. Whereas bulk versions are centrosymmetric, inversion symmetry is broken for monolayers (and in general for odd numbers of layers), which results in novel valley-dependent selection rules,[15,16] as well as piezoelectric[17] and nonlinear optical responses[18,19] emergent in the single layer limit. Little is known about the dynamical electronic and structural processes that underlie these novel effects or the associated differences in the dynamics exhibited by few layer compared to bulk materials. In particular, the extreme stresses these materials are capable of withstanding point toward novel opportunities for dynamic control of these functional responses using light and other time-dependent stimuli. Although prior time-resolved optical pump–probe studies have investigated carrier relaxation and scattering processes at low photoexcitation conditions,[20−26] the electronic dynamics of two-dimensional systems have not been investigated in a regime associated with large amplitude strains, temperature jumps, or electronic excitation conditions, and the structural dynamics have not been probed at all. Here we present first measurements of the time-dependent structural and electronic response of 2D (single layer) MoS_2 following above-bandgap excitation at megahertz repetition rates, in a regime corresponding to of order one absorbed photon per unit cell

* Address correspondence to aaronl@stanford.edu.

Received for review August 9, 2014 and accepted September 22, 2014.

Published online September 22, 2014
10.1021/nn5044542

© 2014 American Chemical Society

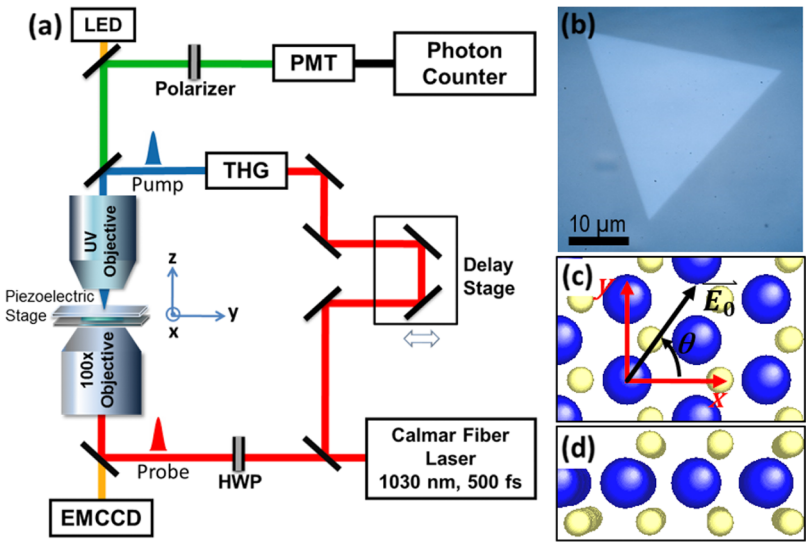


Figure 1. (a) Experimental schematic. 343 or 266 nm light is used to optically excite large-area monolayers of MoS_2, (b) and the time response of the second harmonic generation efficiency is measured. All experiments are done on single crystalline domains of monolayer MoS_2. (c) Top-view schematic of the MoS2 crystal structure with *x* and *y* axes labeled. Blue and yellow spheres correspond to Mo and S atoms, respectively. (d) Side-view along $\hat{y}$ (perpendicular to the plane of the paper) of the MoS_2 crystal structure.

($\sim 10^{15}$/cm^2, ~10% valence band excitation). These excitation conditions transform 2H-MoS_2 into a degenerate semiconductor/metal, with simple estimates of the transient lattice temperature jump of approximately 3000 K,[27] neglecting thermal conduction into the substrate and modifications in the linear optical properties. The associated dynamical response is probed using the second order nonlinear optical susceptibility as reflected in the second harmonic generated by the monolayer. This provides a direct crystallographically sensitive, all-optical probe of the trigonal symmetry of the material and its transient response. Despite these extreme excitation conditions, we observe large amplitude *increases* in the second harmonic generation occurring on few picosecond time-scales, indicative of the stability of these materials, with no evidence for disordering or melting responses as is observed in bulk semiconducting systems[28−30] under similar excitation conditions. Comparison with complementary measurements of the linear optical properties and with first-principles modeling of both the linear and nonlinear optical susceptibility show the observed effects can be associated with the extreme electronic temperatures induced without modification of the unit cell structure. The possibilities of optically inducing such large modifications to the electronic properties of these systems without concomitant structural changes open up new possibilities for reversible all-optical modulation and control of the optoelectronic properties of two-dimensional transition metal dichalcogenide materials under excitation conditions not sustainable in bulk systems.

RESULTS AND DISCUSSION

As reported previously by other groups,[18,19,31,32] we observe strong static second harmonic generation (SHG) from MoS_2 monolayers. A typical plot showing the dependence of the SHG intensity on the polarization of the incident probe light for a fixed output second harmonic (SH) polarization (either parallel or perpendicular to the experimental table, see Figure 1a) is given as Figure S1 (Supporting Information). The observed symmetry is consistent with the known D_{3h} symmetry group for monolayer 2H-MoS_2 with $I_x^{2\omega} \propto \cos^2(2\theta + \theta_0)$ and $I_y^{2\omega} \propto \sin^2(2\theta + \theta_0)$, where x, y, and θ are defined in Figure 1c, and θ_0 is a rotation of the MoS_2 crystallographic axes with respect to the x-direction.

Figure 2a shows the time-dependent response of the SHG efficiency (1030 nm probe) following above-bandgap photoexcitation with 343 nm light at ~10 mJ/cm^2. We observe an initial increase in the second harmonic of a few tens of percent that turns on within ~2 ps. Taking approximately known above-bandgap absorption coefficients of $\sim 10^6$ cm^{-1},[4] corresponding to an absorption of approximately 10% for a single monolayer, an excitation fluence of 10 mJ/cm^2 generates approximately 10^{15} e−h pairs/cm^2 ($\sim 10^{22}$ cm^{-3}), neglecting reflection losses. Under the approximation that carrier−carrier scattering equilibrates the electronic system at a well-defined electron temperature and quasi-Fermi level within a few hundred femtoseconds,[33] treating the electronic system as a degenerate 2D free electron gas then defines a quasi-Fermi energy $\varepsilon_F = \pi N\hbar^2/m \sim 2$ eV above the bottom of the conduction band, where N is the electron density.[34] Under the assumption of a parabolic band, equating the energy density of a 2D Fermi gas to the absorbed energy density then defines an electron temperature of ~1.4 eV = 16 000 K. These estimates are in agreement with density functional theory (DFT) calculations showing that carrier concentrations of 10^{15} cm^{-2}

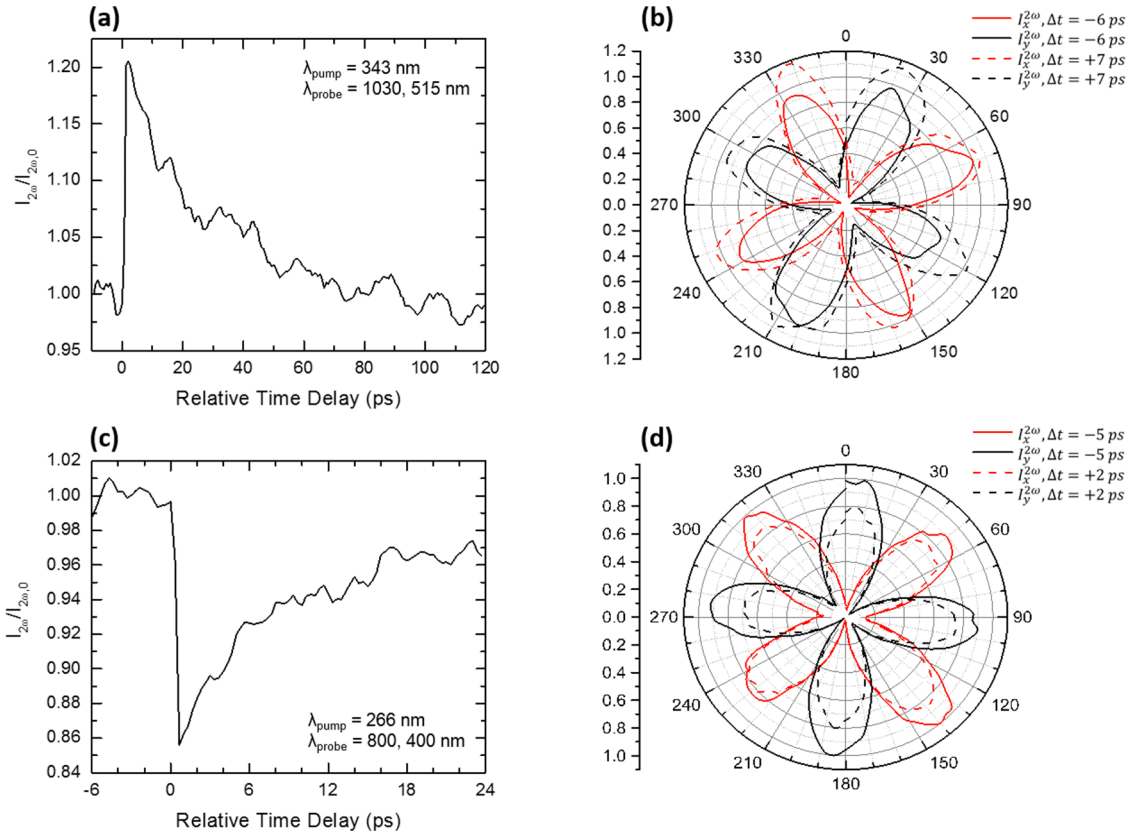


Figure 2. (a,c) Time-dependence of the SH response following above-bandgap excitation with 343 nm pump/1030 nm probe (a) and 266 nm pump/800 nm probe (c). In both cases, the effect reaches its maximum magnitude within the time resolution of the experiment. (b,d) Polarization dependence of the SH response before (solid lines) and after (dashed lines) above-bandgap excitation with 343 nm pump/1030 nm probe (b) and 266 nm pump/800 nm probe (d). The black and red data show *x*- and *y*-polarized SH light, respectively.

correspond to electron temperatures of ~10 000 K (Supporting Information). These conditions essentially define a quasi-half-filled conduction band and metallic-like characteristics, with interelectron spacing comparable to the electron de Broglie wavelength. Similar results are obtained treating the system as a 3D single layer of unit cells. Previous studies[28,30,35,36] have used the static second order susceptibility as a direct measure of photoinduced structural changes, observing large amplitude decreases in the SH under similar excitation conditions, associated with a transition from a noncentrosymmetric structure to a disordered or molten centrosymmetric one. The large-amplitude increases in SH and the fast recovery of the response indicate that these disordering effects are not relevant for monolayer MoS_2 despite the extreme excitation conditions utilized. This is further supported by the well-defined polarization dependence measured at t = 7 ps after time zero, showing no evidence for structural modulations, which would appear as a change in the symmetry of the polarization dependent plot (Figure 2b). Furthermore, a complex wavelength dependence of the induced changes in SH is observed. In contrast to the increase in SH signal seen in Figure 2a, the SHG response of an 800 nm probe beam is decreased by ~14% following above-bandgap excitation at 266 nm at ~10 mJ/cm^2 (Figure 2c), yielding similar densities of photoexcited carriers. Like the 1030 nm probe/343 nm pump conditions, the polarization traces before and after pumping (Figure 2d) change only in their magnitude, indicating that no structural transformation took place. The difference in recovery dynamics between the two probe conditions is likely explained by different carrier relaxation time scales at the two different second harmonic wavelengths, also observed when probing the linear optical properties (see Figure 4b,c and Figure S3d) as described below.

One can understand this unusual dynamical response by taking into the account the quasi-metallic-like state that is created at short times, and in particular, the dependence of the second-order nonlinear susceptibility on electron temperature. The second harmonic efficiency of a solid is often phenomenologically described in terms of contributions from valence band and conduction band states, reflecting bound and free charge contributions.[37−44] In metals, prior studies have shown an enhancement of the second harmonic efficiency with increasing electron temperature, dependent on the occupation of states within a partially filled

band.[37−39] In this model, the effective nonlinear susceptibility for the carriers is determined by considering this process as the absorption by a carrier of energy ε through two states of energy $\varepsilon + \hbar\omega$ and $\varepsilon + 2\hbar\omega$ followed by the subsequent re-emission of a photon at 2ω. The probability of this process will be proportional to the product $f(\varepsilon)[1 - f(\varepsilon - \hbar\omega)][1 - f(\varepsilon - 2\hbar\omega)][1 - f(\varepsilon)]$, where f is the Fermi−Dirac occupation factor, dependent on the electronic temperature. It is seen from this expression that this product increases as the distribution function broadens with increasing electron temperature, qualitatively explaining an effective increase of the susceptibility with electron temperature.

To investigate the potential magnitude of purely electronic changes in the SH response, we compute the linear susceptibility spectrum from first-principles and use the semiclassical two-point proportionality known as Miller's Rule.[45] This states that given a linear susceptibility spectrum, the second harmonic response follows $\chi^{(2)}(2\omega) \sim \chi^{(1)}(\omega)\chi^{(1)}(\omega)\chi^{(1)}(2\omega)$. The linear susceptibility can be derived for a set of independent electron wave functions, resulting in the well-known Kubo−Greenwood formula.[46] We utilize density functional theory (DFT) calculations as implemented in the Elk full-potential linearized augmented plane wave (FP-LAPW) code[47] to obtain independent electron (Kohn−Sham) wave functions. The wave functions are computed with self-consistent Fermi−Dirac occupancies for a given electronic temperature. Elk implements a perturbative approach for computing first-order (Kubo−Greenwood) and second-order optical coefficients from momentum matrix elements computed from these wave functions with Fermi−Dirac occupancies.[48] This approach neglects excitonic self-trapping of carriers and correlation effects that can play a role in the magnitude of quasiparticle gaps and other quantitative spectral features,[49,50] but is expected to provide qualitative guidance regarding trends with respect to electronic temperature.[51−53]

We have computed $\chi^{(1)}$ spectra and the corresponding Miller's Rule $\chi^{(2)}$ spectra for several electronic temperatures between 0 K and 16 000 K, the results of which are shown in Figure 3. We observe that at higher photon energies, Miller's Rule predicts a damping of the SH response with increasing electronic temperature. Below the calculated absorption edge, it is predicted that the SH response will increase dramatically with increasing electronic temperature, with percent-level changes comparable to those observed experimentally, associated with a strong increase in absorption below gap. The sub-bandgap absorption that is predicted to occur with increasing electronic temperature (Figure 3a, bottom) is seen in linear pump−probe experiments at optical and THz wavelengths, shown in Figures S3 and S5, further supporting this argument, and may be qualitatively understood in terms of interband excitations (within both valence and

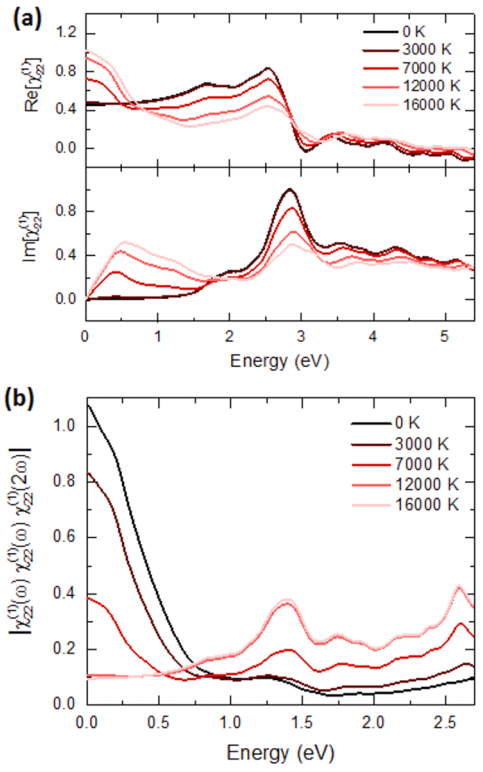


Figure 3. (a) Real (top) and imaginary (bottom) parts of the first order susceptibility, $\chi^{(1)}$. (b) Second harmonic optical response based on the Miller's Rule two-point proportionality to the first-order response spectra.

conduction bands) occurring as the electronic temperature increases and the distribution functions broaden. Additionally, the theory predicts that above a certain photon energy, an increase in electronic temperature leads to a damping of the SH response, consistent with the change in the sign of SHG modulation between the 1030 nm probe and 800 nm probe (Figure 2a,c). It is important to remember that the approach used in the calculations presented here only provide qualitative information concerning trends with changes in electronic temperature. Measurements of the modulation in the transmission (with $\Delta T/T \propto -\Delta\alpha/\alpha$) of the 500 and 400 nm linear probe beams (Figure 4) support the trends given by Miller's Rule: an increase in the absorption at 500 nm (*i.e.*, increase in $\chi^{(1)}(2\omega)$) gives rise to an increase in the second order susceptibility of MoS_2 at λ = 1030 nm. Likewise, a decrease in $\chi^{(1)}$ (400 nm) yields a decrease in $\chi^{(2)}$ (800 nm).

In addition to the Kubo−Greenwood-based Miller's Rule calculations, we have modified a portion of the Elk code to compute $\chi^{(2)}$ spectra with finite electron temperatures by perturbation theory. We expect these computations to provide a qualitative understanding analogous to the Kubo−Greenwood formula for the linear spectra,[54] and we note that both approaches employ DFT wave functions, lacking the excited-state electronic correlations that give accurate quasi-particle energies and electron−hole interactions that give rise

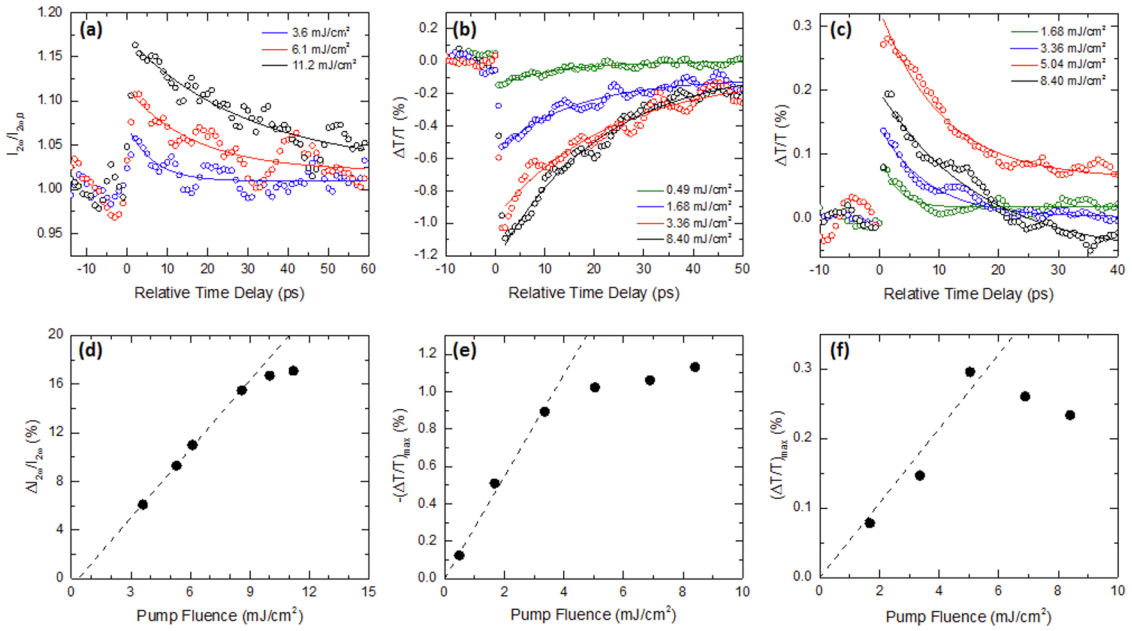


Figure 4. (a−c) Fluence dependence of the time-dependent SH response with 1030 nm probe (a) and linear absorption responses at 500 nm (b) and 400 nm (c) probe wavelengths. (d−f) Magnitude of the maximum change in SH (d), 500 nm absorption (e), and 400 nm absorption (f) as a function of above-bandgap excitation fluence. Some data sets are omitted from (a−c) for clarity.

to excitons. The computational cell of MoS_2 used for these calculations is described in detail in the Supporting Information, Part 4. With the atomic positions and computational cell fixed, we solved the DFT electronic system (density, independent electron wave functions, Fermi energy, and Fermi−Dirac occupancies) for several electronic temperatures between 0 K and 16 000 K. We then applied expression B1 from Hughes *et al.*[48] to obtain the $\chi^{(2)}$ spectra shown in Figure S6. While we expect the SHG efficiency to have a peak at half of the experimental direct optical gap (0.95 eV), the response based on DFT will arise at half of the DFT gap (0.85 eV). Figure S6 shows how transitions between pairs of valence states and between pairs of conduction states (all with fractional occupancy) give rise to a drastic increase in the SH response at low frequencies as electronic temperature increases, which is qualitatively similar to the results predicted using semiclassical Miller's Rule. At higher frequencies, the full perturbative approach yields a more nuanced behavior in the SH response with increasing electronic temperature than Miller's Rule, which predicts a monotonic damping of the SH response with increasing electronic temperature.

Further evidence for the claim that the modulations in the SH response are purely electronic in nature is obtained by examining the fluence dependence of the SH and linear optical time response as shown in Figure 4. Probing with a fundamental wavelength of 1030 nm, we observe a linear dependence of the magnitude of the increase in SHG with pump fluence until ~10 mJ/cm^2, at which point evidence for saturation is observed (Figure 4a,d). At these fluences, simple estimates show that approximately one photon is absorbed per unit cell, and one would expect both removal of valence band states and filling of conduction band states (*e.g.*, a Burstein−Moss shift) to lead to effects consistent with this observed saturation. Linear transmission measurements with a 400 nm pump beam (resonant with the C exciton, Figure S2) and 500 nm (Figure 4b,e) and 400 nm (Figure 4c,f) probe beams indicate evidence for saturable absorption at similar absorbed pump energies (Figure S2). For the 400 nm pump, 400 nm probe linear transmission measurements, a coherent interference effect at time zero was subtracted from the data (Supporting Information, Figure S4). We note that slow modulations observed in the data before and after time zero are likely associated with percent-level drifts in the laser power or detection electronics and not associated with acoustic responses.[55] It has also been reported[23] that dispersions of few-layer MoS_2 nanosheets (E_{gap} ~ 1.2 eV) exhibit saturable absorption of 800 nm (1.5 eV) light at fluences of ~40 mJ/cm^2. These results suggest that the apparent saturation in the magnitude of the increase in SHG from monolayer MoS_2 is due in part to saturable absorption of the 343 nm pump light and show that the SH response follows the linear optical response. Figure 5 directly shows that the modulation of the SH response and the linear transmission response at the corresponding SH wavelength relax on the same time scale. This is true for both the 1030 and 800 nm probes as shown in Figure 5a and Figure 5b, respectively, and is in accordance with the argument that the SH measurements are sensitive to carrier cooling and Miller's Rule. In both wavelength sets displayed in Figure 5, pump fluences were chosen so

that the absorbed energy per pump pulse was similar (Figure S2). This is important in particular because of the variation in decay times with fluence for 400 nm probes (Figure S3d). The tens-of-picosecond decay constants in the exponential fits in Figures 4 and 5 are roughly consistent with those reported at smaller pump fluences,[22,26] which correspond to electron–phonon coupling time-scales. The signal recovery is complete at the 1.28 MHz, 5.12 MHz, and 1 kHz repetition rates of these experiments, with rapid cooling into the sapphire substrate eventually bringing the monolayer system back into its initial state. Although exact values for the interfacial thermal resistances are not known, using rough values for the heat capacity per area and typical values for interfacial thermal resistances ($\sim 10^{-6}$–10^{-7} K·m^2/W) gives a thermal time constant of order 100 ps for thermal transport into the substrate.

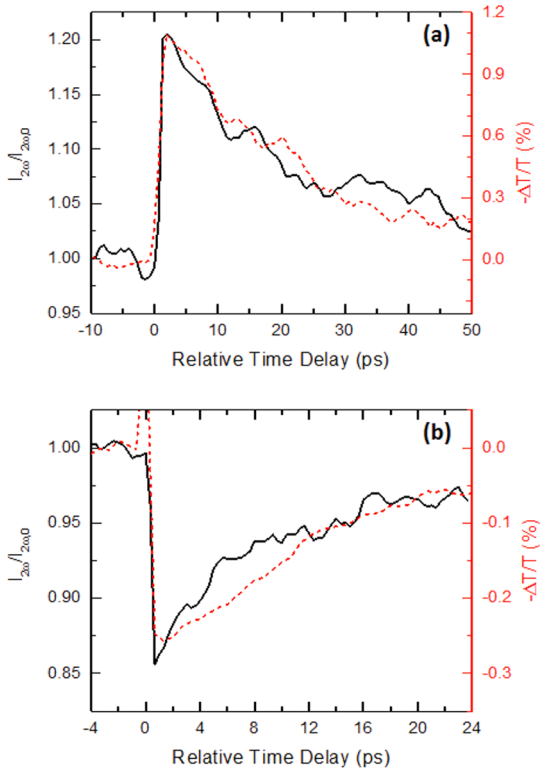


Figure 5. Time-dependent SHG (solid black lines) and linear transmission (dashed red lines) responses at equivalent absorbed pump energies. SH probe wavelengths are 1030/515 nm (a) and 800/400 nm (b). Transmission probe wavelengths are 500 nm (a) and 400 nm (b). 343 nm (a) and 266 nm (b) pump fluences for the SHG measurements were ~10 mJ/cm^2. 400 nm pump fluences for both transmission measurements were ~5 mJ/cm^2.

We note that in contrast to the extreme stability exhibited by these materials to transient photoexcitation, we do not observe similar stability under static heating. We have carried out complementary temperature-dependent transmission electron microscopy (TEM) measurements with static heating up to temperatures of order 1000 °C. These measurements show that single-domain monolayer MoS_2 undergoes an irreversible change at temperatures much lower than those we induce optically. Figure 6 shows selected-area electron diffraction patterns from monolayer MoS_2 at several different temperatures. Starting at ~900 °C, the $\{10\bar{1}0\}$ and the $\{11\bar{2}0\}$ reflections (q = 3.63 nm^{-1} and q = 6.29 nm^{-1}, respectively) begin to disappear and diffuse reflections at ~4.0 and 6.49 nm^{-1} emerge. These diffuse peaks are azimuthally broadened, suggesting decomposition into nanoscale domains with similar orientations to the original film.

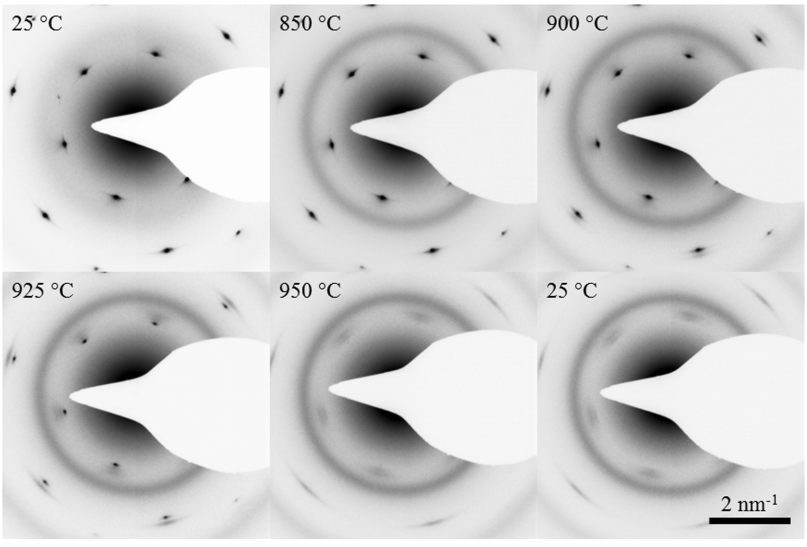


Figure 6. Selected-area electron diffraction patterns from a single-crystal domain of monolayer MoS_2 film at 25, 850, 900, 925, 950 °C, and cooled back to 25 °C. It can be seen that the film begins to undergo an irreversible transition starting at ~900 °C. The sharp reflections from the MoS_2 single crystal begin to disappear while more diffuse reflections in the same orientation but corresponding to smaller *d*-spacings begin to emerge. The diffuse ring in all images is from the ultrathin amorphous carbon film supporting the MoS_2 monolayer.

The diffuse peak at ~4.0 $Å^{-1}$ is additionally split, suggesting symmetry breaking. At ~950 °C, the decomposition is complete and does not recover upon cooling back to room temperature. Molecular dynamics simulations also indicate that monolayer MoS_2 should rapidly decompose when heated to high temperatures (see Supporting Information, Part 5).

CONCLUSIONS

In summary, we present first measurements of the time-dependent structural and electronic response of MoS_2 monolayers following intense above-bandgap excitation at megahertz repetition rates. This excitation regime corresponds to approximately one absorbed photon per unit cell (~10^{15}/cm^2) and transient temperature increases of a few thousand degrees Kelvin. We observe an increase in $\chi^{(2)}$ associated with the contribution of photoexcited carriers to an effective conduction band free electron susceptibility, with the magnitude of the modulation saturating at ~10 mJ/cm^2 excitation fluence. No evidence for disordering, decomposition, or structural rearrangements is observed at any excitation fluence presented here. These measurements open up new opportunities for dynamic control of the electronic and optical properties of two-dimensional transition metal dichalcogenides under excitation conditions not sustainable in bulk systems.

MATERIALS AND METHODS

Large-area, single-crystal domain monolayers of MoS_2 were obtained by chemical vapor deposition (CVD)-growth on sapphire substrates using MoO_3 and S as precursors.[56] We confirmed the thickness of the MoS_2 samples with a combination of optical (Figures 1b, S2) and second-harmonic microscopies (Figure S1) as well as selected area electron diffraction (Figure 5). For the second-harmonic microscopy, we use a 500 fs Yb-doped fiber laser with a 1.28-MHz repetition rate, 2 W average power, and fundamental wavelength of 1030 nm (1.20 eV, below the direct bandgap of 1.9 eV for monolayer MoS_2) in a pump−probe geometry (Figure 1a). The probe beam is focused to a 1 μm diameter onto the sample (mounted on a piezoelectric stage) within a single crystalline domain (Figure 1b) at normal incidence by a 100× objective (NA 1.30) and immersion oil with refractive index 1.518. The transmitted signal is recollimated by a 13× UV objective (NA 0.13) and reflected by a dichroic mirror through a bandpass filter centered at the second harmonic (SH) wavelength (λ = 515 nm, 2.41 eV) to remove the transmitted fundamental and any ambient light. The SH signal is then detected by a photon counting photomultiplier tube and read out by a gated photon counter synchronized to the laser repetition rate. A half wave plate is used to rotate the polarization of the incident probe light with respect to the crystallographic orientation of the sample. For the time-resolved study, we split off a portion of the laser beam and frequency-triple (λ = 343 nm, 3.62 eV) the split-off beam in two nonlinear optical crystals (LBO/BBO) to create the pump beam. This is focused to a 2 μm spot size on the sample antiparallel to the probe beam by the same 13× UV objective that recollimates the SH signal. An electron-multiplying CCD camera allows for monitoring of the positions and spatial overlap of the sample and pump and probe beams. Additional pump−probe measurements using a 50 fs Ti:sapphire laser with a 5.12 MHz repetition rate, 2 W average power, and fundamental wavelength of 800 nm (1.55 eV, also below the direct gap of monolayer MoS_2) utilized the same microscope and photon-detection setup with dichroic mirrors and band-pass filters appropriate for 400 nm (3.10 eV) in place. The third harmonic (λ = 266 nm, 4.66 eV) was used as the pump beam. Complementary measurements of the static and time-dependent linear optical response both below and above bandgap were carried out within large area monolayer films grown by using $MoCl_5$ and S as precursors[57] using a 1 kHz Ti:sapphire-based regenerative amplifier system with white light probe (see Supporting Information).

In all experiments, we observe negligible signal from the bare sapphire substrate. The damage threshold was observed to be >14 mJ/cm^2 for the 343 nm pump (the immersion oil degraded before the MoS_2 was damaged), ~15 mJ/cm^2 for the 266 nm pump, and ~10 mJ/cm^2 for the 400 nm pump. Above the damage threshold, the films were ablated away, and any signal went to zero.

Conflict of Interest: The authors declare no competing financial interest.

Acknowledgment. This work is supported by the US Department of Energy, Basic Energy Science, Materials Science and Engineering Division. Computations were supported in part by NASA Space Technology Research Fellowship (NNX12AM48H) and were performed in part with the computational resources of the National Energy Research Scientific Computing (NERSC) Center, supported by the Office of Science and the United States Department of Energy (DE-AC02-05CH11231). Part of this work was performed at the Stanford Nano Center (SNC)/Stanford Nanocharacterization Laboratory (SNL) part of the Stanford Nano Shared Facilities. L. Cao acknowledges the support by a Young Investigator Award from the Army Research Office (W911NF-13-1-0201).

Supporting Information Available: Symmetry of the SH polarization, linear absorption measurements, THz transmission measurements, electronic structure calculations, *ab initio* molecular dynamics calculations, and figures. This material is available free of charge *via* the Internet at http://pubs.acs.org.

REFERENCES AND NOTES

1. Mak, K. F.; Lee, C.; Hone, J.; Shan, J.; Heinz, T. F. Atomically Thin MoS_2: A New Direct-Gap Semiconductor. *Phys. Rev. Lett.* **2010**, *105*, 136805.
2. Splendiani, A.; Sun, L.; Zhang, Y.; Li, T.; Kim, J.; Chim, C.-Y.; Galli, G.; Wang, F. Emerging Photoluminescence in Monolayer MoS_2. *Nano Lett.* **2010**, *10*, 1271–1275.
3. Britnell, L.; Ribeiro, R. M.; Eckmann, A.; Jalil, R.; Belle, B. D. D.; Mishchenko, A.; Kim, Y.-J. Y.-J.; Gorbachev, R. V. V; Georgiou, T.; Morozov, S. V. V; *et al.* Strong Light-Matter Interactions in Heterostructures of Atomically Thin Films. *Science* **2013**, *340*, 1311–1314.
4. Bernardi, M.; Palummo, M.; Grossman, J. C. Extraordinary Sunlight Absorption and One Nanometer Thick Photovoltaics Using Two-Dimensional Monolayer Materials. *Nano Lett.* **2013**, *13*, 3664–3670.
5. Voiry, D.; Yamaguchi, H.; Li, J.; Silva, R.; Alves, D. C. B.; Fujita, T.; Chen, M.; Asefa, T.; Shenoy, V. B.; Eda, G.; *et al.* Enhanced Catalytic Activity in Strained Chemically Exfoliated WS_2 Nanosheets for Hydrogen Evolution. *Nat. Mater.* **2013**, *12*, 850–855.
6. Yu, Y.; Huang, S.-Y.; Li, Y.; Steinmann, S. N.; Yang, W.; Cao, L. Layer-Dependent Electrocatalysis of MoS_2 for Hydrogen Evolution. *Nano Lett.* **2014**, *14*, 553–558.
7. Eda, G.; Fujita, T.; Yamaguchi, H.; Voiry, D.; Chen, M.; Chhowalla, M. Coherent Atomic and Electronic Heterostructures of Single-Layer MoS_2. *ACS Nano* **2012**, *6*, 7311–7317.

8. Chang, Y. M.; Xu, L.; Tom, H. W. K. Observation of Coherent Surface Optical Phonon Oscillations by Time-Resolved Surface Second-Harmonic Generation. *Phys. Rev. Lett.* **1997**, *78*, 4649–4652.
9. Lin, Y.-C.; Dumcenco, D. O.; Huang, Y.-S.; Suenaga, K. Atomic Mechanism of the Semiconducting-to-Metallic Phase Transition in Single-Layered MoS_2. *Nat. Nanotechnol.* **2014**, *9*, 391–396.
10. Duerloo, K.-A. N.; Li, Y.; Reed, E. J. Structural Phase Transitions in Two-Dimensional Mo- and W-Dichalcogenide Monolayers. *Nat. Commun.* **2014**, *5*, 4214.
11. Bertolazzi, S.; Brivio, J.; Kis, A. Stretching and Breaking of Ultrathin MoS_2. *ACS Nano* **2011**, *5*, 9703–9709.
12. Feng, J.; Qian, X.; Huang, C. C.; Li, J. Strain-Engineered Artificial Atom as a Broad-Spectrum Solar Energy Funnel. *Nat. Photonics* **2012**, *6*, 866–872.
13. Yu, D.; Feng, J.; Hone, J. Elastically Strained Nanowires and Atomic Sheets. *MRS Bull.* **2014**, *39*, 157–162.
14. van der Zande, A.; Hone, J. Inspired by Strain. *Nat. Photonics* **2012**, *6*, 804–806.
15. Xiao, D.; Liu, G.-B.; Feng, W.; Xu, X.; Yao, W. Coupled Spin and Valley Physics in Monolayers of MoS_2 and Other Group-VI Dichalcogenides. *Phys. Rev. Lett.* **2012**, *108*, 196802.
16. Mak, K. F.; He, K.; Shan, J.; Heinz, T. F. Control of Valley Polarization in Monolayer MoS_2 by Optical Helicity. *Nat. Nanotechnol.* **2012**, *7*, 494–498.
17. Duerloo, K.-A. N.; Ong, M. T.; Reed, E. J. Intrinsic Piezoelectricity in Two-Dimensional Materials. *J. Phys. Chem. Lett.* **2012**, *3*, 2871–2876.
18. Li, Y.; Rao, Y.; Mak, K. F.; You, Y.; Wang, S.; Dean, C. R.; Heinz, T. F. Probing Symmetry Properties of Few-Layer MoS_2 and H-BN by Optical Second-Harmonic Generation. *Nano Lett.* **2013**, *13*, 3329–3333.
19. Kumar, N.; Najmaei, S.; Cui, Q.; Ceballos, F.; Ajayan, P. M.; Lou, J.; Zhao, H. Second Harmonic Microscopy of Monolayer MoS_2. *Phys. Rev. B: Condens. Matter Mater. Phys.* **2013**, *87*, 161403.
20. Kumar, N.; Cui, Q.; Ceballos, F.; He, D.; Wang, Y.; Zhao, H. Exciton-Exciton Annihilation in $MoSe_2$ Monolayers. *Phys. Rev. B: Condens. Matter Mater. Phys.* **2014**, *89*, 125427.
21. Cui, Q.; Ceballos, F.; Kumar, N.; Zhao, H. Transient Absorption Microscopy of Monolayer and Bulk WSe_2. *ACS Nano* **2014**, *8*, 2970–2976.
22. Wang, R.; Ruzicka, B. A.; Kumar, N.; Bellus, M. Z.; Chiu, H.-Y.; Zhao, H. Ultrafast and Spatially Resolved Studies of Charge Carriers in Atomically Thin Molybdenum Disulfide. *Phys. Rev. B: Condens. Matter Mater. Phys.* **2012**, *86*, 45406.
23. Wang, K.; Wang, J.; Fan, J.; Lotya, M.; O'Neill, A.; Fox, D.; Feng, Y.; Zhang, X.; Jiang, B.; Zhao, Q.; *et al.* Ultrafast Saturable Absorption of Two-Dimensional MoS_2 Nanosheets. *ACS Nano* **2013**, *7*, 9260–9267.
24. Wang, Q.; Ge, S.; Li, X.; Qiu, J.; Ji, Y.; Feng, J.; Sun, D. Valley Carrier Dynamics in Monolayer Molybdenum Disulfide from Helicity-Resolved Ultrafast Pump-Probe Spectroscopy. *ACS Nano* **2013**, *7*, 11087–11093.
25. Yang, L.; Zhong, D.; Zhang, J.; Yan, Z.; Ge, S.; Du, P.; Jiang, J.; Sun, D.; Wu, X.; Fan, Z.; *et al.* Optical Properties of Metal-Molybdenum Disulfide Hybrid Nanosheets and Their Application for Enhanced Photocatalytic Hydrogen Evolution. *ACS Nano* **2014**, *8*, 6979–6985.
26. Shi, H.; Yan, R.; Bertolazzi, S.; Brivio, J.; Gao, B.; Kis, A.; Jena, D.; Xing, H. G.; Huang, L. Exciton Dynamics in Suspended Monolayer and Few-Layer MoS_2 2D Crystals. *ACS Nano* **2013**, *7*, 1072–1080.
27. The lattice temperature jump was estimated using the specific heat of bulk MoS_2 of 1.89 J cm^{-3} K^{-1}.
28. Shank, C.; Yen, R.; Hirlimann, C. Femtosecond-Time-Resolved Surface Structural Dynamics of Optically Excited Silicon. *Phys. Rev. Lett.* **1983**, *51*, 900–902.
29. Lindenberg, A. M.; Larsson, J.; Sokolowski-Tinten, K.; Gaffney, K. J.; Blome, C.; Synnergren, O.; Sheppard, J.; Caleman, C.; Macphee, a. G.; Weinstein, D.; *et al.* Atomic-Scale Visualization of Inertial Dynamics. *Science* **2005**, *308*, 392–395.
30. Shumay, I.; Höfer, U. Phase Transformations of an InSb Surface Induced by Strong Femtosecond Laser Pulses. *Phys. Rev. B: Condens. Matter Mater. Phys.* **1996**, *53*, 15878–15884.
31. Malard, L. M.; Alencar, T. V.; Barboza, A. P. M.; Mak, K. F.; de Paula, A. M. Observation of Intense Second Harmonic Generation from MoS_2 Atomic Crystals. *Phys. Rev. B: Condens. Matter Mater. Phys.* **2013**, *87*, 201401.
32. Wagoner, G. A.; Persans, P. D.; Van Wagenen, E. A.; Korenowski, G. M. Second-Harmonic Generation in Molybdenum Disulfide. *J. Opt. Soc. Am. B* **1998**, *15*, 1017–1021.
33. Ulbricht, R.; Hendry, E.; Shan, J.; Heinz, T. F.; Bonn, M. Carrier Dynamics in Semiconductors Studied with Time-Resolved Terahertz Spectroscopy. *Rev. Mod. Phys.* **2011**, *83*, 543–586.
34. Ashcroft, N. W.; Mermin, N. D. *Solid State Physics*; Holt, Rinehart and Winston: Boston, 1976.
35. Glezer, N.; Siegal, Y.; Huang, L.; Mazur, E. Behavior of $\chi^{(2)}$ During a Laser-Induced Phase Transition in GaAs. *Phys. Rev. B: Condens. Matter Mater. Phys.* **1995**, *51*, 9589–9596.
36. Akhmanov, S. A.; Koroteev, N. I.; Paitian, G. A.; Shumay, I. L.; Galjautdinov, M. F.; Khaibullin, I. B.; Shtyrkov, E. I. Pulsed-Laser Annealing of GaAs Surface Studied by Time-Resolved Second Harmonic Generation in Reflection. *Opt. Commun.* **1983**, *47*, 202–204.
37. Guo, C.; Rodriguez, G.; Taylor, A. Ultrafast Dynamics of Electron Thermalization in Gold. *Phys. Rev. Lett.* **2001**, *86*, 1638–1641.
38. Guo, C.; Rodriguez, G.; Hoffbauer, M.; Taylor, A. J. Influence of Electronic Temperature and Distribution on the Second-Order Surface Nonlinear Susceptibility of Metals. *Appl. Phys. Lett.* **2001**, *78*, 3211.
39. Papadogiannis, N. A.; Moustaizis, S. D. Nonlinear Enhancement of the Efficiency of the Second Harmonic Radiation Produced by Ultrashort Laser Pulses on a Gold Surface. *Opt. Commun.* **1997**, *137*, 174–180.
40. Bodlaki, D.; Borguet, E. Dynamics and Second-Order Nonlinear Optical Susceptibility of Photoexcited Carriers at Si(111) Interfaces. *Appl. Phys. Lett.* **2003**, *83*, 2357.
41. McClelland, A.; Fomenko, V.; Borguet, E. Ultrafast Time-Evolution of the Nonlinear Susceptibility of Hot Carriers at the Ge(111)−GeO_2 Interface As Probed by SHG. *J. Phys. Chem. B* **2004**, *108*, 3789–3793.
42. McClelland, A.; Fomenko, V.; Borguet, E. Ultrafast Hot-Carrier Dynamics at Chemically Modified Ge Interfaces Probed by SHG. *J. Phys. Chem. B* **2006**, *110*, 19784–19787.
43. Johnson, J. C.; Knutsen, K. P.; Yan, H.; Law, M.; Zhang, Y.; Yang, P.; Saykally, R. J. Ultrafast Carrier Dynamics in Single ZnO Nanowire and Nanoribbon Lasers. *Nano Lett.* **2004**, *4*, 197–204.
44. Son, D.; Wittenberg, J.; Banin, U.; Alivisatos, A. Second Harmonic Generation and Confined Acoustic Phonons in Highly Excited Semiconductor. *J. Phys. Chem. B* **2006**, *110*, 19884–19890.
45. Boyd, R. W. *Nonlinear Optics*; Academic Press: Waltham, MA, 2008.
46. Sharma, S.; Dewhurst, J. K.; Ambrosch-Draxl, C. Linear and Second-Order Optical Response of III-V Monolayer Superlattices. *Phys. Rev. B: Condens. Matter Mater. Phys.* **2003**, *67*, 165332.
47. Dewhurst, K.; Sharma, S.; Nordstrom, L.; Cricchio, F.; Bultmark, F.; Granas, O.; Gross, H.; Ambrosch-Draxl, C.; Persson, C.; Brouder, C.; *et al.* Elk Code, v. 2.3.22; 2014. http://elk.sourceforge.net.
48. Hughes, J. L. P.; Sipe, J. E. Calculation of Second-Order Optical Response in Semiconductors. *Phys. Rev. B: Condens. Matter Mater. Phys.* **1996**, *53*, 10751.
49. Shi, H.; Pan, H.; Zhang, Y.-W.; Yakobson, B. Quasiparticle Band Structures and Optical Properties of Strained Monolayer MoS_2 and WS_2. *Phys. Rev. B: Condens. Matter Mater. Phys.* **2013**, *87*, 155304.
50. Qiu, D. Y.; da Jornada, F. H.; Louie, S. G. Optical Spectrum of MoS_2: Many-Body Effects and Diversity of Exciton States. *Phys. Rev. Lett.* **2013**, *111*, 216805.

51. Alfè, D.; Pozzo, M.; Desjarlais, M. P. Lattice Electrical Resistivity of Magnetic Bcc Iron from First-Principles Calculations. *Phys. Rev. B: Condens. Matter Mater. Phys.* **2012**, *85*, 24102.
52. Knyazev, D. V.; Levashov, P. R. Ab Initio Calculation of Transport and Optical Properties of Aluminum: Influence of Simulation Parameters. *Comput. Mater. Sci.* **2013**, *79*, 817–829.
53. Clérouin, J.; Mazevet, S. Exploring Warm Dense Matter Using Quantum Molecular Dynamics. *J. Phys. IV* **2006**, *133*, 1071–1075.
54. Sharma, S.; Ambrosch-Draxl, C. Second-Harmonic Optical Response from First Principles. *Phys. Scr.* **2004**, *2004*, 128.
55. Ge, S.; Liu, X.; Qiao, X.; Wang, Q.; Xu, Z.; Qiu, J.; Tan, P.-H.; Zhao, J.; Sun, D. Coherent Longitudinal Acoustic Phonon Approaching THz Frequency in Multilayer Molybdenum Disulphide. *Sci. Rep.* **2014**, *4*, 5722.
56. Lee, Y.-H.; Zhang, X.-Q.; Zhang, W.; Chang, M.-T.; Lin, C.-T.; Chang, K.-D.; Yu, Y.-C.; Wang, J. T.-W.; Chang, C.-S.; Li, L.-J.; *et al.* Synthesis of Large-Area MoS_2 Atomic Layers with Chemical Vapor Deposition. *Adv. Mater.* **2012**, *24*, 2320–2325.
57. Yu, Y.; Li, C.; Liu, Y.; Su, L.; Zhang, Y.; Cao, L. Controlled Scalable Synthesis of Uniform, High-Quality Monolayer and Few-Layer MoS_2 Films. *Sci. Rep.* **2013**, *3*, 1866.

PHYSICAL REVIEW B **90**, 041414(R) (2014)

Exciton valley relaxation in a single layer of WS_2 measured by ultrafast spectroscopy

Cong Mai,[1] Yuriy G. Semenov,[2] Andrew Barrette,[1] Yifei Yu,[3] Zhenghe Jin,[2] Linyou Cao,[3,*]
Ki Wook Kim,[2,†] and Kenan Gundogdu[1,‡]

[1]*Department of Physics, North Carolina State University, Raleigh, North Carolina 27695, USA*
[2]*Department of Electrical and Computer Engineering, North Carolina State University, Raleigh, North Carolina 27695, USA*
[3]*Department of Material Science and Engineering, North Carolina State University, Raleigh, North Carolina 27695, USA*

(Received 21 May 2014; revised manuscript received 9 July 2014; published 31 July 2014)

We measured the lifetime of optically created valley polarization in single-layer WS_2 using transient absorption spectroscopy. The electron valley relaxation is very short (<1 ps). However, the hole valley lifetime is at least two orders of magnitude longer and exhibits a temperature dependence that cannot be explained by single-carrier spin/valley relaxation mechanisms. Our theoretical analysis suggests that a collective contribution of two potential processes may explain the valley relaxation in single-layer WS_2. One process involves direct scattering of excitons from K to K' valleys with a spin flip-flop interaction. The other mechanism involves scattering through the spin-degenerate Γ valley. This second process is thermally activated with an Arrhenius behavior due to the energy barrier between the Γ and K valleys.

DOI: 10.1103/PhysRevB.90.041414 PACS number(s): 73.21.−b, 78.47.J−, 71.35.−y

The discovery of graphene, a monolayer of carbon atoms, has inspired considerable interest in other two-dimensional (2D) material systems in search of exotic electronic, optical, and mechanical properties and novel practical applications [1–4]. In particular, two-dimensional transition metal dichalcogenides (TMDCs) recently emerged as promising material systems with many potential electronic applications. With their tunable direct gap in the visible range of the optical spectrum, absence of dangling bonds, and high surface-to-volume ratio, these 2D semiconducting systems are ideal for field-effect transistors, photovoltaics, light-emitting diodes (LEDs), molecule sensing, and electrocatalytic water splitting applications [5–14]. Moreover, due to strong spin-orbit splitting they have been subject to specific spin and valley applications. The optical band gaps in these structures are located at the K and $K' = -K$ points at the edge of the Brillouin zone. A strong spin-orbital coupling results in distinct states with different spin and valley indices so that K to K' elastic transition requires a spin flip for the electrons and holes. One immediate consequence of this property is the ability to control valley polarization, and hence the crystal quasimomentum of electrons, by using circularly polarized light, which is impossible in conventional semiconductors due to the negligible momentum of photons. This could open up opportunities for developing optoelectronic and valleytronic applications based on manipulation of spin and valley polarization of charge carriers [11–13,15–17].

Detailed understanding of intervalley relaxation dynamics is critical for the implementation of valleytronic applications. Very recently, numerous experimental and theoretical efforts have been devoted to characterization of the electronic structure and optical properties of TMDCs [18–27]. However, there are only limited experimental studies that directly address the valley and spin relaxation process. Recently we measured the valley lifetime in single-layer MoS_2 to be 10 ps at 74 K, using time-resolved absorption spectroscopy [28]. Surprisingly this relaxation time is very short, as large spin splitting in the valence band and spin-valley coupling in the K and K' valleys was expected to impede hole-valley scattering [11–13,15–17,28,29]. As of now an accurate picture of valley relaxation mechanisms in atomically thin TDMCs is missing. In the current work, we studied the thermal dependence of valley relaxation of excitons in monolayer WS_2 using broadband transient absorption spectroscopy. In WS_2 the spin-orbit splitting is significantly larger compared to MoS_2 and other TMDCs [13,19–22]. We observe that the hole-valley lifetime is more than an order of magnitude larger in WS_2 compared to MoS_2. As in MoS_2, electron-valley relaxation is dominated by many-body interactions and faster compared to hole-valley relaxation. Based on the temperature dependence of valley lifetimes, we propose a mechanism for an exciton-mediated valley relaxation process for holes in single-layer WS_2.

In order to measure the valley relaxation time, we performed experiments on single-layer WS_2 samples grown on quartz substrates using a chemical vapor deposition technique [30,31]. In time-resolved experiments, circularly polarized 60 fs pump pulses, tuned to the lower-energy tail of the A excitonic transition (1.977 eV), create electron-hole pairs in the K valley. The differential transmission of a same-circularly-polarized (SCP) broadband (white-light continuum) probe pulse measures the population within the same valley and an opposite-circularly-polarized (OCP) probe pulse measures the population in the other valley. The decay of the polarization anisotropy between the SCP and the OCP spectra reveals the intervalley relaxation dynamics.

Figure 1(a) schematically displays the electronic band structure for WS_2 at the K and K' points, adapted from Ref. [13]. The conduction band is composed of $d[1-3z^2]$ orbitals $|L,m\rangle$ of W with zero magnetic quantum number $m = 0$ under orbital moment $L = 2$ and relatively small admixture of $p[x - i\nu y]$ orbitals of S [17] with $m = -\nu$, which constitutes relatively small, 27 meV, spin splitting ($\nu = \pm 1$ correspond to the K and K' valleys) [32]. The valence band is formed by the $d[(x + i\nu y)^2]$ orbitals of W with $m = 2\nu$ and some admixture of p orbitals of S that conditions much

*lcao2@ncsu.edu
†kwk@ncsu.edu
‡kgundog@ncsu.edu

 ©2014 American Physical Society

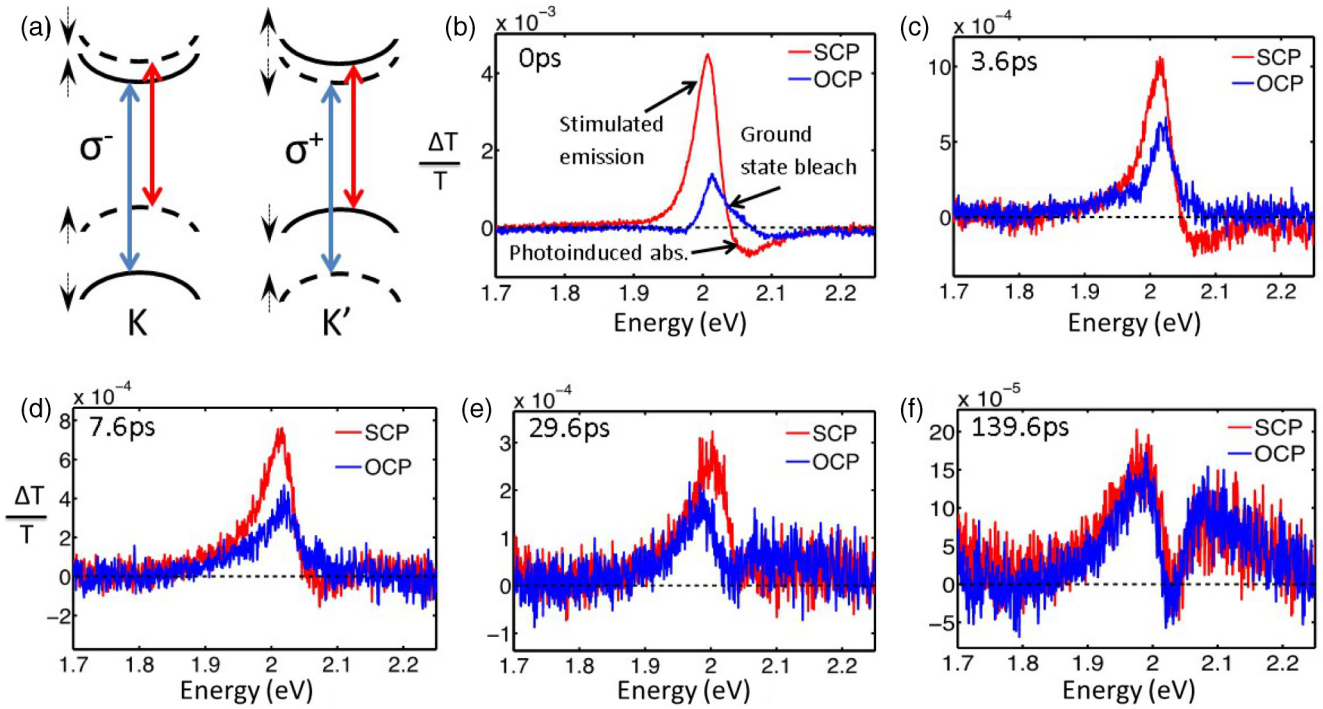


FIG. 1. (Color online) (a) Electronic structure and the optical transition at the K and K' points of monolayer WS_2. The dashed (solid) curves correspond to different spin states in A and B excitonic transitions. (b)–(f) Differential transmission at various delays at 110 K for same (red) and opposite (blue) circularly polarized pump and probe pulses.

larger, 435 meV, valence band spin splitting [13,19,22]. This spin splitting leads to energetically well-separated A and B excitonic transitions shown by red and blue arrows in Fig. 1(a). Their electrodipole interband optical transitions are coupled with circularly polarized light.

Figure 1(b) shows transient SCP and OCP spectra for the A exciton at 110 K. Initially the SCP spectrum shows a dispersive line shape in which the lower-energy tail of the spectrum exhibits ground state bleaching, caused by increased transmission of the probe pulse due to occupied states and stimulated emission, whereby an excited electron-hole pair can recombine and emit a photon. The higher-energy tail exhibits photoinduced absorption (PIA) leading to a dispersive line shape. The spectra evolve into purely absorptive line shape with the PIA feature disappearing in about 7.6 ps. The OCP spectrum also exhibits a dispersive line shape, although less prominent than that of the SCP spectrum. In the later time delays the anisotropy between the SCP and OCP spectra vanishes and a sharp dip shows up at 2.04 eV.

There could be a number of processes that could lead to a dispersive line shape in the early spectra. Previous ultrafast studies show similar dispersive line shapes due to many-body interactions, which induce shifts in the excitonic transitions [33–36]. Monolayer materials exhibit ultratight quantum confinement [21,22,35]. Thus these many-body interactions contribute significantly to the transient spectra [27,34,35]. It is also important to note that recent ultrafast studies on single-layer MoS_2 show a blueshift in the transient absorption spectra due to repulsive exciton-exciton interactions [27]. As for the spectral dip at 2.04 eV, which is observed at later delays, the exact source is unclear. It could be due to an overlapping absorptive transition from the excited state. A better understanding of the band structure and the excited states of WS_2 is needed for analyzing this feature.

The evolution of the polarization anisotropy, measured by the difference between the SCP and OCP spectra in Fig. 1, reveals the valley relaxation time of electrons and holes. The immediate presence of the A exciton feature in the OCP spectra clearly suggests that a significant fraction of the electron population, initially photoexcited in the K valley, quickly delocalizes between the K and K' valleys within 200 fs, which is within the time resolution of the experiment. This is because without any valley relaxation the OCP spectrum should not exhibit any A exciton feature. The electron relaxation into the K' valley (i.e., transition of the direct exciton $[eK,hK]$, with both carriers in the K valley, to an indirect one (dark exciton) $[eK',hK]$) leads to bleaching of the A exciton absorption in the OCP spectra. This immediate electron-valley delocalization has been observed in single-layer MoS_2 and attributed to coherent coupling of excitonic states [28]. While the circularly polarized optical transitions are valley specific, the resulting optically created exciton associated with a specific valley, K or K', is not an eigenstate of the full exciton problem. Strong electron-hole confinement in the exciton with energy 710 meV [37] and radius around 1–2 nm couples the K and K' valleys. As a result the electron in the K valley quickly delocalizes over both valleys. This is further confirmed with analysis of the evolution of the B exciton transition. As observed in Figs. 2(a) and 2(b), the B transition bleached immediately after the pump pulse in both SCP and OCP spectra with equal intensity. Because the B valence levels are very high in energy and are not populated with the pump pulse, the B transition is

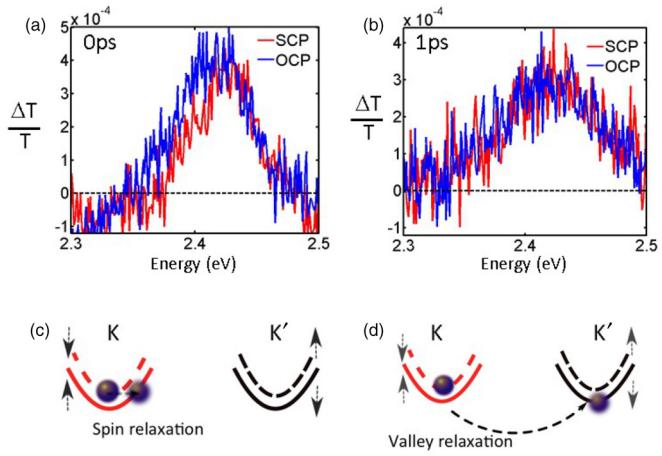


FIG. 2. (Color online) (a), (b) Differential transmission of B exciton peak at various delays at 110 K: delays 0 fs (a) and 1 ps (b). Red is SCP and blue is OCP spectrum. (c), (d) Schematic illustration of spin and valley relaxation of electron.

sensitive only to electron dynamics. Hence electrons occupy the B levels in both valleys immediately after photoexcitation. Because the B levels have opposite spin orientation, these spectra suggest not only that valley relaxation of the electrons is very quick but also that electron-spin relaxation within the same valley is very fast [Figs. 2(c) and 2(d)].

In contrast to the fast conduction band spin and valley relaxation, hole-valley relaxation is not favorable energetically due to the large, $\Delta_{SO} \simeq 450$ meV, spin-orbital splitting, which imposes an energy gap between the parallel spin states in the two valleys [Fig. 1(a)]. Hence hole-valley relaxation takes a much longer time. The total loss of the polarization anisotropy in the SCP and OCP spectra shows that it takes around 100 ps. We note that this is much longer compared to MoS_2 where the valley relaxation takes place in about 10 ps.

In order to resolve the hole-valley relaxation mechanism we performed transient absorption experiments in a range of temperatures from 74 to 298 K. For each temperature, the pump pulses were tuned to the lower-energy side of the A excitonic transition and the resulting dynamics were probed with a broadband white light continuum pulse. At each temperature the early spectra show similar dynamics to the 110 K data, suggesting fast spin and valley relaxation dynamics for the electrons. However, relaxation of the circularly polarized anisotropy clearly evolves at a different rate, revealing the thermal dependence of the hole-valley relaxation dynamics.

In order to quantitatively extract the hole-valley relaxation time, we analyzed the decay of polarization anisotropy at the A exciton transition by taking the difference of the SCP and OCP spectra [30,38]. The valley relaxation clearly exhibits a thermal dependence. While at low temperatures anisotropy lasts more than 100 ps at high temperatures it vanishes within the first 20 ps. Neither single- nor double-exponential decay functions fit the data. For all temperatures the first time constant is around the 100 fs range and the second time constant is in the 1.5–3 ps range [30]. These two fast components do not exhibit significant temperature dependence, because in the first few picoseconds pulse overlap and the spectral evolution from a dispersive to an absorptive line shape dominate the

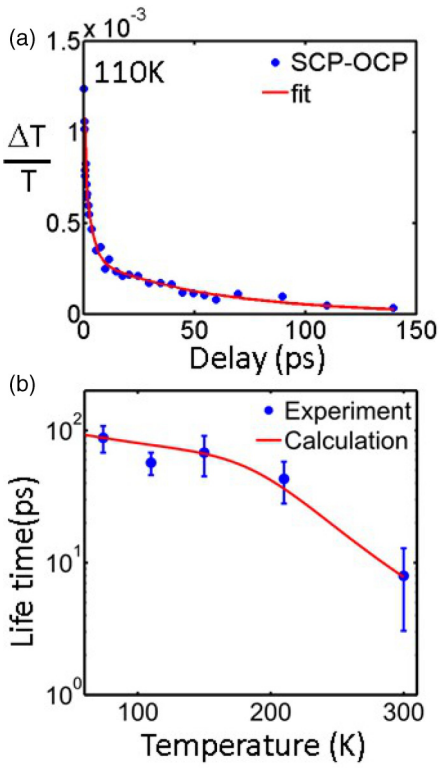


FIG. 3. (Color online) (a) Time evolution of SCP − OCP peak intensity at 110 K and the fit to the three-exponential decay function (solid line). (b) The temperature dependence of the slowest time constant.

transient behavior. The slow component is the only one that exhibits clear temperature dependence, varying from 88 to 8 ps at 74 and 298 K, respectively (Fig. 3). In the following the slow component is used for theoretical analysis of the valley relaxation process.

We considered several previously proposed intervalley relaxation mechanisms to explain the experimental results. Our initial analysis suggests that single-carrier relaxation mechanisms cannot be responsible for the temperature dependence that we observe. For instance, scattering with nonmagnetic impurities has been suggested as a potential valley relaxation process. Reference [39] shows that this mechanism requires a $\sim k^4$ dependence on hole momentum, which leads to a stronger temperature dependence (T^2) than our observation. Relaxation through flexural phonon modes was also considered as a potential mechanism [40]. It predicts an inverse relation between mobility and relaxation rate, and order-of-magnitude longer valley lifetimes compared to our results; hence it is unlikely to be responsible for the valley relaxation in WS_2.

We considered spin relaxation mechanisms such as Elliot-Yafet and Dyakonov-Perel processes as well [41–43]. These processes require scattering of carriers under an inhomogeneous magnetic field. For instance, in conventional semiconductors, the Dresselhaus effect leads to such an effective field. Unlike in many conventional semiconductors the mirror symmetry of 2D TMDCs retains the spin quantization axis in the normal direction over the whole Brillouin zone except at the specific points where spin splitting is reduced to zero. Such a

property is in accordance with the complete optical circular polarization ± 1 for arbitrary wave vectors that is clearly demonstrated in Ref. [17] based on calculations involving 80 energy bands of MoS_2. Our first-principle calculations for WS_2 also reproduce the absence of transversal spin components over the whole Brillouin zone [30,44–46]. Thus the hole/electron diffusive motion cannot mix the states with opposite spin directions along the normal to the layer plane (i.e., the z axis). Therefore the Elliot-Yafet and Dyakonov-Perel mechanisms are irrelevant.

Note however that in a bilayer TMDC [18] or in a realistic structure the spin quantization axis deviates from the normal direction because the mirror symmetry is broken by the substrate. Indeed, modeling the substrate-induced asymmetry by an effective external electric field, we found that the spin quantization axis deviates from the z direction. The proportionality of this deviation to the quasimomentum shift from extremum points represents the Rashba effect with Hamiltonian $H_R = \alpha_\varphi |\Delta\mathbf{k}|$ ($\Delta\mathbf{k} = \pm\mathbf{K} - \mathbf{k}$, and φ is the angle between $\Delta\mathbf{k}$ and the in-plane axis x), which in addition reveals trigonal anisotropy of α_φ in the vicinities of each of the $\mathbf{K}$ and $\mathbf{K}' = -\mathbf{K}$ points. The corresponding spin relaxation rate is

$$\tau_s^{-1} = \frac{2}{\hbar^2}\left\langle \frac{\alpha_\varphi^2 \Delta\mathbf{k}^2 \tau_k}{\tau_k^2 \omega_{\mathrm{SO}}^2 + 1}\right\rangle, \tag{1}$$

where the angular brackets mean thermal averaging, $\omega_{\mathrm{SO}} = \Delta_{\mathrm{SO}}/\hbar$, and τ_k is the momentum relaxation time. Our first-principle calculations estimate the Rashba constant mediated by the potential drop ΔU between two sides of a layer [30,47]. Averaging over the angle φ, we find $\alpha = \beta \Delta U$, where $\beta \simeq 1.1 \times 10^{-10}$ cm, which results in an insignificant contribution ($\tau_s^{-1} \sim 10^{-16}\langle \tau_k^{-1}\rangle$) of this mechanism to intervalley spin relaxation even at $\Delta U = 100$ meV.

We conclude that the previously discussed single-particle relaxation mechanisms are not sufficient to explain exciton intervalley relaxation. On the other hand, the excitonic electron-hole exchange interaction lifts the orthogonality of spin states attributed to different valleys. This effect describes a minimal exciton spin Hamiltonian

$$H_0 = \frac{\tau}{2}\Delta_{\mathrm{SO}}\sigma_z + \frac{\tau}{2}\delta_{\mathrm{SO}} s_z + \Delta_{eh}\boldsymbol{\sigma}\cdot\mathbf{s}, \tag{2}$$

where $\boldsymbol{\sigma}$ and $\mathbf{s}$ are the Pauli matrices for hole and electron spins, $\tau = \pm 1$ the valley index, Δ_{SO} and δ_{SO} the hole and electron spin splitting induced by spin-orbital interaction, and Δ_{eh} the strength of the electron-hole exchange interaction [48]. It is important to note that this interaction mixes the exciton spin states located in different valleys. This is because electrodipole interband transitions occur between electronic states with the same spin that generates electron-hole pair with opposite spin directions, i.e., with zero projections $s_z + \sigma_z = 0$. Thus the transitions between K and $-K$ excitons would be proportional to the spin flip-flop factor $T = |\langle\uparrow,\downarrow|\downarrow,\uparrow\rangle|^2$, where $|\downarrow,\uparrow\rangle$ corresponds to $s_z = -1/2$. If the spin-independent intervalley relaxation rate is $\tau_{KK'}^{-1}$ the net exciton relaxation rate will be

$$\tau_{ex}^{-1} = \tau_{KK'}^{-1}\frac{4\Delta_{eh}^2}{(\Delta_{\mathrm{SO}} - \delta_{\mathrm{SO}})^2 + 4\Delta_{eh}^2}. \tag{3}$$

Exciton scattering on any (not only spin-associated) local defects or phonons actualizes such transitions. In contrast to free carriers, excitons are composed of band states involving those far away from the extrema K or K', due to their short radius. These states admix the conduction band state $|2,0\rangle$ to valence bands of both valley states, which lifts their orthogonality. For instance, a small deviation $\sim 0.1|K - K'|$ from the extremum leads to a non-negligible admixture of the conduction band by a factor of about $\xi \sim 0.01$.

In addition to the excitonic flip-flop mechanism, carrier scattering through the Γ point could also contribute to the valley relaxation. Here the optically excited K exciton scatters to an indirect one $[K_e(K_e')\Gamma_h]$ and then to a direct K' exciton. This mechanism is not subjected to spin restrictions by the factor in Eq. (3) due to zero spin-orbital splitting ($\Delta_{\mathrm{SO}} = \delta_{\mathrm{SO}} = 0$) at the Γ point. Moreover, since the Γ state is composed of $|2,0\rangle$ and $|1,0\rangle$ orbitals, the K-Γ overlap is substantially stronger than direct intervalley overlap. On the other hand the difference $\Delta_{K\Gamma}^{ex}$ between the direct $E_{ex}[K_eK_h] = E_e(K) - E_v(K) - E_X(K)$ and the indirect exciton energy $E_{ex}[K_e\Gamma_h] = E_e(K) - E_v(\Gamma) - E_X(K_e\Gamma_h)$ imposes a thermal activation process with Arrhenius-like temperature dependence

$$\tau_{K\Gamma}^{-1} = r_{K\Gamma}\exp\left(-\Delta_{K\Gamma}^{ex}/kT\right), \tag{4}$$

where $\Delta_{K\Gamma}^{ex} = E_v(K) - E_v(\Gamma) + E_X(K) - E_X(K_e\Gamma_h)$, $E_{e(v)}(B)$ is the energy at the conduction (valence) B band edge ($B = K,\Gamma$), and $E_X(K)$ and $E_X(K_e\Gamma_h)$ are the binding energies for direct and indirect excitons. Our first-principle calculations [30] give $E_v(K) - E_v(\Gamma) = 310$ meV, which slightly differs from previous calculations [22]. In the 2D Wannier-Mott exciton model the difference $E_X(K) - E_X(K_e\Gamma_h) = \Delta E_X$ basically stems from different reduced effective masses $\mu(K)$ and $\mu(\Gamma)$ so that $\Delta E_X = E_X(K)[1 - \mu(\Gamma)/\mu(K)]$ [37].

We estimated the reduced effective masses $\mu(K)$ and $\mu(\Gamma)$ based on our first-principles energy band structure calculations [30,44–46]. The resulting binding energy difference between the direct K exciton and indirect $[K_e(K_e')\Gamma_h]$ exciton, $\Delta E_X \simeq -170$ meV, gives an energy barrier of $\Delta_{K\Gamma}^{ex} \simeq 140$ meV.

Quantitative estimation of $r_{K\Gamma}$, Δ_{eh}, and $\tau_{KK'}^{-1}$ would be grounded on the theory of exciton formation in TMDCs, which is not completed yet. Therefore we will treat these parameters as phenomenological ones. We observe that the low-temperature thermal dependence of $\tau_{KK'}^{-1}$ [Fig. 3(b)] is similar to that of the phonon-assisted momentum relaxation rate $\tau_p^{-1} = \tau_p^{-1}(T)$ calculated from first principles [30,47]. For free holes τ_h^{-1} can be approximated with $\tau_h^{-1}(T) = r_h[1 + (T/T_0)]$ at $r_h = 7.5\cdot$ ps^{-1} and $T_0 \simeq 200$ K in a wide range (70 to 200 K) of temperatures. Adopting a similar dependence for exciton momentum relaxation and combining $\tau_{e,h}^{-1}(T)$ with Eq. (4), the net result of both mechanisms describes the temperature dependence in the form

$$\tau_{ex}^{-1} = r_{KK'}(1 + T/T_0) + r_{K\Gamma}\exp\left(-\Delta_{K\Gamma}^{ex}/kT\right). \tag{5}$$

Figure 3(b) shows that only two free parameters, $r_{KK'} = 0.01$ ps^{-1} and $r_{K\Gamma} = 24$ ps^{-1}, describe all the data with experimental accuracy.

To conclude, we present ultrafast valley relaxation dynamics measurements in monolayer WS_2. The intervalley scattering lifetime in monolayer WS_2 is much longer than that of monolayer MoS_2. The thermal dependence of the

valley relaxation rate indicates that, due to the strong exciton binding energy and exchange interaction, the electron-hole spin flip-flop mechanism becomes an efficient spin relaxation channel. Because such excitonic relaxation mechanisms will not affect free-carrier valley relaxation, we predict much longer valley lifetime for free carriers, which is important for future efforts in developing spintronic/valleytronic devices based on TMDCs.

K.W.K. acknowledges support from SRC/NRI SWAN. L.C. acknowledges the support of a Young Investigator Award from the Army Research Office (Grant No. W911NF-13-1-0201).

[1] K. S. Novoselov, D. Jiang, F. Schedin, T. J. Booth, V. V. Khotkevich, S. V. Morozov, and A. K. Geim, Proc. Natl. Acad. Sci. U.S.A. **102**, 10451 (2005).
[2] A. K. Geim, Science **324**, 1530 (2009).
[3] S. Z. Butler, S. M. Hollen, L. Cao, Y. Cui, J. A. Gupta, H. R. Gutiérrez, T. F. Heinz, S. S. Hong, J. Huang, A. F. Ismach, E. Johnston-Halperin, M. Kuno, V. V. Plashnitsa, R. D. Robinson, R. S. Ruoff, S. Salahuddin, J. Shan, L. Shi, M. G. Spencer, M. Terrones, W. Windl, and J. E. Goldberger, ACS Nano **7**, 2898 (2013).
[4] D. Jariwala, V. K. Sangwan, L. J. Lauhon, T. J. Marks, and M. C. Hersam, ACS Nano **8**, 1102 (2014).
[5] Q. H. Wang, K. Kalantar-Zadeh, A. Kis, J. N. Coleman, and M. S. Strano, Nat. Nanotechnol. **7**, 699 (2012).
[6] B. Radisavljevic, A. Radenovic, J. Brivio, J. V. Giacometti, and A. Kis, Nat. Nanotechnol. **6**, 147 (2011).
[7] L. Britnell, R. M. Ribeiro, A. Eckmann, R. Jalil, B. D. Belle, A. Mishchenko, Y.-J. Kim, R. V. Gorbachev, T. Georgiou, S. V. Morozov, A. N. Grigorenko, A. K. Geim, C. Casiraghi, A. H. Castro Neto, and K. S. Novoselov, Science **340**, 1311 (2013).
[8] R. S. Sundaram, M. Engel, A. Lombardo, R. Krupke, A. C. Ferrari, Ph. Avouris, and M. Steiner, Nano Lett. **13**, 1416 (2013).
[9] F. K. Perkins, A. L. Friedman, E. Cobas, P. M. Campbell, G. G. Jernigan, and B. T. Jonker, Nano Lett. **13**, 668 (2013).
[10] K. He, C. Poole, K. F. Mak, and J. Shan, Nano Lett. **13**, 2931 (2013).
[11] A. Splendiani, L. Sun, Y. Zhang, T. Li, J. Kim, C.-Y. Chim, G. Galli, and F. Wang, Nano Lett. **10**, 1271 (2010).
[12] K. F. Mak, C. Lee, J. Hone, J. Shan, and T. F. Heinz, Phys. Rev. Lett. **105**, 136805 (2010).
[13] D. Xiao, G. B. Liu, W. Feng, X. Xu, and W. Yao, Phys. Rev. Lett. **108**, 196802 (2012).
[14] Y. Yu, S. Huang, Y. Li, S. N. Steinmann, W. Yang, and L. Cao, Nano Lett. **14**, 553 (2014).
[15] K. F. Mak, K. He, J. Shan, and T. F. Heinz, Nat. Nanotechnol. **7**, 494 (2012).
[16] H. Zeng, J. Dai, W. Yao, D. Xiao, and X. Cui, Nat. Nanotechnol. **7**, 490 (2012).
[17] T. Cao, G. Wang, W. Han, H. Ye, C. Zhu, J. Shi, Q. Niu, P. Tan, E. Wang, B. Liu, and J. Feng, Nat. Commun. **3**, 887 (2012).
[18] Z. Gong, G. B. Liu, H. Yu, D. Xiao, X. Cui, X. Xu, and W. Yao, Nat. Commun. **4**, 2053 (2013).
[19] K. Kośmider and J. Fernández-Rossier, Phys. Rev. B **87**, 075451 (2013).
[20] H. R. Gutiérrez, N. Perea-López, A. L. Elías, A. Berkdemir, B. Wang, R. Lv, F. López-Urías, V. H. Crespi, H. Terrones, and M. Terrones, Nano Lett. **13**, 3447 (2013).
[21] H. Zeng, G.-B. Liu, J. Dai, Y. Yan, B. Zhu, R. He, L. Xie, S. Xu, X. Chen, W. Yao, and X. Cui, Sci. Rep. **3**, 1608 (2013).
[22] Z. Y. Zhu, Y. C. Cheng and U. Schwingenschlogl, Phys. Rev. B **84**, 153402 (2011).
[23] W. Zhao, Z. Ghorannevis, L. Chu, M. Toh, C. Kloc, P.-H. Tan, and G. Eda, ACS Nano **7**, 791 (2013).
[24] A. M. Jones, H. Yu, N. J. Ghimire, S. Wu, G. Aivazian, J. S. Ross, B. Zhao, J. Yan, D. G. Mandrus, D. Xiao, W. Yao, and X. Xu, Nat. Nanotechnol. **8**, 634 (2013).
[25] L. Sun, J. Yan, D. Zhan, L. Liu, H. Hu, H. Li, B. K. Tay, J.-L. Kuo, C.-C. Huang, D. W. Hewak, P. S. Lee, and Z. X. Shen, Phys. Rev. Lett. **111**, 126801 (2013).
[26] H. Shi, R. Yan, S. Bertolazzi, G. Gao, A. Kis, D. Jena, H. Xing, and L. Huang, ACS Nano **7**, 1072 (2013).
[27] S. Sim, J. Park, J. Song, C. In, Y. Lee, H. Kim, and H. Choi, Phys. Rev. B **88**, 075434 (2013).
[28] C. Mai, A. Barrette, Y. Yu, Y. G. Semenov, K. W. Kim, L. Cao, and K. Gundogdu, Nano Lett. **14**, 202 (2014).
[29] Q. Wang, S. Ge, X. Li, J. Qiu, Y. Ji, J. Feng, and D. Sun, ACS Nano **7**, 11087 (2013).
[30] See Supplemental Material at http://link.aps.org/supplemental/10.1103/PhysRevB.90.041414 for (1) sample growth method, (2) experimental results of valley polarization relaxation measurements, (3) band structure calculation, (4) rashba effect from first principle calculation, and (5) phonon-assisted momentum relaxation rate from first principle calculation.
[31] Y. Yu, S. Hu, L. Su, L. Huang, Y. Liu, Z. Jin, A. A. Purezky, D. B. Geohegan, K. W. Kim, Y. Zhang, and L. Cao, arXiv:1403.6181.
[32] G.-B. Liu, W.-Y. Shan, Y. Yao, W. Yao, and D. Xiao, Phys. Rev. B **88**, 085433 (2013).
[33] S. W. Koch, M. Kira, and T. Meier, J. Opt. B: Quantum Semiclass. Opt. **3**, 29 (2001).
[34] Y. H. Lee, A. Chavez-Pirson, S. W. Koch, H. M. Gibbs, S. H. Park, J. Morhange, A. Jeffery, and N. Peyghambarian, Phys. Rev. Lett. **57**, 2446 (1986).
[35] D. N. Christodoulides, I. C. Khoo, G. J. Salamo, G. I. Stegeman, and E. W. V. Stryland, Adv. Opt. Photonics **2**, 60 (2010).
[36] N. Peyghambarian, H. M. Gibbs, J. L. Jewell, A. Antonetti, A. Migus, D. Hulin, and A. Mysyrowicz, Phys. Rev. Lett. **53**, 2433 (1984).
[37] B. Zhu, X. Chen, and X. Cui, arXiv:1403.5108v1.
[38] K. C. Hall, K. Gündogdu, E. Altunkaya, W. H. Lau, M. E. Flatté, T. F. Boggess, J. J. Zinck, W. B. Barvosa-Carter, and S. L. Skeith, Phys. Rev. B **68**, 115311 (2003).
[39] H. Lu, W. Yao, D. Xiao, and S. Shen, Phys. Rev. Lett. **110**, 016806 (2013).

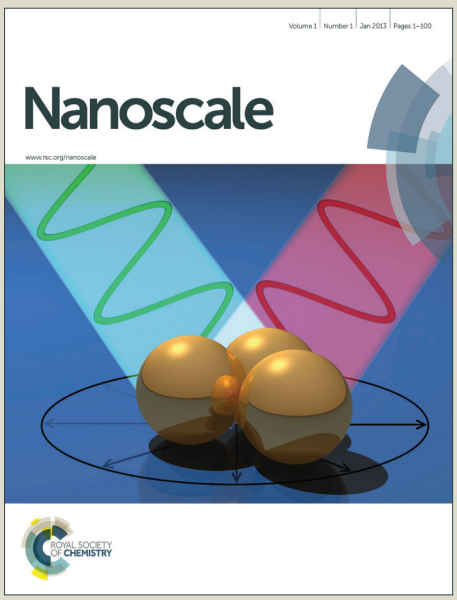
[40] Y. Song, and H. Dery, Phys. Rev. Lett. **111**, 026601 (2013).
[41] M. I. D'yakonov and V. I. Perel, Zh. Eksp. Teor. Fiz. **60**, 1954 (1971) [Sov. Phys. JETP **33**, 1053 (1971)].
[42] Y. Yafet, Phys. Rev. **85**, 478 (1952).
[43] R. J. Elliott, Phys. Rev. **96**, 266 (1954).
[44] P. Giannozzi *et al.*, J. Phys.: Condens. Matter **21**, 395502 (2009).
[45] A. Klein, S. Tiefenbacher, V. Eyert, C. Pettenkofer, and W. Jaegermann, Phys. Rev. B **64**, 205416 (2001).
[46] H.-P. Komsa and A. V. Krasheninnikov, Phys. Rev. B **88**, 085318 (2013).
[47] X. Li, J. T. Mullen, Z. Jin, K. M. Borysenko, M. Buongiorno Nardelli, and K. W. Kim, Phys. Rev. B **87**, 115418 (2013).
[48] H. Yu, G.-B. Liu, P. Gong, X. Xu, and W. Yao, Nat. Commun. **5**, 3876 (2014).

View Article Online
View Journal

Nanoscale

Accepted Manuscript

This article can be cited before page numbers have been issued, to do this please use: L. Su, Y. Zhang, Y. yU and L. cao , *Nanoscale*, 2014, DOI: 10.1039/C3NR06462J.



This is an *Accepted Manuscript*, which has been through the Royal Society of Chemistry peer review process and has been accepted for publication.

Accepted Manuscripts are published online shortly after acceptance, before technical editing, formatting and proof reading. Using this free service, authors can make their results available to the community, in citable form, before we publish the edited article. We will replace this *Accepted Manuscript* with the edited and formatted *Advance Article* as soon as it is available.

You can find more information about *Accepted Manuscripts* in the Information for Authors.

Please note that technical editing may introduce minor changes to the text and/or graphics, which may alter content. The journal's standard Terms & Conditions and the Ethical guidelines still apply. In no event shall the Royal Society of Chemistry be held responsible for any errors or omissions in this *Accepted Manuscript* or any consequences arising from the use of any information it contains.

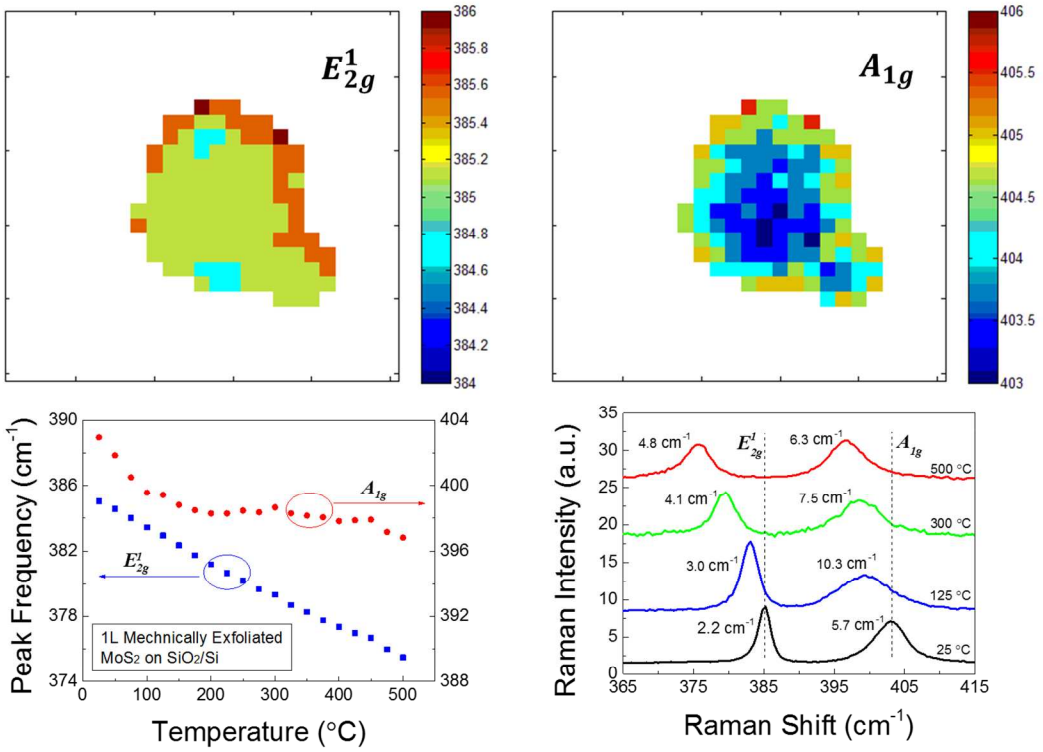
ROYAL SOCIETY OF CHEMISTRY

www.rsc.org/nanoscale

View Article Online
DOI: 10.1039/C3NR06462J

TOC

The coupling of quasi 2-D MoS_2 with substrate on different substrate type has been studied, probed by temperature dependent Raman scattering.



Published on 04 February 2014. Downloaded by North Carolina State University on 12/03/2014 16:08:08.

Nanoscale Accepted Manuscript

View Article Online
DOI: 10.1039/C3NR06462J

Published on 04 February 2014. Downloaded by North Carolina State University on 12/03/2014 16:08:08.

Nanoscale Accepted Manuscript

View Article Online
DOI: 10.1039/C3NR06462J

Nanoscale

RSCPublishing

PAPER

Published on 04 February 2014. Downloaded by North Carolina State University on 12/03/2014 16:08:08.

Cite this: DOI: 10.1039/x0xx00000x

Dependence of Coupling of Quasi 2-D MoS_2 with Substrate on Substrate Type, Probed by Temperature Dependent Raman Scattering

Liqin Su,[a] Yong Zhang,[a,*] Yifei Yu,[b] and Linyou Cao[b]

Received 00th January 2012,
Accepted 00th January 2012

DOI: 10.1039/x0xx00000x

www.rsc.org/

This work reports a study on the temperature dependence of in-plane E_{2g}^1 and out-of-plane A_{1g} Raman modes of single-layer (1L) and bi-layer (2L) MoS_2 films on sapphire (epitaxial) and SiO_2 (transferred) substrates as well as bulk MoS_2 single crystal in a temperature range of 25 – 500 °C. For the films on the transferred SiO_2 substrate, the in-plane E_{2g}^1 mode is only weakly affected by the substrate, whereas the out-of-plane A_{1g} mode is strongly perturbed, showing highly nonlinear, sometimes even non-monotonic, temperature dependence in the Raman peak shift and linewidth. In contrast, for the films on the epitaxial sapphire substrate, E_{2g}^1 is affected more significantly by the substrate than A_{1g}. This study suggests that the 2-D film-substrate coupling depends sensitively on the preparation method, and in particular on the film morphology for the transferred film. These findings are vitally important for the fundamental understanding and application of this quasi 2-D material that is expected to be supported by a substrate in most circumstances.

Nanoscale Accepted Manuscript

Introduction

Two-dimensional (2-D) materials such as graphene and hexagonal boron nitride (h-BN) have attracted tremendous attentions because of their extraordinary physical properties.[1-6] However, graphene is a zero band gap material with vanishing density of states at the Dirac point, making it difficult to be used in electronic devices, particularly in transistors.[7] Although several strategies of band gap engineering have been applied to open the band gap, generating a band gap larger than 400 meV remains a challenge.[8-10] In contrast, h-BN has a band gap of 5.2 eV, too large for an efficient performance in electronic devices.[11] Recently, single-layer molybdenum disulfide (MoS_2), consisting of three atomic layers of one Mo and two S, has been shown to exhibit a direct band gap of ~1.8 eV, while bulk MoS_2 has an indirect band gap of 1.29 eV.[12, 13] Since single-layer MoS_2 shares a number of common properties with graphene such as 2-D layered structure but has a finite band gap, it is considered to be an alternative to graphene, attracting a significant research interest. By using mechanical exfoliation method, single- and few-layer MoS_2 samples have been achieved, showing extremely strong photoluminescence compared to bulk MoS_2. Recently, single-layer MoS_2 based FETs have been reported to have a mobility of at least of 200 $cm^2\ V^{-1}\ s^{-1}$ and a current on/off ratio of 1×10^8.[14] These promising optical and electronic properties can potentially lead to the development of high-quality low-power optoelectronic devices. Synthesis of large area of MoS_2 atomic layers has been demonstrated using a vapor-phase deposition method.[15] Recently, it has been reported that a self-limiting approach can produce thin MoS_2 films over an area of centimeters with the layer number precisely controllable.[16]

A single-layer MoS_2 is formed by the arrangement of a triangular or simple hexagonal plane of Mo atoms sandwiched between two triangular layers of S atoms in a triangular prismatic fashion (see Fig.1(a)). Bulk MoS_2 is a periodically stacked S-Mo-S layers through Van der Waals force. The space group of single layer MoS_2 is *P6m2* (point group D_{3h}), and the four first-order Raman active modes at the center of Brillouin zone are 32 cm^{-1} (E_{2g}^2), 286 cm^{-1} (E_{1g}), 383 cm^{-1} (E_{2g}^1), and 408 cm^{-1} (A_{1g}).[17, 18] The E_{2g}^2 mode arises from the relative motion between two MoS_2 layers, which will vanish in the single layer sample. The E_{1g} mode is forbidden in back-scattering measurement on the basal plane perpendicular to the c axis. The E_{2g}^1 mode is attributed to the in-plane relative motion between the two S atoms and the Mo atom, whereas the A_{1g} mode the out-of-plane vibration of two S atoms in opposite directions. Strictly speaking, the two active Raman modes E_{2g}^1 and A_{1g} (in D_{6h} for bulk MoS_2) should be assigned as E' and A_1' in the monolayer MoS_2 (in D_{3h}).[19, 20] However, to see the evolution

Published on 04 February 2014. Downloaded by North Carolina State University on 12/03/2014 16:08:08.

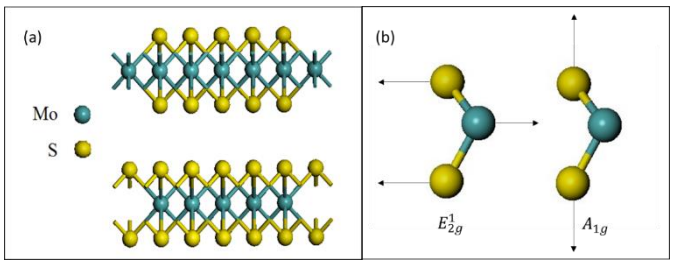


Fig. 1 (a) Schematic model of MoS_2 bulk and single layer. (b) In-plane phonon E^1_{2g} and out-of-plane phonon A_{1g} for single-layer MoS_2.

from the bulk to single-layer,[17, 21] the two modes are simply labelled as $E_{2g}{}^1$ and A_{1g} for all cases, as commonly done in the literature. Raman spectroscopy is a sensitive nondestructive technique to investigate structural and electronic properties of MoS_2. Similar to graphene, the Raman peak positions depend on the number of MoS_2 single layers, which makes it possible to determine the number of layers from Raman spectra.[21, 22]

In this work, we report on the temperature dependent Raman spectra of both single- (1L) and bi-layer (2L) MoS_2, as well as the bulk sample. The knowledge of temperature dependent vibrational properties is important for further understanding electron-phonon interaction, transport properties, and crystal structure of material, which may largely impact the performance of electronic devices. Furthermore, because the MoS_2 is expected to be supported by a substrate in most if not all real applications, thus the coupling with substrate is inevitable, this temperature dependence study offers valuable insights to the effect of substrate, which might not be apparent at a fixed temperature. Since SiO_2/Si is widely used as the substrate for fabricating electronic devices after the film being transferred from the original growth substrate, it is of particular interest to investigate the 2-D film with SiO_2/Si substrate.

The temperature variations of the Raman frequencies in MoS_2 on SiO_2/Si have been studied previously, giving the linear temperature coefficients, respectively, for $E_{2g}{}^1$ and A_{1g} modes: for few layers, -0.0132 cm^{-1}/K and -0.0123 cm^{-1}/K from 83 to 523 K;[23] for single layer, -0.0179 cm^{-1}/K and -0.0143 cm^{-1}/K from 300 to 550 K; and for bi-layer on, -0.0137 cm^{-1}/K and -0.0189 cm^{-1}/K from 300 to 550 K.[24] Apparently, the absolute and relative magnitudes of the temperature coefficients for the two modes differ significantly in these reported values. Furthermore, reliable data for the bulk MoS_2, which may serve as the references, are not readily available in the literature. The intrinsic mechanism for the redshift of Raman frequency with increasing temperature, as is known for most materials, is associated with the anharmonic effect due to weakening of the lattice potential energy.[25] In our work, we report the temperature dependent Raman measurements of single- and bi-layer MoS_2 in a larger temperature range from 300 to 773 K with small temperature increments, which allows us to accurately examine not only the nonlinearity of the temperature dependence but also the dependence of the film-substrate coupling on the substrate type.

Experimental Section

Samples

The samples investigated in this work have been obtained by two methods: mechanical exfoliation and chemical vapor deposition as reported in Ref.16. The 1L MoS_2 flake was mechanically exfoliated from nature crystalline bulk MoS_2 and

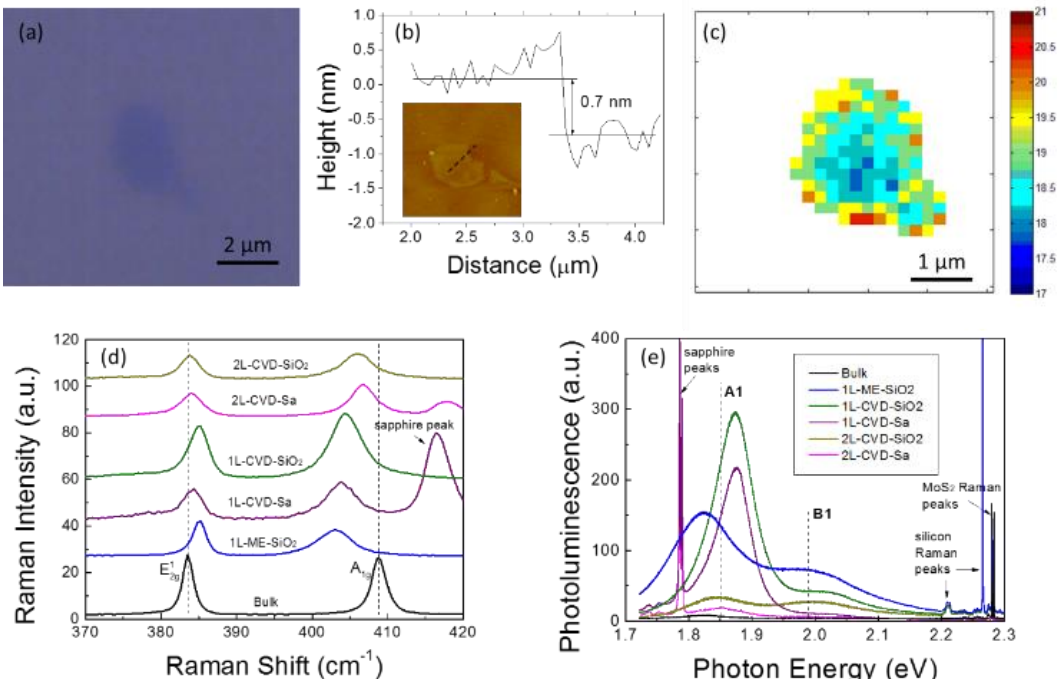


Fig. 2 Optical image (a) and AFM image (b) of mechanically exfoliated 1L MoS_2 on SiO_2/Si. (c) Map of the Raman frequency difference Δω, and the unit is cm^{-1}. (d) and (e) Raman and PL spectra of bulk MoS_2, and 1L and 2L on different substrates.

Nanoscale Accepted Manuscript

This journal is © The Royal Society of Chemistry 2012

View Article Online
DOI: 10.1039/C3NR06462J
ARTICLE

Published on 04 February 2014. Downloaded by North Carolina State University on 12/03/2014 16:08:08.

transferred onto a silicon wafer covered by a 300-nm-thick thermal oxide (SiO_2) layer (Sample 1L-ME-SiO_2). The CVD-grown 1L and 2L samples were prepared on two types of substrates, SiO_2/Si and sapphire labeled as, respectively, 1L-CVD-SiO_2, 1L-CVD-Sa, 2L-CVD-SiO_2, and 2L-CVD-Sa. Originally the MoS_2 films were grown on sapphire wafers, and then transferred to SiO_2/Si wafers by scotch tape. Raman system used in this work is Horiba LabRam HR800 with a spectral resolution smaller than 1 cm^{-1}. A 532 nm laser was used with power ~1 mW, low enough to avoid heating of the samples. The temperature dependent measurements were performed with a 50× long-working-distance lens.

Characterization of Samples

Fig.2(a) shows the optical image of an exfoliated 1L MoS_2 film on the SiO_2/Si wafer, with an AFM image in Fig.2(b), confirming the one-layer thickness which is ~0.7 nm. The Raman frequency difference ($\Delta\omega$) between the $E_{2g}{}^1$ and A_{1g} modes has been shown to correlate with the layer number, with $\Delta\omega$ = 19 cm^{-1} for 1L and 22 cm^{-1} for 2L.[21] Raman mappings of exfoliated films were carried out to examine the thickness distribution of the MoS_2 film at room temperature, and the spatial variation of the frequency difference $\Delta\omega$ is shown in Fig.2(c). All the $\Delta\omega$ values are found less than 20 cm^{-1}, indicating it is indeed single-layer MoS_2. Room temperature Raman and photoluminescence (PL) spectra of all the samples, including a bulk MoS_2 sample, used in this work are shown in Fig.2(d) and 2(e), respectively. With increasing number of layers, the $E_{2g}{}^1$ peak shows a redshift in Raman frequency while A_{1g} peak blueshift. There are small shifts in the peak position among samples of the same thickness but on different substrates, due to residue strain, suggesting some coupling between the film and substrate. In addition, the linewidthes of 1L and 2L samples are somewhat larger than those of the bulk sample, which could be an indication of inhomogeneity of the strain. It has been reported that the PL of MoS_2 has two peaks that correspond to A1 (1.85 eV) and B1 (1.98 eV) direct excitonic transitions of MoS_2.[13] The A1 and B1 transitions are, respectively, at 1.82 eV and 1.98 eV for sample 1L-ME-SiO_2, 1.87 eV and 2.0 eV for single-layer CVD samples, and 1.85 eV and 1.99 eV for bi-layer CVD samples. The variation of PL peak positions of MoS_2 samples could be due to the interaction between the film and the substrate and possibly impurities in the films. Additionally, the 1L MoS_2 samples show the strongest PL signal, while bulk MoS_2 negligible, as expected due to the electronic band structure change.

Experimental Setup

For the temperature dependent study, a Linkam TS1500 heating system, with a temperature control accuracy of 1 °C, was used to heat the samples with a step of 25 °C, and heating rate of 10 °C/min. Five minutes was applied to hold the temperature at each temperature step, allowing sufficient time for stabilization. An extremely low flow rate of nitrogen gas was purged to avoid the oxidization of MoS_2 into MoO_3. After the sample temperature stabilized, Raman spectra were acquired by the Horiba Raman system. A few samples were heated in the ambient environment, and no Raman signals of $E_{2g}{}^1$ and A_{1g} modes were observed when the temperature > 350 °C, implying total oxidization of MoS_2 films.

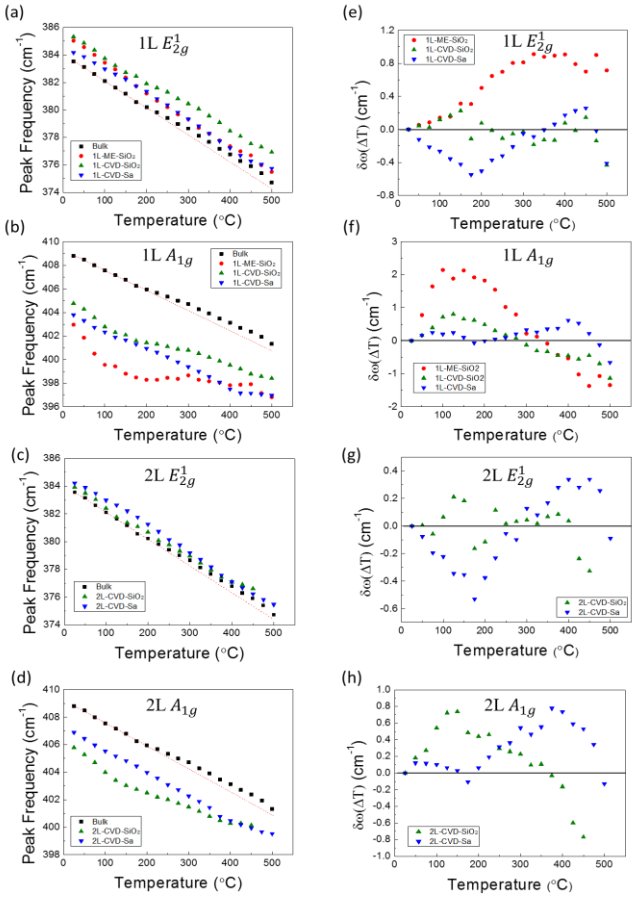


Fig. 3 (a)-(d) Temperature dependence of Raman frequencies of E^1_{2g} and A_{1g} modes in bulk and all other 1L and 2L samples. (e)-(h) The Raman frequency deviation of 1L and 2L MoS_2 relative to bulk MoS2 as the reference.

Results and discussion

Temperature dependence of Raman scattering

The temperature dependences of both $E_{2g}{}^1$ and A_{1g} peak positions were performed in the range from room temperature (25 °C) to 500 °C, shown in Fig.3(a)-(d). The upper temperature range in this work is substantially higher than those in the previous works < 250 °C.[23, 24] The results of bulk MoS_2 are used as a reference. Empirically, the temperature dependence of Raman shift can be described by:

$$\omega(\Delta T) = \omega_0 + \chi_1 \Delta T + \chi_2 (\Delta T)^2 + \chi_3 (\Delta T)^3, \qquad (1)$$

where ω_0 is the frequency at room temperature, ΔT is the temperature change relative to room temperature, and χ_1 is the first-order temperature coefficient. The second (χ_2), third (χ_3) or higher order temperature effects are usually assumed to be small in the literature. In reality, the nonlinear effects are found to be quite significant for 1L or 2L MoS_2 even in a temperature

Nanoscale Accepted Manuscript

Published on 04 February 2014. Downloaded by North Carolina State University on 12/03/2014 16:08:08.

range where the linear dependence might be expected to be adequate, for instance, below 200 °C, depending on the substrate. Even for bulk MoS_2, the nonlinearity occurs at around 200 °C for both E_{2g}^1 and A_{1g}, though rather weak, but nevertheless evident in our data. It is perhaps reasonable to assume that the temperature shift for a free standing few-layer MoS_2 should be rather close to that of the bulk material, despite the difference in the absolute position. Therefore, to show more clearly the substrate effect, we can take the temperature shifts of the bulk sample as references. Fig.3(e)-(h) plot the difference in the Raman frequency shifts between the thin film sample and the bulk, $\delta\omega(\Delta T) = |\omega(\Delta T) - \omega_0|_{\text{thin film}} - |\omega(\Delta T) - \omega_0|_{\text{bulk}}$, for E_{2g}^1 and A_{1g} and for 1L and 2L samples. Below we discuss separately E_{2g}^1 and A_{1g} to examine the effects of two types of substrates.

(1) E_{2g}^1: For both the 1L and 2L samples, as shown in Fig.3(a) and (c), Fig.3(e) and (g), the E_{2g}^1 mode exhibits relatively weak nonlinearity or in general appears to be close to the temperature dependences of the bulk sample. The temperature dependences of the deviations from the bulk mode are qualitatively similar for the same type of substrate: 1L-CVD-Sa and 2L-CVD-Sa vs. 1L-CVD-SiO_2 and 2L-CVD-SiO_2, which is more apparent in Fig.3(e) and (g), due to subtle difference in the film-substrate coupling (to be discussed later). The deviations of 1L-ME-SiO_2 are somewhat different from the other samples, as shown in Fig.3(e).

(2) A_{1g}: For both 1L-ME-SiO_2 and 1L-CVD-SiO_2, as shown in Figs.3(b) and (f), the temperature dependence of A_{1g} mode is drastically different from that of the bulk, showing strong nonlinearity starting at temperature near 100 °C and an overall 'S' shape dependence. The Raman spectra of 1L-ME-SiO_2 at a few representative temperatures are shown in Fig.4. The FWHM of A_{1g} mode is 5.7 cm^{-1} at room temperature, increasing to a maximum of 10.3 cm^{-1} at around 125 °C, then it decreases to 6.3 cm^{-1} when the temperature reaches 500 °C, whereas the FWHM of E_{2g}^1 mode increases from 2.2 cm^{-1} at room temperature monotonically to 4.8 cm^{-1} at 500 °C. However, 1L-CVD-Sa shows only small deviation from the bulk dependence, with an average slope of -0.0159 cm^{-1}/K by using linear fitting, up to 425 °C, then an obvious change occurs, becoming nearly flat with a slope of -0.0027 cm^{-1}/K. As for the 2L samples, Fig.3(d) and (h), similar to 1L-CVD-SiO_2, 2L-CVD-SiO_2 exhibits more significant deviation from the bulk sample than 2L-CVD-Sa when temperature < 400 °C. For 2L-CVD-Sa, the slope changes significantly when T > 400 °C from -0.0162 cm^{-1}/K to -0.0102 cm^{-1}/K. Again, one may notice that the temperature dependences of the deviations from the bulk mode are qualitatively similar for the same type of substrate: 1L-CVD-Sa and 2L-CVD-Sa vs. 1L-CVD-SiO_2 and 2L-CVD-SiO_2, which is more apparent in Fig.3(f) and (h).

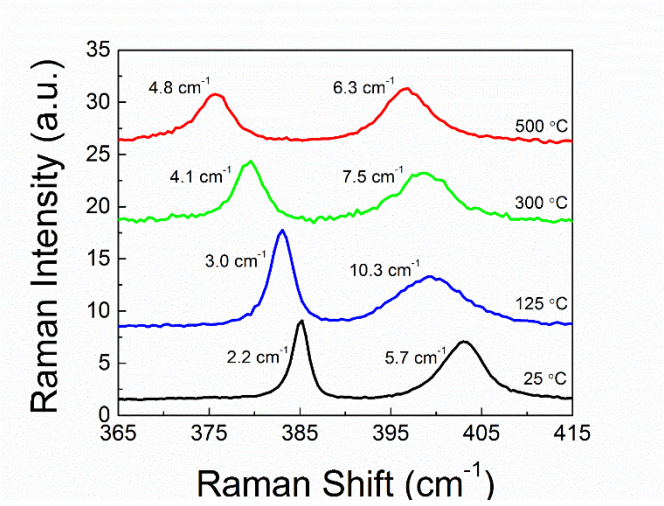


Fig. 4 Representative Raman spectra of 1L-ME-SiO_2 sample at particular temperatures. The FWHM of E_{2g}^1 and A_{1g} are labelled besides the peaks.

Visually from Fig.3(a)-(d), the A_{1g} mode shows more nonlinearity than the E_{2g}^1 mode. Qualitatively similar results have been observed in graphene: the peak position of G band, an in-plane vibrational mode, is less susceptible to the substrate influence than an out-of-plane vibration mode ~861 cm^{-1}.[26, 27] Similarly it is reasonable to expect that in MoS_2 the in-plane mode (E_{2g}^1) will be less affected by the interaction between film and substrate than the out-of-plane mode (A_{1g}). Thus, it is not difficult to understand that the E_{2g}^1 mode typically shows more linear temperature dependent Raman shift than A_{1g} mode for both 1L and 2L samples. The difference between the SiO_2 and sapphire substrate also indicates that the coupling between the film and substrate depends on the substrate type and/or how the film and substrate is bound.

The temperature coefficients of all the samples are fitted to third order with polynomial function according to Eq.(1), listed in Table 1. The linear temperature coefficients of E_{2g}^1 and A_{1g} in bulk MoS_2 are χ_1 = -0.0221 ± 8.9 × 10^{-4} cm^{-1}/K and -0.0197 ± 8.9 × 10^{-4} cm^{-1}/K, respectively. Bulk MoS_2, as the reference, can be treated as a stacking of single-layered MoS_2 films, and each layer has the same properties. With increasing temperature, all layers expand with the same rate without introducing any strain, leading to a nearly linear redshift of the Raman peak position for both E_{2g}^1 and A_{1g} modes. Although the interlayer coupling has led to significant frequency shifts for the two modes between 1L and bulk, the changes in temperature coefficients are expected to be relatively small. For the E_{2g}^1 mode, the first-order temperature coefficients (χ_1) of SiO_2 samples, both 1L and 2L, are close to that of bulk MoS_2, while those of the sapphire samples are much smaller. For A_{1g}, all the SiO_2 samples yield much larger χ_1's than that of bulk MoS_2, while sapphire samples are close to bulk MoS_2. Our results for the films on SiO_2/Si are contradicting to or significantly different from those reported in the literature, because the improved data accuracy allows to examine the nonlinear effect that was neglected.[23, 24]

Because all the SiO_2 samples were produced by mechanical exfoliation, it is possible that wrinkles or ripples were introduced to the films, resulting in a considerable strain in the film.[28] Fig.5 gives the spatial maps of the Raman frequencies of E_{2g}^1 and A_{1g} modes for mechanically exfoliated single-layer MoS_2 film on SiO_2/Si (1L-ME-SiO_2) at room temperature. The maps demonstrate that the frequency of A_{1g} show a larger

Nanoscale Accepted Manuscript

This journal is © The Royal Society of Chemistry 2012

View Article Online
DOI: 10.1039/C3NR06462J

Published on 04 February 2014. Downloaded by North Carolina State University on 12/03/2014 16:08:08.

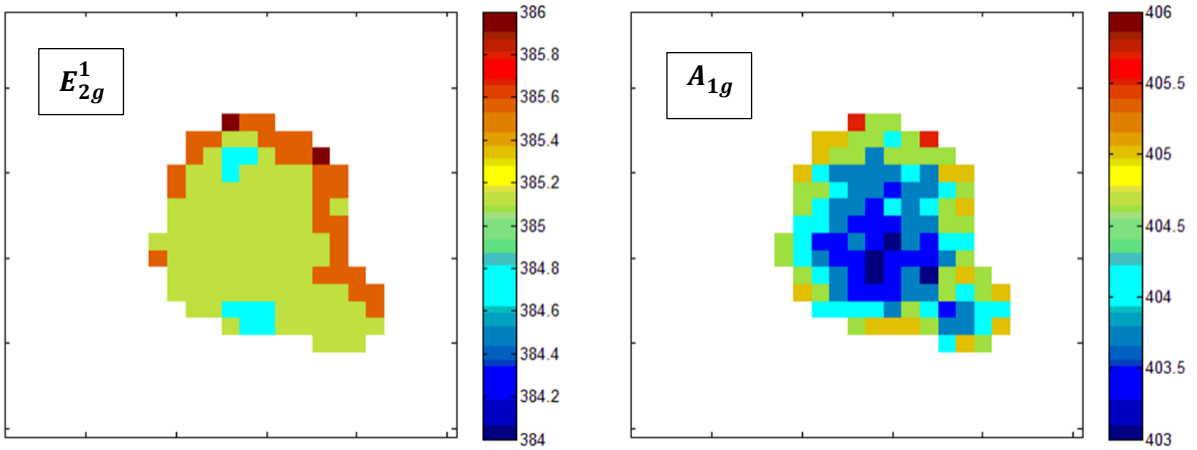


Fig. 5 Spatial maps (6 μm × 6 μm) of the Raman frequencies of (a) E^1_{2g} and (b) A_{1g} modes for 1L-ME-SiO_2 sample, and the unit is cm^{-1}.

Table 1 Temperature coefficients of bulk, 1L and 2L samples with polynomial fitting to third order.

		χ_1	χ_2	χ_3
E^1_{2g}	bulk	$-0.0221 \pm 8.9 \times 10^{-4}$	$2.12 \times 10^{-5} \pm 4.4 \times 10^{-6}$	$-2.94 \times 10^{-8} \pm 6.1 \times 10^{-9}$
	1L-ME-SiO_2	-0.0241 ± 0.0015	--	--
	1L-CVD-SiO_2	-0.0217 ± 0.0017	$2.04 \times 10^{-5} \pm 8.4 \times 10^{-6}$	$-2.68 \times 10^{-8} \pm 1.2 \times 10^{-8}$
	1L-CVD-Sa (till 425 °C)	$-0.0143 \pm 5.7 \times 10^{-4}$	$-1.44 \times 10^{-5} \pm 3.4 \times 10^{-6}$	$7.71 \times 10^{-9} \pm 5.6 \times 10^{-9}$
	2L-CVD-SiO_2 (till 400 °C)	-0.0233 ± 0.0018	$3.00 \times 10^{-5} \pm 1.1 \times 10^{-5}$	$-4.61 \times 10^{-8} \pm 2.0 \times 10^{-8}$
	2L-CVD-Sa (till 425 °C)	$-0.0135 \pm 8.4 \times 10^{-4}$	$-2.54 \times 10^{-5} \pm 5.0 \times 10^{-6}$	$2.93 \times 10^{-8} \pm 8.2 \times 10^{-9}$
	1L ME SiO_2 Ref.[24]	-0.0179		
	2L ME SiO_2 Ref.[24]	-0.0137		
	few layer Ref.[23]	-0.0132		
A_{1g}	bulk	$-0.0197 \pm 8.9 \times 10^{-4}$	$2.49 \times 10^{-5} \pm 4.4 \times 10^{-6}$	$-3.53 \times 10^{-8} \pm 6.1 \times 10^{-9}$
	1L-ME-SiO_2	-0.0626 ± 0.0038	$2.11 \times 10^{-4} \pm 1.7 \times 10^{-5}$	$-2.34 \times 10^{-7} \pm 2.1 \times 10^{-8}$
	1L-CVD-SiO_2	-0.0301 ± 0.0023	$8.15 \times 10^{-5} \pm 1.1 \times 10^{-5}$	$-1.00 \times 10^{-7} \pm 1.6 \times 10^{-8}$
	1L-CVD-Sa (till 425 °C)	-0.0199 ± 0.0012	$3.10 \times 10^{-5} \pm 7.2 \times 10^{-6}$	$-5.77 \times 10^{-8} \pm 1.2 \times 10^{-8}$
	2L-CVD-SiO_2 (till 400 °C)	-0.0310 ± 0.0018	$8.56 \times 10^{-5} \pm 1.2 \times 10^{-5}$	$-1.16 \times 10^{-7} \pm 2.0 \times 10^{-8}$
	2L-CVD-Sa (till 425 °C)	-0.0160 ± 0.0014	--	--
	1L ME SiO_2 Ref.[24]	-0.0143		
	2L ME SiO_2 Ref.[24]	-0.0189		
	few layer Ref.[23]	-0.0123		

variation than that of $E_{2g}{}^1$, indicating that the morphology of the film impacts the Raman frequency of A_{1g} more than that of $E_{2g}{}^1$. On the other hand, both 1L and 2L MoS_2 films were originally grown on sapphire. It has been reported, for graphene, the possibility of forming bonds between mechanically exfoliated graphene and substrate is quite low; however, such bonds are possible with high-temperature growth.[29] It is reasonable to believe that the CVD growth of MoS_2 films at the temperature higher than 800 °C could produce somewhat stronger bonding between the MoS_2 film and sapphire substrate than in the case of transferred film. With increasing temperature, the chemical bonding would influence the in-plane vibration, giving rise to a

Nanoscale Accepted Manuscript

Published on 04 February 2014. Downloaded by North Carolina State University on 12/03/2014 16:08:08.

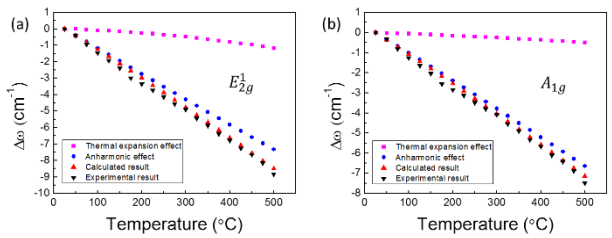


Fig. 6 The model of temperature dependent Raman shift relative to room temperature including the contributions of thermal expansion effect of lattice and anharmonic effect as compared to experimental results of bulk MoS2 for (a) E^1_{2g} and (b) A_{1g} modes .

damping of Raman frequency redshift to $E_{2g}{}^1$ mode at the low temperature region, as manifested on the reduced magnitude of χ_1 for the CVD-grown MoS_2 films on sapphire. Furthermore, the film-substrate coupling leads to the sign changes for both χ_2 and χ_3 compared to the bulk for the $E_{2g}{}^1$ mode of the on-sapphire samples. In contrast, mechanically transferred MoS_2 films on SiO_2/Si do not form the chemical bonding between film and substrate other than Van der Waals force, leading to the temperature dependence of Raman shift or χ_1 of the $E_{2g}{}^1$ mode similar to bulk MoS_2. However, the MoS_2 films on SiO_2/Si are more likely to be affected by the changes in the film morphology such as wrinkles and ripples when temperature increases, due to thermal expansion coefficient mismatch between MoS_2 and SiO_2. These changes of morphology in turn will have a large impact on out-of-plane vibration (A_{1g}), causing not only the nonlinear effect of temperature coefficient but also the large deviation of χ_1 from bulk MoS_2 for the SiO_2/Si samples. As for the sapphire samples, the chemical bonding restricts the MoS_2 film from morphology change, and the coupling with the substrate has a relatively small influence on the A_{1g} mode. Therefore, we can conclude that the morphology of MoS_2 films plays a significant role in temperature dependence of A_{1g} mode, which leads to the large and highly non-linear deviation from the bulk, while the bonding between film and substrate introduces weaker effects, in similar magnitudes, to both $E_{2g}{}^1$ and A_{1g} modes on their temperature induced Raman shifts.

The integrated Raman intensity for both $E_{2g}{}^1$ and A_{1g} modes has been found to decrease in all CVD-grown samples when T is greater than 400 °C, possibly due to the decomposition of MoS_2 films. The thermal decomposition temperature for most samples including bulk is somewhere > 500 °C, except for 2L-CVD-SiO_2 being near 450 °C. For all CVD-grown MoS_2 films on sapphire, no Raman signal is detected when the temperature reaches 575 °C, indicating the decomposition of MoS_2 films. The Raman spectrum does not recover at room temperature after reaching the maximum temperature. The main change is that the frequency difference between A_{1g} and $E_{2g}{}^1$ modes increases by 2.5 cm^{-1} for 1L-ME-SiO_2. In addition, their peak intensities decrease. There are at least two possible reasons: (1) the strain or morphology has changed, as expected, (2) the sample might be partially oxidized or decomposed. Similar results have been reported for graphene.[30]

Simulation model for temperature dependence of Raman shift

The intrinsic temperature dependence of the Raman shift can be divided into thermal expansion of the lattice ($\Delta\omega_E$) and an anharmonic effect ($\Delta\omega_A$) which causes the change of phonon self-energy.[27, 31, 32] In addition, thermally induced strains due to thermal expansion coefficient mismatch ($\Delta\omega_M$) between MoS_2 film and substrate should be considered.[28] Thus, the measured frequency change can be written as

$$\Delta\omega(T)=\Delta\omega_E(T)+\Delta\omega_A(T)+\Delta\omega_M(T), \quad (2)$$

where T is the sample temperature. Firstly, with increasing temperature, the lattice constant of MoS_2 structure increases due to thermal expansion of the film, leading to the Raman shift which is commonly expressed as [32]

$$\Delta\omega_E(T)=\omega_0\exp\left(-n\gamma\int_{25\ ^\circ C}^{T}\alpha\ \mathrm{d}T\right)-\omega_0, \quad (3)$$

where ω_0 is the room temperature frequency, n is the degeneracy, 1 for A_{1g} mode and 2 for $E_{2g}{}^1$ mode, γ is the Gruneisen parameter, and α is the thermal expansion coefficient of the material. The Gruneisen parameters of both E^1_{2g} and A_{1g} modes for bulk MoS2 are $\gamma(E_{2g}{}^1)$ = 0.21 and $\gamma(A_{1g})$ = 0.42, respectively. The in-plane and out-of-plane thermal expansion coefficients for bulk MoS_2 have been derived from the results of Ref.[33]:

$$\alpha_a(T)=\left(\frac{0.6007\times10^{-5}+0.6958\times10^{-7}T}{a}\right)\left(\frac{1}{^\circ C}\right)$$
$$\alpha_c(T)=\left(\frac{0.1064\times10^{-3}+1.5474\times10^{-7}T}{c}\right)\left(\frac{1}{^\circ C}\right), \quad (4)$$

where T is the temperature in °C, a and c are the lattice constants of MoS_2 in Å. They are calculated to be 2.48 × 10^{-6} /°C and 9.14 × 10^{-6} /°C, respectively, for in-plane and out-of-plane thermal expansion coefficients at room temperature. The second term of right-handed side in Eq.(2) is related to pure temperature effect, so called "self-energy" shift due to anharmonic coupling of multiple phonons, which can be written as[31]

$$\Delta\omega_A(T)=A\left(1+\frac{2}{e^x-1}\right)+B\left(1+\frac{3}{e^y-1}+\frac{3}{\left(e^y-1\right)^2}\right), \quad (5)$$

where $x=\hbar\omega/2kT, y=\hbar\omega/3kT$, and the first term corresponds to coupling of the optical phonon to two identical phonons, and the second term represents the coupling to three identical phonons. The coefficients A and B are constants that can be estimated by fitting the frequency shift attributes to anharmonic coupling. The possible remaining change of Raman shift is associated with the thermal expansion coefficient mismatch between film and substrate, introducing strain to the film, which can be expressed as[28]

$$\Delta\omega_M(T)=\beta\int_{25\ ^\circ C}^{T}\left(\alpha_{sub}(T)-\alpha_{MoS_2}(T)\right)\mathrm{d}T, \quad (6)$$

where β is the biaxial strain coefficient, α_{Sub} and α_{MoS_2} are the thermal expansion coefficients of substrate and MoS_2, respectively. For bulk MoS_2, there is no thermal expansion

Nanoscale Accepted Manuscript

This journal is © The Royal Society of Chemistry 2012

View Article Online
DOI: 10.1039/C3NR06462J
ARTICLE

Published on 04 February 2014. Downloaded by North Carolina State University on 12/03/2014 16:08:08.

coefficient mismatch between MoS_2 layers, so that the third term is zero. Eq.(6) assumes that the film and substrate is in coherent strain, which is likely invalid for the transferred film. Fig.6 shows these contributions to the changes in Raman peak positions of both E_{2g}^1 and A_{1g} modes for bulk MoS_2 with good agreement to experimental results. Table 2 shows the fitting parameters of A and B for both E_{2g}^1 and A_{1g} modes.

However, this model, which predicts a monotonic behavior, is not appropriate for MoS_2 films, either 1L or 2L, on substrates. In the case of MoS_2 films on substrates like SiO_2/Si and sapphire, according to Eq.(6) with β being -2.1 cm^{-1} per % strain, the contribution of the thermal expansion coefficient mismatch is expected to be negligible compared to the thermal expansion of lattice and anharmonic effect in the temperature region of interest.[34, 35] With increasing temperature, the biaxial tensile or compressive strain induced by thermal expansion coefficient mismatch increases significantly over the Van der

Table 2 The fitting parameters A and B for both E_{2g}^1 and A_{1g} modes used in three- and four-phonon coupling model.

bulk MoS_2	A (cm^{-1})	B (cm^{-1})
E_{2g}^1	-3.05835	0.04204
A_{1g}	-5.68777	0.26566

Waals force, resulting in the slippage or realignment of MoS_2 films on the surface of the substrate as well as forming wrinkles or ripples. For 1L-ME-SiO_2 sample, the realignment process takes place at ~100 °C where there is an obvious slope transition of A_{1g} peak position. During the realignment process, defects may be introduced into MoS_2 film such as the breakdown of Mo-S bonds and the slow decomposition of the film, showing a broadening of A_{1g} Raman peak (Fig.4). After the MoS_2 layer adjusts to a stable state on the SiO_2/Si substrate at high temperature, the Raman shift of A_{1g} mode again follows what is expected from Eq.(2).

Full Width at Half Maximum (FWHM)

Fig.7 shows the temperature dependent FWHM of both E_{2g}^1 peak and A_{1g} peak for all samples, by fitting to a Lorentzian lineshape function. Bulk MoS_2 has room-temperature FWHMs of 1.6 cm^{-1} and 2.2 cm^{-1}, respectively, for E_{2g}^1 and A_{1g}. Other samples have greater FWHMs, indicating the film-substrate coupling and defects existing in these samples that cause the peak broadening. The FWHM of E_{2g}^1 mode, in general, increases linearly with increasing temperature. However, the A_{1g} mode does not show a monotonic dependence but with a maximum linewidth in the middle of the temperature range. As it is discussed above, the mismatch of thermal expansion coefficients between MoS_2 films and substrates gives rise to changes of morphology e.g. wrinkles or ripples, consequently leading to a significant change of the temperature coefficients of A_{1g} mode. For all 1L and 2L samples, the FWHM of A_{1g} reaches the maximum when the realignment process occurs.

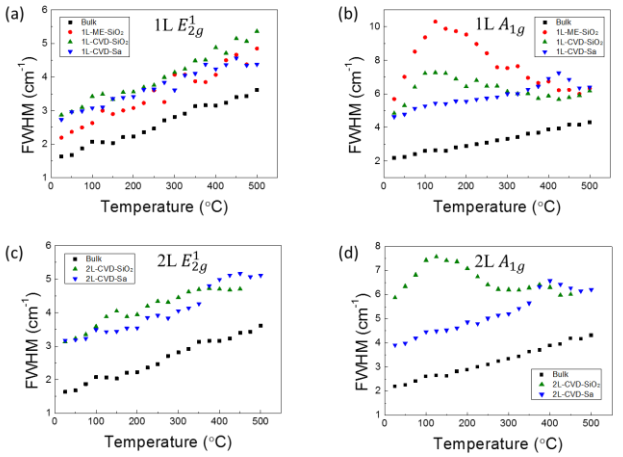


Fig. 7 Temperature dependence of FWHM of E_{2g}^1 and A_{1g} modes in bulk and all other 1L and 2L samples.

For instance, the anomaly of temperature dependent Raman shift of 1L-ME-SiO_2 takes places at the temperatures starting from ~100 °C, while the FWHM reaches the maximum at 125 °C and then starts to decrease afterward. This gives an additional illustration that the change of the morphology by the thermal expansion coefficient mismatch can affect the out-of-plane vibrational mode more than the in-plane mode when the temperature reaches a critical value.

Conclusions

In summary, we have reported temperature-dependent Raman studies of the in-plane E_{2g}^1 and out-of-plane A_{1g} modes on single- and bi-layer MoS_2 samples prepared by CVD growth and mechanical exfoliation on SiO_2/Si and sapphire substrates in a temperature range of 25 - 500 °C. Bulk MoS_2 has also been measured to serve as the references, with the first-order temperature coefficients of the Raman frequency shifts given as $\chi_1(E_{2g}^1)$ = -0.0221 ± 8.9 × 10^{-4} cm^{-1}/K and $\chi_1(A_{1g})$ = -0.0197 ± 8.94 × 10^{-4} cm^{-1}/K, respectively, for the E_{2g}^1 and A_{1g} mode. The thermal decomposition temperature is found to be approximately 575 °C for CVD-grown films on sapphire. The film-substrate coupling affects the temperature dependence of Raman frequency, intensity, and linewidth for both E_{2g}^1 and A_{1g} modes in the 1L and 2L MoS_2. The impact depends on the substrate type and/or film-substrate binding mechanism. For the CVD grown film on the original sapphire substrate with likely chemical bonding between them, the film-substrate coupling significantly reduces the linear temperature coefficients of the Raman shift of the E_{2g}^1 mode to -0.0143 ± 5.7 × 10^{-4} cm^{-1}/K for 1L and -0.0135 ± 8.4 × 10^{-4} cm^{-1}/K for 2L, but has no or small effect on the A_{1g} mode, with -0.0199 ± 0.0012 cm^{-1}/K for 1L and -0.0160 ± 0.0014 cm^{-1}/K for 2L. For the transferred film on SiO_2/Si substrate, originally grown on sapphire by CVD, for the E_{2g}^1 mode, the temperature coefficients were found to be very close to the bulk value as -0.0217 ± 0.0017 cm^{-1}/K for 1L and -0.0233 ± 0.0018 cm^{-1}/K for 2L; but for A_{1g} mode, they increase substantially to -0.0301 ± 0.0023 cm^{-1}/K for 1L and -0.0310 ±

Nanoscale Accepted Manuscript

Published on 04 February 2014. Downloaded by North Carolina State University on 12/03/2014 16:08:08.

0.0018 cm^{-1}/K for 2L. The substrate effects are most pronounced for the A_{1g} mode, showing as stronger nonlinearity on the temperature shift of the Raman frequency and non-monotonic temperature dependence of the Raman linewidth. Similar or even stronger effects were observed on a mechanically exfoliated 1L film from a bulk single crystal. These results suggest that for the mechanically transferred thin film, due to the mismatch in thermal expansion between the film and substrate, the temperature change can lead to significant changes in the thin-film morphology as a result of realignment of the film on the substrate, which can be most easily probed by the temperature dependence of the A_{1g} mode associated with the out-of-plane atomic vibration. Temperature dependent Raman study provides an efficient tool for investigating the coupling between the 2-D material and substrate either with chemical or mechanical bonding.

Acknowledgements

Y.Z. acknowledges the support of Bissell Distinguished Professorship. L.C. acknowledges the support of a Young Investigator Award from the Army Research Office (W911NF-13-1-0201).

Notes and references

[a] Electrical and Computer Engineering Department, University of North Carolina at Charlotte, Charlotte, NC 28223, USA. Email: yong.zhang@uncc.edu

[b] Department of Materials Science and Engineering, North Carolina State University, Raleigh, NC 27695, USA.

† Electronic Supplementary Information (ESI) available: The temperature-dependent Raman of another two mechanically exfoliated 1L MoS2 films on SiO2/Si substrate. See DOI: 10.1039/b000000x/

1. K. S. Novoselov, A. K. Geim, S. V. Morozov, D. Jiang, M. I. Katsnelson, I. V. Grigorieva, S. V. Dubonos and A. A. Firsov, *Nature*, 2005, 438, 197-200.
2. Y.-M. Lin, C. Dimitrakopoulos, K. A. Jenkins, D. B. Farmer, H.-Y. Chiu, A. Grill and P. Avouris, *Science*, 2010, 327, 662.
3. F. Schwierz, *Nat Nano*, 2010, 5, 487-496.
4. K. S. Novoselov, A. K. Geim, S. V. Morozov, D. Jiang, Y. Zhang, S. V. Dubonos, I. V. Grigorieva and A. A. Firsov, *Science*, 2004, 306, 666-669.
5. K. Watanabe, T. Taniguchi and H. Kanda, *Nat Mater*, 2004, 3, 404-409.
6. C. Jin, F. Lin, K. Suenaga and S. Iijima, *Physical Review Letters*, 2009, 102, 195505.
7. I. Meric, M. Y. Han, A. F. Young, B. Ozyilmaz, P. Kim and K. L. Shepard, *Nat Nano*, 2008, 3, 654-659.
8. Y.-W. Son, M. L. Cohen and S. G. Louie, *Physical Review Letters*, 2006, 97, 216803.
9. G. Giovannetti, P. A. Khomyakov, G. Brocks, P. J. Kelly and J. van den Brink, *Physical Review B*, 2007, 76, 073103.
10. Y. Zhang, T.-T. Tang, C. Girit, Z. Hao, M. C. Martin, A. Zettl, M. F. Crommie, Y. R. Shen and F. Wang, *Nature*, 2009, 459, 820-823.
11. Y. Kubota, K. Watanabe, O. Tsuda and T. Taniguchi, *Science*, 2007, 317, 932-934.
12. K. F. Mak, C. Lee, J. Hone, J. Shan and T. F. Heinz, *Physical Review Letters*, 2010, 105, 136805.
13. A. Splendiani, L. Sun, Y. Zhang, T. Li, J. Kim, C.-Y. Chim, G. Galli and F. Wang, *Nano Letters*, 2010, 10, 1271-1275.
14. RadisavljevicB, RadenovicA, BrivioJ, GiacomettiV and KisA, *Nat Nano*, 2011, 6, 147-150.
15. Y. Zhan, Z. Liu, S. Najmaei, P. M. Ajayan and J. Lou, *Small*, 2012, 8, 966-971.
16. Y. Yu, C. Li, Y. Liu, L. Su, Y. Zhang and L. Cao, *Sci. Rep.*, 2013, 3.
17. A. Molina-Sánchez and L. Wirtz, *Physical Review B*, 2011, 84, 155413.
18. E. S. Kadantsev and P. Hawrylak, *Solid State Communications*, 2012, 152, 909-913.
19. X. Zhang, W. P. Han, J. B. Wu, S. Milana, Y. Lu, Q. Q. Li, A. C. Ferrari and P. H. Tan, *Physical Review B*, 2013, 87, 115413.
20. M. Ghorbani-Asl, N. Zibouche, M. Wahiduzzaman, A. F. Oliveira, A. Kuc and T. Heine, *Sci. Rep.*, 2013, 3.
21. H. Li, Q. Zhang, C. C. R. Yap, B. K. Tay, T. H. T. Edwin, A. Olivier and D. Baillargeat, *Advanced Functional Materials*, 2012, 22, 1385-1390.
22. A. C. Ferrari, J. C. Meyer, V. Scardaci, C. Casiraghi, M. Lazzeri, F. Mauri, S. Piscanec, D. Jiang, K. S. Novoselov, S. Roth and A. K. Geim, *Physical Review Letters*, 2006, 97, 187401.
23. S. Sahoo, A. P. S. Gaur, M. Ahmadi, M. J. F. Guinel and R. S. Katiyar, *The Journal of Physical Chemistry C*, 2013, 117, 9042-9047.
24. S. Najmaei, P. M. Ajayan and J. Lou, *Nanoscale*, 2013, DOI: 10.1039/C3NR02567E.
25. P. G. Klemens, *Physical Review*, 1966, 148, 845-848.
26. L. A. Falkovsky, *J. Exp. Theor. Phys.*, 2007, 105, 397-403.
27. I. Calizo, A. A. Balandin, W. Bao, F. Miao and C. N. Lau, *Nano Letters*, 2007, 7, 2645-2649.
28. D. Yoon, Y.-W. Son and H. Cheong, *Nano Letters*, 2011, 11, 3227-3231.
29. Y. y. Wang, Z. h. Ni, T. Yu, Z. X. Shen, H. m. Wang, Y. h. Wu, W. Chen and A. T. Shen Wee, *The Journal of Physical Chemistry C*, 2008, 112, 10637-10640.
30. Z. H. Ni, H. M. Wang, Z. Q. Luo, Y. Y. Wang, T. Yu, Y. H. Wu and Z. X. Shen, *Journal of Raman Spectroscopy*, 2010, 41, 479-483.
31. M. Balkanski, R. F. Wallis and E. Haro, *Physical Review B*, 1983, 28, 1928-1934.
32. J. Menéndez and M. Cardona, *Physical Review B*, 1984, 29, 2051-2059.
33. S. H. El-Mahalawy and B. L. Evans, *Journal of Applied Crystallography*, 1976, 9, 403-406.
34. H. Tada, A. E. Kumpel, R. E. Lathrop, J. B. Slanina, P. Nieva, P. Zavracky, I. N. Miaoulis and P. Y. Wong, *J Appl Phys*, 2000, 87, 4189-4193.
35. C. Rice, R. J. Young, R. Zan, U. Bangert, D. Wolverson, T. Georgiou, R. Jalil and K. S. Novoselov, *Physical Review B*, 2013, 87, 081307.

Nanoscale Accepted Manuscript

This journal is © The Royal Society of Chemistry 2012

Role of Boundary Layer Diffusion in Vapor Deposition Growth of Chalcogenide Nanosheets: The Case of GeS

Chun Li,[†,∥] Liang Huang,[†] Gayatri Pongur Snigdha,[§] Yifei Yu,[†] and Linyou Cao[†,‡,*]

[†]Department of Materials Science and Engineering, [‡]Department of Physics, and [§]Department of Chemical Engineering, North Carolina State University, Raleigh, North Carolina 27695, United States. [∥]Present address: School of Optoelectronics, University of Electronic Science and Technology of China, 610054 Chengdu, China.

ABSTRACT We report a synthesis of single-crystalline two-dimensional GeS nanosheets using vapor deposition processes and show that the growth behavior of the nanosheet is substantially different from those of other nanomaterials and thin films grown by vapor depositions. The nanosheet growth is subject to strong influences of the diffusion of source materials through the boundary layer of gas flows. This boundary layer diffusion is found to be the rate-determining step of the growth under typical experimental conditions, evidenced by a substantial dependence of the nanosheet's size on diffusion fluxes. We also find that high-quality GeS nanosheets can grow only in the diffusion-limited regime, as the crystalline quality substantially deteriorates when the rate-determining step is changed away from the boundary layer diffusion. We establish a simple model to analyze the diffusion dynamics in experiments. Our analysis uncovers an intuitive correlation of diffusion flux with the partial pressure of source materials, the flow rate of carrier gas, and the total pressure in the synthetic setup. The observed significant role of boundary layer diffusions in the growth is unique for nanosheets. It may be correlated with the high growth rate of GeS nanosheets, ~3−5 μm/min, which is 1 order of magnitude higher than other nanomaterials (such as nanowires) and thin films. This fundamental understanding of the effect of boundary layer diffusions may generally apply to other chalcogenide nanosheets that can grow rapidly. It can provide useful guidance for the development of general paradigms to control the synthesis of nanosheets.



KEYWORDS: nanosheets · boundary layer · diffusion-limited · vapor deposition · layered compound

Semiconductor materials with reduced dimensionality construct an important cornerstone for modern materials science.[1] In contrast to one-dimensional (1D) semiconductor nanowires and zero-dimensional (0D) quantum dots, which have been extensively studied,[2−10] studies of two-dimensional (2D) semiconductor nanosheets have remained limited. One key reason is the lack of sophisticated capabilities to synthesize nanosheets with physical features precisely controlled, including morphology, size, structure, and interface. The properties of low-dimensional materials strongly depend on physical features.[1] Therefore, the capability of synthetic control is necessary for employing nanosheets as a functional material platform for both fundamental and applied interest.

Of the most interest is the nanosheet of layered chalcogenide materials, including transition metal dichalcogenides (MoS_2, TiS_2, WS_2, *etc.*) and chalogenides of group III (GaSe, GaTe, InSe), group IV (GeS, GeSe, SnS, SnSe, $GeSe_2$, *etc.*), and group V elements (Bi_2Se_3, Bi_2Te_3). These materials show graphite-like layered structures with strong intralayer covalent bonding and weak interlayer van del Waals forces.[11,12] The chalcogenide nanosheet holds great promise for a wide range of fields such as solar energy conversion,[13] field effect transistors,[14,15] novel optoelectronic devices,[16] and energy storage.[17] Traditional ways to produce chalcogenide nanosheets rely on exfoliations from bulk materials, which provides limited control of the physical features of resulting nanosheets.[18] Synthetic approaches are promising to enable control of physical features from an atomic level. Current synthetic strategies for nanosheets primarily focus on solution-based processes, such as solvothermal reactions.[19−26] However, the solution-produced nanosheet may have solvent residues adsorbed at the surface that are difficult to remove and can substantially modify the nanosheet's intrinsic properties. Nonsolution approaches, for instance, chemical or physical vapor depositions, have also been explored for the growth of nanosheets.[27−37] These methods can provide

* Address correspondence to lcao2@ncsu.edu.

Received for review June 25, 2012 and accepted September 25, 2012.

Published online 10.1021/nn303745e

© XXXX American Chemical Society

clean nanosheets to serve as a useful material platform for fundamental and applied research.[33,38] However, little attention has been paid to the fundamental understanding of the vapor deposition growth of nanosheets. A fundamental understanding is very important for the development of synthetic control.

While vapor deposition techniques have been extensively studied in the growth of thin films and nanomaterials including nanowires,[2,39] nanotubes,[40] and graphene,[41] knowledge obtained from these materials cannot simply apply to the synthesis of single-crystalline 2D nanosheets.[42−44] The vapor deposition growth of the existing nanomaterials often involves catalysts.[40,41,45,46] The catalyst is typically a metal material and sometimes can be the same as one component of the resulting nanomaterials.[47,48] In a typical synthesis, catalysts first react with source materials (vapor phase) to form an alloy, for example, Ni−C alloy formed during the process of nickel-catalyzed growth of graphene.[49] Nanomaterials can be produced by precipitation from the alloy due to a supersaturation of source materials inside. During this process, both nucleation and growth steps are governed by the catalyst. Therefore, rational design of the catalyst is a major strategy to control this catalyzed synthesis.[2,50] In contrast, the synthesis of 2D chalcogenide nanosheets with vapor depositions is not catalytic.[33,35,36,51,52] The anions of chalcogenide materials (sulfide, selenide, and telluride) are highly reactive. It is difficult to find suitable catalysts that can survive the highly reactive chalcogenide vapor at elevated temperatures and can also facilitate a two-dimensional growth to yield nanosheets. Without the guidance of catalysts, the growth of 2D nanosheets may be subject to the strong influence of many experimental parameters, which may play only a negligible role in catalyzed growth,[29,53] for instance, the boundary layer of gas flows. The growth of nanosheets would also be different from the vapor deposition growth of thin films, which is noncatalytic as well, due to different requirements for crystalline quality and different experimental conditions. The nanosheet of interest needs be single crystalline and would grow at low pressure and low temperature, but thin films are typically polycrystalline and grow at high pressure and high temperature.

Here, we report a synthesis of single-crystalline germanium sulfide (GeS) nanosheets using vapor deposition processes. Germanium sulfide is useful for solar energy conversion,[54] nonvolatile memory,[55] and photonics.[56] We demonstrate that the growth mechanism of the nanosheet is indeed different from those of other nanomaterials and thin films. The nanosheet growth is subject to strong influences of the diffusion of source materials through the boundary layer of gas flows. The diffusion is found to be the rate-determining step of the nanosheet growth under typical experimental conditions (~20−30 Torr, ~300 °C). Additionally, we find that high-quality 2D nanosheets can grow only in the diffusion-limited regime, as the crystalline quality substantially deteriorates when the rate-determining step is changed from boundary layer diffusion. We establish a simple model to analyze the diffusion dynamics in experiments. Our analysis quantitatively elucidates the dependence of diffusion flux on the partial pressure of source material vapor, the flow rate of the carrier gas, and the total pressure in the synthetic system. The analysis also suggests that the observed strong influence of boundary layer diffusions can be ascribed to a rapid growth rate of the nanosheet, which is ~3−5 μm/min. The significant role of boundary layer diffusions in the growth of nanosheets is in stark contrast with the vapor deposition growth of other nanomaterials such as nanowires, nanotubes, and graphene, where the boundary layer diffusion typically plays a negligible role.[29,53] The nanosheet growth is also different from the growth of thin films by vapor deposition. The growth of high-quality thin films prefers the rate-determining step to be the growth reaction, rather than the diffusion process as the nanosheet, and the diffusion-limited growth of thin films typically happens with much higher pressures (*i.e.*, ambient pressure) and higher temperatures (*i.e.*, >600 °C) compared with those used in the nanosheet growth.

RESULTS AND DISCUSSION

Figure 1A, B shows scanning electron microscope (SEM) images of typical as-grown GeS nanosheets on silicon substrates with 300 nm thick thermal oxide. Both Raman measurements (see Figure S1 in the Supporting Information) and an energy-dispersive X-ray (EDX) spectrum (Figure S2) confirm that the chemical composition of the nanosheet is germanium monosulfide, the same as the source materials. The sublimation temperature (400−500 °C) in the experiments is designed to ensure that the source materials (GeS powder) sublimate into gaseous GeS molecules, rather than decomposing into Ge or S atoms.[57] The nanosheets show hyperbranched flower structures. This can be attributed to subsequent nucleations on the nanosheet grown earlier in a long growth period (10 min), similar to what was observed in the synthesis of branched PbS nanowires.[58] Shortening the growth time, for instance, to 1−2 min can substantially decrease the branching. The growth rate of the nanosheet is very fast, in the range ~3−5 μm/min under typical experimental conditions. The nanosheet is highly anisotropic in morphology. Its lateral dimension can reach over 40−100 μm (Figure 1A, B), while the thicknesses is in the range 30−50 nm (Figure 1B inset and Figure 1C), giving rise to a size/thickness ratio of ~1000−3000. Atomic force microscope characterizations

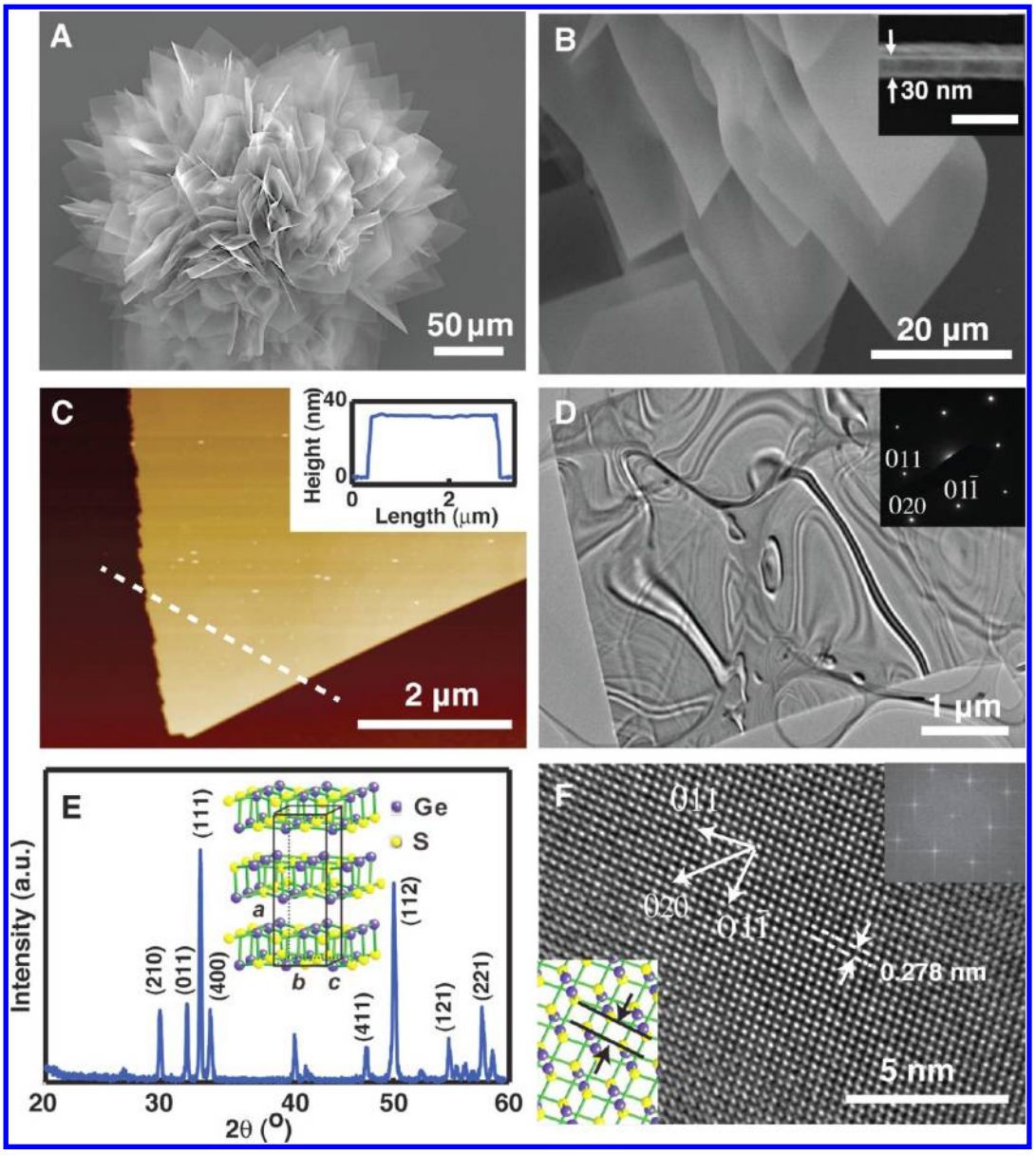


Figure 1. Morphology and crystal structure of GeS nanosheets. (A) SEM image of as-grown GeS nanosheets on substrates. (B) Magnified SEM image of the nanosheets. Inset is a cross-section SEM image showing that the thickness of the nanosheet is 30 nm. Scale bar: 100 nm. (C) AFM image of a nanosheet and a height profile corresponding to the dashed line. (D) TEM image and electron diffraction pattern (inset) of a typical nanosheet. The diffraction pattern is indexed as shown. (E) XRD pattern of the nanosheet, which indicates the structure is orthorhombic. Inset shows a crystal structure model for GeS. (F) HRTEM image of a representative nanosheet. Upper inset is fast Fourier transformation of the HRTEM image; it is not indexed for visual convenience. The HRTEM image shows crystalline directions and (011) interplane spacing. Bottom-left inset is a model of the GeS crystal structure viewed from the [100] direction, the parallel black lines indicating the interspacing between (011) planes.

(Figure 1C and inset) indicate that the surface of the nanosheet is reasonably smooth. We can find steps at a height of 1−2 nm at the surface of the nanosheet.

The synthetic nanosheet exhibits excellent crystalline quality. Figure 1D shows a TEM image of a representative nanosheet and corresponding selected-area electron diffraction (SAED) pattern (inset). Results of X-ray diffraction (XRD) measurements and high-resolution transmission electron microscope (HRTEM) characterizations are given in Figure 1E and F, respectively. The SAED and HRTEM results indicate that the nanosheet is single crystalline. The bent contour lines in the TEM image shown in Figure 1D are possibly caused either by buckling in the nanosheet introduced in the process of TEM sample preparation or by electron-beam-induced thermal strain during the characterization process. All the structural characterizations (SAED, HRTEM, and XRD) demonstrate that the GeS nanosheet has an orthorhombic structure, the same as bulk GeS materials.[59] Analysis of the XRD result indicates the lattice constants of the nanosheet as $a = 10.42$ Å, $b = 3.61$ Å, $c = 4.30$ Å, reasonably consistent

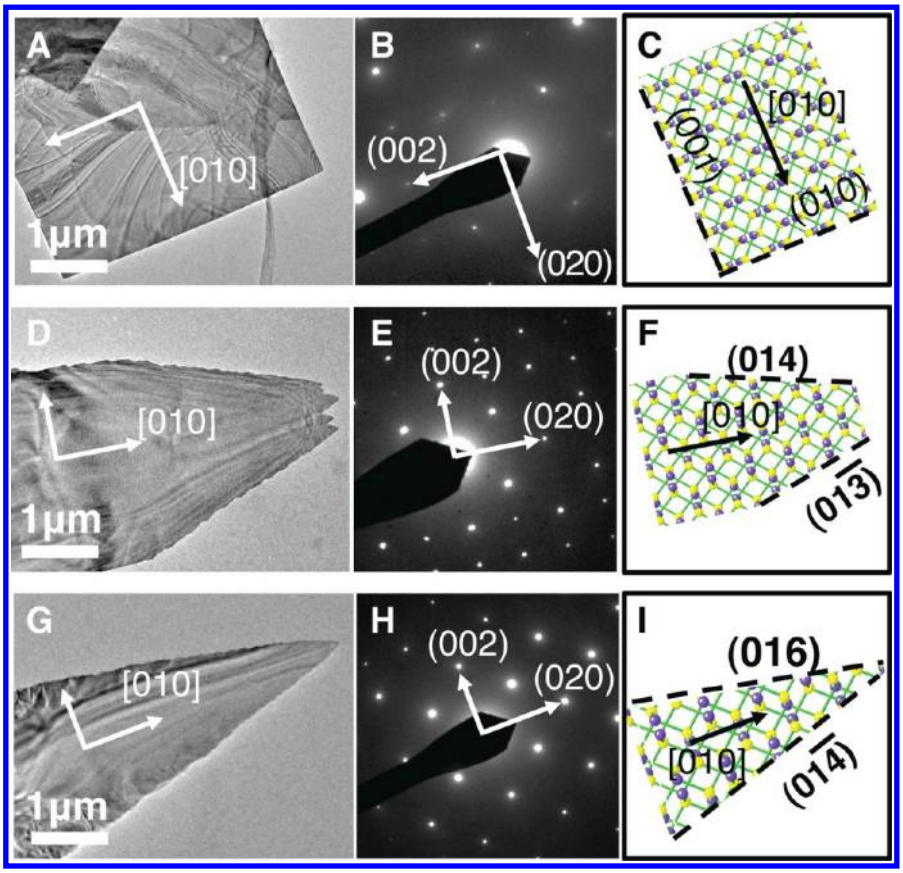


Figure 2. Shape evolution of GeS nanosheets grown at different deposition temperatures. The deposition temperatures are 330 °C (A–C), 310 °C (D–F), and 290 °C (G–I). For each deposition temperature, a TEM image (A, D, G), a corresponding SAED pattern (B, E, H), and a structural model (C, F, I) of representative sheets are given. Important crystalline directions and planes are given and indexed in the images as shown.

with bulk GeS materials and the GeS nanosheets made by wet-chemical methods (bulk GeS, a = 10.47 Å, b = 3.64 Å, c = 4.30 Å; wet-chemical synthetic GeS nanosheets, a = 10.52 Å, b = 3.65 Å, c = 4.30 Å).[19,59] We can also find that the basal plane of the nanosheet is always (100), as indicated by the SAED (Figure 1D inset) and HRTEM (Figure 1F). This is dictated by the nature of GeS materials, which is a layered compound and (100) is the most energetically stable plane.

Typical GeS nanosheets show a rectangular shape with (001) and (010) planes enclosing the long and the short edges, respectively (Figure 2A and C). Nanosheets with other shapes were found in experiments as well. Figure 2 gives TEM images (Figure 2A, D, and G) and corresponding electron diffraction patterns (Figure 2B, E, and H) of nanosheets grown at different deposition temperatures. The nanosheet appears to be rectangular at high deposition temperatures (330 °C), truncated rectangular at low temperature (310 °C), and triangular at even lower temperatures (290 °C). By analyzing the TEM images and related diffraction patterns, we can build a structural model for each of the nanosheets as given in Figure 2C, F, and I. Interestingly, no matter the shape, the direction along the long axis of the nanosheets is always [010] (Figure 2). High-index crystalline planes can be found exposed at the nonrectangular shapes, for instance, $(01\bar{3})$ and (014) planes at truncated rectangular shapes (Figure 2F), $(01\bar{4})$ and (016) at triangular shapes (Figure 2I). This temperature-dependent shape evolution suggests a possible strategy to control the shape of nanosheets.

Of most interest is understanding the mechanism of the nanosheet growth. To do that, we examine the dynamics behavior of the synthetic process. The nanosheet grows in a tube furnace with source materials placed at elevated temperatures and receiving substrates downstream with lower temperatures. As illustrated in Figure 3, five major steps are involved in the growth: (1) sublimation and transport of source materials by a forced flow of carrier gas, (2) diffusion of source material vapor from the gas phase onto receiving substrates, (3) migration of adsorbed species to growth sites, (4) incorporation of the adsorbed source materials into crystalline lattices, (5) resublimation (desorption) of excess adsorbed species into the gas phase. Typically, the migration (step 3) and the incorporation (step 4) of adatoms can be lumped together as the step of growth reaction. Generally, the rate-determining step could be either the diffusion (step 2)

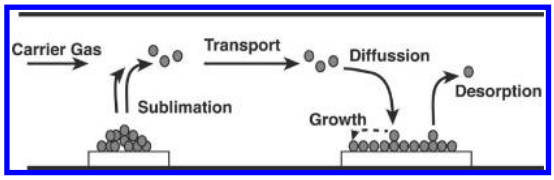


Figure 3. Schematic illustration of dynamics behavior involved in the synthetic process. It includes five major steps: sublimation and transport of GeS vapor, diffusion of GeS vapor onto receiving substrates, migration of adsorbed GeS to growth sites, incorporation of GeS adtoms into crystalline lattices, and desorption of GeS adtoms.

or the growth reaction (step 3 and 4), which is referred to as diffusion-limited or reaction-limited growth, respectively.

We find that the growth of GeS nanosheets is limited by the diffusion. This is evidenced by a strong dependence of the size of nanosheets on the lateral distance away from the upstream edge of the receiving substrate (Figure 4). Figure 4A shows a SEM image of typical as-grown nanosheets on substrates. We can find that the growth occurs only in the area close to the upstream edge of the substrate. The density of the nanosheet right at the upstream edge of the substrate is found to be particularly high (Figure S3). This can be ascribed to a high surface energy of the edge, which can facilitate nucleation of the nanosheets. We also found that the size of the nanosheets decreases with increasing lateral distance (Figure 4B–D). We can exclude the decrease of the local growth temperature as a major cause for this observed size shrinking (Figure 4E). The temperature difference over the growth area (the white area) shown in Figure 4A is estimated at <3 °C. More importantly, we find that the nanosheet grown at the edge of a neighboring substrate downstream (lower temperature) can show a larger size than the nanosheets at the nonedge area (for instance, position 3) of Figure 4A. This indicates that the local temperature is not the major cause of the observed size shrinking. Careful analysis indicates that the size of the nanosheet (L, in length) is inversely proportional to square root of the lateral distance x as $L \propto 1/\sqrt{x}$ (Figure 4E). This relationship strongly suggests that the growth of the nanosheet is limited by a diffusion process through the boundary layer of the gas flow.[60]

The boundary layer diffusion process is very important for nanosheet growth. A distinct line (the dashed black line in Figure 4A) can be found on the growth substrate that separates the areas with (the white area, upstream of the dashed line) and without (the gray area, downstream of the dashed line) nanosheets. This distinct separation suggests that a critical diffusion flux is necessary for the growth of nanosheets. To further investigate the effect of the diffusion, we studied the growth on a series of substrates placed at different positions downstream, as illustrated in Figure 5A. On

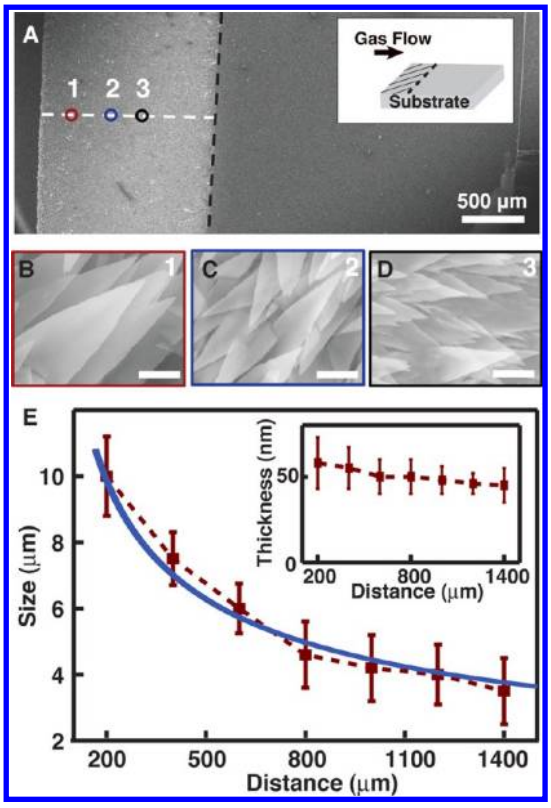


Figure 4. Boundary layer effect on the growth of GeS nanosheets. (A) Low-magnification SEM image of as-grown nanosheets on substrates. The white area is where the nanosheets grow. The gas flow comes from the left side, as illustrated in the inset with the shaded area indicating the growth zone. The black dashed line indicates the boundary beyond which no nanosheet grows. (B, C, D) Magnified top-view SEM images of the GeS nanosheets grown at the positions 1, 2, 3 marked in (A), respectively. The scale bars all are 1 μm. (E) Size L (in length) of nanosheets grown along the white dotted line in (A) as a function of the distance x away from the edge. The size of the nanosheets refers to the length from the base to the tip of the nanosheet that was measured from cross-section SEM images. The solid line is a fitting curve, $L = B/x^{0.5}$, where B is a fitting constant. Inset: Thickness of the sheet as a function of the lateral distance, which shows negligible dependence on the distance.

substrates with relatively high temperatures, >290 °C, the size of the nanosheets shows a substantial dependence on the lateral distance away from the upstream edge, similar to the results given in Figure 4, indicating a diffusion-limited growth (Figure 5B, C). However, no obvious dependence of the size on the lateral distance was found for the growth on the substrates with a lower temperature, 270 °C (Figure 5D, E). This suggests that the growth at the lower temperature is not limited by the boundary layer diffusion, but the growth reaction instead. It has been well documented that lowering the temperature can switch vapor deposition processes from diffusion-limited (high temperature) to reaction-limited (low temperature).[60] This is because the kinetics of the growth reactions exponentially decreases with the temperature, but the diffusion flux only shows a mild dependence on the temperature.

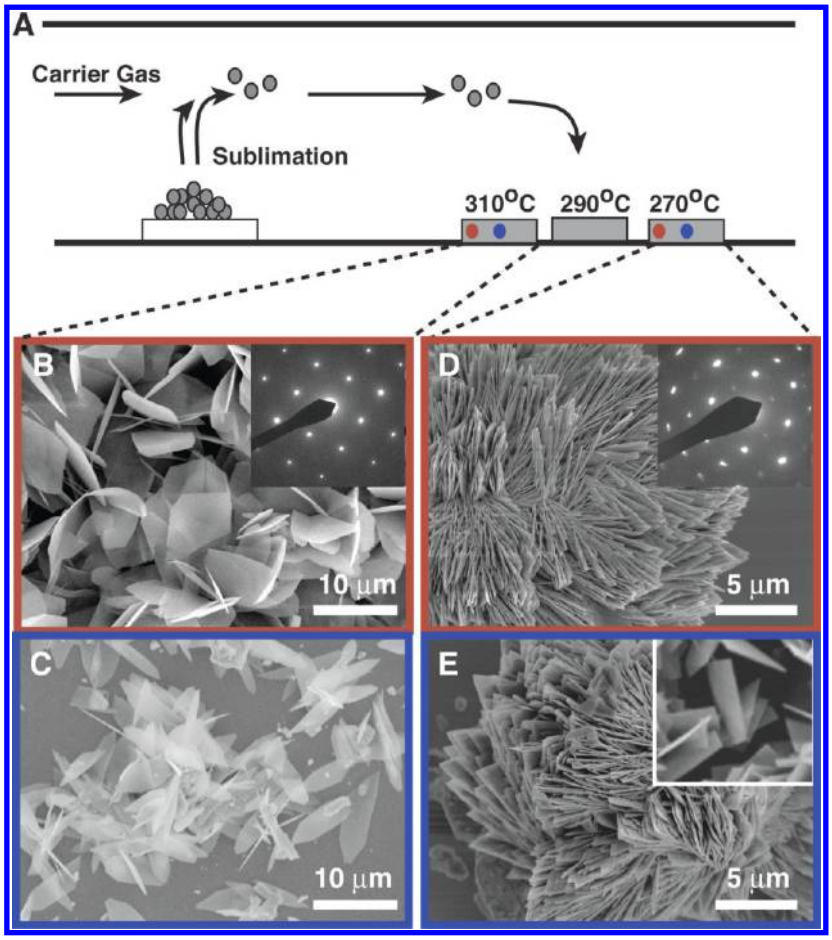


Figure 5. Importance of the diffusion-limited regime for the growth of high-quality GeS nanosheets. (A) Schematic illustration of the growth of GeS nanosheets at different deposition temperatures of 310, 290, and 270 °C. (B, C) SEM images of GeS nanosheets grown on the areas indicated by the red and the blue dots on the 310 °C substrate, respectively. The red and blue dots indicate small and large distances away from the upstream edge of the 310 °C substrate. The inset in (B) is SAED for representative nanosheets. (D, E) SEM images of GeS nanosheets at the areas indicated by the red and the blue dots on the 270 °C substrate, respectively. (The inset in (D) is SAED for representative nanosheets. The inset in (E) is a SEM image of GeS nanosheets grown at the same deposition temperature but with a lower flow rate of carrier gas. Scale bar in the inset is the same as that of (E).)

Moreover, we can find that the nanosheets grown at the diffusion-limited regime are high quality with a smooth surface and single crystalline (Figure 5B and inset). However, those grown at the reaction-limited regime show a rough surface (Figure 5D) and inferior crystalline quality, as evidenced by elongated diffraction spots (Figure 5D inset). Lower deposition temperatures may give rise to a larger supersaturation of GeS vapor. The larger supersaturation might induce condensation of GeS vapor into small clusters in the gas phase, whose deposition could lead to poor crystalline quality in the resulting materials. It is worthwhile to note that the increase in supersaturation may facilitate the condensation of GeS vapor, but does not affect the diffusion flux, which relies on the concentration gradient of the GeS vapor. However, we can reasonably exclude this condensation in the gas phase as the major reason for the observed worse crystalline quality at lower temperatures. We found that the crystalline quality of the nanosheets grown at the lower temperatures could be substantially improved by just decreasing the flow rate of carrier gas, for instance, from 10 to 5 sccm (Figure 5E inset). As we will discuss in the following session, a decrease in the flow rate lowers the diffusion flux. The lowered diffusion flux may then lead to a switch of the rate-determining step from growth reaction back to diffusion. This improvement of crystalline quality by lowering the flow rate of the carrier gas indicates that the observed difference in crystalline quality at different temperatures (Figure 5) is primarily caused by a difference in the rate-determining step. Under the reaction-limited regime, diffusion flux is larger than the kinetics of the growth reaction; for instance, the diffusion flux (step 2 in Figure 3) is larger than the migration rate of adatoms to growth sites (step 3 in Figure 3). In this case, the excess amount of adsorbed GeS atoms, if not resublimated (step 5 in Figure 3) quickly, may aggregate on the surface of the nanosheets to cause poor crystalline quality.

This diffusion-limited growth of nanosheets is in stark contrast with the vapor deposition growth of other nanomaterials (for instance, nanowires), which is typically reaction-limited and where the boundary layer diffusion plays a negligible role.[29,53] It is also different from the growth of thin films by vapor deposition. The growth of high-quality thin films usually prefers the rate-determining step to be the growth reaction, rather than the diffusion process as the nanosheet does. Additionally, the diffusion-limited growth of thin films usually happens when the pressure and temperature are high, for instance, at ambient pressure and >600 °C. In our experiments the pressure is typically less than 40 Torr and the deposition temperature only around or less than 300 °C. We believe that the unusual growth behavior of nanosheets can be linked to the rapid growth of the nanosheet. Under typical experimental conditions, the growth of GeS nanosheets is estimated at ~3−5 μm/min or even higher, substantially larger than that of thin films and nanowires, for instance, silicon nanowires.[61]

To obtain better insights into the diffusion-limited growth, we quantitatively analyzed the diffusion dynamics and elucidated the dependence of diffusion flux on experimental conditions. The diffusion is subject to strong influences of complicated fluidic dynamics in the tube furnace. A full-fledged analysis of fluid dynamics is out of the scope of this work. Instead, we analyze the diffusion process with a simplified model in order to obtain intuitive insights that can be used for guiding experimental designs to control the growth. One key issue for understanding the diffusion-limited growth is to understand the boundary layer of gas flows. The gas flow in experiments is a laminar flow, as the dimensionless parameter Reynolds number, which characterizes the flow of a fluid, is low (<2). The velocity of the gas flow at the upper surface of the receiving substrate is zero due to friction between the gas flow and the substrate. The difference between the flow velocities at the substrate surface and at the bulk gas flow gives rise to a boundary layer in which the flow velocity evolves from zero to that of the bulk gas flow (Figure 6). The diffusion process is essentially a transport of source material vapor through this gas flow boundary layer. As a result, the thickness of the gas flow boundary layer plays an important role in diffusion flux.

The thickness of the gas flow boundary layer is related with the Reynolds number and varies with the lateral distance away from the upstream edge of the substrate as $\delta = (x/Re_x)^{1/2}$.[60] The Reynolds number is $Re_x = \rho_g v_g d/\mu_g$, where ρ_g, v_g, and μ_g are the density, mean velocity, and dynamic viscosity of the gas flow, respectively, and d is the diameter of the tube. The mean velocity v_g can be evaluated from the gas flow rate $Q = J_{Ar}RT'$ (where T' is the local temperature of the substrate, J_{Ar} is the molar flow rate of carrier gas, which is Ar in our experiments, and R is the gas constant), the total pressure P_{tot}, and the cross-section area of the tube A, $v_g = BT'J_{Ar}/P_{tot}$, with the constant $B = R/A$. So, the thickness of the gas flow boundary layer can be written as a function of experimental parameters as

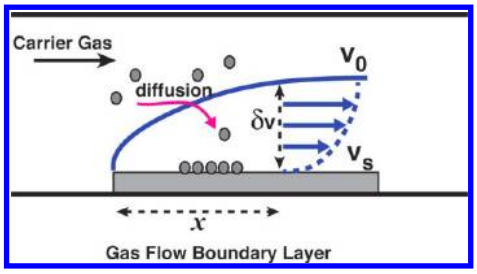


Figure 6. Schematic illustration of the diffusion of source materials through the gas flow boundary layer. The velocity gradient boundary layer is indicated by a solid blue curve. V_0 and V_S are the gas velocity in the bulk gas flow and at the surface of the substrate. δ_V is the thickness of the boundary layer. x is the lateral distance away from the edge. The horizontal arrows indicate a gradual change of gas velocity in the boundary layer.

$$\delta(x) = \sqrt{\frac{\mu_g}{\rho_g B}\frac{P_{tot}}{T'J_{Ar}}x} \quad (1)$$

As a first-order approximation, we can assume a linear concentration gradient across the gas flow boundary layer. The diffusion flux of source materials toward the substrate can be written as

$$\frac{dm}{dt} = -D\frac{P_{par} - P_S}{\delta(x)} = -D\sqrt{\frac{\rho_g BT'}{\mu_g}}[P_{par} - P_S(T')]\sqrt{\frac{J_{Ar}}{P_{tot}x}} \quad (2)$$

where $P_S(T')$ is the equilibrium vapor pressure of GeS at the local deposition temperature T'.

Equation 2 indicates that the diffusion flux inversely depends on the square root of the lateral distance away from the edge of the substrate. This is consistent with our experimental observations (Figure 4). Equation 2 also suggests that the diffusion flux is dependent on the partial pressure of GeS vapor in the gas phase, P_{par}, the flow rate of carrier gas, J_{Ar}, and the total pressure in the synthetic setup, P_{tot}. Our further analysis based on a simplified model indicates that, in typical experiments, the partial pressure, P_{par}, of GeS vapor is close to the equilibrium vapor pressure of GeS materials, P_S, at the sublimation temperature (see detailed analysis in the Supporting Information), showing only a mild dependence on the flow rate of carrier gas (J_{Ar}) and the total pressure (P_{par}). Therefore, when the sublimation temperature is fixed, the diffusion flux is primarily dictated by the flow rate of the carrier gas (J_{Ar}) and

the total pressure (P_{tot}).

$$\frac{dm}{dt} \propto \sqrt{\frac{J_{Ar}}{P_{tot}}} \quad (3)$$

It increases with the flow rate but decreases with an increase in total pressure.

Knowledge of the boundary layer diffusion and its effect on the growth can provide useful guidance for rationally designing experimental conditions to control the growth. For instance, as shown in Figure 5E and inset, we can improve the crystalline quality of nanosheets grown at low temperatures by lowering the flow rate of the carrier gas. According to eq 2, decreasing the flow rate can lower the diffusion flux and may switch the rate-determining step from the growth reaction back to diffusion. We also found in the experiments that, by changing the flow rate of the carrier gas, the region in which high-quality nanosheets may grow can shift either downstream (by decreasing the flow rate) or upstream (by increasing the flow rate). As discussed in the preceding text, high-quality GeS nanosheets can grow only in the diffusion-limited region. This observed shift of growth zone essentially indicates a shift of the diffusion-limited regime and can be predicted from eq 2 as well. Higher diffusion flux caused by larger flow rates can shift the diffusion-limited regime (where the kinetics of the growth reaction is larger than diffusion flux) upstream with higher temperatures, while lower diffusion flux can move the growth region further downstream. This shift of the growth zone is different from what was reported in the vapor deposition growth of nanowires. For instance, the growth zone of ZnO nanowires was found to shift toward lower temperatures with higher flow rates, opposite the trend we observed in the nanosheet growth.[62] This difference further confirms that the growth behavior of chalcogenide nanosheets is indeed different from that of other nanomaterials.

CONCLUSIONS

This work presents a synthesis of GeS nanosheets using vapor deposition processes and demonstrates that the growth behavior of nanosheets is different from those of thin films and other nanomaterials (nanowires, nanotubes, and graphenes) using vapor deposition techniques. The growth of GeS nanosheets is subject to strong influences of the diffusion of the source material through the boundary layer of gas flows. The boundary layer diffusion is the rate-determining step for growth under typical experimental conditions (20−40 Torr, ∼300 °C), and high-quality nanosheets can only grow in the diffusion-limited regime. This is in stark contrast with the synthesis of other nanomaterials (nanowires, nanotubes, and graphene), which is typically reaction-limited and where the boundary layer diffusion plays a negligible role. It is also substantially different from the vapor deposition growth of thin films, whose diffusion-limited growth typically occurs at high pressure (ambient pressure, for instance) and high temperature. Additionally, high-quality thin films prefer the rate-determining step to be the growth reaction rather than diffusion as the nanosheet does. This unusual growth behavior of GeS nanosheets may be correlated with the rapid growth of the nanosheet, typically on a scale of ∼3−5 μm/min, which is almost one order of magnitude larger than that of other nanomaterials and typical thin films. Additionally, our dynamic analysis uncovers an intuitive correlation of the diffusion flux with the flow rate of the carrier gas and the total pressure in the synthetic system. We believe that this model of diffusion-limited growth may generally apply to the synthesis of other chalcogenide nanosheets, whose growth is rapid. The newly acquired knowledge for the diffusion-limited growth can provide useful guidance for the development of general paradigms to control the growth of nanosheets.

EXPERIMENTAL SECTION

Nanosheet Synthesis. The nanosheets were synthesized in a home-built CVD reactor comprising a 1 in. fused silica tube and a horizontal single-zone tube furnace (Lindberg/Blue M TF55035A). In a typical nanosheet growth, a quartz boat loaded with 10 mg of source material (GeS) powder (99.99%, Sigma-Aldrich) was place at the center of the quartz tube. A 500 μm thick and 3−5 mm wide strip of Si(100) substrate or covered with 300 nm of thermal SiO_2 was ultrasonically cleaned in acetone and isopropyl alcohol (IPA) for 5 min, respectively, and then blow-dried with high-purity nitrogen. The substrate was then placed 12−15 cm downstream from the furnace center.

The quartz tube was evacuated to a base pressure of 100 mTorr, flushed three times with high-purity Ar gas (5 N), and then flowed with Ar gas, which was controlled by a mass-flow controller. After the pressure stabilized, the furnace was heated to targeted temperatures at a rate of 50 °C/min and maintained for 10 or 2 min. The temperature at each of the substrates was measured by a Watlow wire-type thermocouple with tip diameter of 1.5 mm. After the deposition, the furnace was naturally cooled to room temperature. Typical conditions for high-quality GeS nanosheet growth include 400−500 °C source temperatures, 290−330 °C deposition temperature, with 10−30 sccm Ar flow, and at 20−40 Torr.

Nanosheet Characterization. The morphology and crystal structure of the resulting products were analyzed with a JEOL-6400 high-resolution field-emission scanning electron microscope, a JEOL-2000, and a JEOL-2010 transmission electron microscope (TEM, operated at 200 kV) with an EDX detector. Nanosheet thickness and surface topology were measured using an atomic force microscope (AFM). Samples for TEM imaging were made by dispersing a solution of nanosheets (prepared by scratching the as-synthesized products from the substrate and sonication in IPA for 10 s) onto holey carbon (Nisshin EM) or Formvar film (Ted Pella) copper grids. The nanosheets on TEM grids in the atmosphere were stable for more than one month without observable structural degeneration. Powder XRD was performed using a Rigaku X-ray diffractometer with a Cu Kα radiation source. Raman spectra were collected with a Renishaw 1000 Raman spectrometer.

Conflict of Interest: The authors declare no competing financial interest.

Acknowledgment. The authors acknowledge support from the Army Research Office (W911NF-11-1-0529). L.C. acknowledges a Ralph E. Powe Junior Faculty Enhancement Award.

Supporting Information Available: Supplemental figures. This information is available free of charge *via* the Internet at http://pubs.acs.org.

REFERENCES AND NOTES

1. Liz-Marzán, L. M.; Giersig, M. *Low-Dimensional Systems: Theory, Preparation, and Some Applications*; Kluwer Academic: Dordrecht, The Netherlands, 2003.
2. Cui, Y.; Lauhon, L. J.; Gudiksen, M. S.; Wang, J.; Lieber, C. M. Diameter-Controlled Synthesis of Single-Crystal Silicon Nanowires. *Appl. Phys. Lett.* **2001**, *78*, 2214–2216.
3. Lauhon, L. J.; Gudiksen, M. S.; Wang, D.; Lieber, C. M. Epitaxial Core-Shell and Core-Multi-Shell Nanowire Heterostructures. *Nature* **2002**, *420*, 57–61.
4. Lee, J. S.; Brittman, S.; Yu, D.; Park, H. Vapor−Liquid−Solid and Vapor−Solid Growth of Phase-Change Sb_2Te_3 Nanowires and Sb_2Te_3/GeTe Nanowire Heterostructures. *J. Am. Chem. Soc.* **2008**, *130*, 6252–6258.
5. Alivisatos, A. P. Semiconductor Clusters, Nanocrystals, and Quantum Dots. *Science* **1996**, *271*, 933–937.
6. Lieber, C. M.; Wang, Z. L. Functional Nanowires. *MRS Bull.* **2007**, *32*, 99–104.
7. Xia, Y.; Yang, P.; Sun, Y.; Wu, Y.; Mayers, B.; Gates, B.; Yin, Y.; Kin, F.; Yan, H. One-Dimensional Nanostructures: Synthesis, Characterization, and Applications. *Adv. Mater.* **2003**, *15*, 353–388.
8. Talapin, D. V.; Lee, J.-S.; Kovalenko, M. V.; Shevchenko, E. V. Prospects of Nanocrystal Solids as Electronic and Optoelectronic Materials. *Chem. Rev.* **2010**, *110*, 389–458.
9. Huang, M. H.; Mao, S.; Feick, H.; Yan, H. Q.; Wu, Y. Y.; Kind, H.; Weber, E.; Russo, R.; Yang, P. D. Room-Temperature Ultraviolet Nanowire Nanolasers. *Science* **2001**, *292*, 1897–1899.
10. Huang, Y.; Duan, X.; Wei, Q.; Lieber, C. M. Directed Assembly of One-Dimensional Nanostructures into Functional Networks. *Science* **2001**, *291*, 630–633.
11. Matte, H. S. S. R.; Gomathi, A.; Manna, A. K.; Late, D. J.; Datta, R.; Pati, S. K.; Rao, C. N. R. MoS_2 and WS_2 Analogues of Graphene. *Angew. Chem., Int. Ed.* **2010**, *49*, 4059–4062.
12. Auerbach, S. M.; Carrado, K. A.; Dutta, P. K. *Handbook of Layered Materials*; CRC Press: New York, 2004.
13. Aruchamy, A. *Photoelectrochemistry and Photovoltaics of Layered Semiconductors*; Kluwer Academic: Dordrecht, The Netherlands, 1992.
14. Radisavljevic, B.; Radenovic, A.; Brivio, J.; Giacometti, V.; Kis, A. Single-Layer MoS_2 Transistors. *Nat. Nanotechnol.* **2011**, *6*, 147–150.
15. Osada, M.; Sasaki, T. Two-Dimensional Dielectric Nanosheets: Novel Nanoelectronics from Nanocrystal Building Blocks. *Adv. Mater.* **2012**, *24*, 210–228.
16. Splendiani, A.; Sun, L.; Zhang, Y.; Li, T.; Kim, J.; Chim, C.-Y.; Galli, G.; Wang, F. Emerging Photoluminescence in Monolayer MoS_2. *Nano Lett.* **2010**, *10*, 1271–1275.
17. Liu, J.; Liu, X.-W. Two-Dimensional Nanoarchitectures for Lithium Storage. *Adv. Mater.* **2012**, *24*, 4097–4111.
18. Coleman, J. N.; Lotya, M.; O'Neill, A.; Bergin, S. D.; King, P. J.; Khan, U.; Young, K.; Gaucher, A.; De, S.; Smith, R. J.; *et al.* Two-Dimensional Nanosheets Produced by Liquid Exfoliation of Layered Materials. *Science* **2011**, *331*, 568–571.
19. Vaughn, Ii, D. D.; Patel, R. J.; Hickner, M. A.; Schaak, R. E. Single-Crystal Colloidal Nanosheets of GeS and GeSe. *J. Am. Chem. Soc.* **2010**, *132*, 15170–15172.
20. Zhang, Y.; Lu, J.; Shen, S.; Xu, H.; Wang, Q. Ultralarge Single Crystal SnS Rectangular Nanosheets. *Chem. Commun.* **2011**, *47*, 5226–5228.
21. Schliehe, C.; Juarez, B. H.; Pelletier, M.; Jander, S.; Greshnykh, D.; Nagel, M.; Meyer, A.; Foerster, S.; Kornowski, A.; Klinke, C.; *et al.* Ultrathin PbS Sheets by Two-Dimensional Oriented Attachment. *Science* **2010**, *329*, 550–553.
22. Son, J. S.; Wen, X.-D.; Joo, J.; Chae, J.; Baek, S.-i.; Park, K.; Kim, J. H.; An, K.; Yu, J. H.; Kwon, S. G.; *et al.* Large-Scale Soft Colloidal Template Synthesis of 1.4 nm Thick CdSe Nanosheets. *Angew. Chem., Int. Ed.* **2009**, *48*, 6861–6864.
23. Feng, J.; Peng, L.; Wu, C.; Sun, X.; Hu, S.; Lin, C.; Dai, J.; Yang, J.; Xie, Y. Ultrathin Nanosheets: Giant Moisture Responsiveness of VS_2 Ultrathin Nanosheets for Novel Touchless Positioning Interface. *Adv. Mater.* **2012**, *24*, 1917–1917.
24. Ithurria, S.; Tessier, M. D.; Mahler, B.; Lobo, R. P. S. M.; Dubertret, B.; Efros, A. L. Colloidal Nanoplatelets with Two-Dimensional Electronic Structure. *Nat. Mater.* **2011**, *10*, 936–941.
25. Peng, Y. Y.; Meng, Z. Y.; Zhong, C.; Lu, J.; Yu, W. C.; Jia, Y. B.; Qian, Y. T. Hydrothermal Synthesis and Characterization of Single-Molecular-Layer MoS_2 and $MoSe_2$. *Chem. Lett.* **2001**, 772–773.
26. Oyler, K. D.; Ke, X.; Sines, I. T.; Schiffer, P.; Schaak, R. E. Chemical Synthesis of Two-Dimensional Iron Chalcogenide Nanosheets: FeSe, FeTe, Fe(Se,Te), and $FeTe_2$. *Chem. Mater.* **2009**, *21*, 3655–3661.
27. Zhao, Y.; Hughes, R. W.; Su, Z.; Zhou, W.; Gregory, D. H. One-Step Synthesis of Bismuth Telluride Nanosheets of a Few Quintuple Layers in Thickness. *Angew. Chem., Int. Ed.* **2011**, *50*, 10397–10401.
28. Han, W.; Gao, M. Y. Investigations on Iron Sulfide Nanosheets Prepared *via* a Single-Source Precursor Approach. *Cryst. Growth Des.* **2008**, *8*, 1023–1030.
29. Bhaviripudi, S.; Jia, X.; Dresselhaus, M. S.; Kong, J. Role of Kinetic Factors in Chemical Vapor Deposition Synthesis of Uniform Large Area Graphene Using Copper Catalyst. *Nano Lett.* **2010**, *10*, 4128–4133.
30. Kong, D.; Dang, W.; Cha, J. J.; Li, H.; Meister, S.; Peng, H.; Liu, Z.; Cui, Y. Few-Layer Nanoplates of Bi_2Se_3 and Bi_2Te_3 with Highly Tunable Chemical Potential. *Nano Lett.* **2010**, *10*, 2245–2250.
31. Kumar, B.; Lee, D.-H.; Kim, S.-H.; Yang, B.; Maeng, S.; Kim, S.-W. General Route to Single-Crystalline SnO Nanosheets on Arbitrary Substrates. *J. Phys. Chem. C* **2010**, *114*, 11050–11055.
32. Etgar, L.; Zhang, W.; Gabriel, S.; Hickey, S. G.; Nazeeruddin, M. K.; Eychmüller, A.; Liu, B.; Grätzel, M. High Efficiency Quantum Dot Heterojunction Solar Cell Using Anatase (001) TiO_2 Nanosheets. *Adv. Mater.* **2012**, *24*, 2202–2206.
33. Zhan, Y.; Liu, Z.; Najmaei, S.; Ajayan, P. M.; Lou, J. Large-Area Vapor-Phase Growth and Characterization of MoS_2 Atomic Layers on a SiO_2 Substrate. *Small* **2012**, *8*, 966–971.
34. Lee, K. H.; Shin, H.-J.; Lee, J.; Lee, I.-y.; Kim, G.-H.; Choi, J.-Y.; Kim, S.-W. Large-Scale Synthesis of High-Quality Hexagonal Boron Nitride Nanosheets for Large-Area Graphene Electronics. *Nano Lett.* **2012**, *12*, 714–718.
35. Lee, Y.-H.; Zhang, X.-Q.; Zhang, W.; Chang, M.-T.; Lin, C.-T.; Chang, K.-D.; Yu, Y.-C.; Wang, J. T.-W.; Chang, C.-S.; Li, L.-J.; *et al.* Synthesis of Large-Area MoS_2 Atomic Layers with Chemical Vapor Deposition. *Adv. Mater.* **2012**, *24*, 2320–2325.
36. Shi, Y.; Zhou, W.; Lu, A. Y.; Fang, W.; Lee, Y. H.; Hsu, A. L.; Kim, S. M.; Kim, K. K.; Yang, H. Y.; Li, L. J.; *et al.* van der Waals Epitaxy of MoS_2 Layers Using Graphene as Growth Templates. *Nano Lett.* **2012**, *12*, 2784–2791.
37. Zeng, Z.; Yin, Z.; Huang, X.; Li, H.; He, Q.; Lu, G.; Boey, F.; Zhang, H. Single-Layer Semiconducting Nanosheets: High-Yield Preparation and Device Fabrication. *Angew. Chem., Int. Ed.* **2011**, *50*, 11093–11097.
38. Peng, H.; Dang, W.; Cao, J.; Chen, Y.; Wu, D.; Zheng, W.; Li, H.; Shen, Z.-X.; Liu, Z. Topological Insulator Nanostructures for Near-Infrared Transparent Flexible Electrodes. *Nat. Chem.* **2012**, *4*, 281–286.
39. Wu, Y. Y.; Yang, P. D. Germanium Nanowire Growth via Simple Vapor Transport. *Chem. Mater.* **2000**, *12*, 605–607.
40. Kong, J.; Cassell, A. M.; Dai, H. J. Chemical Vapor Deposition of Methane for Single-Walled Carbon Nanotubes. *Chem. Phys. Lett.* **1998**, *292*, 567–574.
41. Li, X. S.; Cai, W. W.; An, J. H.; Kim, S.; Nah, J.; Yang, D. X.; Piner, R.; Velamakanni, A.; Jung, I.; Tutuc, E.; *et al.* Large-Area Synthesis of High-Quality and Uniform Graphene Films on Copper Foils. *Science* **2009**, *324*, 1312–1314.

42. Bhaviripudi, S.; Jia, X. T.; Dresselhaus, M. S.; Kong, J. Role of Kinetic Factors in Chemical Vapor Deposition Synthesis of Uniform Large Area Graphene Using Copper Catalyst. *Nano Lett.* **2010**, *10*, 4128–4133.
43. Mohammad, S. N. Analysis of the Vapor-Liquid-Solid Mechanism for Nanowire Growth and a Model for This Mechanism. *Nano Lett.* **2008**, *8*, 1532–1538.
44. Levitt, A. P. *Whisker Technology*; John Wiley & Sons: New York, 1970.
45. Hu, J. T.; Odom, T. W.; Lieber, C. M. Chemistry and Physics in One Dimension: Synthesis and Properties of Nanowires and Nanotubes. *Acc. Chem. Res.* **1999**, *32*, 435–445.
46. Reina, A.; Jia, X. T.; Ho, J.; Nezich, D.; Son, H. B.; Bulovic, V.; Dresselhaus, M. S.; Kong, J. Large Area, Few-Layer Graphene Films on Arbitrary Substrates by Chemical Vapor Deposition. *Nano Lett.* **2009**, *9*, 30–35.
47. Jabeen, F.; Grillo, V.; Rubini, S.; Martelli, F. Self-Catalyzed Growth of GaAs Nanowires on Cleaved Si by Molecular Beam Epitaxy. *Nanotechnology* **2008**, 19.
48. Wang, Z. L. Self-Assembled Nanoarchitectures of Polar Nanobelts/Nanowires. *J. Mater. Chem.* **2005**, *15*, 1021–1024.
49. Li, X. S.; Cai, W. W.; Colombo, L.; Ruoff, R. S. Evolution of Graphene Growth on Ni and Cu by Carbon Isotope Labeling. *Nano Lett.* **2009**, *9*, 4268–4272.
50. Bachilo, S. M.; Balzano, L.; Herrera, J. E.; Pompeo, F.; Resasco, D. E.; Weisman, R. B. Narrow (n,m)-Distribution of Single-Walled Carbon Nanotubes Grown Using a Solid Supported Catalyst. *J. Am. Chem. Soc.* **2003**, *125*, 11186–11187.
51. Kong, D.; Dang, W.; Cha, J. J.; Li, H.; Meister, S.; Peng, H.; Liu, Z.; Cui, Y. Few-Layer Nanoplates of Bi_2Se_3 and Bi_2Te_3 with Highly Tunable Chemical Potential. *Nano Lett.* **2010**, *10*, 2245–2250.
52. Li, J.-M. Mass Production of Graphene-Like Single-Crystalline NbSe Nanosheets *via* Intercalant-Assisted Thermal Cleavage. *Appl. Phys. A: Mater. Sci. Process.* **2010**, *99*, 229–235.
53. Kodambaka, S.; Tersoff, J.; Reuter, M. C.; Ross, F. M. Diameter-Independent Kinetics in the Vapor-Liquid-Solid Growth of Si Nanowires. *Phys. Rev. Lett.* **2006**, *96*, 096105.
54. Antunez, P. D.; Buckley, J. J.; Brutchey, R. L. Tin and Germanium Monochalcogenide IV−VI Semiconductor Nanocrystals for Use in Solar Cells. *Nanoscale* **2011**, *3*, 2399–2411.
55. Kato, N.; Fukano, T.; Takeda, Y.; Takeichi, A.; Motohiro, T.; Kawai, S. GeS_2/Metal Thin Film Bilayered Structures as Write-Once-Type Optical Recording Materials. *J. Appl. Phys.* **2006**, *100*, 113115.
56. Huang, C. C.; Hewak, D. W.; Badding, J. V. Depostion and Characterization of Germanium Sulphide Glass Planar Waveguides. *Opt. Express* **2004**, *12*, 2501–2506.
57. Mills, K. C. *Thermodynamic Data for Inorganic Sulphides, Selenides and Tellurides*; Butterworths: London, 1974.
58. Zhu, J.; Peng, H. L.; Marshall, A. F.; Barnett, D. M.; Nix, W. D.; Cui, Y. Formation of Chiral Branched Nanowires by the Eshelby Twist. *Nat. Nanotechnol.* **2008**, *3*, 477–481.
59. Wiedemeier, H.; Schnering, H. G. V. Refinement of the Structures of GeS, GeSe, SnS and SnSe. *Z. Kristallogr.* **1978**, *148*, 295–303.
60. Daniel Mark Dobkin, M. K. Z. *Principles of Chemical Vapor Deposition*; Kluwer Academic: Dordrecht, The Netherlands, 2003.
61. Kikkawa, J.; Ohno, Y.; Takeda, S. Growth Rate of Silicon Nanowires. *Appl. Phys. Lett.* **2005**, *86*, 123109.
62. Choi, J. H.; Seo, J. S.; Cha, S. N.; Kim, H. J.; Kim, S. M.; Park, Y. J.; Kim, S. W.; Yoo, J. B.; Kim, J. M. Effects of Flow Transport of the Ar Carrier on the Synthesis of ZnO Nanowires by Chemical Vapor Deposition. *Jpn. J. Appl. Phys.* **2011**, *50*, 015001.